Engineering Materials

Tatiana Correia
Qi Zhang *Editors*

Electrocaloric Materials

New Generation of Coolers

Springer

Engineering Materials

Volume 34

For further volumes:
http://www.springer.com/series/4288

Tatiana Correia · Qi Zhang
Editors

Electrocaloric Materials

New Generation of Coolers

Springer

Editors
Tatiana Correia
National Physical Laboratory
Teddington
Middlesex
UK

Qi Zhang
Microsystems and Nanotechnology Centre
Cranfield University
Cranfield
UK

ISSN 1612-1317 ISSN 1868-1212 (electronic)
ISBN 978-3-642-40263-0 ISBN 978-3-642-40264-7 (eBook)
DOI 10.1007/978-3-642-40264-7
Springer Heidelberg New York Dordrecht London

Library of Congress Control Number: 2013953249

Printed on acid-free paper

Springer is part of Springer Science+Business Media (www.springer.com)

Preface

The electrocaloric effect was discovered in 1930 by Kobeko and Kurchatov. This was not an accidental discovery; the magnetocaloric effect was already well known, and those scientists were motivated to look for an electrical analog that seemed likely based upon symmetry considerations. Historically, this has an interesting peripheral aspect: I. Kurchatov later became director of the Soviet atom bomb project. This fact is often obscured by the fact that the original Kobeko-Kurchatov paper was published in German with names transliterated from the Cyrillic in a way that differs from modern standard rendering in English: Kurtschatow rather than Kurchatov. (Adjacent Cyrillic letters "ts" and "ch" would actually be an odd combination in Russian.) Kobeko and Kurchatov indeed found a small electrocaloric cooling effect in Rochelle Salt, but their measurements were not very quantitative, and the effect was small (ca. 0.1 K). Interest in electrocaloric phenomena resumed after World War II, and rather elegant studies were done through the 1970s and 1980s in both Russia and the USA, with Boris Strukov at Moscow State University and David Payne and Bruce Tuttle at the University of Illinois making major contributions. However, in fairness, these studies were examining an academic laboratory curiosity, not a practical method of refrigeration. This changed only in the last half-dozen years. Spurred on by the rapid developments in thin-film ceramics physics, the electrocaloric effect underwent a renaissance, led in part by Neil Mathur, myself, and a talented group of Ph.D. students and postdocs, especially Alex Mischenko, whose death at an early age was a great loss to us. At present the scope of electrocaloric research is blossoming. In addition to the popular oxide (largely perovskite-based) ferroelectrics, polymeric ferroelectrics such as vinylidene difluoride and its copolymers (especially trifluoroethylene) are moving to center-stage. Relaxor ferroelectrics are also justifiably receiving considerable attention.

Some theoretical questions remain moot: It is easier to measure polarization change than entropy change or direct temperature change (it is impossible to buy an entropy meter at your local hardware store), but the Maxwell Relations permit us to extract one from the other. Nevertheless, using the thermodynamic Maxwell Relations in relaxors—which are not in mechanical, chemical, or thermal equilibrium—seems technically unjustified. Applying equilibrium statistical mechanics to non-equilibrium phenomena is risky. So far, however, the direct measurements of change in temperature agree well with their indirect measurement via

polarization. It might be wise to see if these values depend upon frequency. The intended applications probably target three unrelated device systems: First are on-chip coolers for Si or GaAs electronics. Here the thin-film electrocalorics will be fully integrated onto Si chips in the future. Second are consumer refrigerators. My own pet application will be wine coolers (a good French red at exactly 10 °C), but medical cooling devices can be envisioned as well. Several large international corporations have already begun R&D on electrocalorics. The advantages over conventional refrigeration are small size, low power consumption, and perhaps most important—no moving parts or vibration. Military or satellite niche applications might also exist. Combination hybrid devices with magnetocaloric and electrocaloric cooling are possible. The cryogenic temperature range from say 30 mK to 4 K might also merit careful consideration as cheaper alternatives to adiabatic demagnetization. New materials are under extensive investigation. My own favorite is ammonium sulfate, whose entropy change at its order–disorder phase transition is nearly an order of magnitude larger than in most other ferroelectrics (since both the SO_4 and NH_4 ions can undergo rotational disorder). However, this material is too great an ionic conductor to function well in applied voltages. So some chemical modifications might be useful, as well as a broader search of related sulfate or ammonium compounds.

Finally, it is imperative that engineers fabricate several real working prototypes soon. Some of these may involve enhancements via circulating media, which can increase the temperature changes possible from say ca. 10 K to ca. 50 K. Demonstrations of real devices to show numerical efficiency values, cooling ranges, cooling rates, and in–out performance with heat sinks is required for "street-smart" credibility in industry. Joint industry-university partnerships are particularly desirable at present.

J. F. Scott

Contents

Electrocaloric Effect: An Introduction

Tatiana Correia and Qi Zhang

1 Introduction

For over one hundred years vapour compression techniques have dominated the design of refrigeration and air conditioning systems. The most efficient refrigerants to drive these systems were Freon gases or chlorofluorocarbons (CFCs) and hydrochlorofluorocarbons (HCFCs), which, upon entering the atmosphere, deplete the natural barrier against ultraviolet (UV) radiation through a reaction with atmospheric ozone. The rise in UV radiation exposure has led to increased rates of skin cancers and raised concerns in regards to public health [3]. A great deal of effort has gone into developing new refrigeration techniques in order to expand the benefits of artificial cooling, but also to limit, eliminate, and hopefully reverse these disastrous environmental consequences. Liquids and solids are attractive candidate mediums for new refrigeration techniques, not only because their higher mass density makes for higher energy density, but also because they avoid the release of harmful gases.

Innovative cooling technologies are recognized by many industries as a crucial part of their systems design. One example is superconductor-based technology, which requires high-sensitivity cryogenic temperature control. At the other end of the spectrum we have the Hybrid and Electric Vehicle industry, which suffers from excessive heat generated by a vehicle's mechanical and electrical systems, which in turn limits the efficiency, reliability and cost of the electrical systems. For instance, electrolytic-based capacitors used in inverters and filters cannot tolerate temperatures above 70 °C. Therefore, electric-drive vehicles are unlikely to succeed and compete with today's internal combustion engine vehicles without

T. Correia (✉)
National Physical Laboratory, Hampton Road, Teddington, MDX TW11 0LW, UK
e-mail: corretatiana@gmail.com

Q. Zhang
Department of Manufacturing and Materials, Cranfield University, Bedfordshire, MK43 OAL, UK

T. Correia and Q. Zhang (eds.), *Electrocaloric Materials*,
Engineering Materials 34, DOI: 10.1007/978-3-642-40264-7_1,

innovative and effective cooling solutions. Refrigeration through solid state medium seems attractive as it should allow for eco-friendly cooling integration at low cost.

Another example is the ever expanding microelectronics industry. In recent years, electronic miniaturization has become the focus of much interest due to the growing demand for minute, complex and lightweight devices, in which a large number of electronic components can be integrated, i.e., integrated circuits (ICs). Moore's law [18] anticipated the trend of IC development by predicting that the number of components in an IC doubles every 18-24 months. However, there is a major obstacle that may affect the course of IC development as foreseen by Moore. Nowadays, a chip may be comprised of thousands of components, which results in heat generation throughout the whole chip and in hot spots in small chip areas. As such, the future of IC relies on the development of on-chip refrigeration technology.

Wide industry demands for more efficient, flexible and environmentally friendly refrigeration have brought solid-state refrigerators to the fore as potential solutions for a new generation of coolers. Table 1 shows the efficiency of the most developed and widely used solid-state cooling technologies, benchmarking them against conventional vapour-compression refrigeration. Used in many cooling and energy harvesting applications, *thermoelectric* refrigerators are solid-state devices that convert electrical energy into a temperature gradient (known as the "Peltier effect"), or thermal energy from a temperature gradient into electrical energy (the "Seebeck effect"). Thermoelectric cooling technology is far less commonly used for refrigerative purposes than vapour-compression refrigeration due to its intrinsic and characteristically low efficiency (maximum 10 %). On the other hand, the absence of moving parts and circulating liquid, their small size and flexible shape (form factor) render thermoelectric coolers appropriate for niche applications in spot thermal management and energy harvesting. But the fact remains that they do not provide both cost and high power efficiency, which is, in fact, their major disadvantage.

Table 1 Efficiency of energy conversion in different cooling technologies [20, 27]

Novel or existing technology	Efficiency (%)	Comments
Electrocaloric cooler/ pyroelectric power generator	60–70	Small effect in bulk materials Large effect in thin films
Magnetocaloric cooler	60–70	Requires large magnetic field and therefore large magnets
Conventional fridge (vapour compression cycle)	40–50	Everything is optimised, no growth in this market
Micro-vapour-compression system	-	The technology is very difficult, hence no idea about the efficiency
Thermoelectric cooler or power generator	10	More than 60 years of extensive research has not yet delivered a practical and efficient device

Magnetic cooling is based on magnetocaloric effect, which is defined as heat driven by a magnetic field. Upon application of an external magnetic field, the magnetic domains in a ferromagnetic material are orientated in the direction of the applied field, lowering entropy and consequently raising material temperature. As the magnetic field is withdrawn, the magnetic dipoles are able to relax and absorb some heat from the crystal lattice of the material, thereby lowering its temperature. Current magnetocaloric refrigerators require either large and expensive superconducting magnets or heavy permanent magnet arrays in order to generate the large magnetic fields needed to run the devices [7], a requirement that has limited the viability of magnetic cooling on the world market. Also, due to the nature of ferromagnetic phase transitions, these cooling devices can only cool over a 20–30 K span.

Electrocaloric effect is the electrical analogue of magnetocaloric effect, and is defined as the isothermal entropy or adiabatic temperature change of a dielectric material when an electric field is applied or removed. Potentially, electrocaloric effect could be used for efficient refrigeration, air conditioning, heat pumping and for the conversion of heat flows into electrical power [17, 19]. Electrocaloric coolers display high efficiency similar to that found in magnetocaloric coolers, but offer additional benefits as solid-state cooling devices, such as, compact size, less weight, and easy device integration. As is the case with magnetocaloric refrigerators, electrocaloric cooling exploits the large entropy changes induced by an electric field associated with the changes of the lattice cell volume and strain near the phase transitions. Lately, electrocaloric cooling has been the focus of considerable interest due to the recent discovery of a giant electrocaloric effect in thin films ($\sim$12 K) [17].

2 History of Electrocaloric Cooling

Today electrocaloric cooling appears as a very promising alternative to vapour-compression refrigeration and IC thermal management. However, there has not always been such a positive perception of this technology. Table 2, where selected events that have marked the history of electrocaloric cooling are summarized, differentiates two distinct periods where its impact was perceived differently. The first of these initiated in 1878 when electrocaloric phenomena were theoretically put forward as the converse effect of pyroelectricity by William Thomson (Lord Kelvin [25]). It was only more than fifty years later that electrocaloric effect was first observed in Rochelle Salt [14] and quantitatively measured by Hautzenlaub in 1943 [9]. Although only low electrocaloric temperature change has ever been measured in Rochelle Salt ($\sim$0.003 K), these pioneer works instigated innovative research in the field of electrocaloric cooling, mainly focused on the development of new materials with enhanced cooling performance. Maximum electrocaloric performance was found by Karchevskii to occur close to phase transitions [12]. This positioned ferroelectric materials as the best electrocaloric materials of all the pyroelectric

Table 2 Events in the history of electrocaloric effect

Years	Event	References
1878	Major theoretical treatment of pyroelectricity and first prediction of electrocaloric effect	[25]
1930	Electrocaloric effect observed in Rochelle Salt	[14]
1943	Quantitative measurement of electrocaloric effect in Rochelle Salt	[9]
1962	Electrocaloric effect maximum found at Curie Temperature	[12]
1964	Electrocaloric effect measured in $SrTiO_3$	[13]
1968	Electrocaloric effect measured in doped-PZT	[24]
1977	First cryogenic electrocaloric refrigerator concept	[22]
1992	Electrocaloric effect in $PbSc_{0.5}Ta_{0.5}O_3$ ceramics	[23]
2006	Discovery of giant electrocaloric effect in $Pb_{0.05}Zr_{0.95}TiO_3$ thin films	[17]
2008	Large electrocaloric effect measured in P(VDF-TrFE) thin films	[19]
2010	Direct measurement of electrocaloric effect in thin films	[16]
2011	Negative electrocaloric effect proposed for BNT-BT ceramics	[2]

compounds. During this period electrocaloric research was dictated by specific industry demands. Electrocaloric cooling started to come into its own in the seventies at a time when scientific research was rapidly progressing in the area of superconductivity phenomena and their exploitation was deemed a priority. The reason for this resides in the fact that superconductivity devices, like SQUIDS, require temperatures below 15 K. Therefore, cryogenic cooling was seen as crucial to the viability of this technology. Consequently, low phase transition temperature electrocaloric materials, like $SrTiO_3$ and $KTaO_3$, emerged as attractive mediums and a cryogenic electrocaloric refrigerator concept was developed and tested by Raghebaugh in 1977 [22]. This was the very first electrocaloric refrigerator concept. It included $SrTiO_3$ ceramics, with electrocaloric temperature change of 0.3 K operating with a load at 4 K and a heat sink at 15 K. In the meanwhile, the possibility of other electrocaloric cooling applications began to emerge, mainly for operation at room temperature. In this context, antiferroelectric $Pb(Zr_{0.455}Sn_{0.455}Ti_{0.09})O_3$ ceramic [24], which showed an electrocaloric temperature change $\sim$1.6 K, has been put forward for room temperature cooling applications. Lead scandium tantalate, $PbSc_{0.5}Ta_{0.5}O_3$, system also attracted significant interest in room temperature electrocaloric cooling in the nineties, due to the fact that its phase transition temperature and electrocaloric effect could be tailored through processing. This system showed a remarkable electrocaloric temperature change of $\sim$2.4 K in a multilayer structure [23].

During the first six decades following the discovery of electrocaloric effect in solids, only a small number of research groups came to dedicate their research to the development of electrocaloric refrigeration. This was mainly due to the fact that only small electrocaloric effect was measured in bulk materials compared with their magnetic counterparts and thermoelectric materials, which weakened their exploitation for commercial refrigeration devices. This attitude to electrocaloric

materials was to be revolutionized in 2006, when a "giant" electrocaloric temperature change, ~12 K, was indirectly measured in $PbZr_{0.95}Ti_{0.05}O_3$ thin films close to antiferroelectric-paraelectric phase transition at 225 °C [17]. The phenomenon was attributed to the fact that larger electric field is sought to be applied in thin films rather than in bulk. Two years later, a work was published on the large electrocaloric effect (up to 12 °C) found in polyvinylidene fluoride-trifluoroethylene [P(VDF-TrFE)] thin films at 70 °C [19]. These two works were the "seed" of an explosive growth in electrocaloric research, which led to a new and promising era for electrocaloric cooling. Overall, not more than 270 scientific papers[1] have been published since 1960. Yet more than 65 % of these reports have been published in the last seven years. A large majority of these addresses the development of new ferroelectric thin films with enhanced electrocaloric effect close to room temperature. Within the last seven years an extraordinary increase of electrocaloric effect from 1.6 K doped-PZT ceramics [24] to 45.3 K in Ba-doped $PbZrO_3$ [21] thin films has been reported. But such swift progress in the field of electrocaloric materials has also brought about many reservations regarding the accuracy of electrocaloric effect measurements in thin films. Measurement of electrocaloric effect in thin films is often derived from measurements of pyroelectric coefficients rather than from direct electrocaloric measurements, which can introduce significant and unquantifiable errors through the assumptions made in relating the two effects (using thermodynamic constitutive relations). Moreover, direct measurement of electrocaloric effect is rather challenging due to the small heat capacity of a film, deviations from adiabatic conditions and heat transfer to temperature measurement devices, substrates and connections. A few attempts to directly measure electrocaloric effect in bulk and thin films were reported in 2010 [16], indicating, for most of the materials, good agreement with indirect measurements. However, a significant discrepancy has been found in relaxor materials, a fact that has been attributed by some authors to the non-thermal equilibrium nature of these materials [4].

Recent investigations have also put forward a "negative electrocaloric effect", in which the sign of change of the temperature is reversed. This was first indirectly measured in relaxor $Na_{0.5}Bi_{0.5}TiO_3$–$BaTiO_3$ (BNT-BT) ceramics. The phenomenon has been associated with a relaxor performance observed between ferroelectric and antiferroelectric phases [2]. The coexistence of positive and negative electrocaloric effect was later measured in relaxor $70PbMg_{1/3}Nb_{2/3}O_3$-$30PbTiO_3$ single crystals across different phases of the phase diagram [1]. According to this work, negative electrocaloric effect is associated with free energy changes induced by the electric field. Avenues of research have since been put forward to better understand the reversal sign of electrocaloric response in some materials and its potential for use in cooling devices [1, 15].

[1] source: Web of Science search "Electrocaloric Effect", June 2013.

3 Electrocaloric Cooling: How Does it Work?

The basic operating principles of electrocaloric refrigeration are, in principle, analogous to those of magnetic and gas compression cooling. These are constituted by the transportation of heat from a heat load to the surrounding environment through a working body (electrocaloric or magnetocaloric material or gas) that is subjected to a thermodynamic cycle. Refrigeration cycles are driven by the entropy variation of the working body (or refrigerant), whereas an electric field varies (magnetic field or pressure in the case of magnetic and vapour-compression cooling, respectively). Figure 1 shows a schematic representation of an electrocaloric cooling cycle, achieved by two adiabatic and two isothermal processes:

- *Adiabatic polarization* (A → B): An isolated electrocaloric material is subjected to a sudden increase of electric field, from E_1 to E_2, which results in constraint of the electric dipoles. Consequently, refrigerant heat capacity and entropy decrease (S_1 to S_2), and since there is no heat loss (refrigerant is isolated), the temperature of the material increases ($T_0 + \Delta T$).
- *Heat transfer* (B → C): The refrigerant is put in thermal contact with a hot reservoir (T_h), while electric field is varied from E_2 to E_3 to ensure constant refrigerant temperature. Heat is then expelled from the refrigerant to the heat reservoir. The heat expelled during this process is given by

$$Q_h = T_h \Delta S_h \tag{1}$$

where $\Delta S_h = S_3 - S_2$.

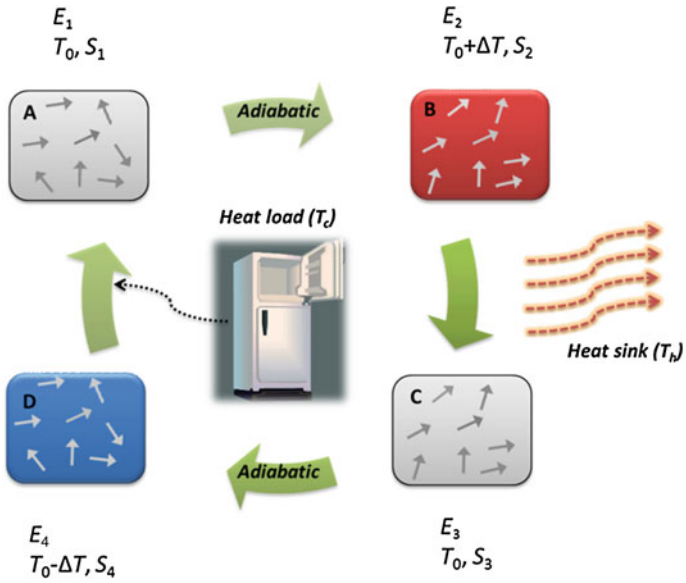

Fig. 1 Schematic diagram of an electrocaloric refrigerator cycle

- *Adiabatic depolarizing* (C → D): The electrocaloric material is again isolated from the heat reservoir while electric field is decreasing from E_3 to E_4. Electric dipole freedom degree is liberated and thus refrigerant heat capacity and entropy increase. As the material is isolated from its surroundings (adiabatic conditions), there is no heat exchange, hence the refrigerant cools down ($T_0-\Delta T$).
- *Entropy transfer* (D → A): The refrigerant is placed in thermal contact with the cold reservoir (or heat load). Heat migrates from the cold reservoir to the refrigerant, and the former then cools down to T_c. The electrocaloric refrigerant absorbs heat from the cold reservoir, expressed as

$$Q_c = T_c \Delta S_c \tag{2}$$

Although the Carnot cycle has been the most commonly reported for electrocaloric refrigeration [6, 22], other thermodynamic cycles, such as the Brayton and Ericsson cycles, have also been considered [10, 11].

The input electrical work W supplied by the electrocaloric material over a cycle is then given by

$$W = Q_h - Q_c = T_h \Delta S_h - T_c \Delta S_c \tag{3}$$

This equation is valid for ideal reversible cycles where $\Delta S_c = \Delta S_h$, but in real cooling cycles further entropy may be generated through irreversible processes and thus,

$$S_{gen} + \Delta S_c = \Delta S_h \tag{4}$$

where S_{gen} is the entropy from irreversible processes. And therefore, the net electrical energy W can be re-written as

$$W = (T_h - T_c)\Delta S_c + T_h S_{gen} \tag{5}$$

Possible sources for irreversibility of the cooling cycle are electrocaloric material hysteresis and/or heat loss due to heat transfer processes, either through regenerators [10, 11] or heat switches [6]. This, in turn, affects the efficiency of the cooling cycle. The coefficient of performance (COP) allows evaluation of cooling cycle performance and assessment of its efficiency, where COP is defined as the relationship between the heat absorbed at the cold reservoir Q_c and the net work performed by the electrocaloric material W,

$$COP = \frac{Q_c}{W} \tag{6}$$

For an ideal Carnot cycle, it is given by

$$COP_{CR} = \frac{T_c}{T_h - T_c} \tag{7}$$

Thus, efficiency of a refrigerator relative to an ideal Carnot cycle (η) is defined as

$$\eta = \frac{COP}{COP_{CR}} \tag{8}$$

Using Eqs 6–8 one can express η as

$$\eta = \frac{1}{1 + \frac{T_h S_{gen}}{\Delta S_c (T_h - T_c)}} \tag{9}$$

Note that from Eq. 9, it is clear that a refrigeration machine approximates an ideal Carnot cycle whenever S_{gen} is small and/or the product of $\Delta S_c(T_h - T_c)$ is large.

4 Electrocaloric Materials

In an electrocaloric cooling cycle, the electrocaloric material is a crucial part of system design, as heat is pumped in and out through the material and cooling performance is reliant on its ability to generate and reverse heat.

4.1 Electrocaloric Effect

A solid material that is subjected to a small change in strain dx_{ij}, electric displacement dD_i and entropy dS, is described by the first and second law of thermodynamics by a change in the integral energy dU as follows:

$$dU = X_{ij} dx_{ij} + E_i dD_i + TdS \tag{10}$$

where X_{ij}, E_i and T are stress, electric field and temperature, respectively. Note that the subscripts indicate the tensorial nature of these physical properties and independent variables. Since in most experimental situations temperature, electric field and stress are independent variables, a Legendre transformation can be performed by defining Gibbs free energy, G, as follows:

$$G = U - X_{ij} x_{ij} - E_i D_i - TS \tag{11}$$

and thus,

$$dG = -x_{ij} dX_{ij} - D_i dE_i - SdT \tag{12}$$

By considering a solid as an isolated material, the following is obtained from the derivative of Gibbs free energy:

$$\left(\frac{\partial G}{\partial X_{ij}}\right)_{E,T} = -x_{ij}, \left(\frac{\partial G}{\partial E_i}\right)_{X,T} = -D_i, \left(\frac{\partial G}{\partial T}\right)_{E,X} = -S \tag{13}$$

These equations represent the so-called principal effects, namely elasticity, dielectric permittivity and heat capacity, respectively. Further derivations obtained from Eq. 13 are the Maxwell relations:

$$-\left(\frac{\partial^2 G}{\partial X_{ij}\partial E_k}\right)_T = \left(\frac{\partial x_{ij}}{\partial E_k}\right)_{X,T} = \left(\frac{\partial D_k}{\partial X_{ij}}\right)_{E,T} = d_{ijk} \tag{14}$$

$$-\left(\frac{\partial^2 G}{\partial X_{ij}\partial T}\right)_E = \left(\frac{\partial x_{ij}}{\partial T}\right)_{X,E} = \left(\frac{\partial S}{\partial X_{ij}}\right)_{E,T} = \alpha_{ij} \tag{15}$$

$$-\left(\frac{\partial^2 G}{\partial E_i\partial T}\right)_X = \left(\frac{\partial D_i}{\partial T}\right)_{X,E} = \left(\frac{\partial S}{\partial E_i}\right)_{X,T} = p_i \tag{16}$$

These disclose that coefficients for converse piezoelectric effect are numerically equal to direct effect, i.e., d_{ijk}. Similarly, thermal expansion coefficients are the same as those for piezocaloric effect (α_{ij}), and pyroelectric coefficient is equal to that of electrocaloric effect (p_i).

In particular, Eq. 16 represents electrothermal coupling in solids, indicating that pyroelectric effect is thermodynamically equivalent to electrocaloric effect. From these equations one may conclude that electrocaloric entropy variation at constant X and in isothermal conditions is then given by

$$dS = \left(\frac{\partial D_i}{\partial T}\right)_{X,E} dE_j \tag{17}$$

and thus,

$$\Delta S = \int_{E_1}^{E_2} \left(\frac{\partial D_i}{\partial T}\right)_{X,E} dE_j \tag{18}$$

where E_1 and E_2 are the starting and final applied fields, respectively. Considering the definition of heat capacity, C

$$C = T\left(\frac{\partial S}{\partial T}\right)_E \tag{19}$$

Electrocaloric effect can be described by the adiabatic temperature change as follows

$$dT = -\frac{T}{C}\left(\frac{\partial D_i}{\partial T}\right)_{X,E} dE_j \tag{20}$$

and,

$$\Delta T = -\frac{T}{C}\int_{E_1}^{E_2}\left(\frac{\partial D_i}{\partial T}\right)_{X,E} dE_j \tag{21}$$

Note that Eq. 21 considers C independent of E.

4.2 Performance of Electrocaloric Materials

The performance of an electrocaloric refrigerator is dictated by the properties of the refrigerant (electrocaloric material), design of the refrigeration cycle and the selection and organization of heat transfer fluid, switches and exchanges. Hence, the selection of an electrocaloric medium cannot be restricted to large electrocaloric effect, but should also take into account other features, namely the amount of heat that the electrocaloric refrigerant transfers per cycle between cold and hot reservoirs (refrigerant capacity); efficiency, determined from existing irreversible processes; characteristic time of heat flow; cost of raw materials and preparation; environmental concerns, etc.

- *Electrocaloric Effect*

When selecting a material for use as a working body in electrocaloric refrigeration, one must ensure that its electrocaloric effect, translating as entropy variation ΔS and temperature change ΔT whilst altering electric field, is large. From Eqs. 18 and 21 it follows that electrocaloric effect may be predicted from temperature evolution of polarization induced by an electric field. Thus far this has been the most common method used to assess electrocaloric effect in dielectric materials, and has been shown to be in agreement with direct measurements of electrocaloric heat and temperature change in some systems [16].

Yet large discrepancies of electrocaloric effect measured indirectly and directly have been reported in some materials, namely in ferroelectric relaxors (See Chap. 6 for more details regarding indirect and direct measurements of electrocaloric effect). One possible explanation for these discrepancies is the fact that Eqs. 18 and 21 are derived from state equations, which consider a system in equilibrium with its surroundings. However, this does not apply to relaxors, where dielectric response is strongly dependent on the thermal history. Therefore, Eqs. 18 and 21 do not suffice to describe electrocaloric effect accurately.

- *Refrigerant Capacity*

In order to benchmark magnetocaloric materials in a reversible cycle, Wood and Potter [26] have defined the concept of refrigerant capacity (RC) as

$$RC = \Delta S_c \times (T_h - T_c) \tag{22}$$

where $\Delta S_c = \Delta S_h$ and, according to the authors, the choice of T_h and T_c optimizes *RC* value. *RC* is the heat that may be transferred through the magnetocaloric material between the cold and hot reservoirs at T_c and T_h, respectively.

Gshneider and co-authors [8], on the other hand, have suggested that *RC* may be calculated from the integrated area under ΔS-T curve by using temperature limits at half-maximum of the ΔS peak (*FWHM*) as follows

$$RC = \int_{T_c}^{T_h} \Delta S dT \approx -\Delta S_m \times FWHM \tag{23}$$

where ΔS_m corresponds to peak maximum.

Although *RC* values have been commonly used to compare magnetocaloric materials for magnetic refrigeration, they have not often been reported in electrocaloric materials. Nonetheless, due to the recent rising interest in electrocaloric cooling, it has become of utmost importance to define a universal metric to benchmark electrocaloric and magnetocaloric materials. *RC* has been put forward as a valuable metric for this purpose [5].

- *Electric and Thermal Hysteresis*

The deviation of a refrigeration cycle from an ideal reversible Carnot cycle is related with several irreversible processes that are intrinsic to either the refrigerant (thermal and electrical hysteresis) or the thermodynamic cycle (losses during heat exchange). As seen in Eq. 9, efficiency of an electrocaloric cooling cycle increases by decreasing the contribution of any hysteretic mechanism (S_{gen}).

Thermal hysteresis is usually observed near a first-order phase transition in ferroelectrics, which undergoes a discontinuous phase transition. Also, "glassy" state in relaxors due to polar nano-regions at low temperatures brings about a non-ergodic response, translating as large thermal hysteresis in electrocaloric performance. This has been confirmed by experiments carried out on $93PbMg_{1/3}Nb_{2/3}O_3$-$7PbTiO_3$ thin films [4]. The large thermal hysteresis apparent within the studied temperature range is indicative of the occurrence of an irreversible cycle when said films are used as refrigerants.

Ferroelectric materials exhibit also significant *electrical hysteresis*. Heat loss underlying such hysteresis brings about an irreversible thermodynamic cycle, i.e., $\Delta S_c \neq \Delta S_h$.

- *Heat Flow Time Scale*

Heat flow time scale is yet another parameter to be considered when assessing electrocaloric materials. This should be less than the time scale for the opening and closing of heat switches or fluid circulation, thereby ensuring completion of heat flow from the thin film to the hot reservoir (or inversely, from the cold reservoir to the thin film). Consequently, identifying heat flow time scale in a material is a determining factor when selecting a refrigeration cycle frequency that best optimizes cooling efficiency.

- *Cost and Environmental Issues*

In order to best assess a material as to its viability as an electrocaloric refrigerant one should keep in mind not only basic parameters, such as electrocaloric effect and efficiency, but also economic sustainability and environmental impact.

The majority of electrocaloric materials reported so far were processed by the conventional solid-state reaction (ceramics), and by sol–gel method or tap casting in the case of thin films and polymers. These methods are known to result in homogeneous film, and to be cost efficient, as raw materials and processing equipment are rather inexpensive in comparison to those deployed in other film growth techniques. In addition, unlike magnetocaloric materials, which require a large magnetic field and thus very powerful and expensive magnets, electrocaloric thin films may display pronounced electrocaloric effect with application of more modest voltages, which suggests the viability of a low cost operating device.

The main driving force behind such great investment, interest and effort in the development of alternative cooling technologies are environmental issues connoted with HCFCs gases, which are used in vapour-compression refrigeration. Electrocaloric refrigeration has come to prominence as a promising eco-friendly cooling technology as it does not involve the emission of gases into the atmosphere. It should be noted, however, that the majority of electrocaloric materials studied so far are lead-based compositions. Lead is a toxic element for which special facilities are required during handling in order to minimize risk to health and to the environment. Nonetheless, much remains to be done to improve safe lead waste disposal and recycling procedures.

5 Outline

Driven by the recent development of electrocaloric materials, electrocaloric cooling is emerging as a promising solution for environmentally-friendly and integrated refrigeration. The publication of this book appears to be timely, at a stage when electrocaloric materials research is active as never before and the exploitation of their promising potential has become the main driving force for the community working in this particular field of science. In this context, this book attempts to provide a comprehensive description of electrocaloric materials and their properties, more specifically those associated with their performance in a real cooler. This work is divided into ten main chapters:

The current chapter, Chap. 1 “Electrocaloric Effect: an introduction”, aims to introduce the reader to the motivation behind the exploitation of electrocaloric materials for cooling applications by presenting the economic, social and technological relevance of alternative refrigeration technologies within the framework of the history of electrocaloric materials. It also underscores the crucial role of an electrocaloric material in the design of an electrocaloric cooler whilst pointing out the main parameters to be taken into account when selecting an electrocaloric material.

Chapter 2, "Electrothermal Coupling in Polar Dielectric Materials and Thin Films", describes a thermodynamic methodology that can be deployed to identify the influence of factors controlling the electrocaloric and pyroelectric performance of thin film materials, including Curie temperature, phase change characteristics, constitutive properties and external parameters of electrical and mechanical boundary conditions.

Chapter 3, "Electrocaloric Effect In Relaxor Ferroelectric-based Materials", provides an overview of electrocaloric behaviour and characteristics in ferroelectric-based inorganic relaxor materials by reviewing experimental results of two important materials systems, PMN-PT and PST, as well as the reasoning behind the behaviours observed.

Chapter 4, "Electrocaloric Effect In Multilayer Structures", assesses the performance of a refrigerator based on multilayer capacitor geometry for electrocaloric cooling applications through the use of appropriate thermal models.

Chapter 5, "Electrocaloric Polymers", reveals the presence of large electrocaloric effect in relaxor ferroelectric polymers due to relatively short polar-correlation length and very high breakdown field (> 400 MV/m).

Chapter 6, "Lead-free and "Exotic" Electrocaloric Materials", introduces the reader to lead-free electrocaloric materials, whilst pointing out essential factors associated with the electrocaloric effect in such materials, among them ferroelectric phase transition, polarization, dipole entropy or heat capacity evaluations. New structures of polar and nonpolar materials are put forward as promising pointers towards lead-free and high power electrocaloric cooling.

Chapter 7, "Indirect and Direct Measurements of the Electrocaloric Effect", reviews and compares indirect and direct electrocaloric effect measurements. Examples of direct electrocaloric effect measuring for a number of materials in the form of bulk, thick and thin films are given.

Chapter 8, "New Approaches to Electrocaloric-Based Multilayer Cooling", simulates a number of electrocaloric structures based on thermodynamic processes and demonstrates how a multilayer structure is, in fact, a rational and viable solution for an EC-based cooling structure.

Chapter 9, "Energy Harvesting From Temperature: Use of Pyroelectric and Electrocaloric Properties", focuses on energy harvesting from thermal variations using pyroelectric and electrocaloric materials. In particular, in the case of an electric field of which the output of "electrocaloric" energy is more pronounced when in play in the vicinity of structural phase transitions, where pyroelectric activity is highly nonlinear.

Chapter 10, "Outlook for Electrocaloric Research" underlines the challenges that need to be addressed in order to make practical application of electrocaloric cooling possible. These range from development of new and more reliable electrocaloric materials to challenges related with measurement, heat transfer and scale-up.

References

1. Axelsson, A.K., Le Goupil, F., Dunne, L.J., Manos, G., Valant, M., McN, N.: Alford, Microscopic interpretation of sign reversal in the electrocaloric effect in a ferroelectric $PbMg_{1/3}Nb_{2/3}O_3$-30$PbTiO_3$ single crystal. Appl. Phys. Lett. **102**, 102902 (2013)
2. Bai, Y., Zheng, G., Shi, S.: Abnormal electrocaloric effect of $Na_{0.5}Bi_{0.5}TiO_3$–$BaTiO_3$ lead-free ferroelectric ceramics above room temperature. Mat. Res. Bull. **46**, 1866–1869 (2011)
3. Cline, W.R.: The economics of global warming. Institute for International Economics, Washington (1992)
4. Correia, T.M., Young, J.S., Whatmore, R.W., Scott, J.F., Mathur, N.D., Zhang, Q.: Investigation of the electrocaloric effect in a $PbMg_{1/3}Nb_{2/3}O_3$-$PbTiO_3$ relaxor thin film. Appl. Phys. Lett. **95**, 182904 (2009)
5. Correia, T.M., Kar-Narayan, S., Young, J.S., Scott, J.F., Mathur, N.D., Whatmore, R.W., Zhang, Q.: PST thin films for electrocaloric coolers. J. Phys. D Appl. Phys. **44**, 165407 (2011)
6. Epstein, R.I., Malloy, K.J.: Electrocaloric devices based on thin-film heat switches. J. Appl. Phys. **106**, 064509/1–064509/7 (2009)
7. Gschneidner Jr, Pecharsky, K.A., Magnetocaloric, V.K.: Materials. Annu. Rev. Mater. Sci. **30**, 287–429 (2000)
8. Gschneidner Jr, K.A., Pecharsky, V.K., Tsokol, A.O.: Recent developments in magnetocaloric materials. Reports on Progress in Physics **68**(6), 1479–1539 (2005)
9. Hautzenlaub, J.F.: Electric and dielectric behavior of potassium dihydrogen phosphate, PhD Thesis, Mass. Inst. of Technology (1943)
10. He, J., Chen, J., Zhou, Y., Wang, J.T.: Regenerative characteristics of electrocaloric Stirling or Ericsson refrigeration cycles. Energy Conv. Manag. **43**, 2319–2327 (2002)
11. He, J., Chen, J., Wang, J.T., Hua, B.: Inherent regenerative losses of a ferroelectric Ericsson refrigeration cycle. Int. J. Therm. Sci. **42**, 169–175 (2003)
12. Karchevskii, A.I.: Electrocaloric effect in polycrystalline $BaTiO_3$. Sov. Phys. Sol. Stat. **3**, 2249 (1962)
13. Kikuchi, A., Sawaguchi, E.: Electrocaloric effect in $SrTiO_3$. J. Phys. Soc. Jpn. **19**, 1497 (1964)
14. Kobeko, P., Kurtschatov, J.: Dielectrische Eigenshaften der Seignettesalykristalle. Zeit. Phys. **66**, 192 (1930)
15. Li, B., Wang, J.B., Zhong, X.L., Wang, F., Zeng, Y.K., Zhou, Y.C.: The coexistence of the negative and positive electrocaloric effect in ferroelectric thin films for solid-state refrigeration. EPL **102**, 47004 (2013)
16. Lu, S.G., Rožič, B., Zhang, Q.M., Kutnjak, Z., Pirc, R., Lin, M., Li, X., Gorny, L.: Comparison of directly and indirectly measured electrocaloric effect in relaxor ferroelectric polymers. Appl. Phys. Lett. **97**, 202901 (2010)
17. Mischenko, A.S., Zhang, Q., Scott, J.F., Whatmore, R.W., Mathur, N.D.: Giant electrocaloric effect in thin film $PbZr_{0.95}Ti_{0.05}O_3$. Science **311**, 1270 (2006)
18. Moore, G.E.: Cramming more components onto integrated circuits, Electronics **38**, 114–117 (1965)
19. Neese, B., Chu, B., Lu, S.G., Wang, Y., Furman, E., Zhang, Q.M.: Large electrocaloric effect in ferroelectric polymers near room temperature. Science **321**, 821 (2008)
20. Pakhomov, O.V., Karamenko, S.F., Semenov, A.A., Starkov, A.S., Eskov, A.V.: Thermodynamic estimation of cooling efficiency using an electrocaloric solid-state line. Tech. Phys. **55**, 1155–1160 (2010)
21. Peng, B., Fan, H., Zhang, Q.: A Giant Electrocaloric Effect in Nanoscale Antiferroelectric and Ferroelectric Phases Coexisting in a Relaxor $Pb_{0.8}Ba_{0.2}ZrO_3$ Thin Film at Room. Adv. Func. Mat. **23**, 2987–2992 (2013)
22. Radebaugh, R., Lawless, W.N., Siegwarth, J.D., Morrow, A.J.: Feasibility of electrocaloric refrigeration for the 4–15 K temperature range. Cryogenics **19**, 187–208 (1979)

23. Shebanovs, L., Borman, K., Lawless, W.N., Kalvane, A.: Electrocaloric effect in some perovskite ferroelectric ceramics and multilayer capacitors. Ferroelectrics **273**, 137–142 (2002)
24. Thacher, P.D.: Electrocaloric effects in some ferroelectric and antiferroelectric PbZrTiO3 compounds. J. Appl. Phys. **39**, 1996 (1968)
25. Thomson, W. On the thermoelastic, thermomagnetic and pyroelectric properties of matter. Phil. Mag. **5**, 4–26 (1878)
26. Wood, M.E., Potter, W.H.: General analysis of magnetic refrigeration and its optimization using a new concept: maximization of refrigerant capacity. Cryogenics **25**, 667–683 (1985)
27. Zimm, C., Jastrab, A., Sternberg, A., Pecharsky, V.K., Gschneidner, K. Jr., Osborne, M., Anderson, I.: Description and performance of a near-room temperature magnetic refrigerator. Adv. Cryog. Eng. **43**, 1759 (1998)

Constitutive Modeling of Electrothermal Properties in Polar Dielectric Materials and Thin Films

Jialan Zhang, S. Pamir Alpay and George A. Rossetti Jr.

1 Introduction

The electrothermal (electrocaloric and pyroelectric) properties of ferroelectric thin films have recently attracted considerable interest for their applications in active solid-state cooling and infrared sensing devices. The electrocaloric effect is a coupling between the electrical and thermal properties of a dielectric solid wherein an adiabatic change in temperature (ΔT) is produced in response to a change in applied electric field. The electrocaloric effect and the converse effect of pyroelectricity are described by the same property coefficient, $p = (\partial S/\partial E)_T = (\partial P/\partial T)_E$ where S is entropy, T is temperature, E is electric field, and P is the electric polarization [21]. The property coefficient p is non-zero only for materials with symmetries referred to one of the ten polar point groups, to which all ferroelectric crystals belong. The temperature change resulting from the electrocaloric effect is analogous to adiabatic demagnetization, which has long been used to cool cryogenic systems to temperatures approaching absolute zero [29]. Like magnetocaloric materials, solid-state coolers based on electrocaloric materials may provide efficiency, size, weight, and device integration benefits relative to conventional vapor compression systems. Electrocaloric materials based on ferroelectrics are known to have high electrothermal conversion factors ($\sim$0.95) and a maximum in response that can be varied over a wide temperature range ($\sim$100–800 K) according to the temperature of the ferroelectric Curie point [17]. The ease of applying electric as opposed to magnetic fields makes electrocaloric coolers especially attractive for cooling device applications.

Although ferroelectric materials have attracted attention for use in solid-state coolers and pyroelectric energy harvesters since the 1960s [8, 12, 41], early measurements at low electric fields demonstrated only small temperature changes,

J. Zhang · S. Pamir Alpay · G. A. Rossetti Jr. (✉)
Department of Materials Science and Engineering and Institute of Materials Science, University of Connecticut, 97 North Eagleville Road, U-3136, Storrs, CT 06269-3136, USA
e-mail: rossetti@ims.uconn.edu

T. Correia and Q. Zhang (eds.), *Electrocaloric Materials*, Engineering Materials 34, DOI: 10.1007/978-3-642-40264-7_2,

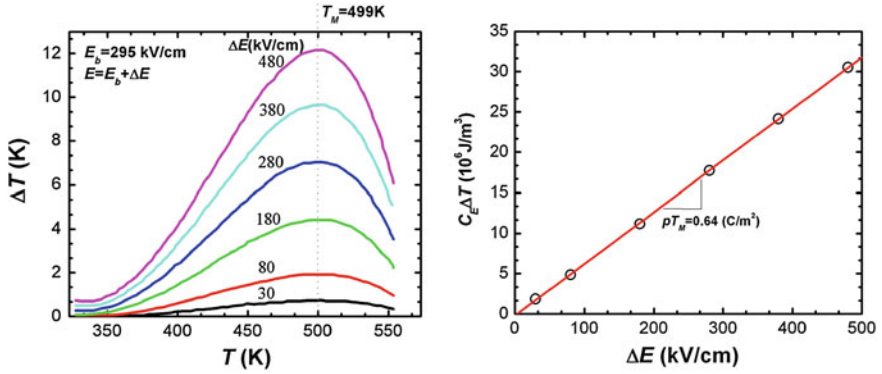

Fig. 1 Adiabatic temperature change ΔT (*left*) and corresponding change in energy density $C_E\Delta T$ (*right*) measured at different electric field levels for a PZT thin film, adapted from [24, 25]

$\Delta T \sim 0.1$ K. Interest in electrocaloric cooling systems was revitalized in 2006 when it was demonstrated that thin film perovskite-structured ferroelectrics with low defect densities could support field strengths of 1,000 k V cm^{-1}, producing a two order of magnitude increase in adiabatic temperature change, $\Delta T > 10$ K [24, 25]. Experimental data demonstrating the observed 'giant' electrocaloric ΔT and the corresponding reversible change in energy density, $Q^{\text{rev}} = C_E\Delta T$ (where C_E is the specific heat at constant electric field), are shown for a lead zirconate-titanate [Pb(Zr,Ti)O_3, PZT] thin film in Fig. 1.

Thermodynamic analyses and constitutive modeling carried out on thin film ferroelectric materials (which will be discussed in detail in Sect. 3) showed that that the large ΔT as observed experimentally at high electric field strengths is, in fact, intrinsic to the strain-free film [1, 2, 43]. The observed and computed pyroelectric coefficients are comparable, $p \cong -1{,}200$ Cm^{-2} K^{-1} near the maximum temperature (T_M), a value that is typical of ferroelectric materials near their Curie points. Since that time, numerous theoretical and experimental studies confirming these findings have been carried out [7, 9, 18, 22, 27, 33, 37] wherein it has been found that the electrocaloric temperature changes reported for ferroelectric thin films are comparable to those reported for thermoelectric-based thin film coolers [35]. As a consequence, optimization of the chemistry, structure, deposition and architecture of ferroelectric thin films may now offer the potential to make electrocaloric materials competitive with thermoelectric materials for active solid-state cooling applications.

Indeed, advances in the growth and processing of epitaxial thin films, polycrystalline ferroelectric ceramics and single crystals, and ferroelectric polymers that achieve low defect densities now make it possible to attain much higher field strengths in these materials. At the same time, progress in the application of dielectric materials to high energy density capacitors, thin film pyroelectric sensing and memory devices, and single crystal piezoelectric transducers provide numerous possibilities for achieving trade-offs among materials properties, form

factors, and fabrication processes suitable for electrocaloric devices. High capacity thin-film architectures involving inter-digitated or other electrode configurations enabling the application of high electric fields while simultaneously reducing volumetric requirements can be envisioned. If realized, solid-state cooling devices could offer significant advantages when compared to thermoelectric-based technologies.

The structural families comprising perovskites, Aurivillius phases, and tungsten bronzes admit a very wide range of isomorphous ion substitutions, making it possible to adjust the crystal lattice parameters, the Curie temperature, and the order and nature of the paraelectric to ferroelectric transition (see Chap. 6 for more details). Relaxor ferroelectric materials, in particular, are expected to exhibit unusually high electrocaloric properties due to the configurational entropy change associated with the large change in macroscopic polarization induced by modest electric field strengths. For relaxor ferroelectric materials, the electrocaloric effect arising due to the spontaneous loss of macroscopic polarization on lifting of the field becomes analogous to adiabatic demagnetization in magnetocaloric materials based on super-paramagnetic phenomena [29]. All of these attributes make perovskite and layer-structured ferroelectric materials especially appealing as objects for investigations of electrothermal coupling in thin film ferroelectrics. The potential for finding lead-free materials makes Aurivillius phase and tungsten bronze materials particularly attractive. Alternatively, a series of reports on polyvinylidene fluoride (PVDF)-based ferroelectric copolymer and terpolymer films have shown electrocaloric effects that are comparable to those observed in ceramic materials [27]. The nature of the ferroelectric transition in these materials may also be varied from normal to relaxor behavior.

Because practical electrocaloric materials exhibit a broad range of ferroelectric behaviors, to be successfully employed in practical cooling devices, the complex phenomena in ferroelectric materials require investigation using both computational and experimental approaches. A thermodynamic methodology that can be used to identify the influence of factors controlling the electrocaloric and pyroelectric performance of thin film materials, including Curie temperature, phase change characteristics, constitutive properties and external parameters of electrical and mechanical boundary conditions is described below.

2 Thermodynamic Behavior of Electrothermal Materials

2.1 Electrothermal Coupling in Ferroelectric Materials

The coupling between electric and thermal fields in polar dielectric solids gives rise to the electrothermal (electrocaloric and pyroelectric) effects. In ferroelectric materials, the direction of the polarization vector $\boldsymbol{P}$ can be reoriented among symmetry equivalent crystallographic directions under the application of an

electric field, $\boldsymbol{E}$. Large electrocaloric effects are expected in ferroelectric materials because of the strong temperature variation of the modulus $P = |\boldsymbol{P}|$ that occurs near the Curie temperature, or alternatively, due to changes in both the modulus *and* direction of $\boldsymbol{P}$ near the temperatures of any inter-ferroelectric phase transitions that may occur between different symmetry ferroelectric phases. In general, the application of an electric field $\boldsymbol{E}$ conjugate to the polarization vector $\boldsymbol{P}$ destroys these phase changes. However, for suitably small field strengths a temperature interval exists for which the contribution of the phase change to the temperature derivative $(dP/dT)_E$ does not vanish, giving rise to large electrocaloric effects.

The reversible change of internal energy (dU) in an elastic dielectric solid follows from the first and second laws of thermodynamics,

$$dU = TdS + \sigma_{ij}du_{ij} + E_i dD_i \tag{1}$$

where T, σ_{ij} are temperature and (external) stress, and dS, du_{ij}, and dD_i are the changes in entropy, strain, and dielectric displacement, respectively. The dielectric displacement D_i is given by the constitutive relation,

$$D_i = \varepsilon_0 E_i + P_i \tag{2}$$

where ε_0 is the dielectric permittivity of vacuum. The total scalar free energy density describing the polar dielectric solid is

$$F = U - TS - \sigma_{ij}u_{ij} - E_i D_i \tag{3}$$

and taking the differential of F and substituting Eq. 1 into 3 yields,

$$dF = -SdT - u_{ij}d\sigma_{ij} - D_i dE_i. \tag{4}$$

As F is an exact differential, we have,

$$dF = \left(\frac{\partial F}{\partial T}\right)_{\sigma,E} dT + \left(\frac{\partial F}{\partial \sigma_{ij}}\right)_{T,E} d\sigma_{ij} + \left(\frac{\partial F}{\partial E_i}\right)_{T,\sigma} dE_i. \tag{5}$$

Equations 4 and 5 give relations for the thermal, elastic, and dielectric responses of the system,

$$\left(\frac{\partial F}{\partial T}\right)_{\sigma,E} = -S, \left(\frac{\partial F}{\partial \sigma_{ij}}\right)_{T,E} = -u_{ij}, \left(\frac{\partial F}{\partial E_i}\right)_{T,\sigma} = -D_i \tag{6}$$

Differentiating the set of Eq. 6, Maxwell relations giving the material compliances of the system are obtained, e.g.:

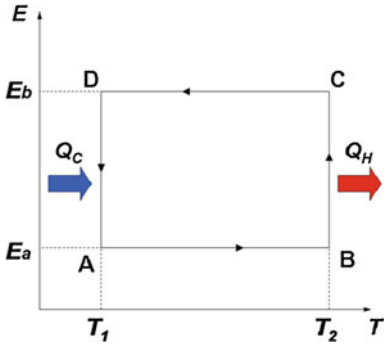

Fig. 2 Schematic of an electrocaloric Ericsson cooling cycle

$$
\begin{aligned}
-\left(\frac{\partial^2 F}{\partial T \partial \sigma_{ij}}\right)_E &= \left(\frac{\partial S}{\partial \sigma_{ij}}\right)_{E,T} = \left(\frac{\partial u_{ij}}{\partial T}\right)_{\sigma,E} \\
-\left(\frac{\partial^2 F}{\partial \sigma_{ij} \partial E_i}\right)_T &= \left(\frac{\partial u_{ij}}{\partial E_i}\right)_{\sigma,T} = \left(\frac{\partial D_i}{\partial \sigma_{ij}}\right)_{E,T} \\
-\left(\frac{\partial^2 F}{\partial E_i \partial T}\right)_\sigma &= \left(\frac{\partial D_i}{\partial T}\right)_{\sigma,E} = \left(\frac{\partial S}{\partial E_i}\right)_{\sigma,T}
\end{aligned}
\tag{7}
$$

The last relation gives the definition of the pyroelectric coefficient, and is valid for all polar dielectric solids.

$$
(p_i)_\sigma = \left(\frac{\partial^2 F}{\partial E_i \partial T}\right)_\sigma = \left(\frac{\partial D_i}{\partial T}\right)_{\sigma,E} = \left(\frac{\partial S}{\partial E_i}\right)_{\sigma,T} \tag{8}
$$

For a ferroelectric material, the adiabatic temperature change ΔT corresponding to a field change of magnitude $\Delta E = E_b - E_a$ can then be explicitly calculated by integration of Eq. 8:

$$
\Delta T(T, E_i, \sigma) = -\int_{E_a}^{E_b} \frac{T}{C_E(T, E_i, \sigma)} \left(\frac{\partial P_i(T, E_i, \sigma)}{\partial T}\right)_E dE_i \tag{9}
$$

The partial derivative on the right hand side of Eq. 9 is primarily controlled by the nature of the ferroelectric transition and plays an important role in determining the electrothermal coupling properties of ferroelectric materials. In thin film structures, the order of the ferroelectric transition may be changed by the chemical composition, as in solid solution ferroelectrics, and/or by a change in the mechanical boundary conditions arising from heteroepitaxial and thermal expansion mismatch with the substrate [3–5, 36, 46]. In general, it is expected that adjusting conditions to produce a transition lying close to a tricritical point (i.e., a crossover from first-order to second-order behavior) will always produce the largest equilibrium electrocaloric response, since the derivative $(dP/dT) \rightarrow \infty$ at this point [40].

2.2 Electrocaloric Cooling Cycles

Electrocaloric materials employed in practical cooling device applications must make use of an appropriate thermodynamic cycle. One example is the Ericsson cycle depicted schematically in Fig. 2. The cycle consists of two constant field steps at E_a and E_b and two isothermal steps at T_1 and T_2. If the electrocaloric material is operated under conditions corresponding to the maximum in response at T_M as shown in Fig. 1, the reversible energy density change occurring as a result of a field change $\Delta E = E_b - E_a$ reduces to $Q^{rev} \cong T_M\, p\Delta E$. The right-hand panel of Fig. 1 shows that this simple relation is approximately obeyed during a field step corresponding to one-half the cycle depicted in Fig. 2, for example, the step corresponding to the segment $B \rightarrow C$. A polar dielectric of volume V operates as a heat pump when a time varying electric field $E_i(t)$ having extrema with values E_b and E_a is impressed on its surfaces. Because the electrocaloric temperature change that results is a volume effect over V, the cycle along the path $A \rightarrow B \rightarrow C \rightarrow D$ can produce useful cooling at the heat source in a bulk material only if the heat flux is rectified. Several methods of doing so utilizing micro-electro-mechanical (MEMS) or thermoelectric thermal switches located at the heat source and sink have been proposed [13, 15, 19, 23], with each switch being alternately open or closed during one-half cycle of operation.

The particular form of the function $E_i(t)$ is expected to depend on the details of the cooling device design. For example, $E_i(t)$ may be a sine, a saw tooth, or a square wave. The impression of $E_i(t)$ on the surfaces of the dielectric will produce a time varying temperature field $T(r_i, t)$ that varies spatially with position, r_i, and exhibits a phase lag with respect to $E_i(t)$. Considering a propagation direction perpendicular to the plane of a thin plate of polar dielectric material having isothermal surfaces, and assuming for simplicity that $T(r_i,t)$ is a sinusoidal thermal wave of wavelength λ, the frequency v of the thermal wave is given by the solution of the thermal conduction equation. For these boundary conditions this is,

$$v(T, E_i) \approx \frac{k(T, E_i)}{\bar{C}(T, E_i) l^2} = \frac{D(T, E_i)}{l^2} \tag{10}$$

where $k(T, E_i)$ is the thermal conductivity, $\bar{C}(T, E_i)$ is the volume specific heat, $D(T, E_i)$ is the thermal diffusivity, and l is the thickness of the polar dielectric material. The cooling capacity, Π, achieved during the cycle $A \rightarrow B \rightarrow C \rightarrow D \rightarrow A$ per unit volume of dielectric V becomes,

$$\Pi(T, E_i) \approx \varphi W v(T, E_i) = \frac{\varphi W D(T, E_i)}{l^2} \tag{11}$$

where W is the work of the cycle and φ is a measure of the material losses, including specifically conduction losses and the dissipative dielectric losses, $tan\delta = \varepsilon''/\varepsilon'$ where ε' and ε'' are the real and imaginary parts of the dielectric permittivity, respectively.

Although the above analysis is highly simplified, it illustrates the influence of the specific heat and thermal conductivity of the polar dielectric material in determining the cooling capacity of practical electrocaloric cooling devices. An understanding of the dependences of these properties on temperature and applied electric field is expected to be an area of future research in the development of electrocaloric materials for cooling devices.

2.3 Pyroelectric/Electrocaloric Property Coefficients

In polar dielectric solids, the center of positive charge does not coincide with the center of negative charge. The electrothermal properties of polar dielectric crystals are determined by the internal atomic rearrangements in the structure that lead to a change in the separation of the charge centers subject to a uniform change in temperature. Such rearrangements may occur under conditions of constant strain (u_{ij}) such that there is no change in the unit cell dimensions, and this change gives rise to the primary pyroelectric effect characterized by the coefficient $(p_i)_u$. If the crystal is not mechanically clamped, the unit cell dimensions may change due to thermal expansion. Further, because all pyroelectric materials lack a center of symmetry, they are also piezoelectric. The secondary pyroelectric coefficient $(p_i)_\sigma$ that is usually measured by experiment on bulk materials at constant stress (σ_{ij}) includes both of these contributions. The two coefficients are not independent, and the primary coefficient is given by the thermodynamic relation,

$$(p_i)_u = (p_i)_\sigma - a^E_{jk} c^{E,\sigma}_{jklm} d^\sigma_{ilm} \tag{12}$$

where a^E_{jk} is the coefficient of thermal expansion, $c^{E,\sigma}_{jklm}$ is the elastic stiffness, and d^σ_{ilm} is the piezoelectric compliance.

Table 1 Primary pyroelectric/electrocaloric coefficients for several polar dielectrics (values taken from Newnham [28])

Polar dielectric	Crystal structure	Crystal symmetry	$(p_i)_u$ @ 298 K ($\mu C\ m^{-2}\ K^{-1}$)
Poled ceramics			
$BaTiO_3$	Perovskite	Tetragonal, 4mm/∞m	−260
$Pb(Zr_{0.95}Ti_{0.05})O_3$	Perovskite	Trigonal, 3m/∞m	−306
Crystals			
$LiNbO_3$	Corundum derivative	Trigonal, 3m	−96
$LiTaO_3$	Corundum derivative	Trigonal, 3m	−175
$(Ba_{0.5}Sr_{0.5})Nb_2O_6$	Tungsten bronze	Tetragonal, 4mm	−502
$SrBi_2Ta_2O_9$	Aurivillius	Orthorhombic, mm2	−240
ZnO	Wurtzite	Hexagonal, 6mm	−6.9
PVDF	Molecular solid	Orthorhombic, mm2	−40

It is apparent from Eq. 12 that large electrocaloric/pyroelectric effects are favored in crystal structures that have weak interatomic binding forces characterized by large amplitude thermal motion and small elastic stiffness. For example, perovskite oxides have corner-sharing oxygen octahedral linkages with small central cations and so tend to exhibit large primary coefficients when compared to more close–packed polar crystal structures such as wurtzite. Table 1 compares the room-temperature values of the primary electrocaloric/pyroelectric coefficients for several different polar oxides and the archetypal polymer ferroelectric, polyvinylidene fluoride. In ferroelectric materials the especially strong temperature dependence of the coefficient $(p_i)_\sigma$ arises due to the proximity of a displacive structural instability, where the polarization near the phase change varies with temperature and is proportional to the amplitude of a soft transverse optic phonon mode that condenses at the Curie temperature, T_C. A general constitutive model for materials having these phase change characteristics is outlined below.

3 Constitutive Modeling of Pyroelectric and Electrocaloric Properties

3.1 Landau Theory

The Gibbs free energy density of a proper ferroic phase transformation of a single-domain system with a three-component order parameter, $\boldsymbol{\eta}$, can be written in general form as:

$$F(\eta, T, x) = \int_V \Big[\alpha_{ij}\eta_i\eta_j + \beta_{ijkl}\eta_i\eta_j\eta_k\eta_l + \cdots + A_{ijkl}(\nabla_i\eta_j \cdot \nabla_k\eta_l) + \delta_{ijk}x_{ij}\eta_k. + \frac{1}{2}q_{ijkl}x_{ij}\eta_k\eta_l + \frac{1}{2}C_{ijkl}x_{ij}x_{kl} - \frac{1}{2}\Omega_i(\text{int})\eta_i - \Omega_i\eta_i\Big]dV \tag{13}$$

where α_{ij}, β_{ijkl} are the free energy expansion coefficients, A_{ijkl} is the coefficient of the gradient term, δ_{ijk} and q_{ijkl} are the bilinear and linear-quadratic coupling coefficients between the order parameter and the strain, x_{ij}, C_{ijkl} are the elastic coefficients, Ω_i is an external field conjugate to the order parameter, and Ω_i(int) is the internal field due to variations in η_i. Proper ferroelectric phase transformations can be described by the above relation with the ferroelectric polarization $\boldsymbol{P}$ as the order parameter and $\boldsymbol{E}$ as the conjugate field.

3.2 Bulk Ferroelectric Materials

The starting point for the analysis of the electrothermal properties of perovskite ferroelectrics such as $BaTiO_3$ and $PbTiO_3$ is the classical 2-4-6 Ginzburg–Landau-Devonshire polynomial [10, 11] expressed in powers of the polarization vector $\boldsymbol{P} = \{P_1, P_2, P_3\}$. Assuming isothermal conditions and considering only the paraelectric-ferroelectric transition between the cubic ($Pm3m$) and tetragonal ($P4mm$) phases, the expansion of the free energy density for the monodomain single crystal in the unconstrained state reduces to

$$F_{bulk}(T, E, P) = F_0 + \alpha_1 P^2 + \alpha_{11} P^4 + \alpha_{111} P^6 - EP \tag{14}$$

where F_0 is the free energy density of the paraelectric phase. In the tetragonal ferroelectric state $P_1 = P_2 = 0$, and $P_3 = P \neq 0$ is the component of the electric polarization directed along one of the cube axes of the high-symmetry phase. Here $E = E_3$ is a component of the applied electric field vector oriented parallel to the polarization direction, and α_1, α_{11}, and α_{111} are dielectric stiffness coefficients. The quadratic coefficient α_1 is given by the Curie–Weiss Law, $\alpha_1 = \alpha_0(T - T_C)$, where $\alpha_0 = 1/(2\varepsilon_0 C)$, ε_0 is the permittivity of free space, T_C is the Curie temperature, and C is the Curie–Weiss constant. The higher-order dielectric stiffness coefficients α_{11} and α_{111} are, in principle, also analytical functions of temperature. However, to reproduce the qualitative features of the paraelectric-ferroelectric phase change at temperatures close to the Curie point, where the Landau series is asymptotically accurate, it is sufficient to take these higher-order coefficients as constants.

When $E = 0$, the spontaneous polarization (P_S) in the tetragonal ferroelectric phases of $BaTiO_3$ and $PbTiO_3$ follows from the condition of thermodynamic equilibrium,

$$\frac{\partial F_{bulk}}{\partial P} = \alpha_1 + 2\alpha_{11} P^2 + 3\alpha_{111} P^4 = 0 \tag{15}$$

or

$$P_S^2(T) = \frac{-\alpha_{11} + \sqrt{\alpha_{11}^2 - 3\alpha_1 \alpha_{111}}}{3\alpha_{111}}. \tag{16}$$

When $E \neq 0$, the equilibrium polarization P^0 has contributions that arise from both the spontaneous polarization and the induced polarization, and its value is determined from the equation of state,

$$\partial F_{bulk}/\partial P = E. \tag{17}$$

3.3 Epitaxial Films and Misfit Strain

For epitaxial thin film materials, the free energy density has to be modified to take into account the clamping effect of the substrate and/or the misfit strain, u_m, due to the lattice mismatch between the film and substrate. Here we consider as examples the particular cases of epitaxial $BaTiO_3$ and $PbTiO_3$ films deposited on cubic substrates with $(001)_{film}//(001)_{substrate}$. Considering the mechanical boundary conditions for this situation, [i.e., equal in-plane biaxial stress components (in contracted notation) $\sigma_1 = \sigma_2$, no shear stresses ($\sigma_4 = \sigma_5 = \sigma_6 = 0$) and no out-of-plane stress ($\sigma_3 = 0$)], the free energy density for the ferroelectrics $BaTiO_3$ and $PbTiO_3$ can be expressed as,

$$F_{film}(T, E, P, u_m) = F_0 + \alpha_1 P^2 + \alpha_{11} P^4 + \alpha_{111} P^6 - EP + F_{el} \tag{18}$$

The elastic energy term, F_{el}, is given by,

$$F_{el} = \tilde{C}(u_m - Q_{12} P^2)^2. \tag{19}$$

Here, u_m is the in-plane polarization-free misfit strain defined as:

$$u_m = \frac{a_{substrate} - a_{film}}{a_{substrate}} \tag{20}$$

where a_{film} and $a_{substrate}$ are the pseudocubic lattice parameters of the free standing film and the substrate, respectively. The product $Q_{12}P^2$ is the self-strain due to polarization, Q_{ij} are the cubic electrostrictive coefficients in polarization notation, and $\tilde{C}$ is an effective elastic modulus,

$$\tilde{C} = C_{11} + C_{12} - \frac{2C_{12}^2}{C_{11}} \tag{21}$$

where C_{ij} are the elastic stiffnesses at constant polarization. After some rearrangement, the following expression obtains [3]:

$$F_{film}(T, E, P, u_m) = F_0 + \tilde{\alpha}_1 P^2 + \tilde{\alpha}_{11} P^4 + \alpha_{111} P^6 - EP + u_m^2 \tilde{C} \tag{22}$$

with modified dielectric stiffness coefficients given by:

$$\tilde{\alpha}_1 = \alpha_1 - 2u_m Q_{12} \tilde{C} \tag{23}$$

$$\tilde{\alpha}_{11} = \alpha_{11} + Q_{12}^2 \tilde{C}. \tag{24}$$

It should be noted if we consider an epitaxial film with no in-plane strain ($u_m = 0$), the Curie temperatures T_C of the ferroelectrics $BaTiO_3$ and $PbTiO_3$ will not change, relative to their values in the unclamped state, since $\tilde{\alpha}_1 = \alpha_1$ in Eq. 23. However, the order of the phase transformation *may be changed* due to the two-dimensional clamping of the film by the substrate as described by $\tilde{\alpha}_{11}$, which is *not* a function of the misfit strain u_m. Hence, if the phase transformation in the

unconstrained single crystal is of first-order (i.e., $\alpha_{11} < 0$), the phase transformation in the corresponding epitaxial film may be of second-order, depending on the magnitude of $Q_{12}^2\tilde{C}$. When the external field $E = 0$, minimization of the modified free energy with respect to the polarization ($\partial F_{film}/\partial P = 0$) yields the spontaneous polarization of the film as a function of the misfit strain,

$$P_S^2(T, u_m) = \frac{-\tilde{\alpha}_{11} + \sqrt{\tilde{\alpha}_{11}^2 - 3\tilde{\alpha}_1\alpha_{111}}}{3\alpha_{111}}. \tag{25}$$

We limit our discussion here only to the phase transformation from a cubic nonpolar to a tetragonal ferroelectric "*c*-domain" phase. As shown theoretically for $BaTiO_3$ and $PbTiO_3$, other tetragonal variants and non-tetragonal ferroelectric phases may also form, depending on the sign and magnitude of the misfit strain [30]. These can be included by modifying the Landau potential to take into account all components of the polarization vector and the corresponding elastic/electrostrictive energies associated with the additional polarization components. Furthermore, the theoretical approach may also be expanded to include polydomain formation as well [34].

It follows from Eq. 13 that for a constant electric field E, the excess entropy S^{XS} and the excess specific heat ΔC_E of the thin film material can be expressed through:

$$S_{E,\sigma}^{XS}(T, E, u_m) = -\left(\frac{\partial F^0}{\partial T}\right)_{E,\sigma} \tag{26}$$

$$\Delta C_{E,\sigma}(T, E, u_m) = -T\left(\frac{\partial^2 F^0}{\partial T^2}\right)_{E,\sigma} \tag{27}$$

where F^0 is the equilibrium total free energy density. The adiabatic temperature change can then be determined explicitly from the relation,

$$\Delta T(T, E, u_m) = -\int_{E_a}^{E_b} \frac{T}{C_{E,\sigma}(T, E, u_m)}\left(\frac{\partial P(T, E, u_m)}{\partial T}\right)_E dE \tag{28}$$

where the total volumetric specific heat $C_{E,\sigma}(T, E, u_m)$ is estimated by adding the computed excess specific heat to the zero-field values of the "hard mode" contributions taken from experimental measurements. The pyroelectric coefficient can then be expressed as:

$$p = \frac{dP^0(E = 0)}{dT} + \int_0^E \left(\frac{\partial \varepsilon}{\partial T}\right)_E dE \tag{29}$$

where $\varepsilon = (\partial^2 F/\partial P^2)^{-1}$ is the dielectric response.

3.4 Polycrystalline Films and Thermal Stresses

For polycrystalline ferroelectric films, thermal stresses can develop in the film due to the differences in the coefficients of thermal expansion (CTEs) between the film and the substrate upon cooling from the film growth (or annealing) temperature, T_G. A variety of substrates ($SrTiO_3$, MgO, $LaAlO_3$, metallized Si and sapphire) can be used to provide different levels of internal stresses. For some device applications, such as active on-chip cooling, integrated circuit (IC)-friendly substrates are required. In these situations, the values of the misfit strain, u_m, in the preceding equations need to be replaced by in-plane thermal strain, u_T, given by,

$$u_T(T, T_G) = \int_T^{T_G} \alpha_F dT - \int_T^{T_G} \alpha_S dT \tag{30}$$

where α_F and α_S are the in-plane coefficients of thermal expansion of the film and the substrate, respectively, T is the temperature of the film, and T_G is the growth/annealing temperature. The way T_G is defined in this analysis depends on the film deposition technique. For physical vapor deposition methods such as pulsed laser deposition (PLD), T_G is the substrate temperature during growth. For chemical deposition techniques such as spin coating or metal–organic chemical vapor deposition (MOCVD), T_G corresponds to the temperature at which the final annealing step is carried out. For perovskite ferroelectrics such as $BaTiO_3$ and $PbTiO_3$ deposited on (001) substrates such as Si and *c*-sapphire, which have isotropic in-plane coefficients of thermal expansion, the thermal strains are equibiaxial. For perovskite ferroelectrics such as $BaTiO_3$ and $PbTiO_3$ deposited on substrates such as *a*-sapphire, however, the in-plane thermal strains are anisotropic, and the in-plane strains along *a*- and *c*-axes are $u_{T1}(T_G)$ and $u_{T2}(T_G)$, respectively.

3.5 Strain-Engineered Thin Films: Strontium Titanate

The thermodynamic analysis described above can also be extended to incipient ferroelectrics, such as strontium titanate, $SrTiO_3$. Although $SrTiO_3$ crystals or polycrystalline ceramics remain paraelectric down to 0 K, the ferroelectric phase can be induced by uniaxial stress [42], an external electrical field [16], or by doping [6]. A thermodynamic analysis by Pertsev et al. [31, 32] has shown that it is possible to induce a variety of different ferroelectric phases in epitaxial thin films of $SrTiO_3$ that are not stable in monolithic single-crystal or polycrystalline forms. Following this work, ferroelectricity at room temperature (RT $\cong$ 300 K) in epitaxial (001) $SrTiO_3$ thin films was observed experimentally by carefully adjusting

the equi-biaxial in-plane misfit strain [14]. Here we describe a thermodynamic analysis for the electrocaloric properties of $SrTiO_3$ films subject to mechanical boundary conditions that involve both perfect clamping and misfit strain. This analysis is summarized in the sections below.

3.5.1 The Ferroelastic Transition

Under stress-free conditions, a structural phase transformation in $SrTiO_3$ takes place below the temperature T_{st} to a centrosymmetric tetragonal phase belonging to space group *I4/mcm*. This *ferroelastic* transition involves a rotation of the oxygen octahedra about the cube axes of the high-symmetry cubic (*Pm3m*) phase. The order parameter for the structural phase transformation is given by $\mathbf{q} = \{q_1, q_2, q_3\}$ with $q_1 = q_2 = 0$ and $q_3 = q \neq 0$. The free energy density for the stress-free monodomain crystal can then be expressed as:

$$F_{bulk}(T, E, q, P) = F_0 + b_1 q^2 + b_{11} q^4 + a_1 P^2 + a_{11} P^4 - t_{11} P^2 q^2 - EP \tag{31}$$

Here, b_1 and b_{11} are the structural order parameter susceptibility coefficients, t_{11} is the coupling coefficient between the structural order parameter q and the field-induced polarization P, and a_1 and a_{11} are the dielectric stiffness coefficients.

For $SrTiO_3$, the equilibrium condition for $E = 0$ (and thus $P = 0$) is given by,

$$\partial F_{bulk}/\partial q = 0 \tag{32}$$

or

$$q_S(T) = \pm\sqrt{-\frac{b_1}{2b_{11}}} \tag{33}$$

When $E \neq 0$, the condition of thermodynamic equilibrium gives,

$$\partial F_{bulk}/\partial q = 0 \tag{34}$$

$$\partial F_{bulk}/\partial P = E \tag{35}$$

yielding two expressions that must be solved simultaneously,

$$b_1 q + 2b_{11} q^3 - t_{11} P^2 q = 0 \tag{36}$$

$$2a_1 P + 4a_{11} P^3 - 2t_{11} P q^2 = E \tag{37}$$

To describe the effects of mechanical boundary conditions on the structural phase transformation in epitaxial $SrTiO_3$ thin films deposited on a cubic substrate with $(001)_{film}//(001)_{substrate}$, we adopt the particular form of the free energy density given by Pertsev et al. [31, 32],

$$F_{film}(T, E, q, P, u_m) = F_0 + \tilde{b}_1 q^2 + \tilde{b}_{11} q^4 + \tilde{a}_1 P^2 + \tilde{a}_{11} P^4 - \tilde{t}_{11} P^2 q^2 - EP \tag{38}$$

in which the re-normalized (structural and dielectric) stiffness and coupling coefficients are,

$$\tilde{b}_1 = b_1 + 2\left(\frac{C_{12}}{C_{11}}\lambda_{11} - \lambda_{12}\right)u_m \tag{39}$$

$$\tilde{b}_{11} = b_{11} - \frac{\lambda_{11}^2}{2C_{11}} \tag{40}$$

$$\tilde{a}_1 = a_1 + 2\left(\frac{C_{12}}{C_{11}}g_{11} - g_{12}\right)u_m \tag{41}$$

$$\tilde{a}_{11} = a_{11} - \frac{g_{11}^2}{2C_{11}} \tag{42}$$

$$\tilde{t}_{11} = t_{11} + \frac{g_{11}\lambda_{11}}{C_{11}} \tag{43}$$

Here, g_{ij} are the electrostrictive constants, and λ_{ij} are the coupling coefficients between the strain and the structural order parameter in contracted notation. For $E = 0$, the shift in the ferroelastic phase transformation temperature as a function of u_m is given by Eq. 39 and the two-dimensional clamping effect of the substrate is described by Eq. 40. The equilibrium structural order parameter for $E = 0$ can be determined from Eq. 33 with the re-normalized stiffness coefficients $\tilde{b}_1$ and $\tilde{b}_{11}$. In the presence of an applied electric field E, the condition for thermodynamic equilibrium is given by the equations of state $\partial F_{film}/\partial q = 0$ and $\partial F_{film}/\partial P = E$ such that:

$$\begin{aligned} \tilde{b}_1 q + 2\tilde{b}_{11} q^3 - \tilde{t}_{11} P^2 q &= 0 \\ 2\tilde{a}_1 P + 4\tilde{a}_{11} P^3 - 2\tilde{t}_{11} P q^2 &= E. \end{aligned} \tag{44}$$

3.5.2 Strain-Induced Ferroelectric Phases

In Sect. 3.5.1, we have not taken into account the possibility of the formation of other ferroelastic/ferroelectric phases as discussed theoretically by Pertsev et al. [31, 32]. We now extend the analysis by considering the formation of other ferroelastic/ferroelectric phases that can be induced by a misfit strain. The free energy density of the film under $u_m \neq 0$ by can be expressed as [31, 32],

$$
\begin{aligned}
F_{film}(P_i, q_i, u_m, E_i, T) = F_0 &+ \tilde{a}_1(P_1^2 + P_2^2) + \tilde{a}_3 P_3^2 + \tilde{a}_{11}(P_1^4 + P_2^4) \\
&+ \tilde{a}_{33} P_3^4 + \tilde{a}_{12} P_1^2 P_2^2 + \tilde{a}_{13}(P_1^2 + P_2^2) P_3^2 \\
&+ \tilde{b}_1(q_1^2 + q_2^2) + \tilde{b}_3 q_3^2 + \tilde{b}_{11}(q_1^4 + q_2^4) \\
&+ \tilde{b}_{33} q_3^4 + \tilde{b}_{12} q_1^2 q_2^2 + \tilde{b}_{13}(q_1^2 + q_2^2) q_3^2 \\
&- \tilde{t}_{11}(P_1^2 q_1^2 + P_2^2 q_2^2) - \tilde{t}_{33} P_3^2 q_3^2 \\
&- \tilde{t}_{12}(P_1^2 q_2^2 + P_2^2 q_1^2) - \tilde{t}_{13}(P_1^2 + P_2^2) q_3^2 \\
&- \tilde{t}_{31} P_3^2 (q_1^2 + q_2^2) - t_{44} P_1 P_2 q_1 q_2 \\
&- \tilde{t}_{44}(P_1 P_3 q_1 q_3 + P_2 P_3 q_2 q_3) \\
&+ (C_{11} + C_{12} - 2C_{12}^2 / C_{11}) u_m^2 \\
&- E_1 P_1 - E_2 P_2 - E_3 P_3
\end{aligned}
\tag{45}
$$

The re-normalized coefficients $\tilde{a}_i$ and $\tilde{a}_{ij}$, $\tilde{b}_i$ and $\tilde{b}_{ij}$, and $\tilde{t}_{ij}$ entering Eq. 45 are given by [31, 32]:

$$
\begin{aligned}
&\tilde{a}_1 = a_1 - \left(g_{11} + g_{12} - 2\frac{C_{12}}{C_{11}} g_{12}\right) u_m, \quad \tilde{a}_3 = a_1 + 2\left(\frac{C_{12}}{C_{11}} g_{11} - g_{12}\right) u_m \\
&\tilde{a}_{11} = a_{11} - \frac{g_{12}^2}{2C_{11}}, \quad \tilde{a}_{33} = a_{11} - \frac{g_{11}^2}{2C_{11}} \\
&\tilde{a}_{12} = a_{12} - \frac{g_{12}^2}{C_{11}}, \quad \tilde{a}_{13} = a_{12} - \frac{g_{11} g_{12}}{C_{11}} - \frac{g_{44}^2}{2C_{44}} \\
&\tilde{b}_1 = b_1 - \left(\lambda_{11} + \lambda_{12} - 2\frac{C_{12}}{C_{11}} \lambda_{12}\right) u_m, \quad \tilde{b}_3 = b_1 + 2\left(\frac{C_{12}}{C_{11}} \lambda_{11} - \lambda_{12}\right) u_m \\
&\tilde{b}_{11} = b_{11} - \frac{\lambda_{12}^2}{2C_{11}}, \quad \tilde{b}_{33} = b_{11} - \frac{\lambda_{11}^2}{2C_{11}} \\
&\tilde{b}_{12} = b_{12} - \frac{\lambda_{12}^2}{C_{11}}, \quad \tilde{b}_{13} = b_{12} - \frac{\lambda_{11} \lambda_{12}}{C_{11}} - \frac{\lambda_{44}^2}{2C_{44}} \\
&\tilde{t}_{11} = t_{11} + \frac{g_{12} \lambda_{12}}{C_{11}}, \quad \tilde{t}_{33} = t_{11} + \frac{g_{11} \lambda_{11}}{C_{11}} \\
&\tilde{t}_{12} = t_{12} + \frac{g_{12} \lambda_{12}}{C_{11}}, \quad \tilde{t}_{13} = t_{12} + \frac{g_{12} \lambda_{11}}{C_{11}} \\
&\tilde{t}_{31} = t_{12} + \frac{g_{11} \lambda_{12}}{C_{11}}, \quad \tilde{t}_{44} = t_{44} + \frac{g_{44} \lambda_{44}}{C_{44}}
\end{aligned}
\tag{46}
$$

where a_i and a_{ij}, b_i and b_{ij}, and t_{ij} are the stress-free, monodomain dielectric stiffness coefficients, structural order parameter susceptibility coefficients, and coupling coefficients between the polarization P_i and the structural order parameter q_i, respectively. In Voigt notation, g_{ij} are the electrostrictive constants and λ_{ij} are the coupling coefficients between the strain and q_i.

Using Eqs. 45 and 46, the equations of state $\partial F_{film}/\partial P_i = 0$ and $\partial F_{film}/\partial q_i = 0$ at $E_i = 0$, the equilibrium polarization $P_i^0(T, E_i, u_m)$ and the equilibrium structural

parameter $q_i^0(T, E_i, u_m)$ are obtained, and the adiabatic temperature change ΔT for the ferroelectric phases can be explicitly calculated from the relation [44],

$$\Delta T(T, E_i, u_m) = \sum_{i=1}^{3} \left(-\int_{E_a}^{E_b} \frac{T}{C_E^0(T, E_i, u_m)} \left(\frac{\partial P_i^0(T, E_i, u_m)}{\partial T} \right)_{E_i} dE_i \right) \tag{47}$$

It should be noted that the constitutive model described in Sects. 3.1–3.5 is expected to be equally applicable to ferroelectric polymer systems. Recently, Li et al. have used the formalism presented here to compute the electrocaloric properties of two poly(vinylidenefluoride-trifluoroethylene) [P(VDF-TrFE)] copolymers (65/35 and 55/45 molar percentages) that exhibit first-order and second-order phase transitions, respectively [20]. Their findings closely parallel the results for ceramic polar dielectrics, and these results will be discussed in detail below.

4 Theory Predictions for Bulk and Thin Film Perovskites

4.1 Influence of Driving and Bias Fields

The effect of an applied electric field on the electrocaloric response of barium titanate ($BaTiO_3$, BTO) as measured by the adiabatic temperature change ΔT and excess entropy change S^{XS} are shown in Fig. 3 [1, 2]. In Fig. 3a, ΔT is plotted as a function of temperature under different electric field changes ($\Delta E = 10 - 100$ kV/cm) for both mechanically free and clamped monodomain BTO above a bias field $E_a = 50$ kV/cm. As expected, it is seen that the computed ΔT of both the

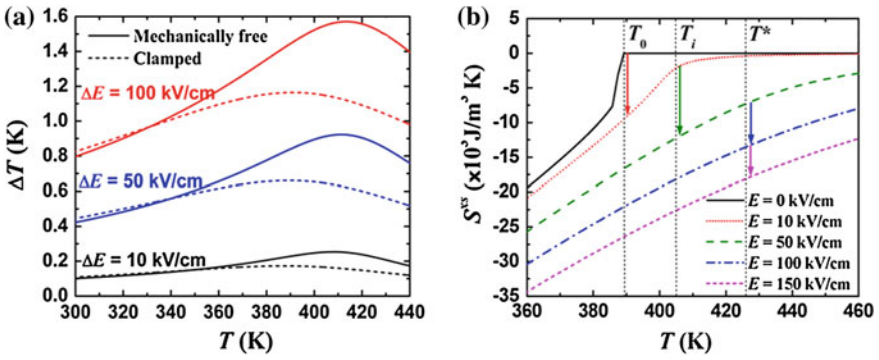

Fig. 3 **a** Adiabatic change of temperature (electrocaloric effect) for both mechanically free and clamped BTO and **b** excess entropy for mechanically free BTO as a function of working temperature at various electric field changes ($E = E_b - E_a$), where E_a is 50 kV/cm. Reprinted with permission from Akcay et al. [1]. Copyright [2007], American Institute of Physics

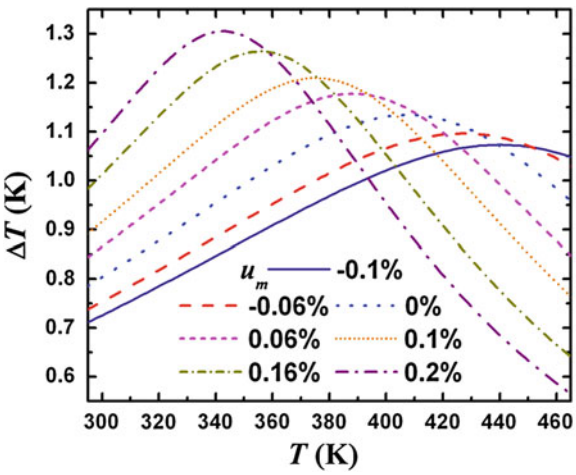

Fig. 4 Adiabatic temperature change in $BaTiO_3$ as a function of temperature at different misfit strains ($\Delta E = 100$ kV/cm, $E_a = 50$ kV/cm). Reprinted with permission from Akcay et al. [2]. Copyright [2008], American Institute of Physics

mechanically free and clamped BTO increase with larger values of the field change ΔE. However, the results also show, as seen in Fig. 3b, that the magnitude of S^{XS} and the temperature at which it is maximized are influenced not only by the change in applied electric field, but also by the value of the bias field. For bias fields smaller than a critical value, S^{XS} is largest at the phase transition temperature and is a strong function of T; for bias fields larger than the critical value, the electrocaloric response is largest at a higher temperature and is a weak function of T. Perfect lateral clamping transforms the first-order ferroelectric-paraelectric transition in BTO into a second-order transition, decreasing the magnitude of ΔT by ~ 20 %, but reducing its sensitivity to temperature (Fig. 3a).

4.2 Influence of Misfit Strain

The results shown in Fig. 3 suggest that in addition to perfect lateral clamping, the misfit strain in epitaxial ferroelectric thin films may also influence the magnitude of the electrocaloric response. The misfit strain depends on the specific film-substrate system and the conditions of film deposition. The misfit strain depends on the temperature-dependent lattice parameter mismatch between film and substrate and includes the self-strain of the ferroelectric phase transformation if the film is grown at temperatures above T_C. The influence of lattice misfit strain on the electrocaloric properties of BTO films is as shown in Fig. 4 [2]. For a given choice of driving and bias fields ($\Delta E = 100$ kV/cm, $E_a = 50$ kV/cm), a tensile misfit strain shifts the maximum in the electrocaloric response to lower temperatures, increasing its magnitude and increasing its dependence on temperature, while a compressive misfit strain has the opposite influence.

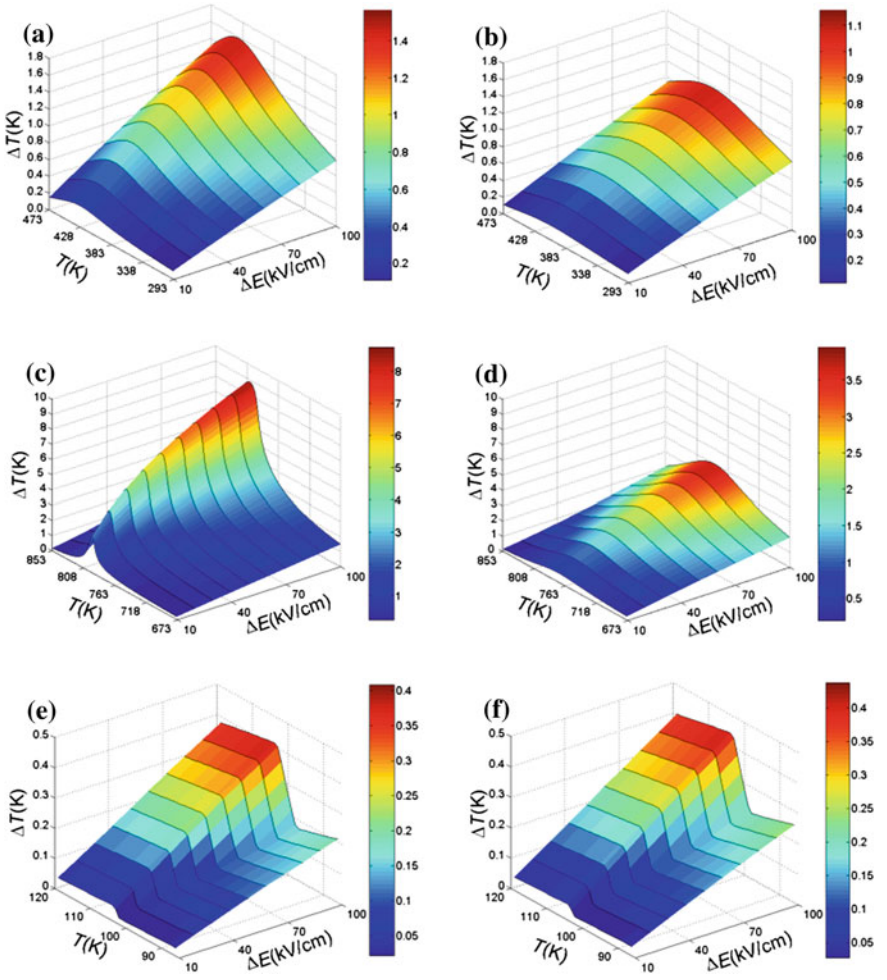

Fig. 5 Three-dimensional plots of the adiabatic temperature change ΔT as functions of T and ΔE ($E_a = 50$ kV/cm) for monodomain uniaxial **a**, **c**, and **e** unclamped stress-free (bulk) $BaTiO_3$, $PbTiO_3$, and $SrTiO_3$, respectively, and **b**, **d**, and **f** $BaTiO_3$, $PbTiO_3$, and $SrTiO_3$ thin films with $u_m = 0$, respectively [43]

4.3 Influence of Composition and Phase Transition Order

Naturally, another factor affecting the electrocaloric response is the material composition, which controls the Curie temperature and may change the order of the ferroelectric-paraelectric phase change. To obtain valid comparisons of the electrocaloric performance of ferroelectric solid solutions with different compositions, the electrocaloric response of three end member compounds $BaTiO_3$, $PbTiO_3$ (PTO) and the "incipient" ferroelectric $SrTiO_3$ (STO) were computed

[43]. Figure 5 shows the effect of the differences in ferroelectric-paraelectric phase transition characteristics of BTO, PTO and STO on their electrocaloric response under both mechanically free and perfectly laterally clamped boundary conditions. It is seen that PTO, which has a stronger first-order ferroelectric-paraelectric phase change, has much larger maximum electrocaloric response ($\sim$9 K) than BTO ($\sim$1.6 K) under the same conditions near the first-order phase transition temperature. For STO, the temperature change shown is not due to the electrocaloric effect, but rather arises from the change in the excess specific heat near the second-order structural phase change. As with BTO, it is seen that in PTO the effect of mechanical clamping is to transform the first-order transition into a second-order transition. Again, this reduces the magnitude and the temperature dependence of the electrocaloric response.

4.4 Influence of Thermal Stresses

In Sect. 4.2, the influence of misfit strain on the electrocaloric effect in epitaxial ferroelectric thin films was discussed. Depending on the choice of substrate and deposition technique, however, the film can also be polycrystalline. When such

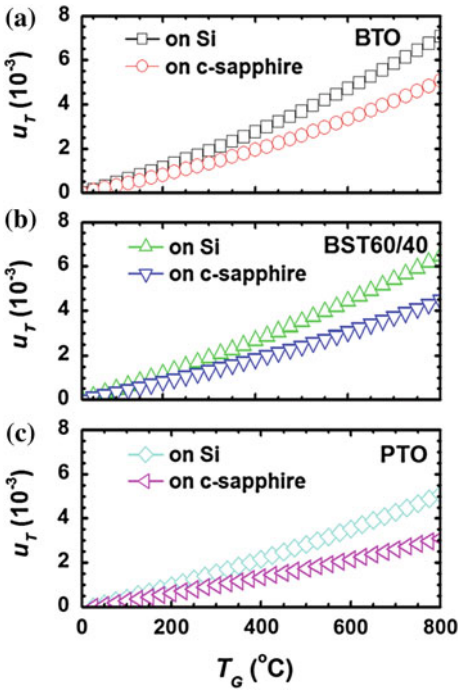

Fig. 6 The variation in u_T as a function of T_G for **a** $BaTiO_3$, **b** BST 60/40, and **c** $PbTiO_3$. Reprinted with permission from Zhang et al. [45]. Copyright [2011], American Institute of Physics

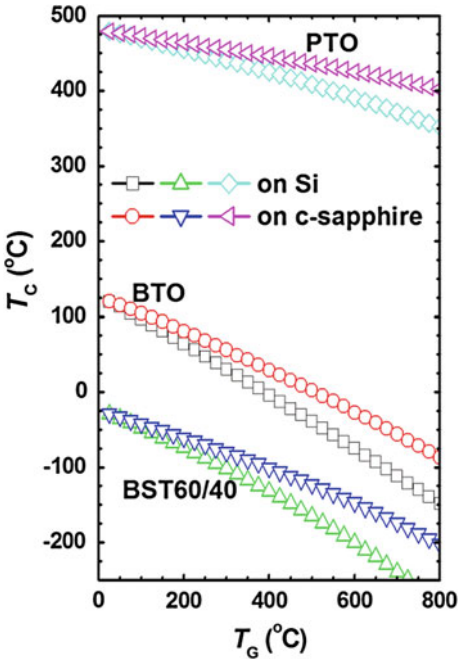

Fig. 7 The dependence of T_C on T_G for $BaTiO_3$, BST 60/40, and $PbTiO_3$ on Si and *c*-sapphire. Reprinted with permission from Zhang et al. [45]. Copyright [2011], American Institute of Physics

films are cooled down from the growth or annealing temperature, thermal stresses develop due to the thermal expansion mismatch between the film and substrate. To illustrate the influence of this mismatch on the electrocaloric properties, the thermal strain (u_T), Curie temperature (T_C), and electrocaloric adiabatic temperature change (ΔT) are computed as a function of the growth temperature (T_G). The results for polycrystalline $BaTiO_3$, for a composition in the solid solution (Ba,Sr)TiO_3 (BST), and for $PbTiO_3$ grown on three substrates (Si, *c*-sapphire, and *a*-sapphire) are presented below.

The dependence of the thermal strains on the growth temperature for (001) textured polycrystalline $BaTiO_3$, BST60/40, and $PbTiO_3$ on various substrates is shown in Fig. 6. Because the polycrystalline averages of the thermal expansion coefficients for the Si, *c*-, and *a*-sapphire substrates are lower than the coefficients of thermal expansion of the ferroelectric films in the temperature range of the analysis (25 °C $\leq T_G \leq$ 800 °C), the in-plane thermal strains are tensile. As seen in Fig. 6, their magnitudes increase with T_G. A principal effect of the tensile strains is to shift the zero-field values of T_C to lower temperatures. This shift in T_C arises due to the modification of the quadratic dielectric stiffness coefficient, depending on the magnitude of the thermal strain (Eqs. 23 and 41). As shown in Fig. 7, the thermal strains produce a decrease in the zero-field value of T_C of $BaTiO_3$, BST 60/40, and $PbTiO_3$ on Si and *c*-sapphire when compared to their bulk values. Naturally, under an applied electric field, the ferroelectric phase change at T_C is destroyed and the polarization versus the electric field curve exhibits an inflection

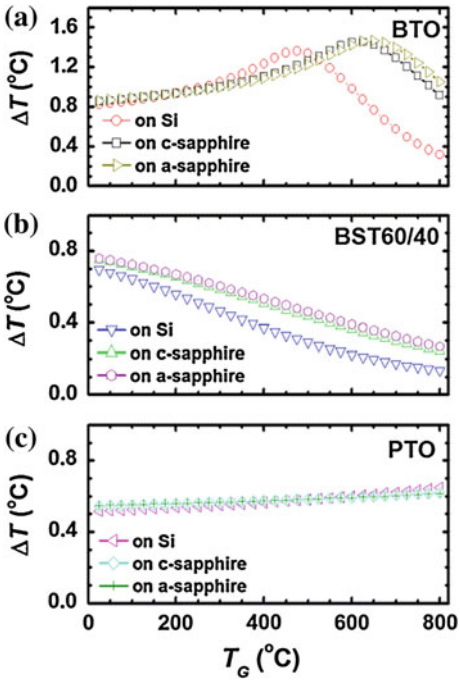

Fig. 8 Adiabatic temperature change in (001) textured polycrystalline **a** $BaTiO_3$, **b** BST 60/40 and **c** $PbTiO_3$ thin films ($E_a = 50$ kV/cm, $\Delta E = 120$ kV/cm) as a function of T_G on Si, *c*-sapphire, and *a*-sapphire at room temperature. Reprinted with permission from Zhang et al. [45]. Copyright [2011], American Institute of Physics

point, approaching zero asymptotically with increasing field. As a consequence, the adiabatic ΔT and other properties that depend on the derivative $\partial P/\partial T$ will show their maximum values at a temperature $T_M > T_C$, slightly above the zero-field values shown in the figure [1].

Figure 8 plots the room-temperature values of the adiabatic ΔT for $BaTiO_3$, BST 60/40, and $PbTiO_3$ on various substrates. For the $BaTiO_3$ films, the thermal stresses are sufficient to shift the zero-field T_C to room temperature. As a result, the electrocaloric response shows a pronounced dependence on T_G. For $BaTiO_3$ on Si, *c*-sapphire, and *a*-sapphire, a maximum in the electrocaloric response can be produced for growth temperatures T_G equal to $\sim$475, 625, and 650 °C, respectively. For comparison, results for the BST 60/40 and $PbTiO_3$ films are also shown in Fig. 8. For BST 60/40 films, T_C always lies below room temperature (Fig. 7). As a result, the electrocaloric response simply decreases with an increase in T_G. In contrast, for the $PbTiO_3$ films, T_C lies far above room temperature and the adiabatic ΔT shows only a slight increase with T_G. In BST 60/40 and $PbTiO_3$ films, the contribution of the phase transition near T_C is avoided; as such, the electrocaloric response is only weakly dependent on T_G. These results clearly illustrate that thermal stresses can be engineered in such a way as to shift the maximum in electrocaloric properties to a desired working temperature.

The influence of thermal stresses on the electrocaloric properties of a $BaTiO_3$ cooling device working near room temperature can be better appreciated by

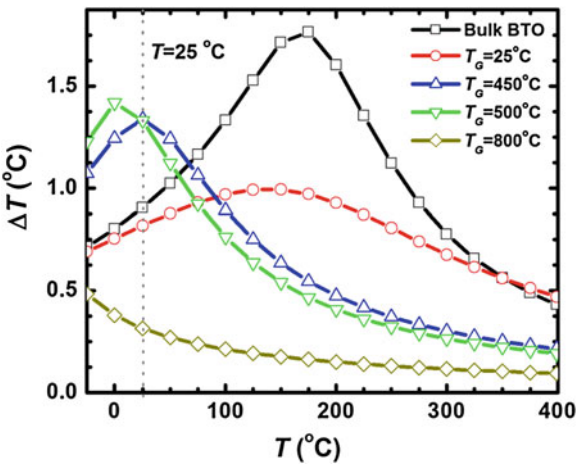

Fig. 9 Adiabatic temperature change in bulk $BaTiO_3$ and (001) textured polycrystalline $BaTiO_3$ on Si ($E_a = 50$ kV/cm, $\Delta E = 120$ kV/cm) as a function of T at different T_G. Reprinted with permission from Zhang et al. [45]. Copyright [2011], American Institute of Physics

comparing the adiabatic ΔT versus temperature curves for polycrystalline thin film $BaTiO_3$ and stress-free monocrystalline bulk $BaTiO_3$, as shown in Fig. 9. Note that the temperature dependence of the thermal strain is included in the calculations, i.e., u_T (T, T_G). For $BaTiO_3$ films on Si, the thermal stresses for films grown at 450 °C are sufficient to shift the zero-field Curie temperature T_C to near room temperature, resulting in a strong enhancement of the electrocaloric properties as compared to the bulk material. It is further seen in Fig. 9 that the adiabatic temperature change occurring at room temperature closely approaches that of the bulk near its Curie temperature. Similar results are obtained for $BaTiO_3$ on sapphire substrates. The curves in Fig. 9 demonstrate that the growth temperature of polycrystalline ferroelectric films is an important parameter to be controlled in optimizing the electrocaloric properties.

4.5 Electrocaloric Properties of Strain-Induced Ferroelectric Phases: Strontium Titanate

One interesting class of materials with electrocaloric properties that have so far not been explored experimentally is incipient ferroelectrics such as $SrTiO_3$ (STO). In this section it is shown that the room-temperature adiabatic temperature change ΔT of epitaxial (001) $SrTiO_3$ films can be controlled by the misfit strain and by varying the thermal and electrical boundary conditions. Depending on the electrode configuration [uniform metal–insulator-metal (MIM) or inter-digitated electrodes (IDE)] and on the field strength, the results demonstrate that a room-temperature ΔT of 1–5 K can be achieved in $SrTiO_3$ films on *both tensile and compressive substrates*.

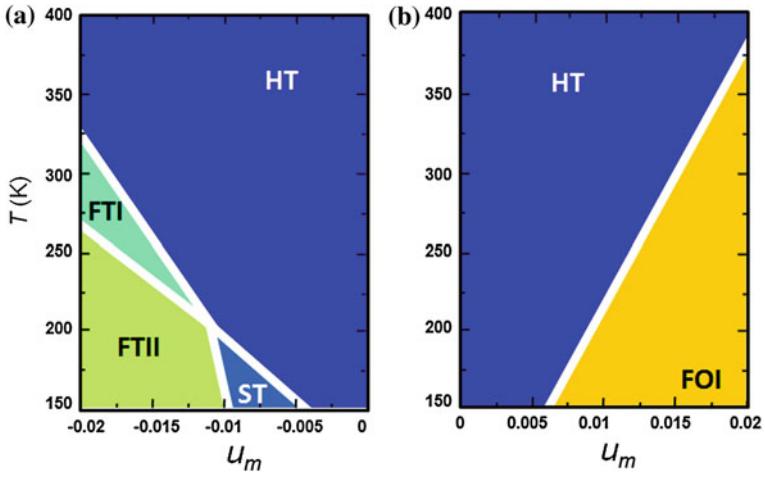

Fig. 10 Misfit strain *versus* temperature phase diagram of epitaxial monodomain (001) $SrTiO_3$ films. The order parameters of the phases appearing in this map are: *HT*: $P_1 = P_2 = P_3 = 0$, $q_1 = q_2 = q_3 = 0$; *ST*: $P_1 = P_2 = P_3 = 0$, $q_1 = q_2 = 0$, $q_3 \neq 0$; *FTI*: $P_1 = P_2 = 0$, $P_3 \neq 0$, $q_1 = q_2 = q_3 = 0$; *FTII*: $P_1 = P_2 = 0$, $P_3 \neq 0$, $q_1 = q_2 = 0$, $q_3 \neq 0$; *FOI*: $|P_1| = |P_2| \neq 0$, $P_3 = 0$, $q_1 = q_2 = q_3 = 0$. Reprinted with permission from Zhang et al. [44]. Copyright [2012], American Institute of Physics

Using Eqs. 45 and 46, the equations of state $\partial F_{film}/\partial P_i = 0$ and $\partial F_{film}/\partial q_i = 0$ at $E_i = 0$, and the values of the property coefficients for $SrTiO_3$ given in Ref. [31], the identical u_m—T phase diagram of epitaxial monodomain $SrTiO_3$ films as given by Pertsev et al. was obtained [32]. Figure 10 shows the stability regions of various phases for 150 K $< T <$ 400 K and $-0.02 < u_m < 0.02$. The analysis is limited to these ranges of T and u_m since lower operating temperatures are not of great interest for electrocaloric cooling devices and misfit strains larger than 2 % in magnitude (depending on the substrate material and film thickness) would be partially or completely relaxed via the formation of two-dimensional periodic arrays of interfacial dislocations [26]. The effect of misfit dislocations can certainly be incorporated into the model using an "effective" substrate lattice parameter [39], but this would unnecessarily complicate the physical interpretation of the results and would obscure the effect of u_m. The possible phases and their corresponding order parameters that appear in Fig. 10a and b are: HT: $P_1 = P_2 = P_3 = 0$, $q_1 = q_2 = q_3 = 0$; ST: $P_1 = P_2 = P_3 = 0$, $q_1 = q_2 = 0$, $q_3 \neq 0$; FTI: $P_1 = P_2 = 0$, $P_3 \neq 0$, $q_1 = q_2 = q_3 = 0$; FTII: $P_1 = P_2 = 0$, $P_3 \neq 0$, $q_1 = q_2 = 0$, $q_3 \neq 0$; FOI: $|P_1| = |P_2| \neq 0$, $P_3 = 0$, $q_1 = q_2 = q_3 = 0$.

Figure 10 shows that, depending on u_m and T, three ferroelectric phases (FTI, FTII, and FOI) can be stabilized by the lattice mismatch between the film and the substrate. For example, at $T = 225$ K and $-0.0127 < u_m < 0.0106$, the HT phase is stable. The HT phase is a tetragonally distorted but non-polar variation of the parent cubic (P$m3m$) phase. The tetragonality [i.e., $(c - a)/a$ where c, a are the

lattice parameters of the HT phase] is positive (negative) for $u_m < 0$ ($u_m > 0$) and is zero for $u_m = 0$, for which $c = a = a_0$ where a_0 is the lattice parameter of unconstrained STO. For tensile misfit strains $u_m > 0.0106$, the ferroelectric FOI phase (which has an equi-biaxial in-plane spontaneous polarization) stabilizes, while for compressive misfit strains $u_m < -0.0127$, the ferroelectric FTI phase is stabilized with an out-of-plane spontaneous polarization along the [001] direction. At this temperature, a transition to the FTII phase occurs for compressive misfit strains $u_m < -0.0144$. This transformation involves the rotation of the TiO_6 octahedra characterized by the structural order parameter q_i and produces a change in the magnitude of polarization along the [001] direction. Hence, the magnitude of the polarization in any of the three ferroelectric phases depends on both u_m and T.

To illustrate the electrocaloric effect in incipient ferroelectrics, a MIM construct having a (001) epitaxial $SrTiO_3$ film sandwiched between uniform metallic electrodes is considered first. For this configuration, $E_i = [0, 0, E_3]$ and it is assumed that the bottom electrode is grown pseudomorphically onto the substrate so that both the sign and magnitude of u_m are entirely controlled by the mismatch between the film and the substrate. As can be appreciated from Fig. 10, compressive misfit strains favor the ferroelectric phases FTI and FTII, while tensile misfit strains favor the ferroelectric phase FOI. Because both the HT and ST phases are non-polar, and because the component of polarization $P_3 = 0$ is parallel to the field direction E_3, the region of interest is restricted to compressive misfit strains $u_m < -0.01$. This is illustrated in Fig. 11a, which shows a two-dimensional pseudo-color plot of the adiabatic temperature change ΔT as a function of u_m and

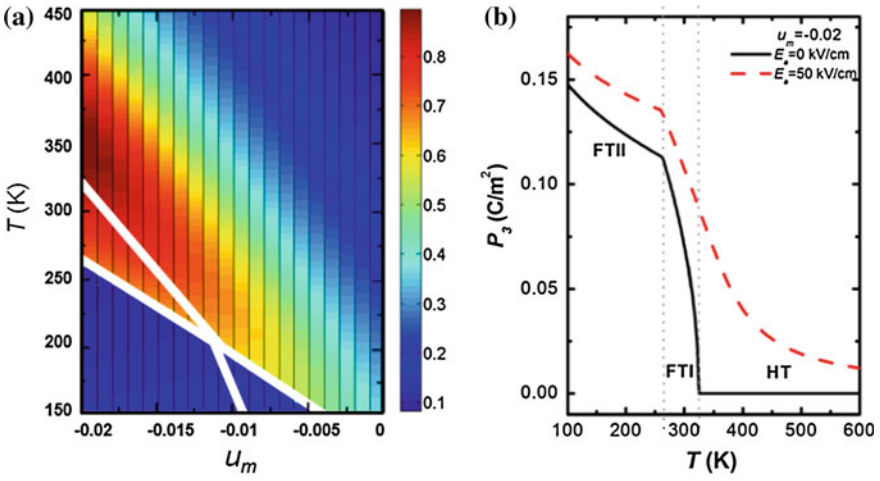

Fig. 11 **a** The adiabatic temperature change ΔT of an epitaxial (001) $SrTiO_3$ film in a MIM configuration as a function of u_m and T for $E_a = 50$ kV/cm and $\Delta E = 120$ kV/cm; **b** the out-of plane polarization P_3 as a function of temperature at $u_m = -0.02$ for $E_a = 0$ kV/cm and $E_a = 50$ kV/cm. Reprinted with permission from Zhang et al. [44]. Copyright [2012], American Institute of Physics

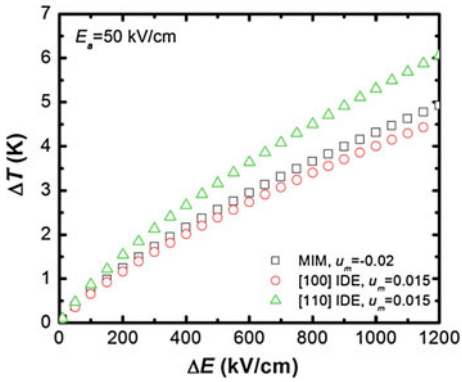

Fig. 12 The room-temperature adiabatic temperature change ΔT of epitaxial (001) $SrTiO_3$ films with MIM ($u_m = -0.020$, *open squares*) and [100]/[010] and [110] IDE configurations ($u_m = 0.015$, *open circles* and *triangles*, respectively) as a function of ΔE for $E_a = 50$ kV/cm. Reprinted with permission from Zhang et al. [44]. Copyright [2012], American Institute of Physics

T for a particular choice of bias field $E_a = 50$ kV/cm and field change $\Delta E = 120$ kV/cm. As expected for conventional ferroelectric materials such as $BaTiO_3$ and $PbTiO_3$ [43], the largest electrocaloric response occurs near the paraelectric to ferroelectric (HT–FTII) phase transition ($T = 350$ K) where the $P_3(T)$ curve experiences an inflection point and the derivative $\partial P_3/\partial T$ passes through a steep minimum. However, at the comparatively low field level of 120 kV/cm, the maximum adiabatic temperature change is modest, $\Delta T < 1$ K. The reason for this can be understood from Fig. 11b where it is seen that the polarization induced along [001] by a field $E_3 = 120$ kV/cm is quite small. It is further apparent that the electrocaloric response is not significantly enhanced near the FTI-FTII phase boundary, because at this transition $P_3(T)$ shows only a small change in slope that is accompanied by comparatively small but discontinuous change in $\partial P_3/\partial T$. It is evident from Fig. 11 that to obtain a larger ΔT, the field strength and/or bias field must be increased. Figure 12 shows how ΔT varies as a function of field change ΔE at room temperature. It is seen in this figure that for field changes $\Delta E = 1{,}200$ kV/cm, a large ΔT of ~ 5 K can be achieved in $SrTiO_3$ films at room temperature. As a point of reference, at these field levels, the electrocaloric response for [001] $SrTiO_3$ in a MIM configuration is closely comparable to that observed in high-quality relaxor PMN-PT films [24, 25] near the temperature of the Curie maximum (~ 350 K). From this it can be concluded that, as shown for $BaTiO_3$ [43], a relatively small bias field (~ 50 kV/cm) is sufficient to destroy the discontinuity in polarization at the HT–FTII transition.

By using an IDE configuration, it is possible to apply in-plane electric fields [38] and by so doing access the HT-FOI phase transformation that occurs under tensile misfit strains. Two IDE configurations are considered, one for which $E_i = [E_1, 0, 0]$ (or $[0, E_2, 0]$) oriented along [100] (or [010]) and a second for

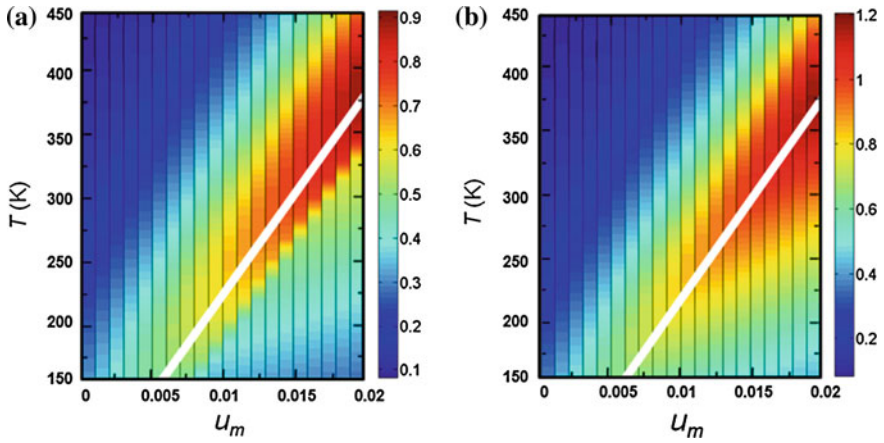

Fig. 13 The adiabatic temperature change ΔT of an epitaxial (001) $SrTiO_3$ film in **a** [100], and **b** [110] IDE configuration as a function of u_m and T for $E_a = 50$ kV/cm and $\Delta E = 120$ kV/cm. Reprinted with permission from Zhang et al. [44]. Copyright [2012], American Institute of Physics

which $E_i = [E_1/\sqrt{2}, E_1/\sqrt{2}, 0]$ oriented along [110]. Pseudo-color plots of the adiabatic temperature change as functions of misfit strain and temperature are shown in Fig. 13a and b under the same conditions as the MIM configuration shown in Fig. 11 (bias field $E_a = 50$ kV/cm and field change $\Delta E = 120$ kV/cm). As seen in Fig. 13a, the largest electrocaloric response ($\Delta T = 0.9$ K) for the configuration with $E_i = [E_1, 0, 0]$ occurs near the HT-FOI phase transformation, due to the strong coupling between the in-plane electrical field and the in-plane spontaneous polarization P_1 or (P_2) of the FOI phase. For an IDE configuration with $E_i = [E_1/\sqrt{2}, E_1/\sqrt{2}, 0]$, the largest electrocaloric response ($\Delta T = 1.2$ K) is about 30 % higher than for the configuration with $E_i = [E_1, 0, 0]$. This can be explained by the fact that for the FOI phase with [100] or [010] IDEs, the electric field only induces polarization along one of the components (P_1 or P_2), while for [110] IDEs, the applied field induces polarization in both components P_1 and P_2 with a magnitude of $|P| = \sqrt{P_1^2 + P_2^2}$. Comparing the results presented in Figs. 11 and 13 it is seen that, under equivalent electrical boundary conditions, both MIM and IDE configurations have comparable electrocaloric responses ($\Delta T \sim 1$ K) at room temperature if the misfit strain is adjusted such that this temperature lies near either the HT-FTI or the HT-FOI phase transformation. The electrocaloric response as a function ΔE for the two IDE geometries is compared with that of the MIM configuration in Fig. 12. As seen in the figure, all three configurations can produce a large ΔT (~ 5 K) at fields greater than 1,000 kV/cm. As expected, the response is slightly larger for the [110] configuration compared with the [100] IDE or the MIM configurations.

5 Summary

The electrothermal (electrocaloric and pyroelectric) properties of ferroelectric thin films have many applications in active solid-state cooling and infrared sensing devices. It has been shown experimentally that some thin-film ferroelectrics can produce much larger electrothermal responses than their bulk counterparts. In this chapter, the electrothermal properties of bulk polar dielectric (ferroelectric and incipient ferroelectric) materials and thin films have been computed using a thermodynamic methodology and the effects of electrical, thermal and mechanical boundary conditions have been illustrated. In particular, the sensitivity of electrocaloric response to bias and driving fields, lateral clamping and misfit strain, thermal stresses and composition have been demonstrated. The computations show that the electrothermal behavior of ferroelectric materials for practical cooling devices depends on a complex interplay of several related sets of physical phenomena. These include the nature of the ferroelectric transition, the particular dependence of the equilibrium and transport properties on electric field and mechanical boundary constraints, and the orientation and thermal expansion coefficients of the thin film and substrate materials. The combined results provide insights concerning how the composition and orientation of the thin film material, the choice of substrate, the deposition/annealing temperature, and the electrode configuration can be used to optimize the electrothermal properties for particular applications.

References

1. Akcay, G., Alpay, S.P., Mantese, J.V., Rossetti Jr, G.A.: Magnitude of the intrinsic electrocaloric effect in ferroelectric perovskite thin films at high electric fields. Appl. Phys. Lett. **90**, 252909 (2007)
2. Akcay, G., Alpay, S.P., Rossetti Jr, G.A., Scott, J.F.: Influence of mechanical boundary conditions on the electrocaloric properties of ferroelectric thin films. J. Appl. Phys. **103**, 024104 (2008)
3. Alpay, S.P., Misirlioglu, I.B., Sharma, A., Ban, Z.-G.: Structural characteristics of ferroelectric phase transformations in single-domain epitaxial films. J. Appl. Phys. **95**, 8118 (2004)
4. Ban, Z.-G., Alpay, S.P.: Phase diagrams and dielectric response of epitaxial barium strontium titanate films: a theoretical analysis. J. Appl. Phys. **91**, 9288 (2002)
5. Ban, Z.-G., Alpay, S.P.: Dependence of the pyroelectric response on internal stresses in ferroelectric thin films. Appl. Phys. Lett. **82**, 3499 (2003)
6. Bednorz, J.G., Muller, K.A.: $Sr_{1-x}Ca_xTiO_3$: an XY quantum ferroelectric with transition to randomness. Phys. Rev. Lett. **52**, 2289 (1984)
7. Chen, H., Ren, T.-L., Wu, X.-M., Yang, Y., Liu, L.-T.: Giant electrocaloric effect in lead-free thin film of strontium bismuth tantalite. Appl. Phys. Lett. **94**, 182902 (2009)
8. Childress, J.D.: Application of a ferroelectric material in an energy conversion device. J. Appl. Phys. **33**, 1793–1798 (1962)
9. Correia, T.M., Young, J.S., Whatmore, R.W., Scott, J.F., Mathur, N.D., Zhang, Q.: Investigation of the electrocaloric effect in a $PbMg_{2/3}Nb_{1/3}O_3$-$PbTiO_3$ relaxor thin film. Appl. Phys. Lett. **95**, 182904 (2009)

10. Devonshire, A.F.: Theory of barium titanate-part II. Philos. Mag. **42**, 1065 (1951)
11. Devonshire, A.F.: Theory of barium titanate-part I. Philos. Mag. **40**, 1040 (1949)
12. Fatuzzo, E., Kiess, H., Nitsche, R.: Theoretical efficiency of pyroelectric power converters. J. Appl. Phys. **37**, 510–516 (1966)
13. Feigl, L., Zheng, S.J., Birajdar, B.I., Rodriguez, B.J., Zhu, Y.L., Alexe, M., Hesse, D.: Impact of high interface density on ferroelectric and structural properties of $PbZr_{0.2}Ti_{0.8}O_3$/$PbZr_{0.4}Ti_{0.6}O_3$ epitaxial multilayers. J. Phys. D Appl. Phys. **42**, 085305 (2009)
14. Haeni, J.H., Irvin, P., Chang, W., Uecker, R., Reiche, P., Li, Y.L., Choudhury, S., Tian, W., Hawley, M.E., Craigo, B., Tagantsev, A.K., Pan, X.Q., Streiffer, S.K., Chen, L.Q., Kirchoefer, S.W., Levy, J., Schlom, D.G.: Room-temperature ferroelectricity in strained $SrTiO_3$. Nature **430**, 758 (2004)
15. He, J., Chen, J., Wang, J.T., Hua, B.: Inherent regenerative losses of a ferroelectric Ericsson refrigeration cycle. Int. J. Therm. Sci. **42**, 169 (2003)
16. Hemberger, J., Nicklas, M., Viana, R., Lunkenheimer, P., Loidl, A., Bohmer, R.: Quantum paraelectric and induced ferroelectric states in $SrTiO_3$. J. Phys. Condens. Matter. **8**, 4673 (1996)
17. Jona, F., Shirane, G.: Ferroelectric Crystals. Dover, New York (1962)
18. Kar-Narayan, S., Mathur, N.D.: Direct and indirect electrocaloric measurements using multilayer capacitors. J. Phys. D Appl. Phys. **43**, 032002 (2010)
19. Karmanenko, S.F., Pakhomov, O.V., Prudan, A.M., Starkov, A.S., Eskov, A.: Layered ceramic structure based on the electrocaloric elements working as a solid state cooling line. J. Eur. Ceram. Soc. **27**, 3109–3112 (2007)
20. Li, B., Ren, W.J., Wang, X.W., Meng, H., Liu, X.G., Wang, Z.J., Zhang, Z.D.: Intrinsic electrocaloric effects in ferroelectric Poly(vinylidene fluoride-trifluoroethylene) copolymers: roles of order of phase transition and stresses. Appl. Phys. Lett. **96**, 102903 (2010)
21. Lines, M.E., Glass, A.M.: Principles and Applications of Ferroelectric and Related Materials. Oxford University Press, New York (1977)
22. Lisenkov, S., Ponomareva, I.: Intrinsic electrocaloric effect in ferroelectric alloys from atomistic simulations. Phys. Rev. B **80**, 140102 (2009)
23. Mathur, N., Mischenko, A.: Solid state electrocaloric cooling devices and methods. U.S. Patent WO 2006/056809 A1
24. Mischenko, A.S., Zhang, Q., Scott, J.F., Whatmore, R.W., Mathur, N.D.: Giant electrocaloric effect in thin-film $PbZr_{0.95}Ti_{0.05}O_3$. Science **311**, 1270 (2006)
25. Mischenko, A.S., Zhang, Q., Whatmore, R.W., Scott, J.F., Mathur, N.D.: Giant electrocaloric effect in the thin film relaxor ferroelectric $0.9PbMg_{1/3}Nb_{2/3}O_3$-$0.1PbTiO_3$ near room temperature. Appl. Phys. Lett. **89**, 242912 (2006)
26. Misirlioglu, I.B., Alpay, S.P., Aindow, M., Nagarajan, V.: Thermodynamic and electrostatic analysis of threading dislocations in epitaxial ferroelectric films. Appl. Phys. Lett. **88**, 102906 (2006)
27. Neese, B., Chu, B., Lu, S.-G., Wang, Y., Furman, E., Zhang, Q.M.: Large electrocaloric effect in ferroelectric polymers near room temperature. Science **321**, 821–823 (2008)
28. Newnham, R.E.: Properties of Materials: Anisotropy, Symmetry, Structure. Oxford University Press, Oxford (2005)
29. Pecharsky, V.K., Gschneidner Jr, K.A.: Magnetocaloric effect and magnetic refrigeration. J. Magn. Magn. Mater. **200**, 44 (1999)
30. Pertsev, N.A., Zembilgotov, A.G., Tagantsev, A.K.: Effect of mechanical boundary conditions on phase diagrams of epitaxial ferroelectric thin films. Phys. Rev. Lett. **80**, 1988 (1998)
31. Pertsev, N.A., Tagantsev, A.K., Setter, N.: Phase transitions and strain-induced ferroelectricity in $SrTiO_3$ epitaxial thin films. Phys. Rev. B **61**, R825 (2000)
32. Pertsev, N.A., Tagantsev, A.K., Setter, N.: Erratum: phase transitions and strain-induced ferroelectricity in $SrTiO_3$ epitaxial thin films. Phys. Rev. B **65**, 219901 (2002)
33. Prosandeev, S., Ponomareva, I., Bellaiche, L.: Electrocaloric effect in bulk and low-dimensional ferroelectrics from first principles. Phys. Rev. B **78**, 052103 (2008)

34. Qiu, Q.Y., Nagarajan, V., Alpay, S.P.: Film thickness versus misfit strain phase diagrams for epitaxial $PbTiO_3$ ultrathin ferroelectric films. Phys. Rev. B **78**, 064117 (2008)
35. Rabus, D.G., Bian, Z.X., Shakouri, A.: A GaInAsP-InP double-ring resonator coupled laser. IEEE Photonics Tech. Lett. **17**, 1770 (2005)
36. Schlom, D.G., Chen, L.-Q., Eom, C.-B., Rabe, K.M., Streiffer, S.K., Triscone, J.-M.: Strain tuning of ferroelectric thin films. Annu. Rev. Mater. Res. **37**, 589–626 (2007)
37. Sebald, G., Pruvost, S., Seveyrat, L., Lebrun, L., Guyomar, D., Guiffard, B.: Electrocaloric properties of high dielectric constant ferroelectric ceramics. J. Eur. Ceram. Soc. **27**, 4021–4024 (2007)
38. Simon, W.K., Akdogan, E.K., Safari, A., Bellotti, J.A.: In-plane microwave dielectric properties of paraelectric barium strontium titanate thin films with anisotropic epitaxy. Appl. Phys. Lett. **87**, 082906 (2005)
39. Speck, J.S., Pompe, W.: Domain configurations due to multiple misfit relaxation mechanisms in epitaxial ferroelectric thin films. I. Theory. J. Appl. Phys. **76**, 466 (1994)
40. Strukov, B.A., Levanyuk, A.P.: Ferroelectric Phenomena in Crystals: Physical Foundations. Springer, Berlin (1998)
41. Thacher, P.D.: Electrocaloric effects in some ferroelectric and antiferroelectric Pb(Zr, Ti)O_3 compounds. J. Appl. Phys. **39**, 1996 (1968)
42. Uwe, H., Sakudo, T.: Stress-induced ferroelectricity and soft phonon modes in $SrTiO_3$. Phys. Rev. B **13**, 271 (1976)
43. Zhang, J., Heitmann, A.A., Alpay, S.P., Rossetti Jr, G.A.: Electrothermal properties of perovskite ferroelectric films. J. Mater. Sci. **44**, 5263 (2009)
44. Zhang, J., Misirlioglu, I.B., Alpay, S.P., Rossetti Jr, G.A.: Electrocaloric properties of epitaxial strontium titanate films. Appl. Phys. Lett. **100**, 222909 (2012)
45. Zhang, J., Alpay, S.P., Rossetti Jr, G.A.: Influence of thermal stresses on the electrocaloric properties of ferroelectric films. Appl. Phys. Lett. **98**, 132907 (2011)
46. Zhong, S., Alpay, S.P., Ban, Z.-G., Mantese, J.V.: Effective pyroelectric response of compositionally graded ferroelectric materials. Appl. Phys. Lett. **86**, 092903 (2005)y

Electrocaloric Effect in Relaxor Ferroelectric-Based Materials

Jani Peräntie, Tatiana Correia, Juha Hagberg and Antti Uusimäki

1 Introduction

Although electrocaloric effect (ECE) has been known for a reasonably long time, it is not until quite recently that the interest has renewed again due to pioneering work by Mischenko et al. [58]. Up to date, a large amount of experimental studies have been performed on various materials, from oxides to polymers, which are expected to show advanced electrocaloric properties. In particular, various ferroelectric-based materials show potential electrocaloric behavior, especially in a thin film form. These previous electrocaloric results have been, in fact, addressed and summarized more extensively in recent review articles [53, 76, 92]. The intention in this chapter is to focus more on two specific inorganic relaxor ferroelectric material systems, $Pb(Mg_{1/3}Nb_{2/3})_{1-x}Ti_xO_3$ (PMN-PT) and $Pb(Sc_{1/2}Ta_{1/2})O_3$ (PST), which have been under extensive electrocaloric research work especially due to their special dielectric and pyroelectric properties. Additionally, these material groups are considered as prototype representatives for two of the most common lead-based relaxor ferroelectric systems, and they are also part of materials group known for an exceptional piezoelectric activity.

In Sect. 2 the first system, $Pb(Mg_{1/3}Nb_{2/3})O_3$-$PbTiO_3$, is introduced. At first, special dielectric and structural characteristics are reviewed especially under the influence of electric field to address the electrocaloric effect. After that, many experimental direct and indirect electrocaloric studies on bulk-type PMN-PT are considered and discussed. Finally, electrocaloric behavior of PMN-PT bulk-system is compared with thin films of same material, and some reasons for deviations are addressed.

J. Peräntie (✉) · J. Hagberg · A. Uusimäki
Microelectronics and Materials Physics Laboratories, University of Oulu,
4500 90014 Oulu, Finland
e-mail: jani@ee.oulu.fi

T. Correia
National Physical Laboratory, Hampton Road, Teddington, Middlesex
TW11 0LW, UK

T. Correia and Q. Zhang (eds.), *Electrocaloric Materials*,
Engineering Materials 34, DOI: 10.1007/978-3-642-40264-7_3,

Another important relaxor system of $Pb(Sc_{1/2}Ta_{1/2})O_3$ with varying *B*-site cation order is reviewed in Sect. 3. Especially, the possibility for *B*-site order modification and its impact on electrocaloric properties are considered.

The main intention of this chapter is to sketch a general picture of the electrocaloric behavior and characteristics in ferroelectric-based inorganic relaxor materials especially by reviewing experimental results of two important material systems, and enlighten the reasons behind observed behaviors.

2 $Pb(Mg_{1/3}Nb_{2/3})O_3$-$PbTiO_3$ System

As it is known, material shows a high electrocaloric effect, when high reversible entropy changes can be induced as a function of temperature and electric field. In ferroelectric and relaxor materials, which show either long-range or partial polar order, significant variation in polarization can be introduced by external stimulus near their phase transition regions [15, 27]. Large polarization changes, when being reversible in nature, may further lead to high entropy changes and a considerable electrocaloric effect. This is the main reason why ferroelectric-based materials are considered to be potential materials to be exploited in future electrocaloric applications. Especially, highly piezoelectric PMN-PT material system with high dielectric constant has been widely considered to also show beneficial electrocaloric properties. Perhaps one of the first reasons to study PMN-PT for electrocaloric effect was its ability to show a high pyroelectric effect [19], which is thermodynamically equivalent to the electrocaloric effect.

Here, we first briefly review some main structural characteristics and phase diagrams established for PMN-PT system. Especially, the influence of external electric field is addressed. For a more detailed discussion on structure and other related electrical properties of PMN-PT and related relaxor ferroelectrics, readers are pointed towards some extensive reviews on different aspects of relaxor ferroelectrics in general contributed for example by Cross [26], Ye [100], Noheda [60], Samara [73], Noheda and Cox [63], Bokov and Ye [8], Davis [30], and Kiat and Dkhil [46]. The rest of the section is dedicated to various experimental results related to electrocaloric performance of PMN-PT in bulk-materials and thin films.

2.1 Some Special Characteristics of PMN-PT System

Lead magnesium niobate, $Pb(Mg_{1/3}Nb_{2/3})O_3$ (PMN), is considered to represent a prototype of a relaxor ferroelectric material, and it has been the most studied relaxor material since its introduction by Smolenskii and Agranovskaya [88]. Pure $Pb(Mg_{1/3}Nb_{2/3})O_3$ relaxor shows a high and broad peak in the temperature dependence of dielectric permittivity with a strong characteristic frequency dispersion (Fig. 1). As a distinction from traditional ferroelectrics, no long range

polar order develops and an average symmetry remains cubic down to very low temperatures [57]. Instead, only polar nanoregions (PNRs) develop at high temperatures close to the Burns temperature $T_B \approx 620$ K on cooling embedded to a non-polar lattice matrix [13, 14]. The number of these nanoregions grows with decreasing temperature and they seem to combine into larger clusters at the freezing temperature $T_f \approx 210$ K [98]. When temperature decreases, a characteristic PNR reorientation time (related to thermal motion) increases and finally below T_f they become frozen (i.e. static) due to increased dipole interaction [9]. It is understood that this phenomenon qualitatively explains the main dielectric characteristics of PMN (high diffused dielectric peak and its strong frequency dispersion) shown in Fig. 1.

Additionally, another type of short-range ordering, which is also important for relaxor behavior, takes place in PMN lattice. This ordering is related to the *B*-site of PMN's perovskite lattice, where Mg^{2+} and Nb^{5+} ions occupy their equivalent sites in a 1:2 stoichiometric ratio. Occupation is mainly random, but there exist small chemically ordered regions (CORs), where alternating *B*-site sublattices are occupied either by Nb^{5+} ions alone or mixture of Mg^{2+} and Nb^{5+} cations so that the overall stoichiometry is preserved [28]. In PMN the size and location of CORs is fixed (quenched), but in other type of relaxors, such as in $Pb(Sc_{1/2}Ta_{1/2})O_3$, the degree of chemical order can be changed by thermal annealing as described in Sect. 3. Relation of chemical order to the relaxation is essential since no relaxor behaviour is found in completely chemically ordered crystals. This means that an appearance of compositional disorder inhibits ferroelectric order from developing

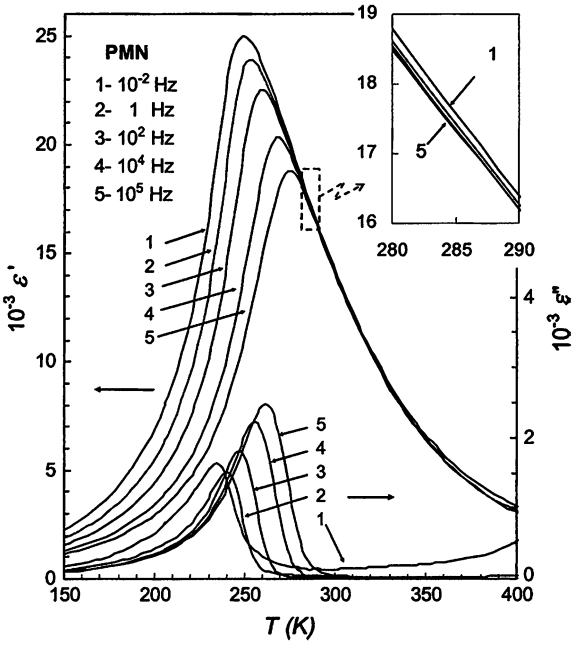

Fig. 1 Real and imaginary parts of the relative permittivity as a function of temperature measured for $Pb(Mg_{1/3}Nb_{2/3})O_3$ at different frequencies [8]

at low temperatures and a relaxor state with PNRs is established. However, the relation between CORs and PNRs is not completely clear. Currently, it seems that an ergodic phase of relaxor involves both dynamic and static PNRs, and of which static PNRs appear only inside CORs [10]. Dynamic PNRs are also found in PMN-55PT, which is completely compositionally disordered (i.e. no CORs).

A quenched disordered distribution of Mg^{2+} and Nb^{5+} in *B*-site leads naturally to the formation of random electric fields, which are also believed to have a significant impact on the formation of polar order in relaxors. Based on various results, two different approaches have mainly been taken [73]. The first approach suggests that PMN is intrinsically a normal ferroelectric, where macroscopic domains are broken up into nanodomains by the quenched random fields, and this leads to the smearing of the ferroelectric transition and the onset of the relaxor state [96]. The second treatment attributes relaxor behavior to a glass state similar to dipolar glasses with randomly interacting polar nanodomains in the presence of random fields [26, 51, 95]. Although there are many arguments for both of these approaches, the majority of the results favour the dipolar glass model [73]. The main difficulty from the experimental point of view is that both of these states exhibit similar average and local structural characteristics [8]. In the spherical random-bond-random-field (SRBRF) model developed by Pirc and Blinc [69], the polar nanoregions in relaxor interact between each other (like in classical dipolar glasses), but also interaction between PNRs and random fields may take place.

An addition of other well-known ferroelectric lead titanate ($PbTiO_3$ or PT) perovskite into $Pb(Mg_{1/3}Nb_{2/3})O_3$ forms a solid-solution, where the dielectric constant is increased [19]. When a ferroelectrically active Ti^{4+}-ion replaces $(Mg_{1/3}Nb_{2/3})^{4+}$ on *B*-site in perovskite lattice, the size of chemically ordered regions is suppressed and a macroscopic rhombohedral ferroelectric order starts to develop [101]. A clear rhombohedral phase has been detected at low temperatures in PMN-*x*PT already with $x \geq 0.05$ [103]. Higher PT concentration in a pseudobinary phase diagram of the (1-x)PMN-*x*PT system leads to formation of a morphotropic phase boundary (MPB) region, which locates between rhombohedral and tetragonal phases at low temperatures quite similarly to the famous piezoelectric $Pb(Zr_{1-x}Ti_x)O_3$ (PZT) solid solution [19, 20]. The relative permittivity and piezoelectric coefficients exhibit maximum values close to this boundary [19]. More detailed higher resolution structural studies around the morphotropic phase boundary have later shown that an additional low-symmetry monoclinic phase regions exist between rhombohedral and tetragonal phases. These experimentally found monoclinic phases were also predicted theoretically by expanding free-energy to the eight-order [94]. Three different monoclinic phases were denoted by M_A (space group *Cm*), M_B (*Cm*), and M_C (*Pm*), all of which have been evidenced in PMN-PT system around the MPB. At first, a monoclinic M_C phase was found in ceramic PMN-PT system [45, 85]. It was found to be a major phase in a narrow region between R and T phases with $x = 0.31 - 0.37$ depending on temperature [61], and a new phase diagram was reported based on this information (Fig. 2a). Further powder neutron diffraction studies suggested also a presence of another monoclinic M_B phase with lower *x* [86]. A refined phase diagram including various

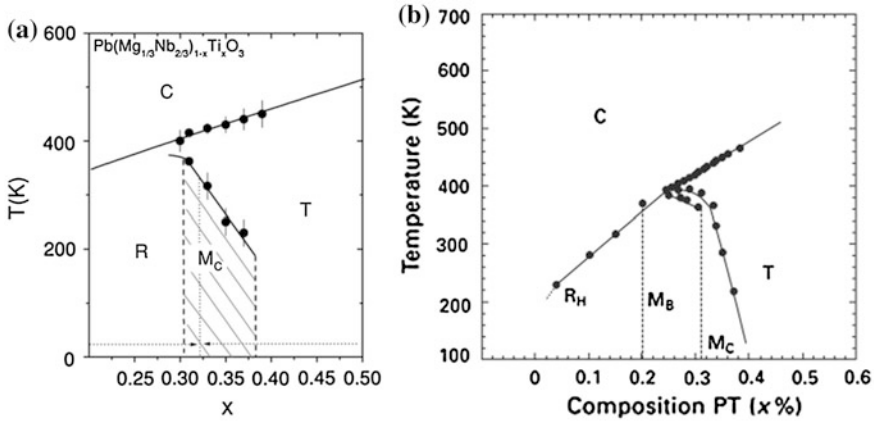

Fig. 2 Phase diagrams of polycrystalline PMN-xPT system around the morphotropic phase boundary region: **a** the proposed phase diagram after M_C phase discovery [61], **b** a refined phase diagram including M_B phase region [46]

recent results is presented in Fig. 2b [46]. Additionally, the monoclinic M_A and orthorhombic O phases have been found in PMN-PT system, when an external electric field is applied [4, 16, 102]. This fact is considered more in the next paragraph, where observed PMN-PT phase diagram is considered under an applied electric field.

From the electrocaloric point of view, it is more interesting to review the PMN-xPT system under an applied electric field. Especially, the effect of isothermal application of electric field corresponds more to the circumstances of the electric-field-induced electrocaloric effect, and the main focus is on these results. Otherwise, the major part of the experiments on PMN-PT has been carried out by heating/cooling with constant electric field. At low x, where the material possess only a limited and confined ferroelectric order at low temperatures, an application of strong enough electric field irreversibly induces a long-range ferroelectric rhombohedral order [2, 99]. Just above the thermal depolarization temperature electric field can induce a reversible phase transition from macroscopically non-polar relaxor state to polar ferroelectric state, such as in ordinary ferroelectrics with first-order phase transition, e.g. in $BaTiO_3$. This phase transition is accompanied by high entropy changes, which directly lead to high electrocaloric effect, as seen in many experimental results throughout this book.

Different polar phases found in PMN-PT system have different directions of polarization. In relation to a pseudocubic shell polar directions for a rhombohedral (R), orthorhombic (O) and tetragonal (T) phases are along <111>, <101> and <001> directions, respectively. On the other hand, polarization of monoclinic phases lie somewhere within mirror planes between the aforementioned higher symmetry phases [94] as described in Fig. 3. These monoclinic phases can thus be regarded as structural bridges between rhombohedral, tetragonal and orthorhombic phases [63]. Close to the MPB, where multiple phase transition regions exist, the

application of electric field into non-polar direction can easily lead to the polarization rotation and electric-field-induced phase transitions within these phases due to flatness of the associated energy profile [27]. In fact, the concept of polarization rotation has been closely related to the unusually high piezoelectricity found especially in single-crystals of relaxor-PT compositions with MPB [37, 60, 63].

The first application of electric field into PMN-PT below T_C creates a macroscopic polarization. In single crystals, where electric field can be directed along desired crystallograhical directions, monodomain structures can be achieved with electric field along the polar direction. Otherwise, the field application to non-polar directions necessarily leads to multidomain configurations. This initial poling also involves a temperature response caused by the loss from irreversible polarization reorientation. All the possible domain variants in each ferroelectric phase in question finally tend to orient so that the angles to the applied electric field are minimized, which results in a formation of domain engineered structures [5]. Further application of electric field into these structures induces polarization rotation and possible electric-field-induced phase transitions.

With reasonably low PT concentrations, the low-temperature structure of a poled PMN-PT is rhombohedral, and an application of <001>-directed electric field starts to rotate the polarization towards tetragonal direction as can easily be visualized from Fig. 3. According to structural studies the polarization rotates in a M_A monoclinic plane, and eventually a strong enough electric field (depending now on the temperature and composition) induces phase transition to a tetragonal T phase [17, 18, 62]. On the other hand, a <011>-directed electric field rotates the polarization towards an orthorhombic O phase through a monoclinic M_B phase [17]. The required electric field strengths for these phase transitions are decreased, when composition closes the MPB and/or temperature increases. Inside the MPB region, a zero-field monoclinic M_C phase structure starts to develop (see Fig. 2) and electric-field-induced phase transition sequences become $M_C \rightarrow O$ for $E \| <011>$ and $M_C \rightarrow T$ for $E \| <001>$ [17]. As special case, a <001>-directed

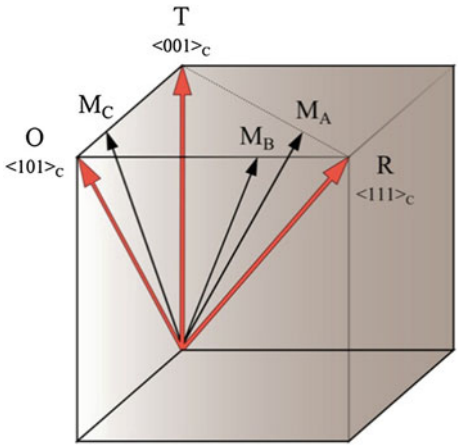

Fig. 3 Schematic description of polarization directions in perovskite ferroelectric rhombohedral (*R*), orthorhombic (*O*), tetragonal (*T*), and monoclinic phases in relation to a pseudocubic cell. Monoclinic phases are denoted as M_A, M_B, and M_C according to Vanderbilt and Cohen [94]

electric field causes a phase transition sequence of R → M_A → M_C → T with additional transition between monoclinic phases in PMN-30PT as described in Fig. 4 [4]. From the major parts, these transitions show a reversible nature, but it seems that monoclinic phases are stable instead of rhombohedral after removal of the electric field [4, 17]. According to many field-induced polarization and strain measurements in PMN-*x*PT, these phase transitions additionally show first-order-like jumps and hysteretic behavior within the otherwise continuos polarization rotation paths [29, 52, 65].

One very interesting discovery, which is also significant from the electrocaloric point of view as shown later, is that the phase transitions in PMN-PT system show critical end points. Kutnjak et al. [47] found out that the first-order nonpolar-polar phase transition in the electric field-composition-temperature phase diagram of PMN-*x*PT system terminates in a line of critical endpoints. Additionally, critical end points were observed also in ferroelectric–ferroelectric phase transitions at lower temperatures, when electric field was applied to [111]- or [110]-directions in PMN-*x*PT [47, 48].

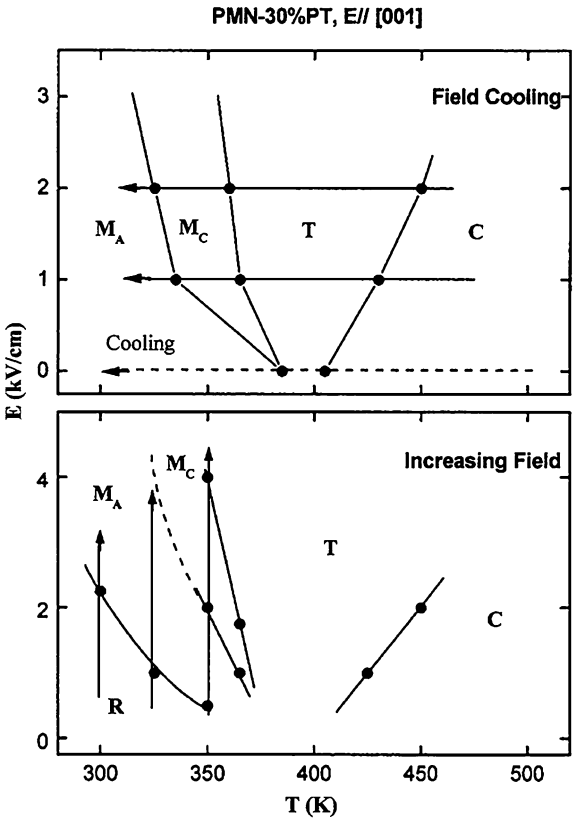

Fig. 4 E-T phase diagrams of PMN-30 %PT single crystal with E‖[001] measured by means of XRD on field-cooling (*top*) and on increasing electric field after ZFC (*bottom*). *Arrows* indicate the scanning direction [4]

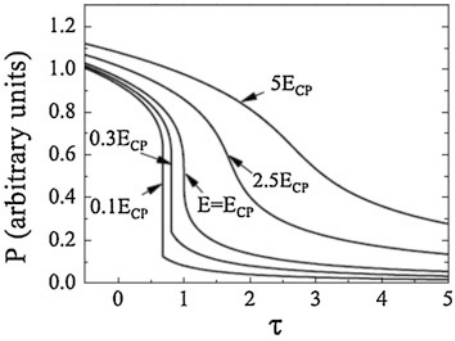

Fig. 5 The order parameter P development as a function of normalized temperature $\tau = T/T_{CP}$ with different constant electrical fields [48]

As a distinction from a tricritical point, which is also suggested to reside in E-T phase diagram of PMN [100], at the critical end point (E_{CP}, T_{CP}) the latent heat goes to zero, first-order transition terminates and supercritical evolution is observed above it [48]. The difference between the two involving phases disappears in a similar way as between the liquid and the vapor phases in the pressure versus temperature phase diagram of water. The calculated temperature behavior of the order parameter (polarization P in this case), which describes the phase transition, is presented in the vicinity of the critical point in Fig. 5 [48]. With electric fields below the critical E_{CP}, a clear step in the order parameter P is seen as an indication of the first-order transition. At the critical point ($E = E_{CP}$ and $T/T_{CP} = \tau = 1$) the step vanishes, and no phase transition exists at higher fields.

This means that, for example in electric-field-temperature phase diagram of [111]-oriented PMN crystal, the presence of the critical point is seen as shown in

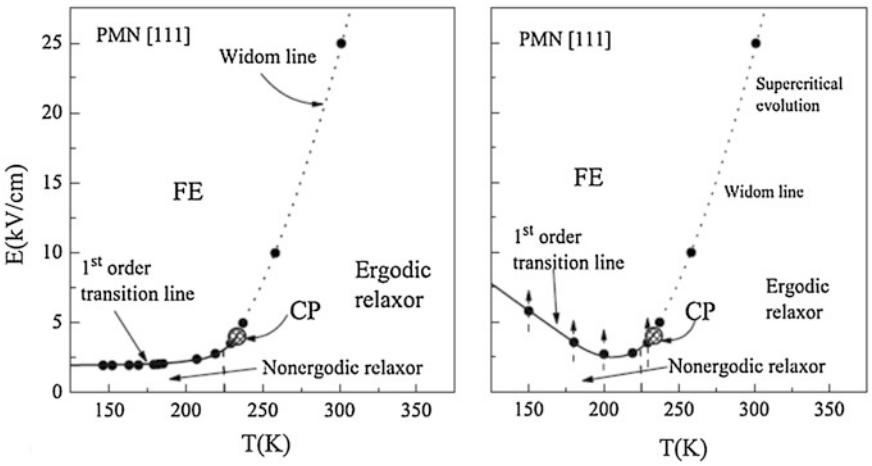

Fig. 6 Phase diagrams of PMN with the electrical field applied in the [111] direction: E = const, T = variable (*left*) and E = variable, T = const. (*right*). Beyond the critical point (CP) a supercritical evolution is observed [49]

Fig. 6 [49]. Below the critical temperature T_{CP} the electric field needed to initiate the transition depends on the route the final state is achieved. In Fig. 6 (left), the phase diagram is presented under field-cooling. As the applied field is increased the transition temperature is increased. In Fig. 6 (right) the phase transition is initiated by increasing electric field after the zero-field-cooling. However, in this case the critical points in both diagrams locate very close to each other. Other significant point worth of noting is a strong anisotropy found in PMN. In opposite to [111]-directed electric field, an application of electric field along [001] produced only smooth field dependence of polarization indicating an absence of co-operative behaviour. Naturally, this also means that no critical points were observed with $E \| [001]$.

Significantly, it was observed that the energy cost and electric field for polarization rotation decreased remarkably on approaching the critical end point, which led to maximized piezoelectric coefficient. This observation reveals a new mechanism for the explanation of the giant electromechanical response observed in this type of relaxor ferroelectrics [47].

Several special characteristics of PMN-PT system presented above make it interesting also for electrocaloric considerations. This system shows high dielectric polarization changes as a function of electric field and temperature, which may lead to high entropy change and electrocaloric effect. Although PMN-PT system contains many ferroelectric phases, especially around the MPB region, and electric field can be used to transform between these phases to produce polarization and temperature changes, the most interesting and highest electrocaloric effect from application point of view is generally observed close to the highest polar-nonpolar phase transition temperature (i.e. the Curie temperature). And with a first-order phase transition, the application of electric field can reversibly induce spontaneous polarization and high entropy change in temperature range well above the highest transition temperature. Additionally, characteristic temperatures in PMN-PT system can be adjusted by changing the $PbTiO_3$ concentration. In this way, for example, the Curie temperature range with the highest activity can be altered from $T \sim -60$ °C (zero-field thermal depolarization temperature for pure $PbMg_{1/3}Nb_{2/3}O_3$) up to $T = 490$ °C (Curie temperature for pure $PbTiO_3$). Another interesting point of PMN-PT system is its underlying relaxor nature. Some experimental results and theoretical works imply that characteristic polar nanodomains have significant additional contribution to the electrocaloric effect in relaxors [6, 34, 40, 84]. In addition, Pirc et al. [70] have provided a self-consistent relation for the electrocaloric temperature change in relaxors from the Landau theory. By using parameters of the spherical random-bond-random-field model [69] and numerically minimizing the mean field free energy, they calculated the electrocaloric ΔT as a function of electric field and temperature for relaxor ferroelectrics. Especially, it was shown that with field-induced first-order phase transition line terminating at a specific critical point, the ECE responsivity R ($=\Delta T/E$) reaches a maximum value near that point.

2.2 Electrocaloric Characteristics in Bulk-Type PMN-PT

Although the PMN-PT solid-solution is the most studied electrocaloric system (along with PST), there is still a rather limited amount of published data on its electrocaloric behaviour. The measurements are generally performed either by indirect evaluation from polarization data or by directly recording the field-induced temperature change or heat flow. In this way, the electrocaloric temperature change ΔT is characterized as a function of electric field and temperature. Some studies also calculate the corresponding field-induced entropy change ΔS ($=C\Delta T/T$), which is also an important parameter when the actual refrigeration function is considered (see e.g. Chap. 1).

Shebanov et al. [81] published the first results in Russian on electrocaloric experiments with PMN bulk. After that the next paper considering ECE in PMN-PT system was published not until in 1998. The rest of the electrocaloric results on PMN-PT have been published during the 21st century. Here, these published EC characterizations with some related structural considerations of PMN and PMN-*x*PT ceramics and single crystals are reviewed. All the electrocaloric results are reviewed by gradually increasing the PT concentration, starting from pure PMN and ending up with pure PT.

PMN-xPT compositions with low x

The aforementioned first article on EC effect measurement of PMN ceramic by Shebanov et al. [81] showed a maximum EC effect of 0.15 °C with electric field of 15 kV/cm at −47 °C (226 K). Thereafter the electrocaloric effect of PMN has been studied in wider temperature and electric field range by Rožič et al. [71]. They measured the EC effect using a high resolution calorimeter with a small bead thermistor attached to the sample. Electric field pulses with typical time scales of 10–20 s in duration were applied to the sample so that the thermal equilibrium with the surrounding bath was reached. The electrocaloric temperature change was extracted from the thermistor response signal using zero-dimensional model taking the geometry of the system into account. Figure 7 shows the measured temperature dependence of the EC effect in PMN bulk ceramics as a function of temperature and the field-dependence of a single measurement result at 16 °C (289 K). As it can be seen, the maximum EC effect around 2.5 °C at 67 °C (340 K) with electric field of 90 kV/cm was observed. The overall EC effect seems to be very weakly dependent on temperature in the measurement range of 220–340 K (Fig. 7a), which lies just above the freezing temperature of PMN. This type of behavior is beneficial, when concerning refrigeration and cooling applications acting within wide temperature intervals. As shown in Fig. 7b, the EC effect is relatively linear function of electric field, which seems to be quite typical behavior for EC effect in the range considerably distant from any type of critical temperatures, where more abrupt temperature changes are met.

One of the first electrocaloric studies with PMN-PT was performed by directly measuring a series of PMN-*x*PT ceramics with $x = 8$, 10, and 25 % immersed in silicone oil [97]. Temperature range of measurements was limited to between 23

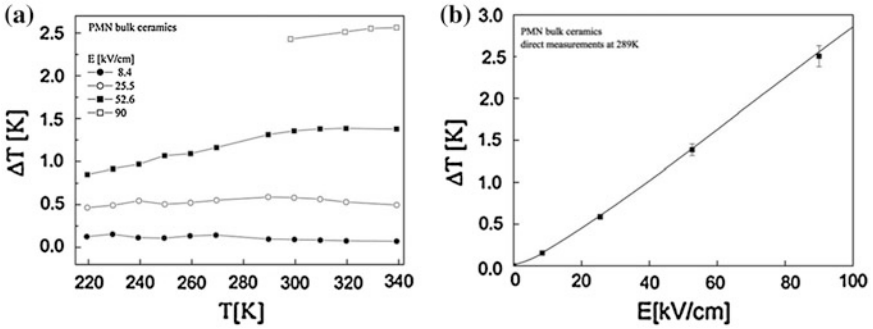

Fig. 7 Electrocaloric effect in PMN: **a** temperature dependence of the EC effect in PMN bulk ceramics as a function of temperature for several electrical fields, **b** EC effect as a function of electric field at 16 °C (289 K). [71]

and 41 °C. A considerable variance in ΔT was observed in this range which makes it difficult to follow any trends. Significantly, the PMN-8PT and PMN-10PT compositions with depolarization temperatures below the measurement range showed the highest EC effects of 1.35 and 1.25 °C, respectively. A local maximum in ECE ($\Delta T = 0.4$ °C at around $T = 32$ °C) was also observed for PMN-25PT composition although its depolarization temperature is well above the measurement range. These measured values gave the first indications that a reasonably high EC effect can be achieved on PMN-PT.

A more detailed direct electrocaloric study on PMN-10PT ceramics by Shebanov et al. [84] with electric fields of 18.2 and 29.1 kV/cm is shown in Fig. 8. At first, the electrocaloric temperature change raises rapidly at around −45 °C, having a maximum value of $\Delta T = 0.45$ °C at 50 °C with electric field of 29.1 kV/cm. According to these results it seems that that this composition shows phase transition temperature close to −45 °C above which it turns to a relaxor phase showing higher electrocaloric response due to the electric-field-induced reversible relaxor-ferroelectric phase transformation. Remarkably, a clear enhancement in ECE was

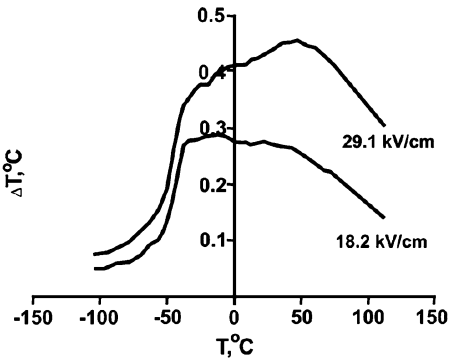

Fig. 8 Temperature dependence of electrocaloric temperature change measured for 90 %PMN-10 %PT at two different fields [84]

observed for the first time with stronger electric field when an additional peak forms above the transition.

More direct measurements on PMN-PT ceramics within this composition range were executed in 2004, when electrocaloric measurements by an infrared detector were reported for PMN-10 %PT and PMN-15 %PT compositions [80]. The highest effect of $\Delta T = 1.75$ °C was observed at 18 °C with an electric field of 16 kV/cm. In comparison to other direct measurement results in this composition range, this value appears to agree with results by Xiao et al. [97]. However, those values are significantly higher than values in Fig. 8 obtained by higher electric fields.

Figure 9 presents the electrocaloric characteristics reported for PMN-13 %PT ceramic [40]. The electrocaloric temperature change was measured from the largest sample face directly by an attached alumel-chromel thermocouple under adiabatic conditions. The thermocouple voltage was measured before, during, and after an applied rectangular voltage pulse of 6.2 s in duration.

At low electric fields the EC effect is strongest around the thermal depolarization temperature of 18 °C, but at higher fields the maximum effect seems to move towards higher temperatures as was indicated previously in Fig. 8. The maximum electrocaloric temperature change was $\Delta T = 0.558$ °C at $T = 70$ °C with an electric field of $E = 24$ kV/cm. The first peak appearing at small field strengths occupies a narrow temperature range around $T \geq 18$ °C, whereas the other developing peak seems to grow gradually with increasing field. A pronounced peak in the EC effect found previously in several ferroelectrics near the Curie or depolarization temperature has been explained by an electric-field-induced phase transformation from a paraelectric-like or antiferroelectric state to a ferroelectric polar state (see e.g. [7, 84]). As pointed out earlier, this first-order transformation involves a critical point with certain temperature and the applied electric field in PMN-PT [47, 48]. Overall, the shape of temperature dependence and the magnitude of EC effect for PMN-13 %PT (Fig. 9) are comparable to the one observed for PMN-10 %PT (Fig. 8).

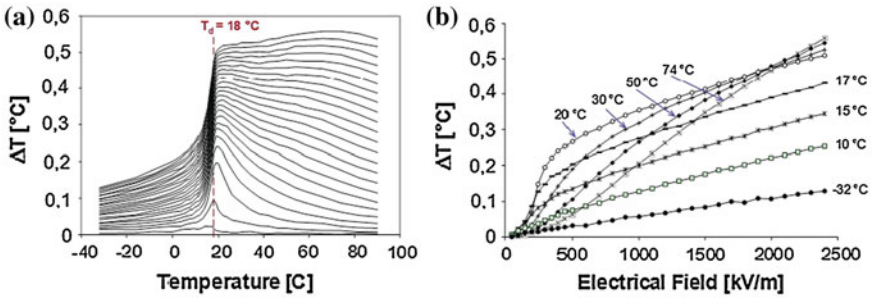

Fig. 9 **a** EC temperature rise ΔT as a function of temperature within a range of electric fields from 1 to 24 kV/cm, and **b** electrocaloric temperature rise ΔT as a function of applied electric field E at different temperatures [40]

Figure 9b presents the electrocaloric ΔT as a function of the applied electric field at some fixed temperatures. At $T = -32$ °C, far below the depolarization temperature $T_{dp} = 18$ °C, the $\Delta T/E$ dependence is weak and linear. Closer to T_{dp}, at 15, 17, and 20 °C, there is first a clear jump, indicating a first-order-type phase transition, and after that the dependence is more linear. Relatively far above T_{dp}, at 30, 50, and 74 °C, this clear jump disappears, when the actual transition smears out and the continuous-like dependence becomes evident as the temperature increases. Generally in ferroelectrics with first-order transition, there is a limited temperature range between T_C and the critical end point T_{CP} where electric field can induce ferroelectric order [75].

The results for PMN-13 %PT ceramics were supplemented with more detailed temperature measurements in response to sequentially applied electric fields on initially depoled samples around thermal depolarization temperature T_{dp} [64]. As was shown already in Fig. 9, the EC effect displays a marked peak just around the depolarization temperature of $T_{dp} = 18$ °C due to the reversible field-induced phase transition to the ferroelectric phase. However, at lower temperatures reversible ΔT_{ECE} drops rapidly to below 0.1 °C, and at the same time, an additionally irreversible thermal response is observed for depoled samples without initial macroscopic polarization. This means that the total field-induced temperature response to an increasing electric field in a depoled PMN-13PT changes from a fully reversible ($T > T_{dp}$) to only partially reversible ($T < T_{dp}$). Below T_{dp}, the field-induced reversible phase transition from non-polar to polar phase disappears, and either a non-ergodic relaxor state, ferroelectric state or their possible mixture are possible after ZFC. When a reversible electrocaloric effect (ΔT_{ECE}) and poling hysteresis related loss ($\Delta T_{x\mathrm{Hy}}$) were evaluated and subtracted from the temperature response, and additional irreversible and reasonably strong temperature response (ΔT_{PT}) was observed to remain (Fig. 10). It was suggested that the additional response is caused by field-induced transition to a macroscopic ferroelectric state.

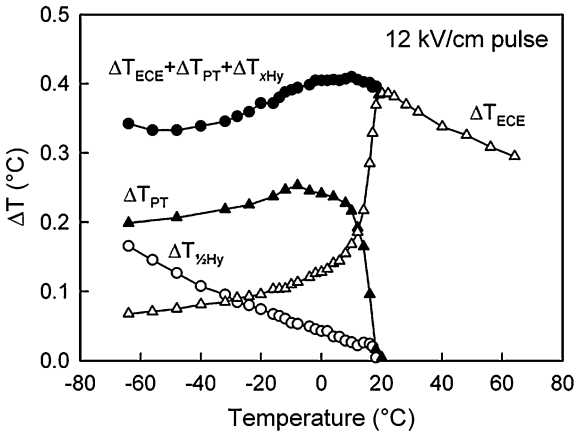

Fig. 10 Field-induced thermal response from a virgin state PMN–13 %PT ceramics as a function of temperature. Thermal changes are assigned for irreversible transition (ΔT_{PT}), reversible EC effect (ΔT_{ECE}), and polarization formation and switching hysteresis losses (ΔT_{xHy} and $\Delta T_{½\mathrm{Hy}}$) [64]

Although previous structural studies show that rhombohedral order can develop with x as low as 5 % [103], it seems that this order might still be partially confined and electric field is needed to fully induce the macroscopic ferroelectric order. Furthermore, this shows that considerable irreversible thermal effects might be present during the field application. These nonreproducible effects should be identified and separated from the actual reversible electrocaloric response.

The aforementioned additional temperature response ΔT_{PT} increases rapidly from zero to a broad maximum value of 0.25 °C below the zero-field depolarization temperature T_{dp}, and it decreases monotonically at lower temperatures. It is noteworthy to see that the EC temperature change ΔT_{ECE} above T_{dp} in Fig. 9a coincides with the summed temperature response $\Delta T_{ECE} + \Delta T_{PT} + \Delta T_{xHy}$ below T_{dp}, and forms a continuous field-induced temperature response of a virgin PMN-13 %PT sample with a broad maximum value around $T = 10$ °C. Also, the dielectric hysteresis loop area of the ferroelectric phase increases towards lower temperatures, leading to an increase in induced temperature changes caused by initial polarization development (ΔT_{xHy}) and polarization switching ($\Delta T_{½Hy}$).

The first ECE evaluation on single crystalline PMN-PT with critical temperatures closer to the room temperature was performed indirectly on <111>-oriented PMN-10PT composition using isothermal polarization measurements [55]. This evaluation was performed by measuring dielectric hysteresis at 1 Hz frequency using up to 40 kV/cm electric fields. As a result of this simulation, a rounded maximum EC effect of around 1 °C was observed at around 55 °C (Fig. 11). The shape of the simulated EC effect is typical for indirect measurements, and it is affected by the use of polynomial function fits in the derivation of the electrocaloric effect. Use of fitted functions gives smooth responses, and some details of the actual behavior might be lost. On the other hand, indirect measurements are known to give reasonably good evaluations for the maximum EC values, and the value of $\Delta T = 1$ K is reasonably comparable for example to the results of direct measurements of PMN-13PT ceramics.

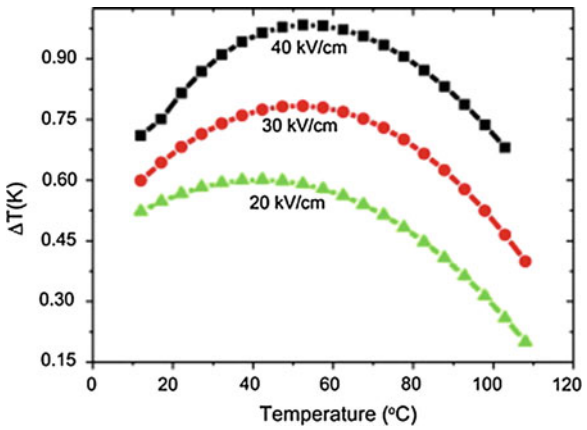

Fig. 11 Adiabatic temperature change ΔT due to different change of electric field [55]

Compositions closer to the MPB region

Electrocaloric behavior in PMN-25 %PT composition using both poly- and single-crystalline materials has been investigated by Sebald et al. [77, 78] using differential scanning calorimetry (DSC). Single crystals were cut to (111), (011), and (001) plates of $12 \times 4 \times 1$ mm^3 in size. The EC measurements with DSC were executed in silicone oil by applying electric field in the range of 5–30 kV/cm for 500 s, and the heat flow was measured during and after the field application. Figure 12 shows the measured EC effect as a function of temperature for <110>- and <111>-oriented crystals. The trend of the EC effect as a function of temperature resembles the one measured for PMN-10 %PT and PMN-13 %PT ceramics materials described earlier. Now, because of the increased PT content, the depolarization temperature is approximately 90 °C and the maximum EC effect is at around 100 °C for both orientations. Figure 12 shows also the indirect simulated EC effect, which follows the direct DSC measurement results very well. Temperature dependence of the electrocaloric temperature response for a polycrystalline sample somewhat resembles that shown for <011> and <111>-orientations. However, the <001>-oriented single crystal shows more linear response, and no any clear peaks are observed.

The maximum EC effect for each type of sample measured at electric field of 25 kV/cm were shown in units of heat. For comparison, the corresponding electrocaloric temperature change values (when using $c_p = 0.35$ J/gK) are approximately 0.56, 0.89, 1.1, and 0.9 for <001>, <011>, <111>, and polycrystalline orientations, respectively. Results show that there might be a reasonably anisotropy in the electrocaloric effect. The EC effect is strongest in the <111> direction, but effect of similar magnitude is observed in polycrystalline sample and <011>-oriented single crystal. Interestingly, the maximum EC effect in <001>-oriented single crystal was only around half of that measured for other samples.

PMN-*x*PT compositions that are very close to the MPB region (*x* around 0.26–0.35) show different phases close in energy which is also reflected in their

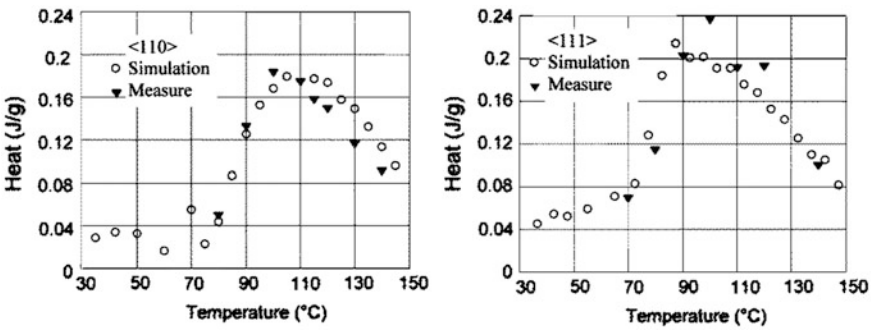

Fig. 12 Simulated and experimental EC effect heat as a function of temperature for 10 kV/cm electric field step for PMN-25 %PT single crystal orientations of <110> (*left*) and <111> (*right*) [77]

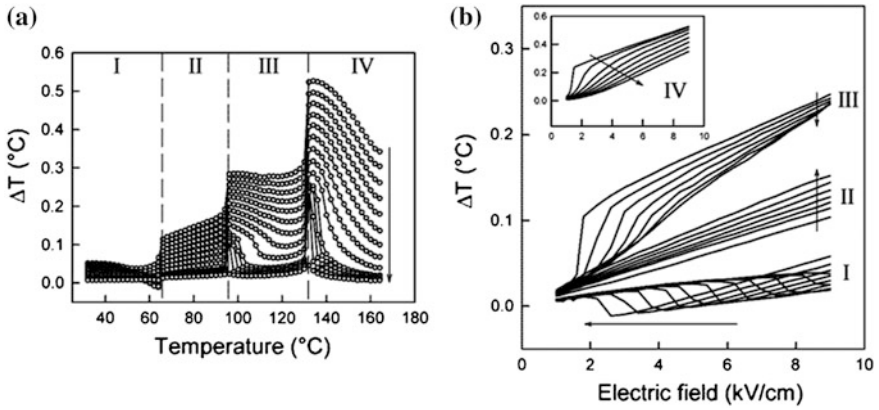

Fig. 13 **a** Temperature dependence of EC temperature change in <011>-oriented PMN-28 %PT single crystal with electric fields of 9–1.8 kV/cm. **b** Field-induced temperature change in the same crystal in the temperature ranges of I–IV measured with descending field strengths. The direction of the increasing temperature is marked with *arrows* [65]

electrocaloric properties. Especially in single crystalline PMN-*x*PT samples, where electric field is directed along specific crystallographical directions, various peculiar effects are shown. For instance, regions of different behaviour are shown in electrocaloric temperature response for PMN-28 %PT crystals with E along the <011> direction as shown in Fig. 13 [65]. Three distinct anomalies have been identified in the temperature responses. The strongest temperature change of $\Delta T = 0.53$ °C with $E = 9$ kV/cm was measured just above the crystal's depolarization temperature at around 131 °C, and other two lower temperature transitions were detected at 96 and 66 °C (Fig. 13a).

Each temperature region between the observed anomalies was found to show unique thermal response to the applied electric field (Fig. 13b). Clear jumps in electrocaloric temperature change were observed with certain electric fields close to the transition regions just above temperatures 130 and 96 °C as well as just below 66 °C. A total ECE temperature change showed also negative values in a range below 66 °C. Characterized temperature range was divided into four different ranges with different behaviours as a function of electric field: 31–71 °C (range I), 73–97 °C (range II), 101–127 °C (range III), and 130–162 °C (range IV), respectively (Fig. 13b). When the electric field reached a critical value in temperature range I, the crystal temperature was decreased rapidly, whereas conversely above in the range III it abruptly increased during the field-inducement. Between the regions I and III, the electrocaloric temperature change showed a linear dependence after poling. Above the thermal depolarization temperature (range IV), a typical sudden jump in EC effect was observed. Accompanying polarization hysteresis measurements performed from a virgin state were also supporting the field-induced temperature measurements, and abrupt reversible

changes with involving hysteresis were observed in polarization close to abrupt electrocaloric temperature changes.

Different behaviours in electrocaloric effect as well as in measured polarization were attributed to the presence of different phase stability regions in the corresponding temperature regions. Electric field along <110>-direction is known to drive the phase stability towards orthorhombic phase in PMN-PT, and depending on the PT concentration both $R/M_B \leftrightarrow O$ and $M_C \leftrightarrow O$ phase transition sequences have been detected at low temperatures in PMN-*x*PT [17]. It was suggested that the reversible $R/M_B \leftrightarrow O$ phase transition at low temperatures explains the observed field-induced polarization and temperature behavior in temperature range I. Different electrocaloric behavior at higher temperature (range III), where temperature increases suddenly with increasing field, could be caused by another type of field-induced phase transition, namely $M_C \rightarrow O$. A linear electrocaloric response observed in temperature range II implied a presence of a single stable phase after poling.

In addition, when the polarization and temperature changes in temperature regions I and III were followed, it was discovered that the amount of hysteresis and induced abrupt changes were both decreased when the required critical electric fields were increased; especially the abrupt temperature change in region III decreases rapidly, and thus resembles more of a continuous behavior. Similarly, above the depolarization temperature (region IV), the drastic increase in the field dependence of the temperature change smears out little by little with increasing temperature, turning into a more linear response, which at even higher temperatures starts to resemble exponential behavior with an increasing field, such as observed in <110>-oriented PZN-PT [91].

Similar electrocaloric behaviour has also been observed when electric field is applied along the <001> direction in PMN-*x*PT compositions close to the MPB region [50, 56, 66]. Figure 14 presents the electrocaloric effect measured for PMN-30PT single crystal with $E = 10$ kV/cm along the <001> direction [50].

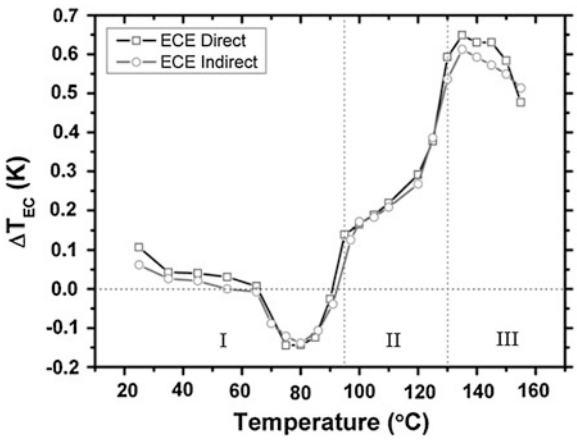

Fig. 14 Indirectly and directly obtained ECE as a function of temperature for PMN-30PT with $E = 10$ kV/cm applied along the <001> direction [50]

A negative electrocaloric effect is again measured at low temperatures which means that the dipolar entropy is temporarily increased by the applied field. This also reflected in the temperature dependence of polarization through the Maxwell relation so that the $(\partial P/\partial T)_E$ is positive in this region [50]. In this case, the negative effect was attributed to a reversible phase transition from pseudo-rhombohedral towards tetragonal phase with increasing field. Importantly, the indirect and direct measurements were found to show very similar behaviour where a maximum EC effect of $\Delta T = 0.65$ °C appeared at $T = 135$ °C.

Rožič et al. [72] measured EC effect in mechanochemically synthesized and sintered PMN-30 % PT ceramics having 97 % of theoretical density. The thickness of the ceramic samples varied from 60 to 100 μm. The EC effect was measured as described earlier in this section for PMN ceramics characterized by the same group. Figure 15 shows the measured EC effect as a function of temperature together with zero-field dielectric constant. A maximum EC effect of 2.7 °C was measured with electric field of 90 kV/cm at 157 °C. The development of electrocaloric effect shows remarkable increase when temperature of maximum dielectric constant is approached. Especially, electric field strengths above 7.5 kV/cm greatly enhance the temperature change ΔT. Although the electrocaloric effect seems to increase at high temperatures, conclusions about the development of ΔT are hard to make due to low amount of measurement data. However, these measurements show that polycrystalline bulk-type PMN-PT materials can also show reasonably high electrocaloric temperature changes. In addition, these measurements show quite similar type of results in comparison to direct measurements on pure PMN. Relatively thin sample thickness enabled the use of

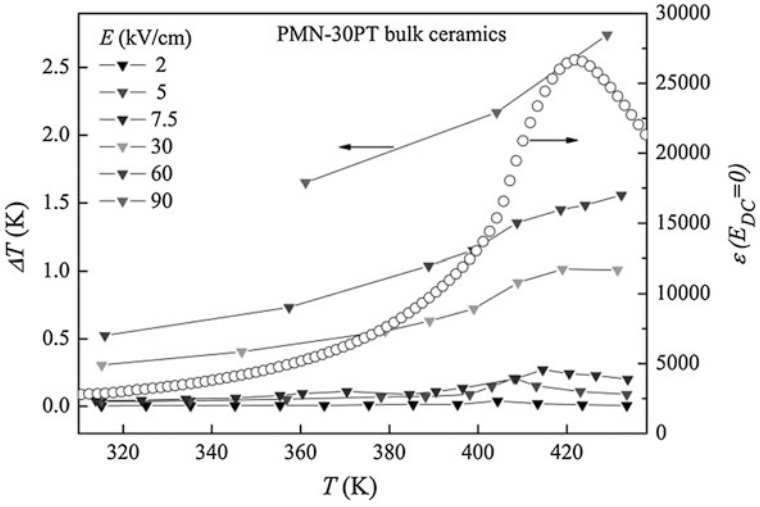

Fig. 15 The EC effect in PMN-30 %PT bulk ceramics as a function of temperature for several applied electrical-fields. Zero-field dielectric constant, *open circles*, is also shown [72]

higher electrical fields, which correspondingly led to higher electrocaloric temperature changes.

Chukka et al. [22] measured the EC effect indirectly from polarization data of 200 μm thick [111]-oriented PMN-30 %PT single crystal. The highest EC effect of 2.7 °C at 127 °C with relatively low electric field of 12 kV/cm was simulated, which is considerably higher value in comparison to directly measured values reviewed above. This value of ΔT is the highest one obtained for bulk-type PMN-PT and the normalized value $\Delta T/E = 225$ cm K/MV is among one of the highest measured for any EC material.

Lead titanate, being the other end member of PMN-PT, was actually characterized already in 1976, when Katpatal and Deshmukh measured the electrocaloric effect in pure $PbTiO_3$ [44]. The EC effect was measured in adiabatic conditions directly with thermocouple attached on a sintered ceramic sample. The highest electrocaloric temperature change of 0.7 °C was measured at 480 °C with electric field of 5 kV/cm.

The temperature response of EC effect in PMN-*x*PT shows abrupt changes in the vicinity of the phase transitions like seen in Figs. 8, 9, 11and 12. The main reason for this is that a reversible phase transition occurs with the help of external electric field. Above the depolarization temperature this transition occurs between paraelectric cubic phase and ferroelectric phase, and shows the highest electrocaloric effect. Depending on the composition and orientation (in the case of single crystal), the ferroelectric phase can be tetragonal, rhombohedral, orthorhombic, and/or monoclinic one. Additionally, other reversible ferroelectric–ferroelectric phase transitions induced at lower temperatures have their own weaker contribution to the electrocaloric effect.

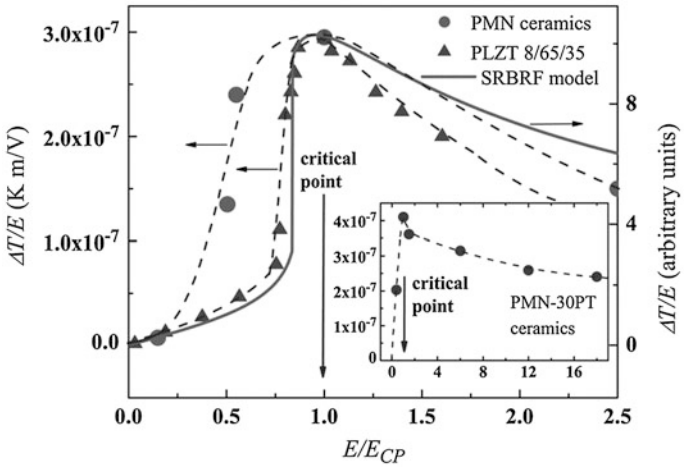

Fig. 16 The electrocaloric responsivity $\Delta T/E$ data as a function of normalized electric field E/E_{CP} for PMN, PMN-30PT and PLZT ceramics at T_{CP}. *Solid line* based presents a mean-field calculation from the SRBRF model [72]

As was mentioned in Sect. 2.1, the expression for electrocaloric effect developed from Landau theory showed an increased electrocaloric responsivity R in relaxor ferroelectrics near the critical point (E_{CP}, T_{CP}), where a first-order field-induced phase transition from relaxor to ferroelectric phase terminates [70]. This prediction was also confirmed experimentally for PMN and PMN-30PT ceramics presented earlier [72]. Figure 16 presents the measured electrocaloric responsivity $\Delta T/E$ for mentioned PMN and PMN-30PT as well as for similar-type PLZT ceramics at T_{CP}. Additionally, a calculated response (based on values from SRBRF model) of relaxors is presented. It is shown that all these samples exhibit a maximum close to the critical point.

The numerical evaluation of electrocaloric effect using the expression and parameters provided by Pirc et al. [70] has been replotted in Fig. 16 with an expanded electric field range. Above the transition the shape of EC effect as a function of temperature (now $\Delta T/T_{CP}$ vs. T/T_{CP}) shows similar qualitative behavior with increasing electric field to the experimentally measured results for PMN-13 %PT in Fig. 9. For PMN-13 %PT the E_{CP} can be estimated to be around 2.5 kV/cm, which means that the highest electric field in Fig. 9a (24 kV/cm) corresponds to $\sim 10E_{CP}$ in Fig. 17. For higher electrical fields the general trend of the EC response maximum seems to transfer towards higher temperatures and EC dependence becomes more linear as a function of temperature, which also seems to be the general trend for PMN-30 %PT ceramic at higher electric fields (Fig. 13). The model graph shown in Fig. 17 is not valid below the transition temperature, where the material is in ferroelectric state with changed material parameters.

Dunne et al. [34] have described the "dual-peak" characteristics of EC effect temperature response in relaxors by means of a statistical mechanical model taking into account the formation and ordering of the polar nanoregions. The phrase "dual-peak" is used here to refer to the shape of the electrocaloric effect as a function of temperature. The first peak forms close to the depolarization temperature with lower electric fields (e.g. Fig. 9a) while another peak forms with increasing electric fields at higher temperatures above T_m.

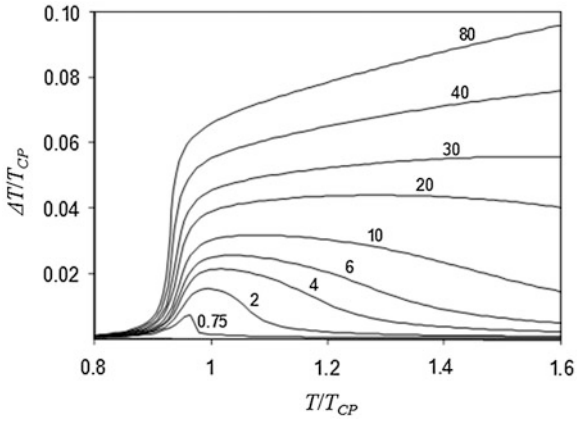

Fig. 17 Calculated electrocaloric ΔT (in units of T_{CP}) as a function of temperature (T/T_{CP}) for different values of E/E_{CP}. Calculations are based on the expression and parameters provided by Pirc et al. [70]

Table 1 Electrocaloric parameters measured for bulk-type PMN-PT

Material	ΔT_{max} (°C)	T_{max} (°C)	E_{max} (kV/cm)	Method[a]	Bulk form[b]	d (μm)	Reference
PMN	0.15	−47	15	TC	PC	unkn.	Shebanov et al. [81]
PMN	2.5	67	90	Th	PC	80	Rožič et al. [71]
PMN-8PT	1.35	23	15	TC	PC	3,000	Xiao et al. [97]
PMN-10PT	1.25	28	15	TC	PC	3,000	Xiao et al. [97]
PMN-10PT	0.45	50	29.1	TC	PC	500	Shebanovs et al. [84]
PMN-10PT	1.0	55	40	ID/1[d]	SC (111)	600	Luo et al. [55]
PMN-10PT	1.0	10	16	IR	PC	100	Shaobo and Yanqiu [80]
PMN-13PT	0.56	70	24	TC	PC	1,000	Hagberg et al. [40]
PMN-15PT	1.71	18	16	IR	PC	100	Shaobo and Yanqiu [80]
PMN-25PT	0.40	32	15	TC	PC	3,000	Xiao et al. [97]
PMN-25PT	0.56[c]	120	25	DSC	SC (100)	1,000	Sebald et al. [77]
PMN-25PT	0.89[c]	100	25	DSC	SC (110)	1,000	Sebald et al. [77]
PMN-25PT	1.1[c]	100	25	DSC	SC (111)	1,000	Sebald et al. [77]
PMN-25PT	0.9[c]	110	25	DSC	PC	1,000	Sebald et al. [77]
PMN-28PT	0.53	131	9	TC	SC (110)	1,000	Peräntie et al. [65]
PMN-29PT	2.3	171	50	ID/200[d]	SC [100]	250	Luo et al. [56]
PMN-29PT	2.0	167	50	ID/200[d]	SC (111)	250	Luo et al. [56]
PMN-30PT	2.7	157	90	Th	PC	60–100	Rožič et al. [72]
PMN-30PT	2.7	127	12	ID/1000[d]	SC (111)	200	Chukka et al. [22]
PMN-30PT	0.65	135	10	DSC	SC [100]	1,000	Le Goupil et al. [50]
PT	0.70	480	5	TC	PC	unkn.	Katpatal et al. [44]

[a] Measurement performed by thermocouple (*TC*), thermistor (*Th*), infrared sensor (*IR*), differential scanning calorimeter (*DSC*) or using an indirect (*ID*) evaluation, [b] Material in a form of polycrystalline (*PC*) ceramics or single crystalline (*SC*) plates, [c] Evaluated from the corresponding heat data using $c = 0.35$ J/gK, [d] Frequency (Hz) used in indirect measurement

As a brief summary, all the mentioned experimental electrocaloric results on bulk-type PMN-PT are collectively presented in Table 1. Although a majority of results have been obtained by different direct measurement techniques, a considerable variance is still seen among the results. Evidently some of these differences can be explained by different measurement techniques. On the other hand, a combination of indirect and direct measurements by the same authors produce similar results in many case (see e.g. [50]). Generally, it seems that somewhat higher results are obtained by indirect measurements. The variance is particularly

high in single crystalline samples which could also be an indication of strong anisotropy. The highest ΔT values of 2.7 °C have been measured for single crystalline and ceramic PMN-30PT composition with electric fields of 12 and 90 kV/cm, respectively.

Some of the interesting experimental findings during the short history of EC research on bulk-type PMN-PT include an appearance of "double-peak" [84, 40], a high EC activity around the critical point [72], a negative ECE and other phase transition effects [50, 56, 65, 66], just to name a few.

2.3 Electrocaloric Effect in PMN-PT Thin Films

For a long time it was believed that electrocaloric properties are not sufficient to be exploited in real cooling applications. However, Mischenko et al. [58] found out by indirect estimations from isothermal polarization measurements that thin films of PZT showed giant electrocaloric effect of $\Delta T_{max} = 12$ °C with $E_{max} = 776$ kV/cm ($\Delta E_{max} = 480$ kV/cm) at around $T = 226$ °C. This observation motivated a series of studies, where giant electrocaloric effect was found in different ferroelectric-based thin films by similar indirect method.

Naturally, the PMN-PT system was among the first studied thin film systems. In the first electrocaloric study of PMN-PT thin film (Fig. 18a), an electrocaloric temperature change of $\Delta T_{max} = 5$ °C with $E_{max} = 895$ kV/cm at around $T = 75$ °C was discovered in PMN-10PT composition [59]. This means that the effect was maximized around the temperature of the maximum permittivity T_m, which is considerably higher than the thermal depolarization temperature of this composition.

In order to find out if the high electrocaloric effect of PZT films could be achieved at lower temperatures, Correia et al. [23] studied thin films of PMN-7PT composition where dielectric anomalies are closer to room temperature. They found out that PMN-7PT thin film on thin PZT seed layer produced $\Delta T_{max} = 9$ °C with $E_{max} = 723$ kV/cm at around $T = 25$ °C on heating as shown in Fig. 18b [23]. Interestingly, a considerable difference in the location and magnitude of the maximum electrocaloric effect was observed between heating and cooling runs, and electrocaloric temperature change of $\Delta T_{max} \approx 6.8$ °C with $E_{max} = 723$ kV/cm was found on cooling at around $T = 0$ °C. Significantly, these results were among the first to show that prominent electrocaloric properties in thin films can be achieved closer to room temperature.

Other electrocaloric studies on PMN-PT thin films have concentrated more on compositions closer to the morphotropic phase boundary (MPB) region, where piezoelectric properties are also maximized. Feng et al. [35, 36] performed indirect electrocaloric evaluations for radio-frequency magnetron sputtered and highly (001)-oriented thin films of PMN-32PT and PMN-33PT. Both films showed similar electrocaloric characteristics of $\Delta T_{max} = 13.4$ °C (for PMN-32PT) and $\Delta T_{max} = 14.5$ °C (for PMN-33PT) with $\Delta E_{max} = 600$ kV/cm at around T_C. Significantly, this was achieved using two different bottom layers; platinum with thin

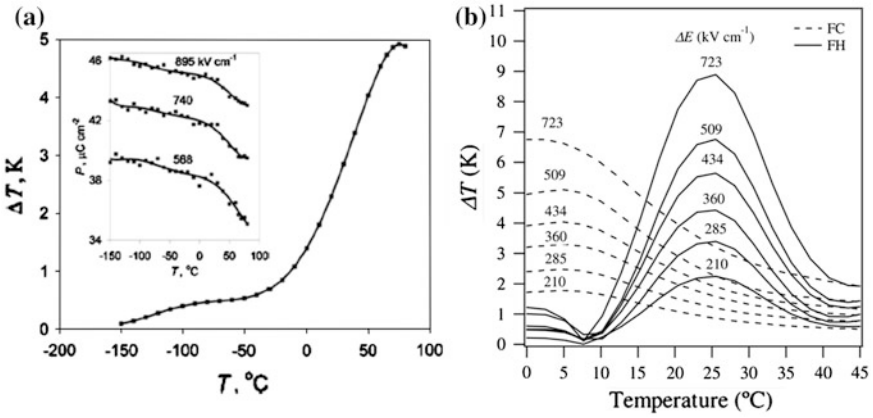

Fig. 18 Electrocaloric effect predicted in thin films of PMN-PT around the room temperature: **a** the EC effect in PMN-10 %PT thin films as a function of temperature for $E = 895$ kV/cm. Inset: isothermal polarization values as a function of temperature and their polynomial fits used in the evaluation [59]. **b** Electrocaloric data in PMN-7 %PT extracted from *P*–*E* loops on heating (FH) and cooling (FC) [23]

PZT/PbO buffer for PMN-32PT and perovskite $LaNiO_3$ conductor for PMN-33PT. The same PMN-33PT composition thin film has also been studied by Het et al. (2011). In comparison to the study by Feng et al. [35, 36], temperature of the ECE maximum was significantly higher.

The highest electrocaloric temperature change of $\Delta T_{max} = 31$ °C with $\Delta E_{max} = 747$ kV/cm at 140 °C in PMN-PT thin film was found in polycrystalline 240 nm thick PMN-35PT pulse laser deposited on $La_{1/2}Sr_{1/2}CoO_3$ template layer [74]. As with other measurements on thin films, the position of ECE peak is nearly independent on temperature (Fig. 19). The maximum value of ΔT is drastically higher than any other evaluation in PMN-PT thin films, in spite of relatively small differences in applied electric field strengths. Similar high temperature changes, however, has been obtained in PLZT thin films as well [54].

Electrocaloric properties of PMN-PT thin films are summarized in Table 2. As in case of bulk materials, some variance in results is observed with ΔT values of around 4–31 °C. Applied electric fields are typically more than the order of magnitude higher to bulk-type materials. Values of this magnitude can already be considered as sufficient for regenerative cooling cycles [32]. However, one major advantage of bulk materials is their naturally large thermal mass, which greatly simplifies the design and construction of macroscopic electrocaloric cooling devices [93].

It should be mentioned that all the results on electrocaloric properties of thin film PMN-PT are obtained by indirect measurements from polarization data (see the separate measurement chapter in this book for details). Basically, this method can be used to evaluate the order of magnitude of the EC effect, but direct measurements are needed in order to extract more reliable results for a better

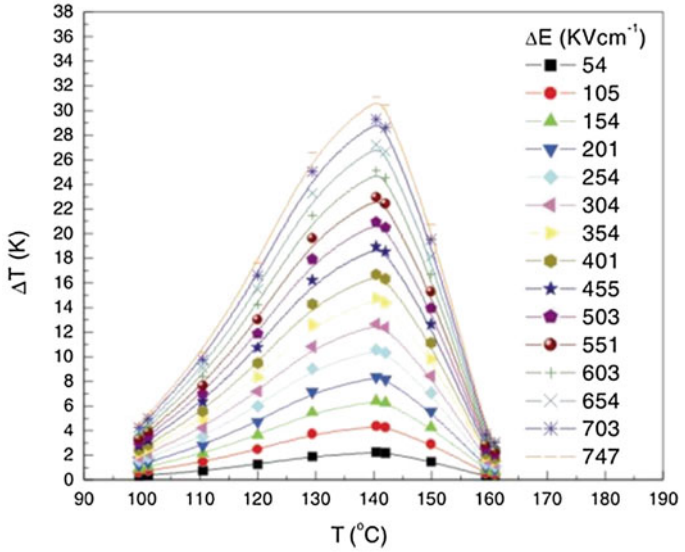

Fig. 19 Indirectly measured variation of adiabatic temperature change ΔT with respect to temperature and electric field in PMN-35PT thin film [74]

Table 2 Electrocaloric parameters measured for PMN-PT thin films

Material	ΔT_{max} (°C)	T_{max} (°C)	E_{max} (kV/cm)	Method[a]	Orientation[b]	d (nm)	Reference
PMN-7PT	9 (6.8)[c]	25 (0)[c]	723	ID/0.1	PC	210	Correia et al. [23]
PMN-10PT	5.0	75	895	ID/10	PC	260	Mischenko et al. [59]
PMN-32PT	13.4	145	600	ID/0.1	(001)	200	Feng et al. [35]
PMN-33PT	14.5	145	600	ID/1	(001)	200	Feng et al. [36]
PMN-33PT	4.25	235	116	ID/5	PC	430	He et al. [42]
PMN-35PT	31.0	140	747	ID/0.2	PC	240	Saranya et al. [74]

[a] *ID* refers to indirect measurement at given frequency (kHz), [b] *PC* polycrystalline, no strong preferred orientation, [c] Values in parenthesis measured on cooling

understanding of underlying structure-property relations. The main reason for the lack of direct measurements on thin film samples is its inherent difficulty; the surrounding elements, such as the substrate, possible buffer layers and electrodes, constitute a major part of the total thermal system, and thermal evaluation of all these components can be very complicated and prone to errors. Furthermore, the

electrocaloric temperature change induced in thin films escapes very fast into these surrounding elements.

It can be seen that considerably higher electrocaloric temperature changes are generated in thin films in comparison to bulk-type counterparts. Mainly this is attributed to significantly higher electric fields used for thin films because of their higher dielectric breakdown fields [93]. This means that higher electric fields can be applied to induce larger polarization changes, and consequently larger temperature changes [53]. Additionally, as a side of indirect measurements, many theoretical investigations are devoted to study special effects arising generally in thin films rather than particularly in PMN-PT system. These effects, such as orientation, clamping, thickness, and misfit strain, have been shown to have clear influences on electrocaloric properties of thin films (see e.g. [1, 67, 68]), and they might play a very significant role also in enhancement/degradation of thin film properties. Therefore, it is not a surprise to see such variation in obtained EC results.

3 $Pb(Sc_{0.5}Ta_{0.5})O_3$ System

Lead Scandium Tantalate, $Pb(Sc_{0.5}Ta_{0.5})O_3$—abbreviated throughout this section as PST—has awakened considerable interest due to its exceptional pyroelectric properties near room temperature, which puts this material forward for use in infrared detectors, thermal imaging and energy harvesting [31, 38, 43, 90]. Since pyroelectricity is the converse of electrocaloric effect, PST system is expected to show large electrocaloric effect and thus may find applications also in cooling (or heating) devices. This is weighted by the fact that dielectric and ferroelectric response of PST-based materials can be manipulated during processing and, as a consequence, ought to optimize and customize their electrocaloric cooling properties and efficiency. Despite such evident potential of the PST system as electrocaloric refrigerants, only a relatively small number of studies have sought to explore its electrocaloric properties. This section reviews the investigations performed to date on PST materials in terms of their electrocaloric properties.

3.1 Chemical Order and Dielectric Properties in PST

Lead Scandium Tantalate, $Pb(Sc_{0.5}Ta_{0.5})O_3$, system belongs to the perovskite family $A(B'_xB''_{1-x})O_3$, characterized by B-site multioccupancy where $B' = Sc^{3+}$ and $B'' = Ta^{5+}$, as schematically represented in Fig. 20a. In general, in a complex perovskite structure where the lattice sites are occupied by different cations a doubled perovskite unit cell can be formed in which B' and B'' (or A' and A'') cations are placed in specific sub-lattices to minimize structure energy. Figure 20b schematically represents the 1:1 ordered structure, whereas every other {111}

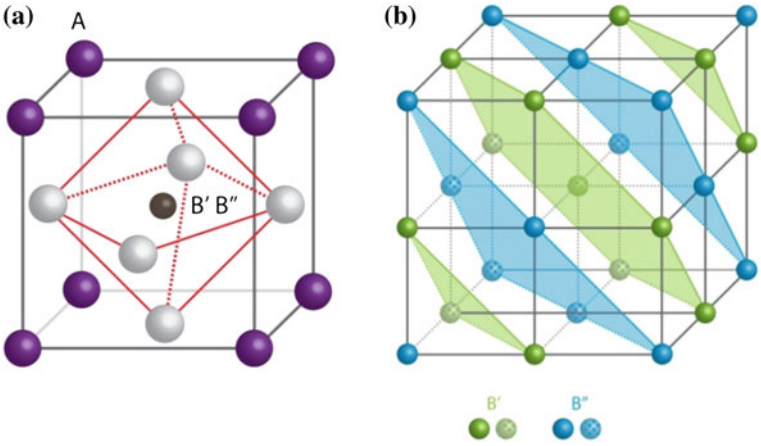

Fig. 20 **a** Schematic diagram of $A(B', B'')O_3$ perovskite structure. **b** Double perovskite crystalline structures. To simplify, *A*-site cation and oxygen are not shown

plane belongs to Sc^{3+} sublattice (B'—green), and the remaining planes to Ta^{5+} sublattice (B''—blue).

However, full compositional order is not always achieved in these structures as thermal vibrations may be strong enough to inhibit *B*-site 1:1 ordering, and as consequence small regions of the ordered state (polar nanoregions, PNRs) may coexist with a disordered matrix. This compositional ordering inhomogeneous state has been ascribed to being the origin of relaxor response, i.e.: (1) frequency dependent maximum permittivity temperature T_m, (2) diffuse phase transition, (3) spontaneous polarization above T_m and (4) slim *P*-*E* loops. This relaxor behaviour is evident in Fig. 21, where disordered PST ceramic is characterized by frequency dispersive permittivity maximum at around T_m, which marking a spontaneous relaxor-ferroelectric phase transition. The complexity of relaxor-ferroelectric

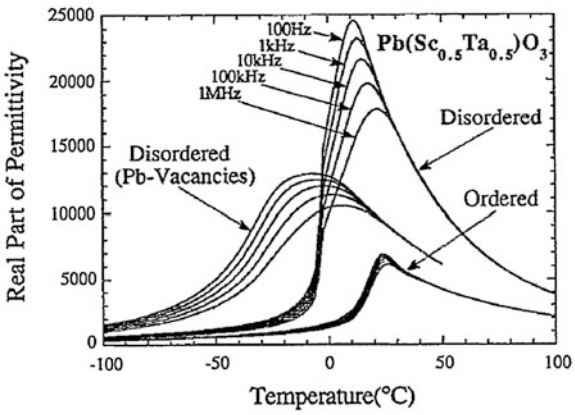

Fig. 21 Real part of permittivity measured in disordered (stoichiometric and non-stochiometric) and ordered PST ceramics (non-stochiometric disordered) as a function of temperature and frequencies [21]

phase transition in disordered PST ceramics was identified by means of transmission electron microscopy [3], which disclosed the presence of an incommensurate antiferroelectric phase coexisting with paraelectric and ferroelectric phases close to T_m. Fig. 21 also illustrates the different dielectric responses measured in stoichiometric and non-stochiometric (lead deficient) disordered PST ceramics. Although both ceramics exhibit a broad relaxation spectrum at T_m, the ceramic containing lead vacancies, showed a broader permittivity peak and is observed at lower temperatures than that obtained in the stoichiometric ceramic. According to the authors [21], lead vacancies in disordered PST ceramic have been responsible to the inhibition of the stabilization of ferroelectric phase below T_m, i.e., the presence of lead vacancies prevented the ceramic to undergo a relaxor-ferroelectric phase transition at higher temperatures.

In some relaxor compounds like PST, compositional ordered PNRs may be manipulated during material processing when Sc^{3+} and Ta^{5+} cations can be forced to exchange sites by diffusion and create 1:1 ordered nanoregions (see Fig. 20b) [79, 89]. The presence of ordered nanoregions in PST compounds are normally identified from the appearance of the superlattice (½ ½ ½) reflection peak in the X-ray diffraction patterns at 19°. The degree of order of any relaxor, denominated as S, can then be assessed by relating lattice and superlattice reflection peaks as follows:

$$S^2 = \frac{I_{(1/2\ 1/2\ 1/2)}/I_{(100)}observed}{I_{(1/2\ 1/2\ 1/2)}/I_{(100)}calculated, for\ S=1} \quad (1)$$

where, $I_{(½\ ½\ ½)}$ is the integrated intensity area of superlattice peak reflection stemming from the ordered arrangement of B' and B'' ions, and which is usually compared with (100) reflection peak. In the case of PST, when $S = 1$ $I_{(1/2\ 1/2\ 1/2)}/I_{(100)} = 1.4$. Figure 21 also presents the dielectric response measured in a highly ordered PST ceramic ($S = 0.9$) which was post-sintered at 950 °C for 10 h. The ordered ceramic behaves as an ordinary ferroelectric and undergoes a first-order paraelectric-ferroelectric phase transition marked by a sharp and frequency independent maximum of permittivity at T_m.

Dielectric properties and order degree

A number of works have posited a distinct dielectric response in disordered and ordered PST compounds. In an attempt to scrutinize the trend of dielectric response in PST system with *B*-site order degree, Stenger et al. [89] investigated dielectric properties in a number of PST ceramics, with S ranging from 0 to 0.83. Ceramics were processed by solid-state reaction and *B*-site ordering was achieved at sintering temperatures 1500–1560 °C. The authors' investigations are summarized in Fig. 22a. A monotonous decrease of maximum permittivity and peak diffusivity is observed as S increases. These results are validated by measurements of latent heat by means of Differential Scanning Calorimetry, which show an increase of latent heat, detected at T_m, whilst S increases [89]. In particular, for highly ordered ceramic (PST4, $S = 0.83$), latent heat detected near T_m is high, which suggests that a first-order phase transition takes place.

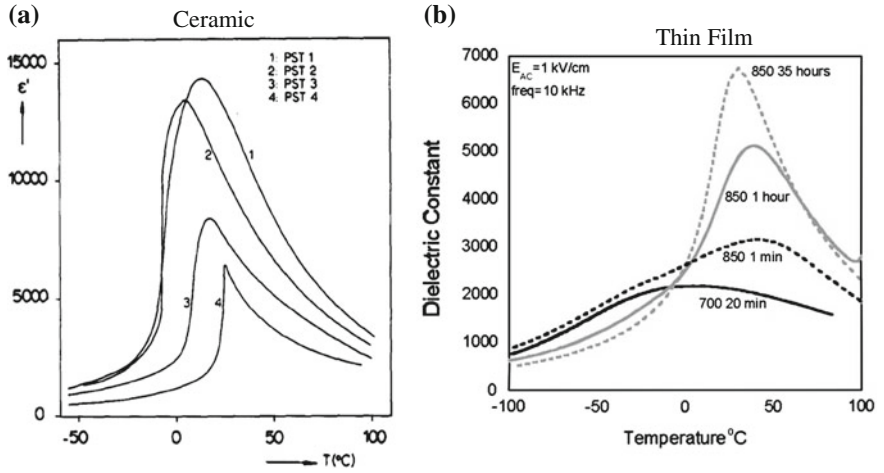

Fig. 22 **a** Real part of permittivity (ε') as a function of temperature (T) observed in PST 1 ($S = 0$), PST 2 ($S = 0.53$), PST 3 ($S = 0.74$) and PST 4 ($S = 0.83$) ceramics [89]. **b** Dielectric constant observed in PST thin film on sapphire annealed at 700 °C for 20 min ($S = 0$); 850 °C for 1 min ($S = 0$), 1 h ($S = 0.55$) and 35 h ($S = 0.91$) [11]

B-site order in PST thin films may be also tailored through suitable heat treatments. According to Brinkman and co-authors [11], the higher the annealing temperature and the longer the annealing period, the higher the order degree *S*. Higher order degree was achieved in PST thin films deposited on sapphire and epitaxial $SrTiO_3$ and MgO substrates, as higher temperatures were allowed to anneal the thin films without the occurrence of any film degradation. As in ceramics, dielectric properties in thin films are likewise strongly affected by *B*-site order degree. As seen in Fig. 22b, maximum of permittivity is enhanced by increasing *S*, while T_m shifts towards higher temperatures. This particular research also pointed out that different thermal induced stress of the substrates results in variations of maximum of dielectric constant and T_m.

Although *B*-site order–disorder transformation is traditionally tailored by suitable heat treatment, other approaches have been suggested, namely, *B*-site doping, which has been used in an attempt to increase chemical order degree in PMN and PST compounds [33, 41]. Another approach suggested to induce order degree in PST is through mechanical activation [39]. The latter method has the advantage of preventing lead and oxygen vacancy formation, which, in turn, will contribute to conductivity.

Compositional order or secondary effects?

When studying the impact of the *B*-site order degree on the dielectric properties of PST system, the impact of extrinsic effects that follows the variation of sintering and annealing temperature should not be underestimated. These may be associated with material microstructure (e.g. grain size and internal stress) and quality (e.g.,

porosity, defects and inhomogeneities). Secondary effects may have a great impact on the dielectric response of materials. This is well demonstrated in Fig. 21, where the introduction of lead vacancies in disordered PST ceramic drastically changed relaxor behavior compared to that found in the stoichiometric disordered ceramic. In fact, according to the authors [21], the presence of lead vacancies resulted in the inhibition of ferroelectric stabilization below T_m. In ceramics prepared by Stenger [89], the increase of broadness of the permittivity peak is accompanied by the increase of values of permittivity, as seen in Fig. 22a. Contrariwise all the above-mentioned secondary effects are recognized to broaden the dielectric constant peak, accompanied by the reduction of dielectric constant value. This boosted the authors' underlying belief that *B*-site order effect overlaps any secondary extrinsic effect stemming from heat treatment conditions.

Similar reservations appear in Brinkman's investigations in PST thin films [11, 12]. Unlike ceramics, *B*-site order degree in thin films increases by increasing annealing temperature, which in turn can also affect film quality and microstructure. These uncertainties were further heightened by measurements on PST thin film on sapphire substrate, which show a monotonous increase of dielectric constant and T_m with increasing of S (see Fig. 22b), whilst Scanning Electron Microscopy images do not disclose any alteration in film quality and microstructure [12].

Disordered PST thin film versus bulk: a dissimilar state of disorder?

Ordered PST thin films exhibit a dielectric response similar to their ceramic counterparts, with like values of permittivity and T_m, as presented in Fig. 22a and b [11, 89]. Conversely, disordered PST thin films show a marked difference in the positioning of the dielectric maximum as opposed to ceramics. Investigations carried out in disordered PST thin films deposited on different substrates suggest a strong contribution of the strain induced by thermal expansion mismatch between the film and substrate [12]. The T_m moves towards lower temperatures for significant levels of compression or tension stress. PST thin film on a sapphire substrate exhibits its maximum position close to that found in bulk ceramic with lead vacancies (see Fig. 22b). Nonetheless, even for almost zero stressed PST thin films on sapphire substrate, values of dielectric constant in disordered thin films are significantly lower than that of disordered PST ceramics. Brinkman [11, 12] put forward a possible explanation for this phenomenon based on the significantly different processing conditions of ceramic as opposed to those of thin films, which may account for a distinct disorder state in each of them. According to this hypothesis, a *Low Temperature Disordered State* must have formed due to the low annealing temperature used in fabricating disordered PST thin films (700 °C) when compared to PST ceramics (1500 °C). Low temperature disordered state in thin films is characterized by diluted and inhomogeneous polar nanoregions state, which brings about a significant reduction of dielectric constant values.

3.2 Electrocaloric Effect in PST Compounds

3.2.1 Origin of Electrocaloric Effect

In polar dielectrics, maximum of electrocaloric effect is observed at or near phase transitions, suggesting phase transitions to be the main drivers for large field-induced entropy variation. Yet, in the absence of structural phase transitions, as in relaxor PMN and PMN-PT (low PT concentrations), maximum electrocaloric effect has been associated with polar nanoregions re-orientational dynamics, where its maximum occurs close to the freezing and/or depolarizing of polar nanoregions [23]. Contrarily to PMN-based materials, relaxor PST undergoes a relaxor-ferroelectric phase transition translated by a permittivity maximum at T_m. Field-induced X-Ray Diffraction (XRD) patterns obtained in a highly ordered PST ceramic ($S = 0.8$) indicated a field induced *Fm3m-R3m* structural phase transition at 2.5 °C, as evidenced by the (222) reflection peak split at a critical electric field, E_c [82]. Simultaneous measurements of field-induced spontaneous polarization (P_s) agree well with XRD results, where a sharp phase transition was indicated at 2.5 °C, brought about by the abrupt drop of P_s, suggesting a first-order phase transition.

Electrocaloric temperature change at phase transition temperature and at a critical field can be defined as:

$$\Delta T = \frac{T_C}{C}\frac{dE_c}{dT}\Delta P_s \tag{2}$$

where, T_C is the phase transition temperature, C is the heat capacity, E_c is the critical field at which phase transition occurs and ΔP_s is the spontaneous polarization jump across a temperature range. Electrocaloric $\Delta T = 1.6$ °C was determined driven by a structural phase transition by using data obtained from XRD and polarization measurements and Eq. 2. Said electrocaloric effect prediction was in good agreement with the temperature drop directly measured through the use of a thermocouple ($\Delta T = 1 - 1.8$ °C). This suggested that the principal contribution to electrocaloric effect in PST near T_c is first-order field-induced *F3m-R3m* phase transition, which brings about a large change in volume of the unit cell, $\Delta V = 0.078$ Å [82].

3.2.2 "Shape" Electrocaloric Properties

The technological application of an electrocaloric device dictates the choice of electrocaloric media. Therefore, electrocaloric effect is not the sole metric when benchmarking electrocaloric media performance. In fact, from a technological perspective, engineers are more interested in the amount of heat a refrigerant can pump in one cycle, i.e., refrigerant capacity (*RC*) or cooling power and its inherent efficiency (refer Sect. 4.2 in Chap. 1, for electrocaloric refrigerant capacity and

efficiency definition). Also, device specifications put forward the media rated voltage and operating temperature. In this context, PST compounds emerge as very attractive electrocaloric media, not only due to their characteristically high electrocaloric effect, but also because their macroscopic properties are very sensitive to processing conditions and can be tailored to fulfil application specifications. In this section, the investigations carried out in the quest for achieving optimization of electrocaloric properties through heat treatment, doping and thickness adjustment are reviewed.

Heat Treatment

Heat treatment is a crucial step in the processing of materials. This stage dictates material crystallization and microstructure, which, in turn, will affect their macroscopic properties. As mentioned previously, PST system is characterized by the multioccupancy of the *B*-site of the lattice by Sc^{3+} and Ta^{5+} cations. By means of suitable processing conditions, these cations may exchange sites and create 1:1 ordered nano-regions (see Fig. 20b). Investigations effected in PST bulk and thin films have shown that sintering and annealing temperatures and periods play an important role on the *B*-site ordering, which, in turn, strongly affects material dielectric properties (see Sect. 3.1). The impact of chemical ordering through heat treatment in electrocaloric properties has already been investigated both in ceramic and thin films [11, 12, 82, 83, 84]. As seen in Table 3, higher sintering temperature lead to disordered ceramics, whilst highly ordered ceramics were achieved at lower sintering temperatures, but with longer soaking time and fast quenching. Maximum of electrocaloric temperature change (ΔT_{max}) is found to monotonously increase with increasing *S*. Such a result does not come as a surprise, as *S* increasing is followed by the transformation of a diffuse (second-order) to sharp (first-order) phase transition. This is consistent with previous work carried out by Shebanov [82], which proposed the first-order phase transition to be the origin of

Table 3 Electrocaloric characteristics observed in PST ceramics and thin films with different *B*-site ordering degree, *S*

S	Sintering	T_{max} (°C)	ΔT_{max} (°C)	Phase transition	References
Ceramic					
0.2	1650 °C, 2 h	0	<0.1	Diffuse	Shebanovs et al. [84]
0.6	1590 °C, 2 h	0	0.5	Diffuse	Shebanovs et al. [84]
0.85	1480 °C, 20 h and fast quenching	18	1.8	Sharp	Shebanovs et al. [84]
Thin Film					
0	650 °C, Hotplate	31(FC)[a] 65(FH)[a]	2.4 1.8	Diffuse	[25]
0.32	650 °C, RTA, 18 °C/s	65	6.5	Diffuse	[25]

[a] *FC* field-cooling; *FH* field heating

high electrocaloric effect in highly ordered PST ceramics. Another important characteristic of electrocaloric materials is the temperature of the maximum of electrocaloric effect, T_{max}, which imposes the operating temperature of the cooling/heating device. Contrary to what is expected, in these ceramics the increasing order degree from $S = 0$ to $S = 0.32$ does not result in the change of the maximum of electrocaloric effect (T_{max}). The observed pinning of T_{max}, whilst S increases, may be evidence of the significant effect of extrinsic variations in microstructure and the appearance of defects in the material's electrocaloric properties due to heat treatment. Despite this, with further increasing of S up to 0.8, T_{max} does shift towards higher temperatures. A good example of the technological exploitation of the adaptable T_{max} in PST ceramics, is the electrocaloric refrigerator prototype designed and developed by Sinyavsky et al. [87]. This cryogenic refrigerator used PST ceramics as a working body. In order to maintain high $\Delta T > 1$ in a wide temperature range, they exploited the T_m shift behaviour of ceramics tailored by different sintering temperatures, and propose a cascade cooling concept. The tested prototype was based on a series of modified PST ceramics with $\Delta T > 1$ K and successive decreasing phase transition temperatures up to 250 K, as seen in Fig. 23.

Disordered ($S = 0$) and partially-ordered ($S = 0.32$) PST thin films were fabricated by sol–gel method and annealed at 650 °C on a hotplate and Rapid Thermal Annealing (RTA), respectively [24, 25]. Both thin films are characterized by a diffuse and frequency-dependent relaxor-ferroelectric phase transition, as evidenced by temperature-dependent permittivity measurements. Electrocaloric effect in PST thin films was indirectly measured from field-induced polarization data and using Eq. 21 in Chap. 1. As seen in Table 3, electrocaloric ΔT is higher in the partially-ordered PST thin film than in the disordered. These results corroborate those obtained in ceramic, which indicate the Sc^{3+} and Ta^{5+} 1:1 ordering as the main drive for large unit cell volume change and therefore, enhanced electrocaloric effect. Note, however, that disordered PST thin film shows two distinct values of ΔT_{max}, measured upon cooling and heating, as characteristic of a

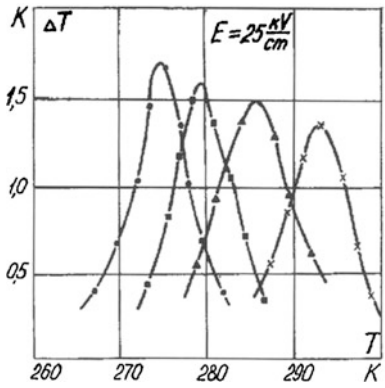

Fig. 23 Electrocaloric temperature of PST ceramics sintered at different temperatures, with different T_{max} [87]

"glassy-state" in relaxors. Such a thermal hysteresis is absent in partially-ordered film. It is recommended the reader find a more comprehensive description of electrocaloric effect in PST thin films in Sect. 3.2.

Doping

As abovementioned, high electrocaloric effect in highly ordered PST compounds is the consequence of the field-induced first-order paraelectric-ferroelectric phase transition. But despite the benefits of promoting chemical order in PST to enhance electrocaloric effect, from a technological point of view this approach may bring about some compromises. One of the main limitations while increasing electrocaloric effect by increasing chemical ordering in PST is that this is accompanied by a shift of the maximum of electrocaloric effect towards higher temperatures, and an increase in sharpness of the phase transition (in highly order PST $\Delta T_{max} > 1$ is only observed within a small temperature span of 5 K). This limits these applications to high temperature devices, whilst near-room temperature and cryogenics devices are excluded. In order to exploit high electrocaloric effect in PST compounds ($\Delta T > 1$) whilst exploiting the flexibility to extend or adjust the operating temperature of the device, Shebanov [83] proposed a method that relies on the substitution of *A*-site and/or *B*-site cations by ions. An extensive study was performed on solid-solutions of PST with 10 mol % dopant amount. Electrocaloric adiabatic temperature change ΔT in solid-solutions of PST was directly measured using an iron–constantanium thermocouple. Diagrams presented herein, namely Fig. 24a and b, reveal three distinct groups of solid-solutions characterized by their phase transition: strongly diffused (solid line area), diffused (shadowed area) and sharp (dashed line area). From this representations follows that solid-solutions characterized by sharp first-order phase transitions disclose higher electrocaloric temperature change than that measured in those categorized in the diffused phase transition group. These observations extend to doped-PST solid–solutions and Shebanov's preposition, which establishes the first-order phase transition as the drive for high electrocaloric

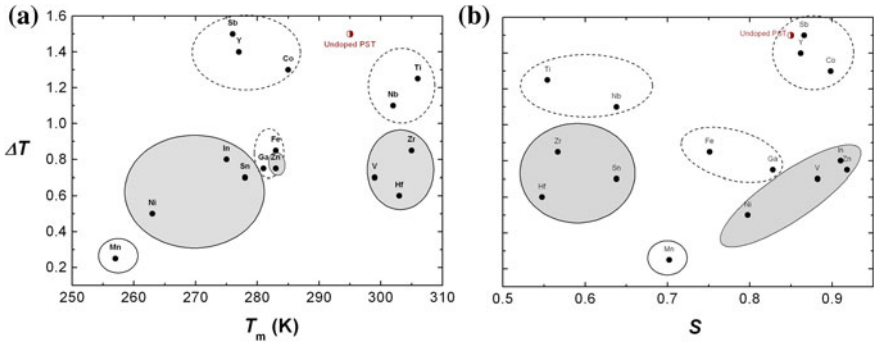

Fig. 24 Electrocaloric temperature change (ΔT) as a function of **a** maximum temperature, T_m and **b** *B*-site order degree, *S*. *solid line area*—strongly diffuse; *shadowed area*—diffuse; *dashed line area*—sharp phase transition, $E = 25$ kV/cm. Data extracted from Shebanov et al. [83]

effect in highly ordered PST ceramics. But unlike undoped PST ceramics, where electrocaloric is enhanced by ordering degree, in PST solid-solutions other structural features may affect electrocaloric effect, as such:

- *B-site ordering degree*. High ordering structure is required to achieve high electrocaloric effect. This essential condition is clear in Fig. 24b, with the observation of monotonous increase of S through B-site substitution by Mn, Fe, Co, leading to a monotonous increase in ΔT.
- *Stability of perovskite structure*. Under the condition of highly ordered lattice, the stability of the initial perovskite PST structure is crucial to maintaining high electrocaloric effect, i.e., Goldshmith tolerance factor of stable solid solutions must be close to that of the undoped PST ($t = 0.85$). The appearance of non-ferroelectric phase may significantly degrade electrocaloric effect. This is apparent in Fig. 24b in the group formed by the substituents Ti, Nb, showing high electrocaloric ΔT (>1 K), even though these are characterized by much lower S than Sb, Co group.
- *Electronic polarizability*: Well demonstrated by the unstable Y-doped PST solid solution, which is characterized by high electrocaloric effect. This has been associated with the high electronic polarizability of the substituent Y, which then indicates this property as a requirement for high electrocaloric effect, under the condition of high ordering degree.

A secondary effect resulting from the substitution of Sc^{3+} and Ta^{5+} is the shift of the phase transition temperature—and thus, the maximum of electrocaloric effect—to lower or higher temperatures. This is clear in Fig. 24a, which suggests that high electrocaloric effect and low operating temperatures (up to 250 K) are attained by introducing Sb^{5+}, Co^{3+}, Y^{3+} into the lattice. On the other hand, high temperature cooling applications may take advantage of PST Nb- or Ti-doping, which shifts the operating temperature up to 310 K.

The drawback of enhancing electrocaloric effect by sharpening phase transition is the resulting narrow operating temperature interval. This can be overcome by tailoring PST solid-solutions with a characteristic diffuse phase transition by using suitable dopants covered by the solid line areas in Fig. 24a and b.

Thickness adjustment

Despite great efforts to obtain large electrocaloric effect in PST ceramics, temperature change observed has nevertheless been too small for their use as working bodies in electrocaloric refrigerators. Electrocaloric ΔT is proportional to the applied electric field ΔE, a value which is rather limited in bulk ceramics, where breakdown field is somewhat low. A further enhancement of electrocaloric effect, ΔT from 1.5 up to 2.3 K, in Sb-doped PST ceramics was observed when an electric field was increased from 25 to 48 kV/cm [84]. Also, undoped PST multilayer structure, with internal layers from 56 to 64 μm, has been shown to result in the high electrocaloric effect $\Delta T = 2.4$ K (at 138 kV cm^{-1}) [84]. Such enhanced electrocaloric effect is associated with high applied electric field. In the particular

case of a PST multilayer structure, high field was only possible to apply without causing electrical breakdown due to small material thickness. But reducing the electrocaloric material thickness to enhance electrocaloric effect is an approach that only became of interest in 2006, when a giant electrocaloric was predicted in $PbZr_{0.95}Ti_{0.05}O_3$ thin films near the paraelectric-antiferroelectric phase transition [58]. An electric field as high as 250 kV/cm was applied and a $\Delta T = 12$ °C was indirectly measured. Electrocaloric effect in PST thin films was reported two years later [25], when it was found that high electrocaloric temperature drop may be obtained even with low order degree. This is described in more detail in the ensuing section.

3.3 Electrocaloric Effect in PST Thin Films

More than a decade after the works on PST ceramics by Shebanov [82, 83] and Sinyavsky [87] were first published, investigations on the electrocaloric effect in PST in thin films were carried out by Correia et al. [24, 25].

The authors aimed to achieve high electrocaloric effect by combining the promising electrocaloric properties found in PST system, attributed to relaxor-ferroelectric phase transition, with the characteristic high breakdown field of thin films. In those works, PST thin films were fabricated by a sol–gel method and different *B*-site ordering degrees were obtained through suitable annealing conditions (see Table 3): (1) disordered, $S = 0$, annealed film at 650 °C in a hotplate for 5 min; (2) partially-ordered film, $S = 0.32$, annealed at 650 °C for 10 min using a Rapid Thermal Annealer with a heating ramp 18 °C/s and natural cooling for 20 min (nonlinear cooling rate). Dielectric response measured in the films suggested a typical relaxor behaviour, whereas the permittivity was characterized by a broad and frequency dependent maximum at T_m, which, in turn, is strongly frequency-dependent [24, 25]. Relaxor behaviour was then confirmed by data analysis undertaken within the framework of Vogel-Fulcher law, according to which T_m relates to frequency f as follows:

$$f = f_0 \exp\left[\frac{-E_a}{k(T_m - T_f)}\right]$$

where, E_a is the activation energy, f_0 is the attempt frequency, which is related with PNR relaxation time τ_0 ($\tau_0 = 1/f_0$), and k is the Boltzmann constant. T_f is the "freezing temperature", at which dipole–dipole interaction between PNRs is strong enough, due to PNRs growth, preventing its motion. In the case of relaxor PST, such PNR growth can result in the development of long-range ordered domain below T_f, and the material undergoes a ferroelectric phase transition. From Vogel-Fulcher fitting, activation energies E_a and relaxation time τ_0 were determined [24]. Both E_a and τ_0 vales were found higher in partially-ordered PST film than in the disordered film ($E_a = 0.0065$ eV and $\tau_0 = 5.88 \times 10^{-8}$ s for

disordered and $E_a = 0.0089$ eV $\tau_0 = 1.85 \times 10^{-9}$ s for partially-ordered PST film). Although relaxation properties have been shown to be strongly affected by *B*-site order degree [11, 83], this did not allow quantifying the impact of *B*-site order degree in relaxation behavior, as this effect may be overlapped by contribution from other secondary effects related with film microstructure and quality (such as defects, impurities, grain size, etc.). Another interesting observation pointed out by the authors was that T_m is higher in partially-ordered than in the disordered thin film, which corroborates with findings in other PST ceramics and thin films, where it has been established that T_m increases while increasing *B*-site order degree, i.e., while enhancing ferroelectric domain stabilization (see Table 3). In addition, thermal hysteresis of permittivity near T_m was found in both PST films. This was marked by a different temperature dependence of permittivity and distinct T_m, when measured upon heating and cooling, respectively. Such "memory" effect of the films' dielectric properties may be associated with the previously reported coexistence of an incommensurate antiferroelectric phase with paraelectric and ferroelectric phases in PST ceramics observed by TEM [3].

The effect of the application of an electric field in the PST films polar response was evaluated by means of field-induced reversible *P-E* loops carried out at different temperatures [24, 25]. Using this data, electrocaloric effect was predicted using Maxwell relations (see Sect. 4.1 in Chap. 1). Temperature dependence of electrocaloric ΔS is characterized by a maximum value, which, according to Correia et al. [24], is the result of a field-induced relaxor-ferroelectric phase transition, as previously observed in ceramics. Figure 25 shows the maximum values of electrocaloric ΔS resulting from the removal of an alternated field indirectly measured for disordered and partially-ordered PST thin films. One can be seen that electrocaloric ΔS depends linearly with *E*. Moreover, within the measured *E* range, partially-ordered PST thin film shows higher electrocaloric effect (ΔS) than that measured in the disordered film, a finding that is in good

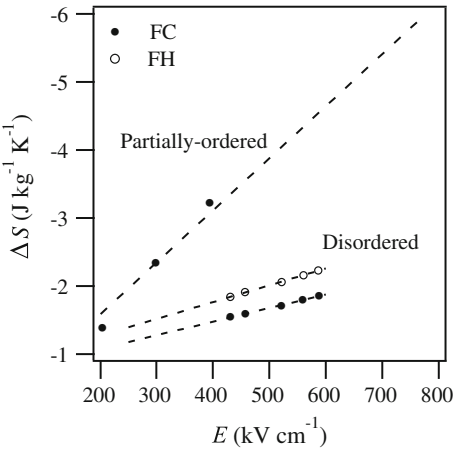

Fig. 25 Entropy variation, ΔS, at field-induced relaxor-ferroelectric phase transition, obtained in disordered and partially-ordered PST thin films [24]

agreement with Shebanov's [83] investigations in ceramics, which pointed out that electrocaloric effect is enhanced by Sc^{3+} and Ta^{5+} ordering.

It is also evident that disordered PST thin film is characterized by thermal hysteresis, i.e., different electrocaloric effect measured upon field-cooling (FC) and field-heating (FH), whilst in the partially-ordered PST thin films thermal hysteresis is suppressed by the application of an electric field. Moreover, temperature at which maximum electrocaloric ΔS occurs, i.e., field-induced relaxor-ferroelectric phase transition, is higher in partially ordered film (65 °C) than that of disordered films (25 °C FC and 56 °C for FH).

PST thin films potential for cooling devices

Disordered PST thin film was characterized by low values of $|\Delta S|$ and $|\Delta T|$ (=1.35 J kg^{-1} K^{-1} and 1.5 K on FC and 2.2 J kg^{-1} K^{-1} and 2.4 K on FH), and was found to be history dependent. These evidences indicate that disordered PST thin films has a limited potential for cooling applications. Nonetheless, by increasing *B*-site cation order degree through the use of suitable heat treatments, thermal hysteresis of electrocaloric response was totally removed, and an enhancement and single values of $|\Delta S|$ and $|\Delta T|$ (=5.76 J kg^{-1} K^{-1} and 6.5 K, respectively) were obtained at 65 °C at field-induced relaxor ferroelectric phase transition in partially-ordered PST thin film. Moreover, electrocaloric effect ΔS does not change much over a wide temperature range, as one can be seen in Fig. 26.

To benchmark partially-ordered PST thin films against other electrocaloric materials, one should take into account other parameters, namely refrigeration capacity (*RC*). *RC* is the heat that may be transferred through the electrocaloric material between the cold and hot reservoirs at T_c and T_h, respectively, and is defined as $RC = \int_{T_c}^{T_h} \Delta S dT$. The higher *RC* is, the higher the efficiency and useful heat, and high *RC* can be achieved by increasing ΔS and/or $T_h - T_c$. Disordered PST thin film displayed a broad field-induced relaxor–ferroelectric phase transition

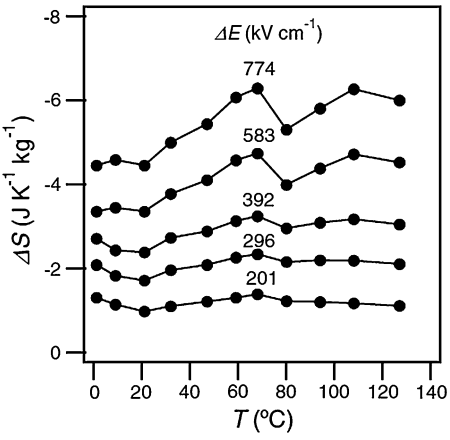

Fig. 26 Electrocaloric effect indirectly measured in partially-ordered PST thin film. Data refer to FC and FH measurements, which are coincident [25]

at 56 °C upon heating, revealing an $RC = 157.2$ J kg^{-1} within the 15–99 °C temperature span (RC values were calculated from ΔS-T curves obtained upon heating). However, an improvement of $RC = 382.5$ J kg^{-1} was detected when PST order degree was increased up to $S = 0.32$. This is related not only with the underlying increase of ΔS associated with increasing ordered regions in the PST thin film, but also with an enlargement of the temperature span (5–90 °C).

PNR interaction at low temperatures in relaxors also brings about a non-ergodic response, translating as large thermal hysteresis in electrocaloric effect. The large thermal hysteresis apparent within the studied temperature range is indicative of the occurrence of an irreversible cycle when said films are used as refrigerants. However, ordering of PST thin film ($S = 0.32$) caused not only a rise in ΔS and ΔT near room temperature (at 65 °C), but also the suppression of thermal hysteresis. This follows that partially-ordered PST thin film is a very interesting candidate for use in refrigerators operating at room temperature due to their large electrocaloric effect and intrinsic efficiency.

References

1. Akcay, G., Alpay, S.P., Rossetti Jr, G.A., Scott, J.F.: Influence of mechanical boundary conditions on the electrocaloric properties of ferroelectric thin films. J. Appl. Phys. **103**, 024104 (2008)
2. Arndt, H., Sauerbier, F., Schmidt, G., Shebanov, L.A.: Field-induced phase transition in $Pb(Mg_{1/3}Nb_{2/3})O_3$ single crystals. Ferrolectrics **79**, 145–148 (1988)
3. Baba-Kishi, K.Z., Pasciak, M.: Transmission electron microscope studies of phase transitions in single crystals and ceramics of ferroelectric $Pb(Sc_{1/2}Ta_{1/2})O_3$. J. Appl. Cryst. **23**, 43–54 (1990)
4. Bai, F., Wang, N., Li, J., Viehland, D., Gehring, P.M., Xu, G., Shirane, G.: X-ray and neutron diffraction investigations of the structural phase transformation sequence under electric field in $0.7Pb(Mg_{1/3}Nb_{2/3})$-$0.3PbTiO_3$. J. Appl. Phys. **96**, 1620–1627 (2004)
5. Bell, A.: Phenomenologically derived electric field-temperature phase diagrams and piezoelectric coefficients for single crystal barium titanate under fields along different axes. J. Appl. Phys. **89**, 3907–3914 (2001)
6. Birks, E.H.: The electrocaloric effect in $Pb(Sc_{0.5}Nb_{0.5})O_3$ ceramic. Phys. Stat. Sol. (a) **94**, 523–527 (1986)
7. Birks, E., Shebanov, L., Sternberg, A.: Electrocaloric effect in PLZT ceramics. Ferroelectrics **69**, 125–129 (1986)
8. Bokov, A.A., Ye, Z.-G.: Recent progress in relaxor ferroelectrics with perovskite structure. J. Mater. Sci. **41**, 31–52 (2006)
9. Bokov, A.A., Ye, Z.-G.: Double freezing of dielectric response in relaxor $Pb(Mg_{1/3}Nb_{2/3})O_3$ crystals. Phys. Rev. B **74**, 132102 (2006)
10. Bokov, A.A., Rodriguez, B.J., Zhao, X., Ko, J.-H., Jesse, S., Long, X., Qu, W., Kim, T.H., Budai, J.D., Morozovska, A.N., Kojima, S., Tan, X., Kalinin, S.V., Te, Z.-G.: Compositional disorder, polar nanoregions, and dipole dynamics in $Pb(Mg_{1/3}Nb_{2/3})O_3$-based relaxor ferroelectrics. Z. Kristallogr. **226**, 99–107 (2011)
11. Brinkman, K., Wang, Y., Su, D., Tagantsev, A., Muralt, P., Setter, N.: The impact of chemical ordering on the dielectric properties of lead scandium tantalate $Pb(Sc_{1/2}Ta_{1/2})O_3$ thin films. J. Appl. Phys. **102**, 044110/1–7 (2007)

12. Brinkman, K.: Positional order in lead scandium tantalate (PST) as a "tool" for the investigation of relaxor ferroelectric behavior in thin films. PhD Thesis, École Polytechnique Fédérale de Lausanne, (2004)
13. Burns, G., Scott, B.A.: Index of refraction in 'dirty' displacive ferroelectrics. Sol. Stat. Commun. **13**, 423–426 (1973)
14. Burns, G., Dacol, F.H.: Glassy polarization behavior in ferroelectric compounds $Pb(Mg_{1/3}Nb_{2/3})O_3$ and $Pb(Zn_{1/3}Nb_{2/3})O_3$. Solid State Commun. **48**, 853 (1983)
15. Budimir, M., Damjanovic, D., Setter, N.: Piezoelectric anisotropy-phase transition relations in perovskite single crystals. J. Appl. Phys. **94**, 6753 (2003)
16. Cao, H., Bai, F., Wang, N., Li, J., Viehland, D., Xu, G., Shirane, G.: Intermediate ferroelectric orthorhombic and monoclinic M_B phases in [110] electric-field-cooled $Pb(Mg_{1/3}Nb_{2/3}O_3)$-30%$PbTiO_3$ crystals. Phys. Rev. B **72**, 064104 (2005)
17. Cao, H., Li, J., Viehland, D., Xu, G.: Fragile phase stability in (1-*x*)$Pb(Mg_{1/3}Nb_{2/3}O_3)$-*x*$PbTiO_3$ crystals: a comparison of [001] and [110] field-cooled phase diagrams. Phys. Rev. B **73**, 184110 (2006)
18. Chien, R.R., Schmidt, V.H., Tu, C.-S., Hung, L.-W., Luo, H.: Field-induced polarization rotation in (001)-cut $Pb(Mg_{1/3}Nb_{2/3})_{0.76}Ti_{0.24}O_3$. Phys. Rev. B **69**, 172101 (2004)
19. Choi, S.W., Shrout, T.R., Jang, S.J., Bhalla, A.S.: Dielectric and pyroelectric properties in the $Pb(Mg_{1/3}Nb_{2/3})O_3$-$PbTiO_3$ system. Ferroelectrics **100**, 29–38 (1989)
20. Choi, S.W., Shrout, T.R., Jang, S.J., Bhalla, A.S.: Morphotropic phase boundary in $Pb(Mg_{1/3}Nb_{2/3})O_3$-$PbTiO_3$ system. Mater. Lett. **8**, 253–255 (1989)
21. Chu, F., Setter, Tagantsev, N., A.K.: The spontaneous relaxor-ferroelectric transition of $Pb(Sc_{0.5}Ta_{0.5})_{O3}$. J. Appl. Phys. **74**, 5129–5134 (1993)
22. Chukka, R., Cheah, J.W., Chen, Z., Yang, P., Shannigrahi, S., Wang, J., Chen, L.: Enhanced cooling capacities of ferroelectric materials at morphotropic phase boundaries. Appl. Phys. Lett. **98**, 242902 (2011)
23. Correia, T.M., Young, J.S., Whatmore, R.W., Scott, J.F., Mathur, N.D., Zhang, Q.: Investigation of the electrocaloric effect in a $PbMg_{1/3}Nb_{2/3}O_3$-$PbTiO_3$ relaxor thin film. Appl. Phys. Lett. **95** (18), 182904/1–3. ISSN: 0003-6951 (2009)
24. Correia, T.M.: Exploring electrocaloric effect in thin films. PhD Thesis, Cranfield University (2010)
25. Correia, T.M., Kar-Narayan, S., Young, J.S., Scott, J.F., Mathur, N.D., Whatmore, R.W., Zhang, Q.: PST thin films for electrocaloric coolers. J. Phys. D Appl. Phys. **44**, 165407 (2011)
26. Cross, L.E.: Relaxor ferroelectrics. Ferroelectrics **76**, 241–267 (1987)
27. Damjanovic, D.: A morphotropic phase boundary system based on polarization rotation and polarization extension. Appl. Phys. Lett. **97**, 062906 (2010)
28. Davies, P., Akbas, M.A.: Chemical order in PMN-related relaxors: structure, stability, modification, and impact on properties. J. Phys. Chem. Sol. **61**, 159–166 (2000)
29. Davis, M., Damjanovic, D., Setter, N.: Electric-field-, temperature-, and stress-induced phase transitions in relaxor ferroelectric single crystals. Phys. Rev. B **73**, 014115 (2006)
30. Davis, M.: Picturing the elephant: giant piezoelectric activity and the monoclinic phases of relaxor-ferroelectric single crystals. J. Electroceram. **19**, 23–45 (2007)
31. De Kroon, A.P., Dunn, S.C., Whatmore, R.W.: Piezo- and pyroelectric properties of lead scandium tantalate thin films. Integ. Ferroelectrics **35**, 209–218 (2001)
32. Dieckmann, J., Cooperman, A., Brodrick, J.: Solid-state cooling, Part 2. ASHRAE J. **53**, 66–68 (2011)
33. Dul'kin, E., Mihailova, B., Gospodinov, M., Roth, M.: Effect of A-site La and Ba doping on threshold field and characteristic temperatures of $PbSc_{0.5}Ta_{0.5}O_3$ relaxor studied by acoustic emission. J. Appl. Phys. **112**, 064107 (2012)
34. Dunne, L.J., Valant, M., Axelsson, A.K., Manos, G., Alford, N.M.: Statistical mechanical lattice model of the dual-peak electrocaloric effect in ferroelectric relaxors and the role of pressure. J. Phys. D-Appl. Phys. **44**, 375404 (2011)

35. Feng, Z., Shi, D., Zeng, R., Dou, S.: Large electrocaloric effect of highly (100)-oriented $0.68PbMg_{1/3}Nb_{2/3}O_3$-$0.32PbTiO_3$ thin films with a $Pb(Zr_{0.3}Ti_{0.7})O_3/PbO_x$ buffer layer. Thin Solid Films **519**, 5433–6436 (2011)
36. Feng, Z., Shi, D., Dou, S.: Large electrocaloric effect in highly (001)-oriented $0.67PbMg_{1/3}Nb_{2/3}O_3$-$0.33PbTiO_3$ thin films. Sol. State Commun. **151**, 123–126 (2011)
37. Fu, H., Cohen, R.E.: Polarization rotation mechanism for ultrahigh electromechanical response in single-crystal piezoelectrics. Nature **403**, 281–283 (2000)
38. Fuflyigin, V., Salley, E., Vakhutinsky, P., Osinsky, A., Zhao, J., Gergis, I., Whiteaker, K.: Free-standing films of $PbSc_{0.5}Ta_{0.5}O_3$ for uncooled infrared detectors. Appl. Phys. Lett. **78**, 365–367 (2001)
39. Gao, X.S., Xue, J.M., Wanga, J., Yu, T., Shen, Z.X.: B-site disordering in $Pb(Sc_{1/2}Ta_{1/2})O_3$ by mechanical activation. Appl. Phys. Lett. **82**, 4773 (2003)
40. Hagberg, J., Uusimäki, A., Jantunen, H.: Electrocaloric characteristics in reactive sintered 0.87 $Pb(Mg_{1/3}Nb_{2/3})O_3$-0.13 $PbTiO_3$. Appl. Phys. Lett. **92**, 132909 (2008)
41. Harmer, M.P., Chen, J., Peng, P., Chan, H.M., Smyth, D.M.: Control of microchemical ordering in relaxor ferroelectrics and related compounds. Ferroelectrics **97**, 263 (1989)
42. He, Y., Li, X.M., Gao, X.D., Leng, X., Wang, W.: Enhanced electrocaloric properties of PMN-PT thin films with LSCO buffer layers. Funct. Mater. Lett. **4**, 45–48 (2011)
43. Huang, Z., Donohue, P.P., Zhang, Q., Williams, D.J., Anthony, C.J., Whatmore, R.W., Todd, M.A.: Comparative microstructure and electrical property studies of lead scandium tantalate thin films as prepared by LDCVD, sol–gel and sputtering techniques. J. Phys. D Appl. Phys. **36**, 270–279 (2003)
44. Katpatal, A.G., Deshmukh, K.G.: Electro caloric effect in ferroelectric lead titanate. Indian J. Pure Appl. Phys. **14**, 395–398 (1976)
45. Kiat, J.-M., Uesu, Y., Dkhil, B., Matsuda, M., Malibert, C., Calvarin, G.: Monoclinic structure of unpoled morphotropic high piezoelectric PMN-PT and PZN-PT compounds. Phys. Rev. B **65**, 064106 (2002)
46. Kiat, J.-M., Dkhil, B.: From the strucutre of relaxors to the structure of MPB systems. In: Ye, Z.-G. (ed.) Handbook of advanced dielectric, piezoelectric and ferroelectric materials: synthesis, properties and applications, pp. 391–446. Woodhead Publishing Ltd., Cambridge (2008)
47. Kutnjak, Z., Petzelt, J., Blinc, R.: The giant electromechanical response in ferroelectric relaxors as a critical phenomenon. Nature **441**, 956–959 (2006)
48. Kutnjak, Z., Blinc, R., Ishibashi, Y.: Electric field induced critical points and polarization rotations in relaxor ferroelectrics. Phys. Rev. B **76**, 104102 (2007)
49. Kutnjak, Z., Vodopivec, B., Blinc, R.: Anisotropy of electric field freezing of the relaxor ferroelectric $Pb(Mg_{1/3}Nb_{2/3})O_3$. Phys. Rev. B **77**, 054102 (2008)
50. Le Goupil, F., Berenov, A., Axelsson, A.-K., Valant, M., Alford, N.M.: Direct and indirect electrocaloric measuremnts on $< 001 >$ -$PbMg_{1/3}Nb_{2/3}O_3$-$30PbTiO_3$ single crystals. J. Appl. Phys. **111**, 124109 (2012)
51. Levstik, A., Kutnjak, Z., Filipič, C., Pirc, R.: Glassy freezing in relaxor ferroelectric lead magnesium niobate. Phys. Rev. B **57**, 11204–11211 (1998)
52. Li, F., Zhang, S., Xu, Z., Wei, X., Luo, J., Shrout, T.R.: Composition and phase dependence of the intrinsic and extrinsic piezoelectric activity of domain engineered $(1\text{-}x)Pb(Mg_{1/3}Nb_{2/3}O_3)$-$xPbTiO_3$ crystals. J. Appl. Phys. **108**, 034106 (2010)
53. Lu, S.G., Zhang, Q.M.: Electrocaloric materials for solid-state refrigeration. Adv. Mater. **21**, 1983–1987 (2009)
54. Lu, S.G., Rožič, B., Zhang, Q., Kutnjak, Z., Li, X.Y., Furman, E., Gorny, J.L., Lin, M.R., Malic, B., Kosec, M., Blinc, R., Pirc, R.: Organic and inorganic relaxor ferroelectrics with giant electrocaloric effect. Appl. Phys. Lett. **97**, 162904 (2010)
55. Luo, L., Chen, H., Zhu, Y., Li, W., Luo, H., Zhang, Y.: Pyroelectric and electrocaloric effect of ⟨111⟩-oriented 0.9PMN-0.1PT single crystal. J. Alloys Compd. **509**, 8149–8152 (2011)

56. Luo, L., Dietze, M., Solterbeck, C.-H., Es-Souni, M., Luo, H.: Orientation and phase transition dependence of the electrocaloric effect in $0.71Pb(Mg_{1/3}Nb_{2/3})O_3$-$0.29PbTiO_3$ single crystal. Appl. Phys. Lett. **101**, 062907 (2012)
57. Mathan, N., Husson, E., Calvarin, G., Gavarri, J.R., Hewat, A.W., Morell, A.: A structural model for the relaxor $PbMg_{1/3}Nb_{2/3}O_3$ at 5 K. J. Phys.: Condens. Matter **3**, 8159 (1991)
58. Mischenko, A.S., Zhang, Q., Scott, J.F., Whatmore, R.W., Mathur, N.D.: Giant electrocaloric effect in thin-film $PbZr_{0.95}Ti_{0.05}O_3$. Science **311**, 1270–1271 (2006)
59. Mischenko, A.S., Zhang, Q., Whatmore, R.W., Scott, J.F., Mathur, N.D.: Giant electrocaloric effect in the thin-film relaxor ferroelectric 0.9 $PbMg_{1/3}Nb_{2/3}O_3$–0.1 $PbTiO_3$ near room temperature. Appl. Phys. Lett. **89**, 242912 (2006)
60. Noheda, B.: Structure and high-piezoelectricity in lead oxide solid solutions. Curr. Opin. Solid State Mater. Sci. **6**, 27–34 (2002)
61. Noheda, B., Cox, D.E., Shirane, G., Gao, J., Ye, Z.-G.: Phase diagram of the ferroelectric relaxor $(1\text{-}x)Pb(Mg_{1/3}Nb_{2/3})O_3$-$xPbTiO_3$. Phys. Rev. B **66**, 054104 (2002)
62. Noheda, B., Zhong, Z., Cox, D.E., Shirane, G., Park, S.-E., Rehrig, P.: Electric-field-induced phase transitions in rhombohedral $Pb(Zn_{1/3}Nb_{2/3})_{1-x}Ti_xO_3$. Phys. Rev. B **65**, 224101 (2002)
63. Noheda, B., Cox, D.E.: Bridging phases at the morphotropic boundaries of lead oxide solid solutions. Phase Transit. **79**, 5–20 (2006)
64. Peräntie, J., Hagberg, J., Uusimäki, A., Jantunen, H.: Field-induced thermal response and irreversible phase transition enthalpy change in $Pb(Mg_{1/3}Nb_{2/3})O_3$-$PbTiO_3$. Appl. Phys. Lett. **94**, 102903 (2009)
65. Peräntie, J., Hagberg, J., Uusimäki, A., Jantunen, H.: Electric-field-induced dielectric and temperature changes in a $\langle 011 \rangle$-oriented $Pb(Mg_{1/3}Nb_{2/3})O_3$-$PbTiO_3$ single crystal. Phys. Rev. B **82**, 134119 (2010)
66. Peräntie, J., Hagberg, J., Uusimäki, A., Tian, J., Han, P.: Characteristics of electric-field-induced polarization rotation in $< 001 >$-poled $Pb(Mg_{1/3}Nb_{2/3})O_3$-$PbTiO_3$ single crystals close to the morphotropic phase boundary. J. Appl. Phys. **112**, 034117 (2012)
67. Qiu, J.H., Jian, Q.: Film thickness dependence of electrocaloric effect in epitaxial $Ba_{0.6}Sr_{0.4}TiO_3$ thin films. J. Appl. Phys. **103**, 034119 (2008)
68. Qiu, J.H., Jian, Q.: Orientation dependence of the electrocaloric effect of ferroelectric bilayer thin film. Sol. State Commun. **149**, 1549–1552 (2009)
69. Pirc, R., Blinc, R.: Spherical random-bond-random-field model of relaxor ferroelectrics. Phys. Rev. B **60**, 13470–13478 (1999)
70. Pirc, R., Kutnjak, Z., Blinc, R., Zhang, Q.M.: Electrocaloric effect in relaxor ferroelectrics. J. Appl. Phys. **110**, 074113 (2011)
71. Rozic, B., Malic, B., Ursic, H., Holc, J., Kosec, M., Kutnjak, Z.: Direct measurements of the electrocaloric effect in bulk $PbMg_{1/3}Nb_{2/3}O_3$ (PMN) ceramics. Ferroelectrics **421**, 103–107 (2011)
72. Rožič, B., Kosec, M., Uršič, H., Holc, J., Malič, B., Zhang, Q.M., Blinc, R., Pirc, R., Kutnjak, Z.: Influence of the critical point on the electrocaloric response of relaxor ferroelectrics. J. Appl. Phys. **110**, 064118 (2011)
73. Samara, G.A.: The relaxational properties of compositionally disordered ABO_3 perovskites. J. Phys.: Condens. Matter **15**, R367-411 (2003)
74. Saranya, D., Chaudhuri, A.R., Parui, J., Krupanidhi, S.B.: Electrocaloric effect of PMN-PT thin films near morphotropic phase boundary. Bull. Mater. Sci. **32**, 259–262 (2009)
75. Scott, J.F.: Switching of ferroelectric without domains. Adv. Mater. **22**, 5315–5317 (2010)
76. Scott, J.F.: Electrocaloric materials. Annu. Rev. Mater. Res. **41**, 1–12 (2011)
77. Sebald, G., Seveyrat, L., Guyomar, D., Lebrun, L., Guiffard, B., Pruvost, S.: Electrocaloric and pyroelectric properties of $0.75Pb(Mg_{1/3}Nb_{2/3})O_3$-$0.25PbTiO_3$ single crystals. J. Appl. Phys. **100**, 124112 (2006)
78. Sebald, G., Pruvost, S., Seveyrat, L., Lebrun, L., Guyomar, D., Guiffard, B.: Electrocaloric properties of high dielectric constant ferroelectric ceramics. J. Eur. Ceram. Soc. **27**, 4021–4024 (2007)

79. Setter, N., Cross, L.E.: The role of B-site cation disorder in diffuse phase transition behavior of perovskite ferroelectric. J. Appl. Phys. **51**, 4356–4361 (1980)
80. Shaobo, L., Yanqiu, L.: Research on the electrocaloric effect of PMN/PT solid solution for ferroelectrics MEMS microcoolers. Mater. Sci. Eng. B **113**, 46–49 (2004)
81. Shebanov, L.A., Kapostin'sh, P.P., Birks, E.H., Zvirgzds, Y.A.: Some peculiarities in the rearrangement of the crystal structure and electrocaloric effect in single crystal of lead magnoniobate in the region of the diffuse phase transition. Kristallografiya **31**, 317–320 (1986)
82. Shebanov, L.A., Birks, E.H., Borman, K.J.: X-ray studies of electrocaloric lead scandium tantalate ordered solid solutions. Ferroelectrics **90**, 165–172 (1989)
83. Shebanov, L., Borman, K.: On lead-scandium tantalate solid solutions with high electrocaloric effect. Ferroelectrics **127**, 143–148 (1992)
84. Shebanovs, L., Borman, K., Lawless, W.N., Kalvane, A.: Electrocaloric effect in some perovskite ferroelectric ceramics and multilayer capacitors. Ferroelectrics **273**, 137–142 (2002)
85. Singh, A.K., Pandey, D.: Structure and the location of the morphotropic phase boundary region in $(1 - x)[Pb(Mg_{1/3}Nb_{2/3})O_3]$-$xPbTiO_3$. J. Phys.: Condens. Matter **13**, L931–L936 (2001)
86. Singh, A.K., Pandey, D.: Evidence of M_B and M_C phases in the morphotropic phase boundary region of $(1 - x)[Pb(Mg_{1/3}Nb_{2/3})O_3]$-$xPbTiO_3$: a rietveld study. Phys. Rev. B **67**, 064102 (2003)
87. Sinyavsky, Y.V., Pashkov, N.D., Gorovoy, Y.M., Lugansky, G.E., Shebanov, L.: The optical ferroelectric ceramic as working body for electrocaloric refrigeration. Ferroelectrics **90**, 213–217 (1989)
88. Smolenskii, V.A., Agranovskaya, A.I.: Dielectric polarization of a number of complex compounds. Sov. Phys. Solid State, 1429 (1959)
89. Stenger, C., Burggraaf, A.: Ordering and diffuse phase transitions in Pb(Sc0.5Ta0.5)O3 ceramics. Sol. Stat. Comm. **32**, 989–992 (1979)
90. Todd, M.A., Donohue, P.P., Harper, M.A.C., Jones, J.C.: Sputtered lead scandium tantalate thin films for dielectric bolometer mode thermal detector arrays. Integ. Ferroelectrics **35**, 115–124 (2001)
91. Valant, M., Dunne, L.J., Axelsson, A.-K., Alford, N.McN., Manos, G., Peräntie, J., Hagberg, J., Jantunen, H., Dabkowski, A.: Electrocaloric effect in a ferroelectric Pb(Zn1/3Nb2/3)O3-PbTiO3 single crystal. Phys. Rev. B **81**, 214110 (2010)
92. Valant, M.: Electrocaloric materials for solid-state refrigeration technologies. Prog. Mater Sci. **57**, 980–1009 (2012)
93. Valant, M.: Electrocaloric temperature change constrained by the dielectric strength. Mat. Chem. Phys. **136**, 277–280 (2012)
94. Vanderbilt, D., Cohen, M.H.: Monoclinic and triclinic phases in higher-order Devonshire theory. Phys. Rev. B **63**, 094108 (2001)
95. Viehland, D., Jang, S.J., Cross, L.E., Wuttig, M.: Freezing of the polarization fluctuations in lead magnesium niobate relaxors. J. Appl. Phys. **68**, 2916–2921 (1990)
96. Westphal, V., Kleemann, W., Glinchuk, M.D.: Diffuse phase transitions and random-field-induced domain states of the "relaxor" ferroelectric $PbMg_{1/3}Nb_{2/3}O_3$. Phys. Rev. Lett. **68**, 847–850 (1992)
97. Xiao, D.Q., Wang, Y.C., Zhang, R.L., Peng, S.Q., Zhu, J.G., Yang, B.: Electrocaloric properties of $(1\text{-}x)Pb(Mg_{1/3}Nb_{2/3})O_3$-$xPbTiO_3$ ferroelectric ceramics near room temperature. Mater. Chem. Phys. **57**, 182–185 (1998)
98. Xu, G., Shirane, G., Copley, J.R.D., Gehring, P.: Neutron elastic diffuse scattering study of $Pb(Mg_{1/3}Nb_{2/3})O_3$. Phys. Rev. B **69**, 064112 (2004)
99. Ye, Z.-G., Schmid, H.: Optical, dielectric and polarization studies of the electric field-induced phase transition in $Pb(Mg_{1/3}Nb_{2/3})O_3$ [PMN]. Ferrolectrics **145**, 83–108 (1993)
100. Ye, Z.-G.: Relaxor ferroelectric complex perovskites: structure, properties and phase transitions. Key Eng. Mater. **155–156**, 81–122 (1998)

101. Ye, Z.-G., Dong, M.: Morphotropic domain structures and phase transitions in relaxor-based piezo-/ferroelectric (1-*x*)$Pb(Mg_{1/3}Nb_{2/3})O_3$-*x*$PbTiO_3$ single crystals. J. Appl. Phys. **87**, 2312–2319 (2000)
102. Ye, Z.-G., Noheda, B., Dong, M., Cox, D., Shirane, G.: Monoclinic phase in the relaxor-based piezoelectric/ferroelectric $Pb(Mg_{1/3}Nb_{2/3})O_3$-$PbTiO_3$ system. Phys. Rev. B **64**, 184114 (2001)
103. Ye, Z.-G., Bing, Y., Gao, J., Bokov, A.A., Stephens, P., Noheda, B., Shirane, G.: Development of ferroelectric order in relaxor (1-*x*)$Pb(Mg_{1/3}Nb_{2/3})O_3$-*x*$PbTiO_3$ ($0 \leq x \leq 0.15$). Phys. Rev. B **67**, 104104 (2003)

Electrocaloric Multilayer Capacitors

S. Kar-Narayan, S. Crossley and N. D. Mathur

1 Introduction

Given that conventional refrigeration is associated with high energy consumption and greenhouse gases, there is considerable interest in alternative technologies that are energy efficient and environmentally friendly. Electrocaloric (EC) refrigeration [23, 32, 39], based on electric field-driven temperature/entropy changes near phase transitions of ferroelectric materials, is a candidate solid-state cooling technology. However, EC refrigeration is difficult to implement because cooling devices based on bulk or films present orthogonal difficulties. For bulk [11, 19, 29, 34, 37, 38, 40], EC effects are small as they are limited by the low breakdown fields ($<$50 kV cm^{-1}) in bulk materials, heat transfer is inefficient due to low surface-to-volume ratio and low thermal conductivity (K), and large voltages are required and these can induce arcing. Films, generically possessing large breakdown fields ($\sim 10^3$ kV cm^{-1}), are predicted to show large EC effects [6, 7, 10, 22, 26–28, 31], a few of which have been experimentally confirmed recently [21, 24, 25]. However films cannot pump significant heat and are often thermally anchored by substrates. Multilayer capacitors (MLCs) comprising stacks of ferroelectric films separated by interdigitated metal electrodes have been proposed as the way forward towards practical EC refrigeration. MLCs have been shown to overcome the difficulties identified in bulk and films while simultaneously preserving all of the corresponding advantages [15, 16]. This is possible as first, MLCs can exploit the large EC effect in films without having a substrate present while simultaneously possessing the large thermal mass associated with bulk EC samples; second, MLCs ensure efficient heat transfer between the EC material and heat loads/dumps due to the large surface-to-volume ratio of the constituent EC films and the high K of the interdigitated metallic electrodes; and last, large electric fields are easily generated in MLCs by small

S. Kar-Narayan (✉) · S. Crossley · N. D. Mathur
Department of Materials Science and Metallurgy, University of Cambridge, 27 Charles Babbage Road, Cambridge CB3 0FS, UK
e-mail: sk568@cam.ac.uk

T. Correia and Q. Zhang (eds.), *Electrocaloric Materials*,
Engineering Materials 34, DOI: 10.1007/978-3-642-40264-7_4,

voltages across the constituent films, and proper packaging of MLCs ensures that arcing due to such large fields is not a frequent failure mechanism [33]. Therefore MLCs represents the optimal geometry for EC cooling applications. This chapter traces the evolution of this idea from the pioneering experiments on commercially available MLCs, through thermal models of EC MLCs, to possible ways of integrating MLCs in EC fridges.

2 Electrocaloric Effect in Multilayer Capacitors

Electrocaloric studies of multilayers are rare as fabrication is challenging, but multilayer capacitors (MLCs) have been developed for electronic applications through significant commercial investment. MLCs consisting of alternating layers of dielectric material and metal electrodes (see Fig. 1) are widely used as standard electronic components. The dielectric material is often chosen to be a doped ferroelectric to ensure high dielectric permittivity and stable operation over a wide temperature range. These MLCs can have inadvertent uses as was shown in an MLC made of doped Y5V $BaTiO_3$ and Ni-based electrodes which could function

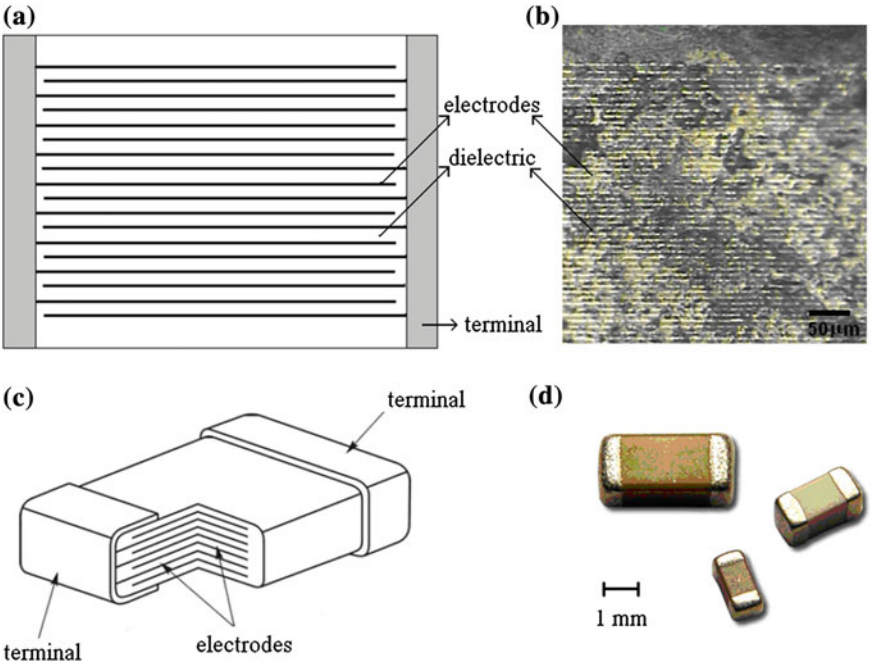

Fig. 1 Multilayer capacitor (MLC) geometry. **a** Schematic of MLC cross section, **b** optical microscope image obtained after sawing and polishing, **c** schematic of a surface mount MLC chip, and **d** commercial surface mount MLCs of different sizes

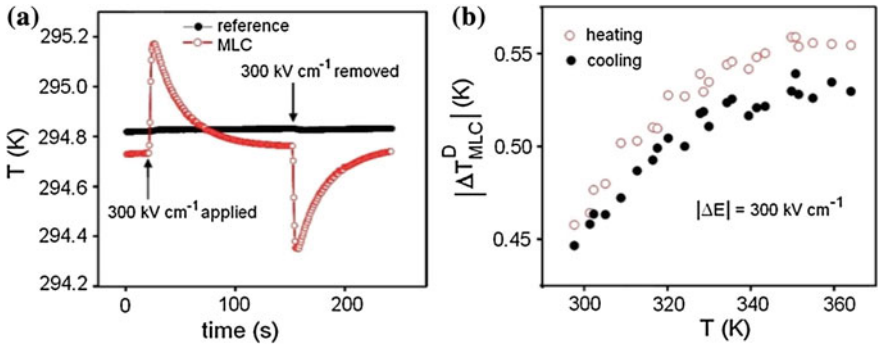

Fig. 2 Direct EC temperature change measurements in an MLC. **a** At room temperature, the MLC thermometer records temperature changes over time due to the application and subsequent removal of 300 kV cm^{-1}, not seen in the reference thermometer. **b** Magnitudes of the EC heating and cooling jumps plotted as a function of starting temperature. (Adapted from [16])

as a magnetoelectric sensor [12]. A similar MLC, comprising 200 alternating layers of 6.5 μm-thick doped $BaTiO_3$ [Y5V formulation (AVX Corporation Datasheet] films and 2 μm-thick Ni-based electrodes, was used to demonstrate the EC effect through direct measurements of temperature changes [16]) upon the application and subsequent removal of an electric field, as shown in Fig. 2. These EC temperature changes were measured using a Pt-100 thin-film thermometer mounted on one of the MLC terminals. The thermometer recorded an EC temperature change of $\sim$0.5 K at room temperature for an electric field change, $\Delta E \sim 300$ kV cm^{-1}. The experimental results were found to be in reasonably good agreement with theoretical predictions of the EC effect in the doped Y5V $BaTiO_3$, as derived from thermodynamic analysis of ferroelectric hysteresis loops.

The EC effect measured in the commercial MLC was small as the parent $BaTiO_3$ compound is predicted to show only small EC temperature changes ($\sim$1 K for $\Delta E = 100$ kV cm^{-1}) [1], and large enough electric fields ($\sim 10^3$ kV cm^{-1}) could not be accessed as the MLC was based on thick films. Additionally, clamping of the films by the unaddressed dielectric as well as doping of the Y5V dielectric suppress the phase transition which is essential for standard MLC applications, but result in an associated deterioration of EC performance. However, despite the small EC effect observed, the study was noteworthy as it (1) identified the important role played by the high-K interdigitated metal electrodes in efficiently extracting EC heat from the MLC, and (2) suggested the use of MLCs as practical EC devices where cooling is achieved via both MLC terminals. This is particularly significant as previous EC work with thick-film ($\sim$50 μm) MLCs [20, 35] failed to identify the ability of the electrodes to conduct heat and were motivated purely by the desire to determine EC materials performance. In other words, the MLCs themselves were not regarded as devices for EC applications. Lawless and Clark [20] conducted EC measurements on dense tape-cast $(Cd_{0.83}Pb_{0.17})_2Nb_2O_7$-based MLCs as these structures could withstand higher electric fields than the corresponding bulk

ceramic. They reported $\Delta T \sim 1$ K for $\Delta E \sim 100$ kV cm^{-1} in $(Cd_{0.83}Pb_{0.17})_2Nb_2O_7$ near 77 K, but the smaller measured ΔT of the multilayer itself (as expected when taking the thermal mass of the electrodes into account) was not reported and cannot be extracted from the paper. Furthermore the role of the metal electrodes in EC heat conduction was neglected, as was evident from the thermometer being mounted away from the terminal, unlike in [16] (see Fig. 3). Shebanovs et al. [35] simply reported an EC ΔT of 2.4 K for $\Delta E = 138$ kV cm^{-1} in $PbSc_{0.5}Ta_{0.5}O_3$-based MLCs which were fabricated to withstand the high electric field, but they did not give details of the fabrication techniques or measurement scheme, or even the temperature at which the reported EC effect was measured. Thus their work on EC effects in MLCs is unclear at best.

Interestingly, the EC temperature change in MLCs similar to the kind reported in Ref. [16] were verified using two novel EC measurement techniques [17]: scanning thermal microscopy (SThM) and infrared imaging (IRI). It was shown that by measuring the side (parallel to the electrode plates) of the MLC rather than the terminal, both measurement techniques recorded larger EC temperature changes ($\sim$0.75 K in SThM, $\sim$0.70 K in IRI) and significantly reduced decay times. This is because measurements of the side come closer to probing individual EC layers. By contrast, when measuring the terminal, electrode thermal mass reduces EC temperature change and lengthens thermal decay time. Therefore the $\sim$70 % reduction in EC temperature change on moving from the side to the terminal was similar to the calculated [16] 68 % reduction of EC layer temperature change due to electrode thermal mass.

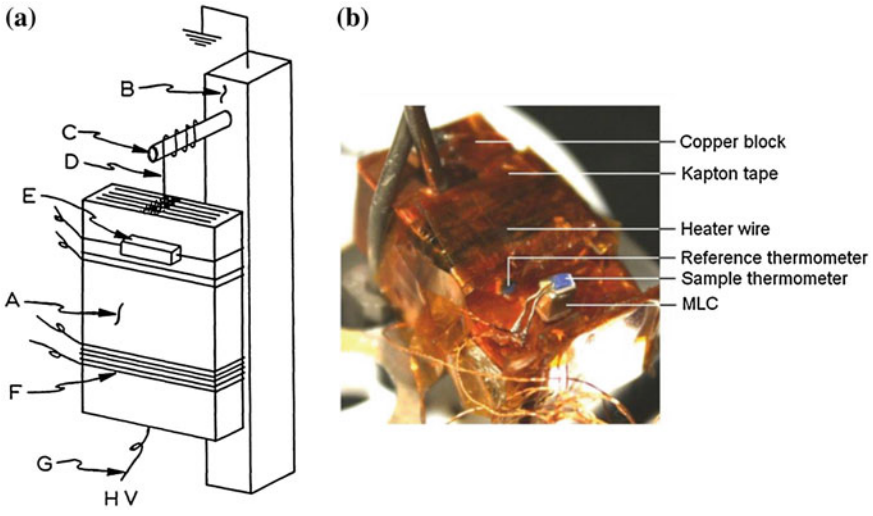

Fig. 3 MLC as an EC device. **a** Previous study on MLC failed to identify role of the metallic electrodes in EC heat conduction, as the thermometer (*E*) used to measure EC temperature change was mounted away from the MLC terminals. (Adapted from [20]). **b** The role of metallic electrodes in EC heat conduction was identified in this study and the thermometer to measure EC temperature change was mounted on an MLC terminal. (Adapted from [16])

Bai et al. [3, 5] measured EC effects in two different $BaTiO_3$-based MLCs fabricated using the tape-casting technique in which alternating layers of undoped $BaTiO_3$ and Ni were printed and co-fired. The Ni layers were structured such that they formed two sets of offset interleaved planar electrodes extending to the two opposite terminals of the MLC. In both these studies, the heat changes in the MLCs arising due to EC effect were measured in a differential scanning calorimeter (DSC). Figure 4 shows an example of such a DSC heat flow measurement taken on a sample comprising eight $BaTiO_3$ MLCs in parallel. A maximum heat change of 0.91 J g^{-1} (corresponding to $\Delta T \sim 1.8$ K) [3] was recorded at 80 °C for $\Delta E \sim 176$ kV cm^{-1}, in MLCs comprising 180 $BaTiO_3$ layers with an average thickness of 1.4 μm. An even larger maximum heat change of 3.5 J g^{-1} (corresponding to $\Delta T \sim 7.1$ K) [5] was recorded at 80 °C for $\Delta E \sim 800$ kV cm^{-1}, in an MLC comprising 63 $BaTiO_3$ layers with an average thickness of 3 μm (Fig. 5 shows the temperature dependence of the endothermal EC heat change in this MLC). Even though the $BaTiO_3$ layers are thicker in the second MLC, they are able to withstand an electric field four times higher than the first MLC, thus resulting in a concomitant increase in EC ΔT. These promising results indicate that improvements in materials parameters, such as breakdown field and transition temperature, could enhance the potential for room-temperature MLC-based EC cooling applications.

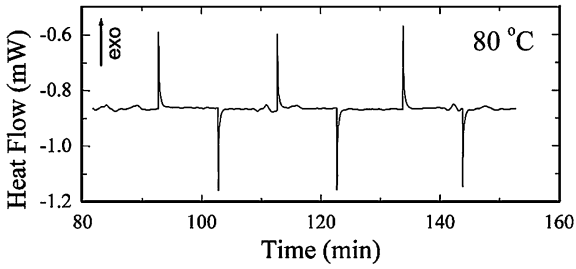

Fig. 4 Differential scanning calorimetry measurements of an MLC comprising 180 layers of undoped $BaTiO_3$ and Ni electrodes, recorded at 80 °C for $\Delta E \sim 176$ kV cm^{-1}. (Adapted from [3])

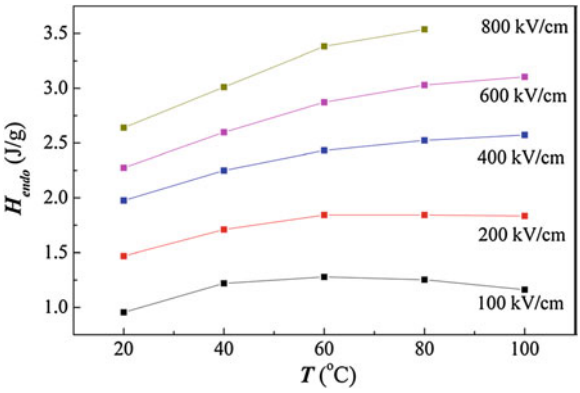

Fig. 5 The temperature dependence of EC endothermal values measured by DSC on an MLC comprising 63 layers of undoped $BaTiO_3$ and Ni electrodes at different applied electric fields. (Adapted from [5])

3 Thermal Modeling of Multilayer Capacitors

3.1 Lumped Thermal Model

Thermal modeling represents a novel type of contribution to the field of electrocalorics providing insight into the physics of EC heat flow, and is critical to the future of the field. While MLCs provide the optimal geometry for EC cooling, integration of MLCs in actual fridges require understanding of EC heat flow in and out of the MLCs and estimation of the cooling powers that they can be expected to deliver. A simple thermal model [15] was developed by Kar-Narayan and Mathur to establish the cooling power that can be achieved from an MLC at the heart of an ideal EC refrigerator. The model was applied to predict the cooling power of the existing commercial doped-$BaTiO_3$ MLC from Ref. [16], for which the EC temperature change was experimentally determined. It was then used to show that better cooling powers could be achieved using more suitable EC materials for which EC data had been previously reported in the literature. It went further to suggest optimisations based on MLC geometry and electrode materials.

The thermal model of the MLC was based on a lumped equivalent thermal circuit, shown in Fig. 6, used to describe the flow of EC heat from the dielectric layers to the two thermally equivalent MLC terminals, via the metal electrodes. Conduction of heat along the electrodes was identified as the primary mode of heat

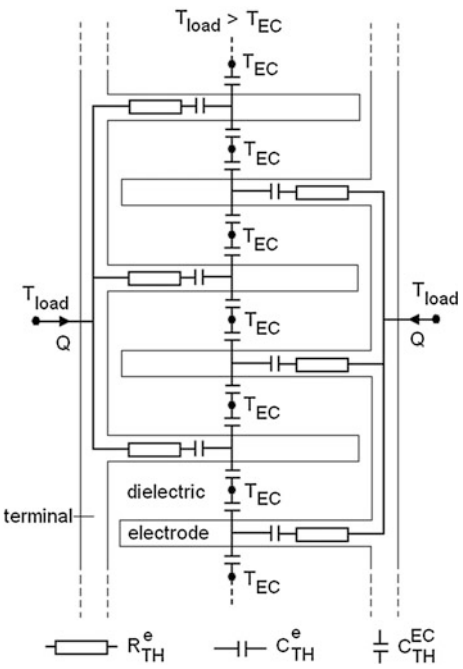

Fig. 6 Lumped equivalent thermal circuit for an MLC. Both terminals provide thermal as well as electrical access. (Adapted from [15])

flow while the conduction of heat from the dielectric layers to the electrodes was neglected as this process is instantaneous in comparison due to the large surface area of contact between the dielectric layers and the electrodes. In other words, the thermal resistance along the length of the electrodes is much larger than the thermal resistance between the dielectric layers and the electrodes, and so the latter was neglected. Each dielectric layer was thus modeled as two thermal capacitances in series (to preserve the symmetry of the model) while each electrode was modeled as a thermal resistance and a thermal capacitance in series. The total thermal capacitance and the total thermal resistance of the MLC were then calculated over the total number of dielectric layers (n) by considering n parallel branches of the thermal circuit.

Each electrode having thermal conductivity κ_e, effective length L, cross-sectional area A_e, volume $v_e = A_e L$, density ρ_e and specific heat capacity c_e was modelled as a thermal resistance $R_{TH}^{e} = \frac{L/2}{\kappa_e A_e}$ in series with a thermal capacitance $C_{TH}^{e} = \rho_e c_e v_e$. Each half of each EC layer, of density ρ_{EC}, specific heat capacity c_{EC} and volume $v_{EC}/2$, was modeled in terms of a thermal capacitance $C_{TH}^{EC} = \rho_{EC} c_{EC} (v_{EC}/2)$ only, given the minimal thermal resistance perpendicular to the layers. End effects were ignored in this model and thus the thermal circuit comprised n parallel branches, each equivalent to a series arrangement of R_{TH}^{e}, C_{TH}^{e} and $2C_{TH}^{EC}$. For n identical branches, the circuit was regarded as a single thermal resistance $R_{total} = R_{TH}^{e}/n$ in series with a single thermal capacitance C_{total} where $n/C_{total} = \left(1/C_{TH}^{e} + 1/2C_{TH}^{EC}\right)$.

This lumped thermal circuit was used to evaluate the instantaneous cooling power Q of an MLC that was initially at the same temperature T_{load} as a heat load connected to both MLC terminals. The removal of an electric field caused cooling in EC layers to T_{EC} at time $t = 0$, causing heat to flow from the load to the EC layers at rate $Q(t) = Q_{max} \exp(-t/R_{total}C_{total})$, where the maximum cooling power $Q_{max} = (T_{load} - T_{EC})/R_{total}$ at $t = 0$. In a refrigerator comprising one or more MLCs, Q_{max} corresponds to the initial cooling power per MLC in the cooling step of a four-step refrigerator cycle comprising: (1) adiabatic EC heating of the MLC(s); (2) rejection of heat from the MLC(s) to a heat sink; (3) adiabatic EC cooling of the MLC(s); and (4) withdrawal of heat from the load to the MLC(s). It was assumed that each of the four steps could occur over e.g. $5R_{total}C_{total}$ if heat transfer were efficient. Therefore during cooling step [4], the average cooling power was evaluated to be $\overline{Q}(t) \sim Q_{max}/5$ and so, taking into account all four steps, the average cooling power per MLC $Q_{av} \approx Q_{max}/20$ at an operating frequency of $(20R_{total}C_{total})^{-1}$.

For the commercially available MLC, the lumped thermal model predicted values of $Q_{max} \sim 4.3$ mW and $R_{total}C_{total} \sim 0.15$ s, such that $Q_{av} \sim 2.15$ mW (shaded circle, Fig. 7a) at an operating frequency of 0.33 Hz. The model was also used to analyse the effect of MLC geometry on EC performance. It was found that Q_{av} may be increased by increasing n to reduce R_{total} without changing the $20R_{total}C_{total}$ period (thin black line, Fig. 7a). Reducing L (which reduces $20R_{total}C_{total}$) or increasing A_e (which leaves $20R_{total}C_{total}$ unchanged) would also

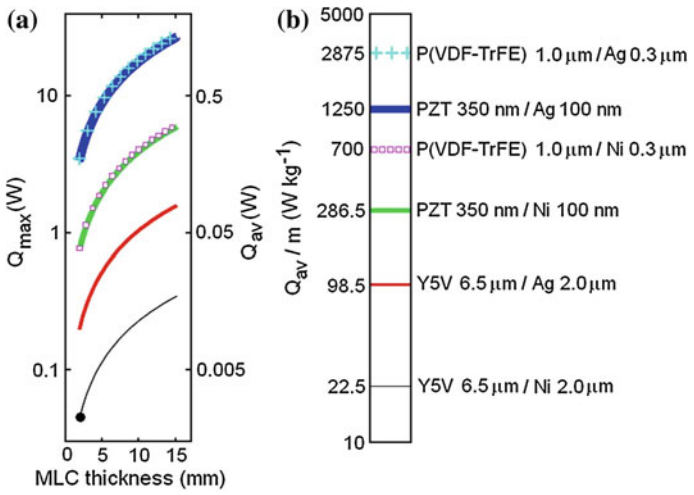

Fig. 7 Lumped thermal modelling of MLCs. **a** Predicted MLC cooling powers for different EC materials, with either Ni or Ag electrodes, as a quasi-continuous linear function of n and therefore MLC thickness. **b** Values of Q_{av} from (**a**), normalised by MLC mass m. (Adapted from [15])

reduce R_{total} and increase Q_{av}. It was identified that the reduction in L represented a materials cost saving, and the concomitant increase in operating frequency $\propto (20R_{total}C_{total})^{-1}$ could be attractive for mains operation, but may pose technical challenges in refrigerator design.

EC performance would be significantly improved by better materials selection. For example, it was shown that replacing the nickel electrodes ($K_{Ni} \sim 94$ W m^{-1} K^{-1}) with silver electrodes ($K_{Ag} \sim 428$ W m^{-1} K^{-1}), to exploit the higher thermal conductivity of silver, would increase Q_{av} by a factor of $\sim$4.5 (red line, Fig. 7a). The cost of silver electrodes could be reduced by alloying, or by using e.g. copper instead as this also has a high thermal conductivity ($K_{Cu} \sim 403$ W m^{-1} K^{-1}), i.e. expensive electrode materials are not required for good EC performance.

The lumped thermal model was also used to predict the average cooling power that could be derived from an EC refrigerator based on giant EC materials. For example, exploiting the 12 K EC temperature changes predicted in either PZT films [26] at 226 °C, or P(VDF-TrFE) films [28] at 80 °C, would further increase Q_{av} for nickel or silver electrodes (Fig. 7a). The best values of Q_{av}, for PZT or P(VDF-TrFE) films with silver electrodes, were normalized by MLC terminal area to yield $\sim$17.9 kW m^{-2}, assuming cooling through both terminals (as demonstrated in [36]).

Figure 7b shows Q_{av} independent of n, normalized with respect to the total mass m of the constituent layers, i.e. MLC mass ignoring minor contributions from terminals and packaging. The resulting quantity Q_{av}/m represents the continuous cooling power per unit MLC mass that could be delivered by one or more MLCs at

the heart of a refrigerator. All values of Q_{av}/m for MLCs based on PZT or P(VDF-TrFE) were shown to exceed the 200 W kg^{-1} for a magnetocaloric refrigerator based on Gd spheres [41], and the largest value of $Q_{av}/m \sim 2875$ W kg^{-1} for P(VDF-TrFE)/Ag still provides a buffer for losses associated with refrigerator design. The study was important as it showed that if an EC refrigerator based on MLCs could only deliver the same cooling power as a magnetocaloric refrigerator, it would not require large magnetic fields or expensive magnetocaloric materials. MLCs may therefore be employed in EC refrigerators, e.g. of the type reported [36] from Moscow in 1992.

3.2 Finite Element Method Thermal Model

The lumped thermal circuit model described in Ref. [15] ignored the thermal impedance of the MLC terminals and the electrically unaddressed sections of EC material at the ends of the layers. A computer simulation using the Finite Element Method (FEM) was developed by Crossley et al. [8] using the free program Calculix, along with a specially written program to create the FEM mesh. The FEM model used a mesh of more than 1,000 brick-shaped elements encompassing all parts of the MLC. The model was perturbed by heating and then cooling the EC layers to simulate the effect of applying and then removing an electric field (Fig. 8a). Simulated outward heat flow followed an exponential decay with time, allowing a thermal time constant τ to be extracted (Fig. 8b). Cooling powers were predicted as $Q_{EC}/[20\tau]$, where Q_{EC} is the total amount of heat removed from the EC layers, and 20τ is the time-scale derived for the lumped thermal circuit model. The program to create the FEM mesh was an automated shell script, so it was straightforward to run the simulation over a large number of model MLCs with different geometries and thus predict the optimal geometry for EC cooling. (The results of the FEM simulations will be submitted for publication in 2013.)

4 Integration into Electrocaloric Fridges

While it is clear from Sect. 3 that MLCs have the potential to deliver high cooling powers, the performance of practical refrigerators based on these MLCs would depend on other factors as well, e.g. the quality of heat switches and the actual cooling cycle that is implemented. There have been a few reports in recent years dealing with these issues and suggesting routes by which MLCs can be integrated in practical EC fridges.

Epstein and Malloy [9] suggested that layers of EC material coupled with thin-film heat switches can work as either refrigerators and heat pumps or electrical generators, depending on the phasing of the applied voltages and heat switching. They argued that reliable and robust thin-film heat switches would have to be

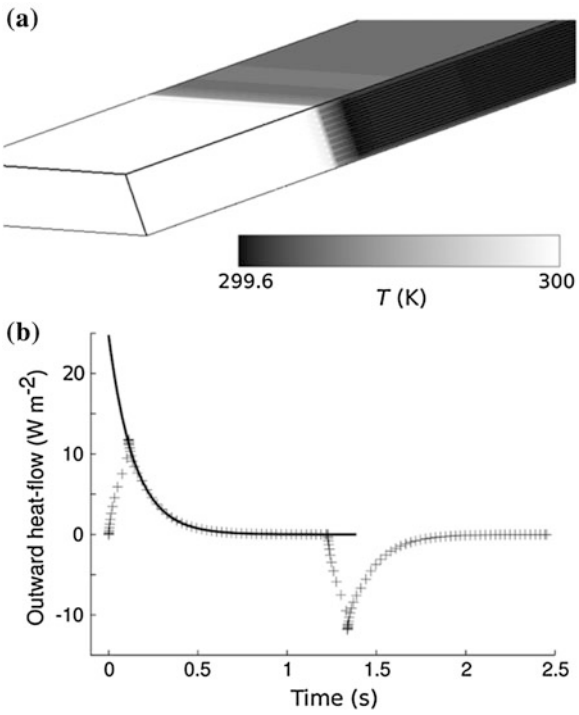

Fig. 8 Thermal modelling of MLCs by finite element method. **a** FEM-predicted temperature field of one end of an MLC shortly after EC heat has been removed from the dielectric layers. **b** FEM-simulated outward heat flow as a function of time (data points) showing fit of exponential decay to extract thermal time constant τ

based on materials whose thermal conductivity can be changed using an electric field, e.g. liquid crystals [18, 30]. It was shown that with heat switches based on thin layers of liquid crystals, the efficiency of EC thin-film devices can be at least as high as that of current thermoelectric devices. Advanced heat switches using carbon nanotubes were also suggested that would enable thin-film refrigerators and generators to outperform conventional vapor-compression devices.

More recently, Jia and Ju [13] reported the implementation and experimental characterization of a continuous EC refrigeration cycle (of the kind described in Sect. 3.1) using switchable liquid-based thermal interfaces to achieve reliable high-contrast thermal switching between an MLC and a heat source/sink. Figure 9 shows the experimental setup where an MLC based on doped $BaTiO_3$ [16] was mechanically actuated up and down using a motorized z-stage to make alternating thermal contacts with a heat source (cooling load) or a heat sink. The application and removal of an electric field was synchronized with the mechanical motion of the MLC between the heat source and sink to achieve a controlled EC cooling cycle. It was ensured that the interdigitated electrodes in the MLC were oriented parallel to the direction of heat transfer to enable efficient heat diffusion in and out of the MLC.

The heat source was a silicon chip with a thin-film heater through which a constant current was passed to induce Joule heating. The heat source was set at an

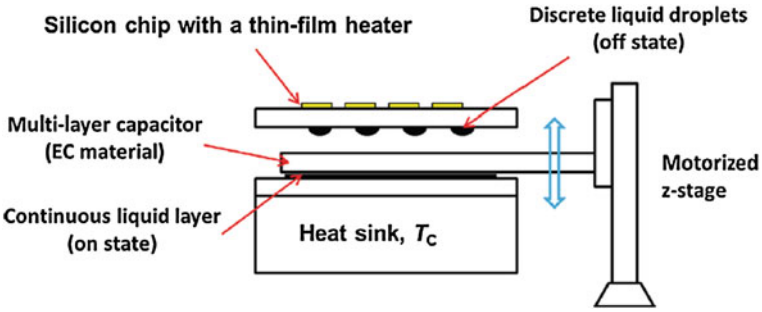

Fig. 9 Experimental setup used to characterize EC cooling cycle based on MLC and liquid-based switchable thermal interfaces. (Adapted from [13])

unperturbed steady state temperature of 27 °C while the heat sink was maintained at ambient temperature of 25.7 °C. The liquid-based switchable thermal interfaces were formed [14] by first coating the backside of the heater chip and the top surface of the heat sink with layers of Teflon®, and then lithographically patterning the Teflon layers to form circular hydrophilic islands of diameter ~ 1 mm. Liquid droplets dispensed onto these islands underwent reversible morphological transformation between the discrete droplet state (thermal contact off) and the continuous thin-film state (thermal contact on). This thermal switching scheme could provide high off-state thermal resistance ($R_{off} > 10^{-2}$ m^2 kW^{-1}) as well as high switching ratio ($R_{off}/R_{on} > 100$).

The EC refrigeration cycle was then implemented by applying an electric field while bringing the MLC in contact with the heat sink to get rid of the excess EC heat and then removing the electric field while bringing the MLC in contact with the heat source thus causing heat to flow into the MLC just as it had undergone EC cooling. The temperature of the heat source was continuously monitored throughout the cycle using a small-diameter (~ 50 μm) K-type thermocouple bead attached to the thin-film heater.

Figure 10a shows the measured transient temperature under different operating conditions. In the first instance, a baseline was set by mechanically actuating the MLC without applying any electric field such that the MLC passively transfers the thermal energy generated by Joule heating in the heater to the heat sink resulting in oscillations in the measured heater temperature. The cycle period was a sum of the residence times on both the heater surface and the heat sink surface (~ 3.5 s in the specific case shown in Fig. 10a) and a finite round-trip mechanical traveling time between the two surfaces (~ 1 s). The electric field was then applied and removed in concert with the mechanical motions to implement the EC cooling cycle. This resulted in a net decrease in the baseline temperature of the heater (see Fig. 10a) due to the increased temperature difference between the heater and the MLC cooled by the EC effect (i.e. during Step 3 of the EC cooling cycle described in Sect. 3.1).

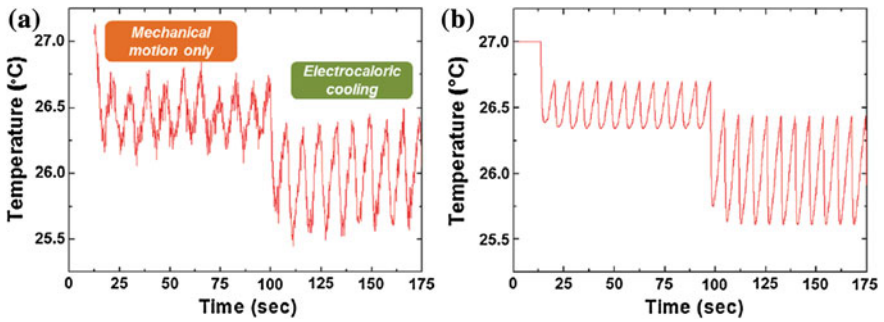

Fig. 10 Continuous cooling of an MLC-based EC fridge. **a** The experimentally measured and **b** numerically simulated temporal temperature profile of the heater under the initial steady state, under the mechanical oscillation only and under EC cooling conditions. The cycle frequency was fixed at 0.12 Hz. (Adapted from [13])

Figure 10b shows the results of a transient one-dimensional heat transfer model that was used to validate the experimental results. The thin-film heater was modeled using the finite volume method as a lumped thermal mass with a uniform heat source and transient heat diffusion across the MLC and the liquid thermal interfaces, whose thicknesses were measured directly from optical images. The EC heating and cooling effects were modeled using the quasi-adiabatic temperature changes directly measured from a nominally identical MLC. The measured transient heater temperature profiles were found to be in good agreement with the prediction from the transient heat transfer simulations (Fig. 10a, b). The overall performance of the EC cooling cycles was found to be limited as the doped-$BaTiO_3$ MLC used was not optimized for good EC performance [15]. Nevertheless this study marked an important step towards the realization of practical EC fridges based on MLCs.

Bai et al. [4] showed that a kinetic EC effect provides a solution for the design of practical EC refrigerators without the need for heat switches. They argued that a feasible method of refrigeration could be achieved using MLCs by controlling the driving electric field rate. Giant net cooling (0.37 J/g) in an electric field cycle was shown to have been achieved from DSC experiments on MLCs comprising 180 layers of $BaTiO_3$ (1.4 μm thick) and Ni electrodes, and subjected to $\Delta E \sim 176$ kV cm^{-1} with controlled driving electric field rates. The rising field rate varied from 1.4 to 176 kV cm^{-1} s^{-1}, and the falling field rate was kept constant at 176 kV cm^{-1} s^{-1}. Under these conditions, DSC measurements were taken at 40 and 80 °C as shown in Fig. 11a , b respectively. The exothermal peaks (i.e. upward peaks) correspond to EC heating while the endothermal peaks (i.e. downward peaks) correspond to EC cooling. Integrating the endothermal peak revealed an EC heat change of 0.70 J g^{-1} at 40 °C and 0.89 J g^{-1} at 80 °C under a falling field rate of 176 kV cm^{-1} s^{-1}, corresponding to an EC temperature change of 1.3 and 1.8 K respectively. It can be seen from Fig. 11a, b that while the exothermal peaks decreased as the rising field rate was reduced, the endothermal

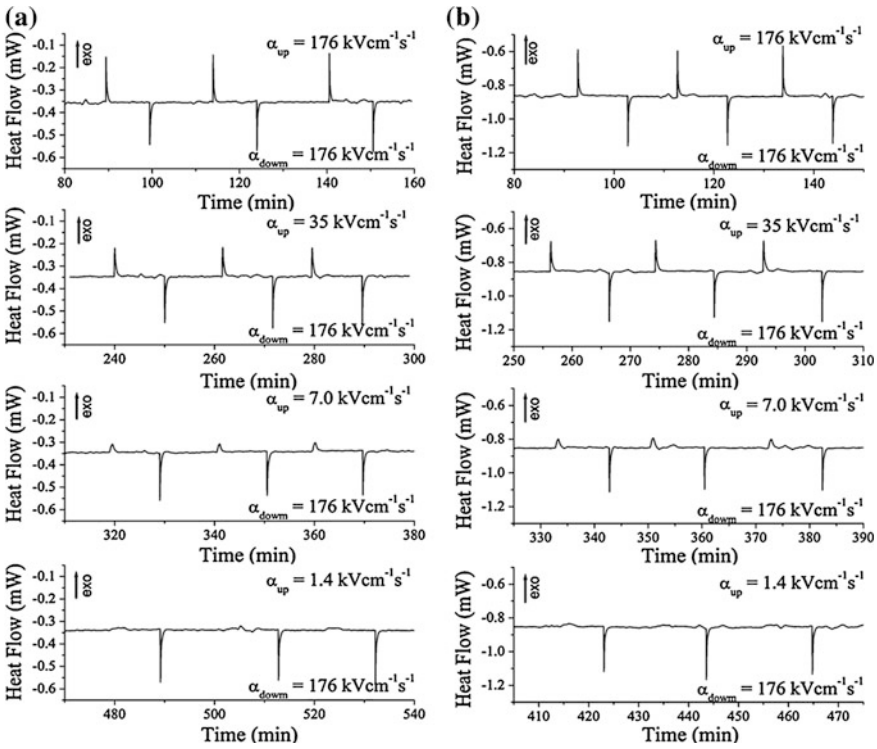

Fig. 11 Kinetic EC effect. DSC measurements of EC heat flow into and out of an MLC comprising layers of $BaTiO_3$ and Ni electrodes for varying rising field rates and a fixed falling field rate at **a** 40 °C and **b** 80 °C. (Adapted from [4])

peaks remained constant under the fixed falling field rate. This study therefore showed that an EC cooling cycle depends not just on static parameters, such as electric field and temperature, but also on kinetic processes, such as the rising and falling rates of electric field. Net cooling in a single EC cycle was thus realized by controlling only the driving field rate.

5 Conclusions

It has been established that the MLC geometry is attractive for EC cooling applications as it provides a macroscopic assembly of thin films to which the interdigitated metallic electrodes provide electrical and thermal access, allowing the MLC to pump significant heat like a bulk EC material while possessing a high breakdown field like a thin film. EC performance of existing MLCs can be dramatically improved, via materials selection and geometric modification.

The performance of a refrigerator based on MLCs can be analyzed using appropriate thermal models. Such models also serve to optimize important parameters such as cooling powers and operating frequencies. The eventual implementation of MLCs in practical refrigerators would also crucially depend on the actual fridge design, including heat switches and electric field cycles. While there has been considerable effort in recent times in bringing MLCs to the forefront of EC cooling technology, there still remain several challenges in terms of fabrication of MLCs based on giant EC materials and the integration of these in practical cooling devices.

References

1. Akcay, G., Alpay, S.P., Mantese, J.V., Rossetti, G.A.: Appl. Phys. Lett. **90**, 252909 (2007)
2. AVX Corporation Datasheet http://www.avx.com/docs/Catalogs/cy5v.pdf
3. Bai, Y., Zheng, G.-P., Shi, S.-Q.: Appl. Phys. Lett. **96**, 192902 (2010)
4. Bai, Y., Zheng, G.-P., Shi, S.-Q.: J. Appl. Phys. **108**, 104102 (2010)
5. Bai, Y., Zheng, G.-P., Ding, K., Qiao, L., Shi, S., Guo, D.: J. Appl. Phys. **110**, 094103 (2011)
6. Chen, H., Ren, T.-L., Wu, X.-M., Yang, Y. & Liu, L.-T.: Appl. Phys. Lett. **94** (2009)
7. Correia, T., Young, J.S., Whatmore, R.W., Scott, J.F., Mathur, N.D., Zhang, Q.: Appl. Phys. Lett. **95**, 182904 (2009)
8. Crossley, S., McGinnigle, J.R., Kar-Narayan, S., Mathur, N.D.: Finite element optimisation of electrocaloric multilayer capacitors for heat pumps. Transcript Prep. (2013)
9. Epstein, R.I., Malloy, K.J.: J. Appl. Phys. **106**, 064509 (2009)
10. Feng, Z., Shi, D., Doue, S.: Solid State Commun. **151**, 123 (2011)
11. Hegenbarth, E.: Cryogenics **1**, 242 (1961)
12. Israel, C., Mathur N.D., Scott, J.F. Nature Mater. **7**, 93 (2008)
13. Jia, Y., Ju, Y.S.: Appl. Phys. Lett. **100**, 242901 (2012)
14. Jia, Y., Cha, G., Ju, Y.S.: Micromachines **3**, 10 (2012)
15. Kar-Narayan, S., Mathur, N.D.: Appl. Phys. Lett. **95**, 242903 (2009)
16. Kar-Narayan, S., Mathur, N.D.: J. Phys. D Appl. Phys. **43**, 032002 (2010)
17. Kar-Narayan, S., Crossley, S., Moya, X., Kovacova, V., Abergel, J., Bontempi, A., Baier, N., Defay, E., Mathur, N.D.: Appl. Phys. Lett. **102**, 3 (2013)
18. Kato, T., Nagahara, T., Agari, Y., Ochi, M., J.: Polym. Sci. Part B, Polym. Phys. **43**, 3591 (2005)
19. Lawless, W.N.: Phys. Rev. B **16** (1977)
20. Lawless, W.N., Clark, C.F.: Phys. Rev. B **36**, 459 (1987)
21. Li, X., Qian, X-S., Gu, H., Chen, X., Lu, S. G., Lin, M., Bateman, F., Zhang, Q. M.: Appl. Phys. Lett. **101**, 132903 (2012)
22. Liu, P.F., Wang, J.L., Meng, X.J., Yang, J., Dkhil, B., New, J.: Physics **12**, 023035 (2010)
23. Lu, S.G., Zhang, Q.M.: Adv. Mater. **21**, 1983 (2009)
24. Lu, S.G., Rožič, B., Zhang, Q.M., Kutnjak, Z., Pirc, R., Lin, M., Li, X., Gorny, L.: Appl. Phys. Lett. **97**, 202901 (2010)
25. Lu, S.G., Rožič, B., Zhang, Q.M., Kutnjak, Z., Neese, B.: Appl. Phys. Lett. **98**, 122906 (2011)
26. Mischenko, A.S., Zhang, Q., Scott, J.F., Whatmore, R.W., Mathur, N.D.: Science **311**, 1270 (2006)
27. Mischenko, A.S., Zhang, Q., Whatmore, R.W., Scott, J.F., Mathur, N.D.: Appl. Phys. Lett. **89**, 242912 (2006)
28. Neese, B., Chu, B., Lu, S.-G., Wang, Y., Furman, E., Zhang, Q.M.: Science **321**, 821 (2008)

29. Olsen, R.B., Butler, W.F., Payne, D.A., Tuttle, B.A., Held, P.C.: Phys. Rev. Lett. **45**, 1436 (1980)
30. Rondelez, F., Urbach, W., Hervet, H.: Phys. Rev. Lett. **41**, 1058 (1978)
31. Saranya, D., Chaudhuri, A.R., Parui, J., Krupanidhi, S.B.: Bull. Mater. Sci. **32**, 259 (2009)
32. Scott, J.F.: Annual. Rev. Mater. Res. **41**, 229 (2011)
33. Scott, J.F., Morrison, F.D.: Ferroelectrics **371**, 3 (2008)
34. Shebanovs, L., Borman, K., Lawless, W.N., Kalvane, A.: Ferroelectrics **273**, 137 (2002)
35. Shebanovs, L., Borman, K., Lawless, W.N., Kalvane, A.: Ferroelectrics **273**, 137 (2002)
36. Sinyavsky, Y.V., Brodyansky, V.M.: Ferroelectrics **131**, 321 (1992)
37. Thacher, P.D.: J. Appl. Phys. **39**, 1996 (1968)
38. Tuttle, B.A., Payne, D.A.: Ferroelectrics **37**, 603 (1981)
39. Valant, M.: Prog. Mater Sci. **57**, 980 (2012)
40. Wiseman, G.G., Kuebler, J.K.: Phys. Rev. **131**, 2023 (1963)
41. Zimm, C., Jastrab, A., Sternberg, A., Pecharsky, V., Gschneidner, K., Osborne, M., Anderson, I.: Adv. Cryo. Eng. **43**, 1759 (1998)

Electrocaloric Polymers

Xinyu Li, Sheng-Guo Lu, Xiaoshi Qian, Minren Lin and Q. M. Zhang

1 Introduction

When an electric field is applied to a dielectric material, it will induce a change in the material's polarization. The consequent changes in the entropy and/or temperature of the material are referred to as the electrocaloric effect (ECE). The ECE may provide an efficient means to realize solid-state cooling devices for a broad range of applications such as on chip cooling and temperature regulation for sensors and electronic devices, provided that materials with large ECE can be developed [7, 13, 15]. Refrigeration based on the ECE approach is more environmentally friendly and hence may also provide an alternative to the existing vapor-compression approach.

The basic principle of electrocaloric effect is the entropy change associated with the change of polarization ordering in a dielectric material, induced by an external electric field (see schematic illustration Fig. 1). When changing from a non-polar phase to a polar phase or vice versa, there will be an accompanying entropy change. Application of an electric field to the material causes partial alignment of dipoles and consequently a reduction of entropy of the dipolar system. In an isothermal condition, the dipolar material ejects heat $Q = T\Delta S$ to the surrounding, where T is the temperature and ΔS is the isothermal entropy change. Or in an adiabatic process, to keep the total entropy of the material constant, the temperature of the dielectric is increased by ΔT, the adiabatic temperature change which is related to the $Q = c\Delta T$ where c is specific heat capacity of the dielectric. In a reverse process, as the applied electric field is reduced to zero and the dipoles return to the less ordered state (or disordered state), an increase in the entropy of dipolar system occurs and under an isothermal condition, the dielectric will absorb heat Q from the surrounding.

X. Li · S.-G. Lu · X. Qian · M. Lin · Q. M. Zhang (✉)
Department of Electric Engineering and Materials Research Institute,
Pennsylvania State University, University Park, PA 16802, USA
e-mail: qxz1@psu.edu

T. Correia and Q. Zhang (eds.), *Electrocaloric Materials*,
Engineering Materials 34, DOI: 10.1007/978-3-642-40264-7_5,

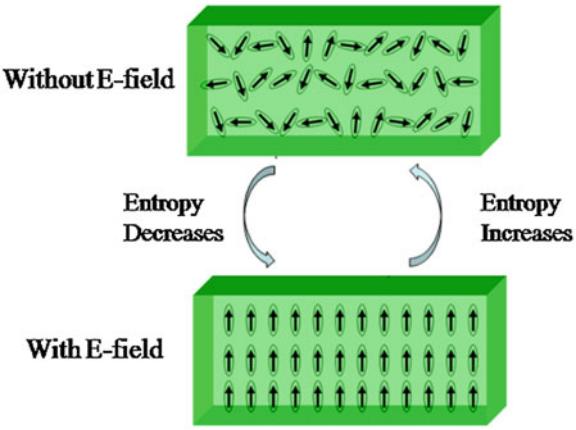

Fig. 1 Schematic illustration of the molecular mechanism of ECE in dielectric materials. When $E = 0$, the dipoles orient randomly, having higher dipolar entropy. When $E > 0$, the dipoles orient along the electric field direction, lowering the dipolar entropy

To realize large electrocaloric effect, it is necessary that there is a large entropy change associated with the polarization change in the material. Moreover, the dielectric material should be able to support large polarization change and these polarization changes can be induced effectively by external field. The latter considerations indicate that it is advantageous to use ferroelectric materials for the ECE and operate the materials at temperatures just above a ferroelectric (polarization ordered)-paraelectric (polarization disordered) phase transition (FE-PE) where the largest electric field induced polarization change in a material can be achieved.

As will be shown in this Chapter, among various ferroelectric materials, poly(vinylidene fluoride/trifluoroethylene) [*P*(*VDF-TrFE*)] ferroelectric polymers are promising for realizing large EC responses. Moreover, compared with ferroelectric ceramics, the light weight and fracture tolerance of polymers make them very attractive for practical cooling devices. P(*VDF-TrFE*) copolymers is the best known ferroelectric polymers. Presented in Fig. 2 is the phase diagram of this copolymer. At room temperature, the copolymer is in a ferroelectric phase (dipole

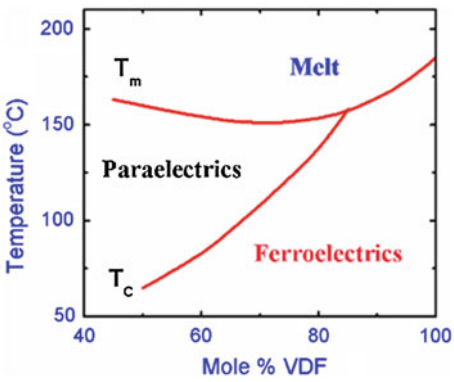

Fig. 2 The phase diagram of *P(VDF-TrFE)* copolymer [8]

ordered phase) and for compositions with about more than 20 mol % of *TrFE*, there is a FE-PE phase transition below the melting and FE-PE transition temperature becomes lower with increased *TrFE* content until about 60 °C (at 50/50 mol %). The monomer unit of *VDF* possesses a dipole moment of 2.1 Debye while for *TrFE*, the dipole moment is reduced by half ($\sim$1.05 Debye). Therefore, the dipole moment per unit cell reduces as *TrFE* content increases. For copolymers at compositions with *VDF/TrFE* ratio higher than 60/40 mol %, the transition is first order. At compositions below 60/40 mol %, the FE-PE transition is continuous.

In an ideal refrigeration cycle the working material (refrigerant) must absorb entropy (or heat) from the cooling load while in thermal contact with the load (isothermal entropy change ΔS). The material is then isolated from the load while the temperature is increased due to the application of external field (adiabatic temperature change ΔT). The material is then in thermal contact with the heat sink and entropy that was absorbed from the cooling load is ejected to the heat sink. The working material is then isolated from the heat sink and the temperature is reduced back as the field is reduced. The temperature of the refrigerant will be the same as the temperature of the cooling load when they are contacted. The whole process is repeated to further reduce the temperature of the load. Therefore, both the isothermal entropy changes ΔS and the adiabatic temperature change ΔT are the key parameters for the ECE of a dielectric material for refrigeration [5, 13, 22]

2 Thermodynamic Considerations on Materials with Large ECE

2.1 Maxwell Relations

Based on the consideration using the Maxwell relation, which links the electrocaloric effect to the pyroelectric effect for a thermodynamically reversible system, the following equations can be derived [7],

$$\Delta S = \int_{E_1}^{E_2} \left(\frac{\partial D}{\partial T}\right)_E dE \tag{1}$$

$$\Delta T = -\frac{T}{\rho}\int_{E_1}^{E_2} \frac{1}{c_E}\left(\frac{\partial D}{\partial T}\right)_E dE \tag{2}$$

Equations 1 and 2 indicate that in order to achieve large ΔS and ΔT, the dielectric materials should possess a large pyroelectric coefficient over a relatively broad electric field and temperature range. For ferroelectric materials, a large

pyroelectric effect exists near the ferroelectric (FE)—paraelectric (PE) phase transition temperature and this large effect may be shifted to temperatures above the transition temperature when an external electric field is applied. It is also noted that a large ΔT may be achieved even if ΔS is small when the c_E of a dielectric material is small. However, as has been pointed out in the Introduction, for practical refrigeration applications both large ΔS and ΔT are required.

It is noted that in the temperature region including a first-order FE-PE transition, Eq. (3) should be modified to take into account of the discontinuous change of the polarization ΔD at the transition [11], i.e.,

$$\Delta S = \int_0^E \left(\frac{dD}{dT}\right)_E dE - \Delta D\left(\frac{\partial E}{\partial T}\right) \tag{3}$$

Although a few studies on the ECE were conducted in which direct measurement of ΔT was made [21], most experimental studies were based on the Maxwell relations where the electric displacement D versus temperature T under different electric fields was characterized. ΔS and ΔT were deduced from [7], Eq. (1) and (2) (see above for details). For dielectric materials with low hysteresis loss and the measurement is in an ideal situation, results obtained from the two methods should be consistent with each other. However, as will be shown later that for the relaxor ferroelectric polymers, the ECE deduced from the Maxwell relations can be very different from that measured directly and hence the Maxwell relations cannot be used for these materials in deducing ECE. In general, the Maxwell relations are valid only for thermodynamically equilibrium and ergodic systems.

2.2 Phenomenological Theory of ECE

Phenomenological theory has been widely utilized to illustrate the macroscopic phenomena that occur in the polar materials, e.g. ferroelectric or ferromagnetic materials near their phase transition temperatures. In principle the ECE is one of the characteristics of ferroelectric materials that are associated with the phase transition in terms of the order–disorder transition derived entropy change. Therefore, phenomenological theory can be used to estimate the ECE of ferroelectrics. The general form of the Gibbs free energy in terms of the electric displacement can be expressed as [7]

$$G = \frac{1}{2}\alpha D^2 + \frac{1}{4}\xi D^4 + \frac{1}{6}\zeta D^6 \tag{4}$$

where $\alpha = \beta(T - T_0)$, and β, ξ and ζ are temperature-independent phenomenological coefficients. Since $\left(\frac{\partial G}{\partial T}\right)_D = -\Delta S$, one can obtain,

$$\Delta S = -\frac{1}{2}\beta D^2 \tag{5}$$

Then the adiabatic temperature change ΔT ($= -T\Delta S/c_E$) can be obtained, i.e.

$$\Delta T = \frac{1}{2c_E}\beta T D^2 \tag{6}$$

Based on Eqs. 5 and 6, the entropy will be reduced when the material changes to a polar state from a non-polar state when an external action, e.g. temperature, electric field or stress, is applied. The entropy change and temperature change are associated with the phenomenological coefficient β and electric displacement D, viz. proportional to β and D^2. Both parameters will affect the ECE values of the materials. A material with large β and large D will generate large ECE entropy change and temperature change near the FE—PE phase transition temperature. In searching for electrocaloric materials to achieve giant ECE at ambient temperature, one critical question is how to design dielectric materials to significantly enhance the entropy in the polar-disordered state since ECE is directly related to the entropy difference between the polar-disordered and ordered states in a dielectric material. In other words, to design a ferroelectric material to increase β while maintaining large D in Eqs. 5 and 6.

For ferroelectric *P*(*VDF-TrFE*) polymers, phenomenological theory predicts large ECE values. For example, *P*(*VDF-TrFE*) 65/35 mol % copolymer, with $\beta = 3.5 \times 10^{-7}$ Jm/(C^2K^1) and $D = 0.08$ C/m^2 [3], will exhibit a $\Delta S = 62$ J/(kgK). Making use of its specific heat capacity $c_E = 1.4 \times 10^3$ J/(kgK) [2] and Curie temperature $T_c = 102$ °C [3], yields $\Delta T = 16.6$ °C. The large ΔS and ΔT values suggest that a large ECE may be achieved in ferroelectric *P*(*VDF-sTrFE*) copolymers. Furthermore, relaxor ferroelectric polymers based on *P*(*VDF-TrFE*) such as *P*(*VDF-TrFE-CFE*) (*CFE*-chlorofluoroethylene) relaxor ferroelectric terpolymers also have potential to reach a large ECE because the β and D are still large.

In addition, the latent heat of FE-PE phase transition can also be used to assess the ECE ($Q = T\Delta S$) in a ferroelectric material at temperatures above the FE-PE transition. For instance, *P*(*VDF-TrFE*) 68/32 mol % copolymer shows a heat of FE-PE transition of more than 2.1×10^4 J/kg (or $\Delta S \sim 56.0$ J/(kgK)) [15]. This is approximately 10 times larger than its inorganic counterparts. Large ECE, i.e., both large ΔS and ΔT can be induced in the ferroelectric poly(vinylidene fluoride-trifluoroethylene) (*P*(*VDF-TrFE*) copolymers. As shown in Fig. 3, for (*P*(*VDF-TrFE*) 65/35 mol % copolymer, the heat of FE-PE transition is more than 16 J/g (or $\Delta S \sim 45$ J/(kgK)), which is even larger than the recently reported "giant" magnetocaloric effect. All these considerations and results suggest that ferroelectric *P*(*VDF-TrFE*) polymers have potential to realize giant ECE.

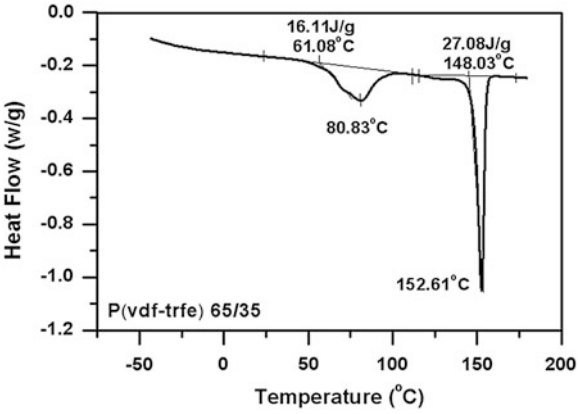

Fig. 3 The large heat of FE-PE transition (16 J/g) for *P*(*VDF-TrFE*) 65/35 mol % copolymer, which is even comparable to the heat of melting (27 J/g)

2.3 Thermodynamic and Statistic Considerations of ECE in Polar-Dielectrics

In polar-dielectrics, as the electric field is increased from 0 to E, the isothermal entropy change ΔS and adiabatic temperature change ΔT can be expressed as,

$$\Delta S = S_{dip}(E,T) - S_{dip}(0,T) \text{ and } \Delta T = TS/c_E \tag{7}$$

where c_E is the specific heat and $S(E, T)$ is the total entropy at a temperature T and electric field E. Since the lattice entropy is field independent, ΔS is determined by the dipolar entropy S_{dip}. In order to maximize ΔS, it is necessary to maximize the entropy $S_{dip}(0, T)$ at $E = 0$ and minimize $S_{dip}(E, T)$, occurring under a field E sufficiently large to induce polarization saturation. As shown in a recent thermodynamic and statistical analysis, for a system of N dipolar entities, each having Ω discrete equilibrium orientations, the maximum entropy corresponds to the case where all directions i are equally populated or $N_i = N/\Omega$, where N_i is the number of dipoles along symmetry direction i with the condition $\sum_i N_i = N$,

$$\Delta S = \frac{ln\Omega}{3\varepsilon_0 \Theta} P^2 \tag{8}$$

where Θ is the Curie constant in the asymptotic behavior of the linear dielectric susceptibility, $\varepsilon_0/(T-T_0)$, and T_0 the Curie–Weiss temperature for a ferroelectric, ε_0 is the vacuum permittivity. In Eq. (5) it was assumed that $S_{dip}(E, T) = 0$, corresponding to the minimum of entropy occurring when all dipoles are aligned along the field E. For normal ferroelectric materials such as a tetragonal ferroelectric phase, $\Omega = 6$ due to 6 possible polarization directions (see schematic in Fig. 4). Therefore, a dipole system with a larger number of dipole entities Ω and small dipole correlation (small Θ) will have the potential to realize very large ECE. This is analogous to that of the magnetocaloric effect where a larger number

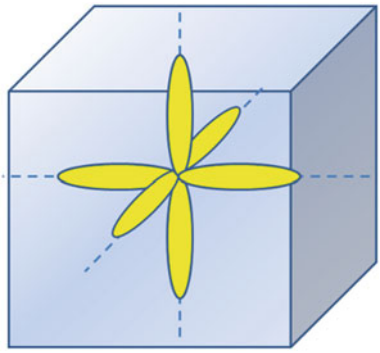

Fig. 4 Schematic of 6 possible polarization directions in a tetragonal ferroelectric phase when transformed from a cubic phase

of angular momentum states lead to higher magnetic entropy in the disordered state [18].

Relaxor ferroelectrics in which the long-range polarization correlation is disrupted by random defects field, leading to polar-glass states which can be switched to polar-state with high polarization (large P in Eq. 8),may provide dipolar systems to realize high ECE. The defect fields also break up the global symmetry of lattice, causing large number of disordered fluctuating polarization entities (local polar-states) and nano-polar-regions, which may lead to larger number of Ω and provide a scenario for achieving giant ECE, compared with normal ferroelectrics. The experimental results obtained from the normal ferroelectric and from defects modified ferroelectric (relaxors) seem to be consistent with this hypothesis (see Table 1, which summarizes recent experimental results on ferroelectrics).

3 Experiment Results

3.1 ECE Measurement Methods

ECE in dielectric materials can be deduced from the Maxwell relations, i.e., Eqs. 1 and 2, which is referred as to the indirect method in characterizing ECE, since the ECE is not directly measured. This indirect method was employed to characterize ECE in ferroeletctric P(VDF-TrFE) polymers and the results will be summarized here and compared with the directly measured ECE results. In the study of ECE in ferroelectric polymers, two different methods were also used/developed to directly characterize ECE. A calorimeter developed by Rozic et al. (2010) [19] was employed in the initial study of ECE in P(VDF-TrFE) polymer films. A specially designed calorimeter was also developed at The Pennsylvania State University to directly measure ECE in polymer films (see Fig. 5). In the calorimeter developed at Penn State, the heat generated by ECE of the sample is compared with the heat generated by a standard reference resistor R, from which ΔS is determined. When a

Table 1 Comparison of ECE in polymers and ceramics, ceramic thin films and with MCE materials

Materials	Operat. Temp. (°C)[i]	Applied field[ii]	ΔS (J/kgK)	ΔT (K)	ΔSΔT
Irradiated P(VDF-TrFE)[a]	33	160	95	20	1900
P(VDF-TrFE-CFE) Terpolymer[b]	30	150	80	15.7	1256
Normal ferroeletricP(VDF-TrFE)[c]	80	200	60.8	12.6	768
PLZT 8/65/35 thin film[d]	45	120	50	40	2000
$PbZr_{0.95}Ti_{0.05}O_3$ thin films[e]	226	48	7.9	12	95
0.65PMN-0.35PT thin film[f]	140	75	33.4	31	1036
PMN-PT bulk[g]	23	1.5	1.0	1	1
$Gd_5(Si_2Ge_2)$[h]	-3	10	23.9	21	502

[i] T is the temperature where ECE maximum was observed. [ii] For ECE, the unit for electric field is MV/m. For MCE, the unit of magnetic field is Tesla (T)

[a] Reference: [10]

[b] Reference: [6]

[c] Reference: [15]

[d] Reference: [10]

[e] Reference: [14]

[f] Reference: [1]

[g] Reference: [8]

[h] Reference: [4]

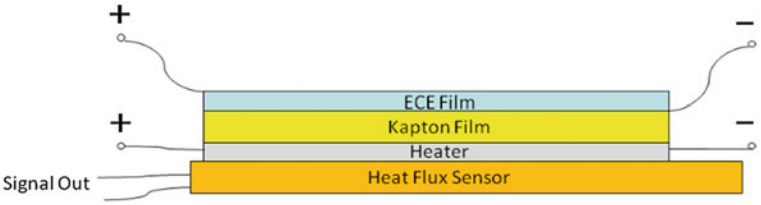

Fig. 5 Schematic of polymer ECE measurement setup

voltage, V, with a pulse time duration, t, is applied to the resistor heater, it would produce a joule heat $Q_h = (V^2/R)t$. The heat generated is detected by a heat flux sensor directly attached to the sample surface. Now, if the ECE film under an applied electric field also generates the same amount of heat as detected by the same flux sensor, then the heat Q_{ECE} from the ECE material is equal to Q_h. From $Q_h = Q_{ECE} = T\Delta S$, ΔS, the isothermal entropy change can be obtained. If the ECE material has a heat capacity of c_E, a density ρ, and a volume of U, then the adiabatic temperature change can be obtained, $\Delta T_{ECE} = Q_{ECE}/(c_E\ \rho\ U)$. ECE as function of both temperature and applied electric field E were characterized. Presented in Fig. 6 are typical ECE signals from a terpolymer film measured by the heat flux sensor in which both heat generation and absorption, corresponding to the field increase and decrease, were recorded [10, 12, 19, 20].

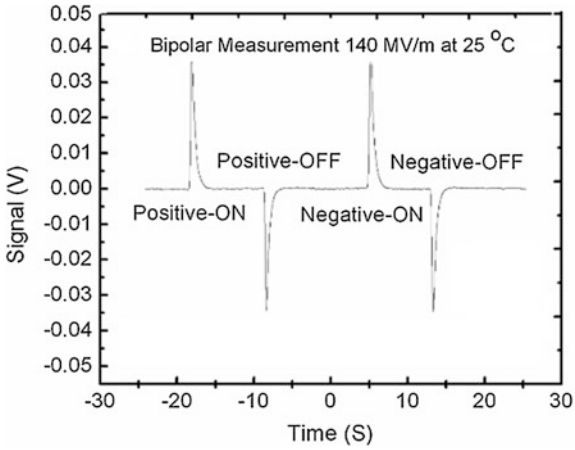

Fig. 6 ECE signal, recorded from a terpolymer film at both field on (heat) and field off (cooling) cycles and using measurement set-up in Fig. 7

3.2 ECE in Normal Ferroelectric P(VDF-TrFE)

As indicated in Sect. 2, the ferroelectric copolymer may produce large ECE near its phase transition temperature. *P*(*VDF-TrFE*) 55/45 mol % was chosen because its FE-PE phase transition is of second-order (continuous), thus avoiding the thermal hysteresis effect associated with the first-order phase transition. In addition, among all available *P*(*VDF-TrFE*) copolymers, this composition exhibits the lowest FE- PE phase transition temperature (∼70 °C), which is favorable for refrigeration near room temperature (see Fig. 2 for the phase diagram).

Polymer films used for the indirect ECE measurement were prepared using a spin-casting method on metalized glass substrates. The film thickness for this study was in the range of 0.4–1 μm. The free-standing films for the direct ECE measurement were fabricated using a solution cast method and the film thickness is in the range of 4–6 μm. Figure 7a shows the permittivity as a function of temperature for *P*(*VDF-TrFE*) 55/45 mol % copolymers measured at 1 kHz. It can be seen that the thermal hysteresis between the heating and cooling runs is pretty small (∼1 °C). The remanent polarization as a function of temperature shown in Fig. 7b further indicates a second-order phase transition occurred in the material. The FE-PE phase transition temperature is about 70 °C. At temperature higher than 100 °C, the loss tangent rises sharply, which is associated with the thermally activated conduction.

Figure 8a presents the electric displacement *D* versus electric field *E* hysteresis loops measured at various temperatures. At temperatures below the transition temperature, the polymer film is in a ferroelectric state, the normal hysteresis loop is observed, while at higher temperatures, the loop becomes slimed, remanent polarization diminishes, and saturation polarization still exists. Hence the electric displacement as a function of electric field at different temperatures can be procured, which is presented in Fig. 8b [13].

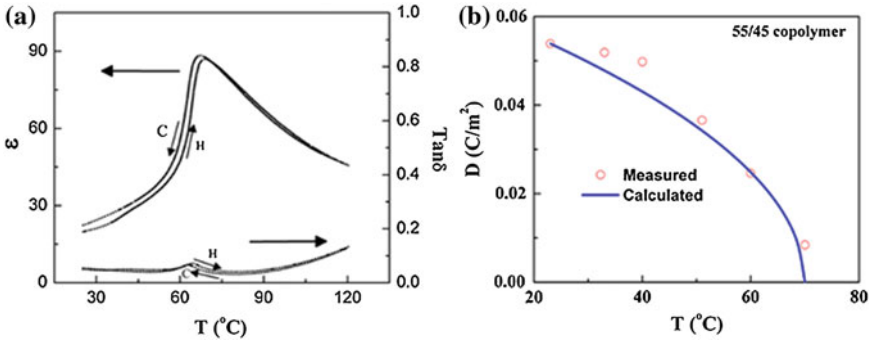

Fig. 7 **a** Permittivity as a function of temperature and **b** Remanent polarization as a function of temperature for *P*(*VDf-TrFE*) 55/45 mol % copolymers. The solid curve is calculated results based on phenomenological theory

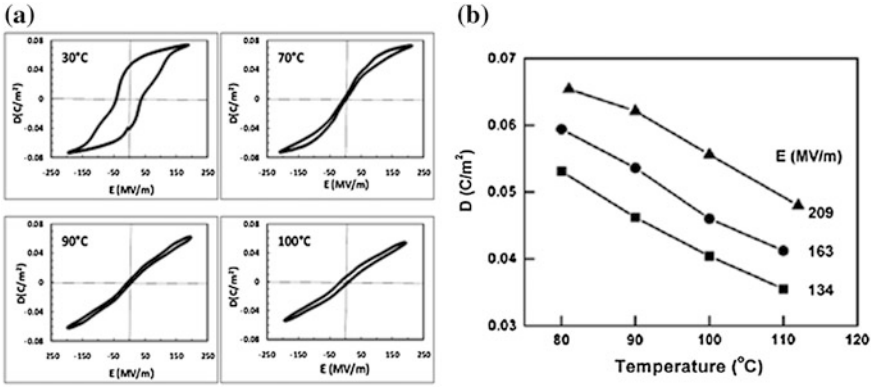

Fig. 8 **a** Electric displacement *D*– electric field *E* hysteresis loops at temperature below and above the phase transition and **b** Electric displacement as a function of temperature at different electric fields for *P*(*VDF-TrFE*) 55/45 mol % copolymers [15, 13]

One can see that the electric displacement monotonically decreases with temperature above the phase transition. The Maxwell relations were used to calculate the isothermal entropy change and adiabatic temperature change as a function of ambient temperature. The results deduced are presented in Fig. 9.

Presented in Fig. 10 is the directly measured ΔS and ΔT as a function of temperature measured under several electric fields for the unstretched *P*(*VDF-TrFE*) 55/45 mol % copolymer [9]. As can be seen, the ECE effect reaches maximum at the temperature of FE-PE transition, where a $\Delta T = 12$ °C can be induced under a 120 MV/m electric field. A comparison between the directly measured and deduced ECE is also presented in Fig. 10, the result indicates that within the experimental error, the ECE deduced from the Maxwell relation is consistent with that directly measured. Therefore, for a ferroelectric material at

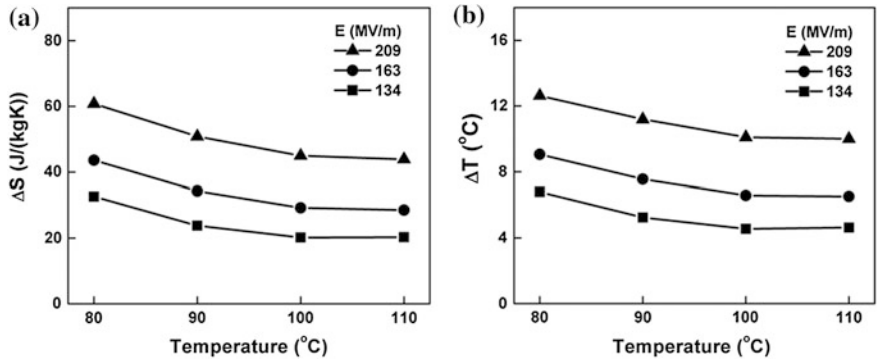

Fig. 9 **a** Isothermal entropy change ΔS and **b** adiabatic temperature change ΔT, measured by indirect method, as a function of ambient temperature at different electric fields for *P*(*VDF-TrFE*) 55/45 copolymer Neese et al. [15]

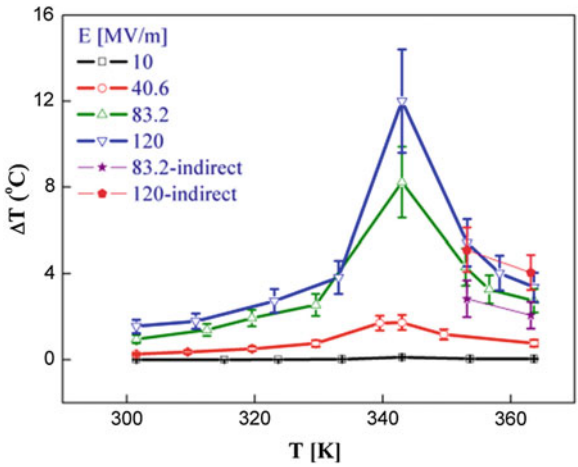

Fig. 10 Directly measured ΔT as a function of temperature under several electric fields for unstretched *P*(*VDF-TrFE*) 55/45 mol % copolymers and comparison with that indirectly measured

temperatures above FE-PE transition, Maxwell relation Eqs. (1) and (2) can be used to deduce ECE.

3.3 ECE in Relaxor Polymers

3.3.1 ECE in Relaxor Ferroelectric *P*(*VDF-TrFE-CFE*) Terpolymers

ECE in the relaxor ferroelectric *P*(*VDF-TrFE-CFE*) terpolymers have been studied. Presented in Fig. 11a is the dielectric constant data for the *P*(*VDF-TrFE-CFE*) 59.2/33.6/7.2 mol % terpolymer, which shows typical relaxor dielectric behavior,

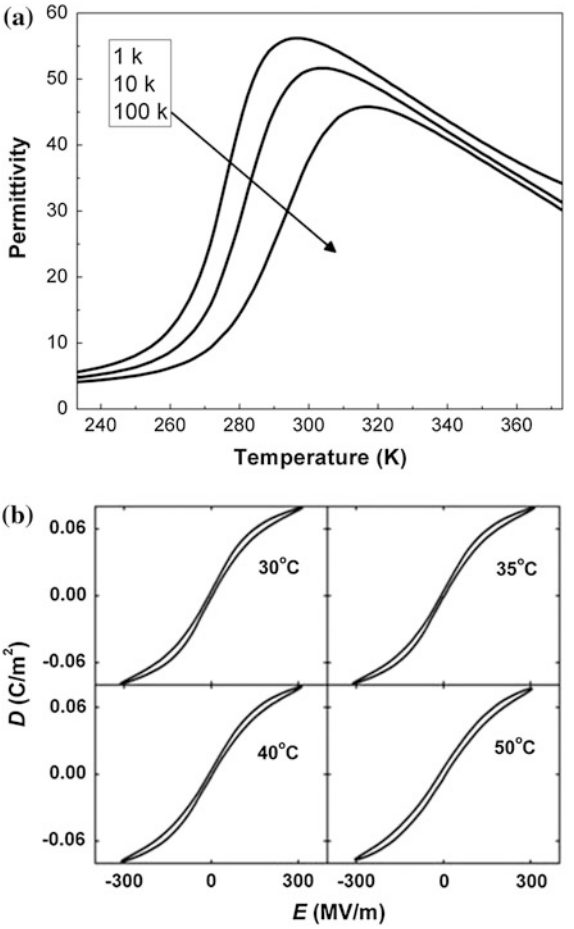

Fig. 11 **a** Permittivity as a function of temperature at 1, 10 and 100 kHz and **b** *D–E* hysteresis loops measured near the broad dielectric constant maximum for *P*(*VDF-TrFE-CFE*) 59.2/33.6/7.2 mol % terpolymer [16, 17]

i.e., a broad dielectric constant peak whose peak position moves progressively towards higher temperature with frequencies. The *D–E* loops for the same terpolymer are presented in Fig. 11b, which show very slim *D–E* loops at temperatures near the dielectric constant maximum, typical of ferroelectric relaxor. The large polarization change in the relaxor suggests a large ECE near room temperature. Indeed, ECE of the *P*(*VDF-TrFE-CFE*) 59.2/33.6/7.2 mol % terpolymer directly measured at 30 °C, as presented in Fig. 12a shows a very large ΔT, $\sim$16 °C induced under 160 MV/m electric field.

Besides the large ECE, several relaxor ferroelectric polymers also display a nearly temperature independent ECE as presented in Fig. 12b [6]. For a *P*(*VDF-TrFE-CFE*) 59.2/33.6/7.2 mol % relaxor ferroelectric terpolymer, the ECE response is nearly temperature independent from 0 to 45 °C, which is in sharp contrast to that in normal ferroelectrics where ECE peaks at the FE-PE transition and displays strong temperature dependence. Such temperature independent ECE

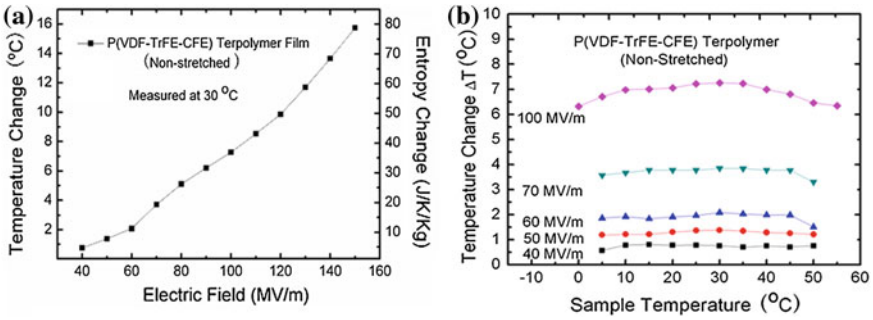

Fig. 12 Directly measured ECE of 59.2/33.6/7.2 mol % terpolymer **a** ΔT versus applied electric field at 30 °C and **b** ΔT versus sample temperature under different applied fields. [6]

is attractive for practical cooling device applications. These results reveal the intricate roles played by the defects in tailoring the ferroelectric response and its polar nano-structures to generate large ECE and its temperature response behavior.

Besides the direct measurement of ECE in the relaxor terpolymer, Maxwell relations have also been used to deduce ECE in the relaxor polymers. Presented in Fig. 13 is ΔT deduced from the Maxwell relations and its comparison with that directly measured. The data show a large difference between the data acquired by the direct and indirect methods. First of all, the directly measured ECE from the relaxor terpolymer is much larger than that deduced from the Maxwell relation. Moreover, the directly measured ECE displays much weaker temperature dependence at $E < 70$ MV/m. The results indicate that the Maxwell relation is not suitable for ECE characterization for the relaxor ferroelectric polymers even at temperatures above the broad dielectric constant maximum. This is likely caused by the non-ergodic behavior of relaxor ferroelectric polymers even at temperatures

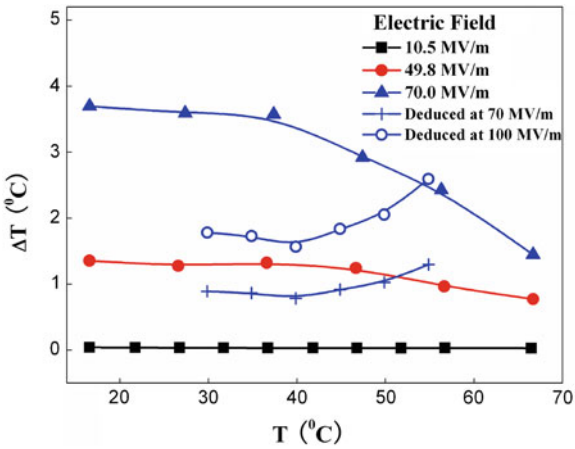

Fig. 13 Temperature dependences of the directly measured ΔT (solid symbols) of the terpolymer under different measuring electric fields. The ΔT deduced from the Maxwell relation at 70 and 100 MV/m (open circles and crosses) is also shown for comparison. The ΔT deduced from the Maxwell relation is much smaller than that directly measured. Data points are shown and solid curves are drawn to guide eyes. [10, 12]

above the dielectric constant maximum while the Maxwell relations are valid only for thermodynamically equilibrium systems (ergodic systems) [10, 12].

In analogous to the normal ferroelectric polymers whose responses can be tailored by varying the processing conditions [16, 17], the ECE responses in defects modified polymers can also be tailored by controlling the processing conditions. For eaxmple, ECE in unstretched terpolymer films displays virtually flat temperature response from 0 to 45 °C (see Fig. 12b). In contrast, for uniaxially stretched (5X) *P(VDF-TrFE-CFE)* terpolymer films, the ECE response shows a pronounced temperature dependence as displayed in Fig. 14, although at 30 °C the stretched and non-stretcehd terpolymer films exhibit the same ECE response.

ECE in a dielectric is determined by the dipolar entropy change ΔS_p between the polar- and non-polar states, $\Delta S_p = S_p(0, T) - S_p(E, T)$; where $S_p(0,T)$ is the dipolar entropy when $E = 0$ and $S_p(E, T)$ corresponds to the dipole aligned state when an external electric field E is applied. As shown by Pirc et al. [18], for a dipolar disordered state at $E = 0$ such as the relaxor at temperatures above the broad dielectric constant peak, here $S_p(0, T)$ is proportional to $P^{ln2}(\Omega)$, where Ω is the number of possible polar states in the dielectrics, while $S_p(E, T)$ can be approximated as zero (much smaller than $S_p(0, T)$) when E is high. Therefore, in general, ΔS_p or ΔT under a given field E will increase as temperature is reduced towards the broad dielectric constant peak (P increases with reduced temperature). As the temperature is further lowered towards the freezing temperature of the relaxor, remanent polarization will be developed after application of high electric fields, which will result in a decrease of ΔS_p with reduced temperature. Uniaxial stretching of terpolymer films causes preferred polymer chain orientation and, hence, reduces the number of possible polar states in the dipolar-disordered states and hence Ω. Consequently, ΔS_p is reduced due to a reduced Ω at temperatures above the broad dielectric peak. In addition, uniaxial stretching in general will favor all-trans molecular conformation and, hence, increase the polar-correlation

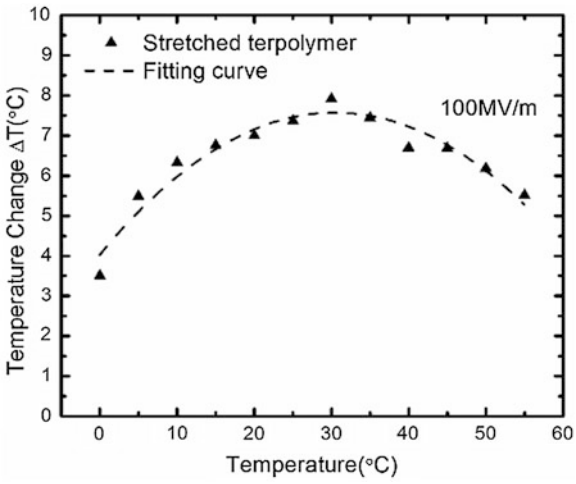

Fig. 14 ECE response (ΔT) of a 5X uniaxially stretched *P(VDF-TrFE-CFE)*terpolymer film versus temperature from 0 to 60 °C. The applied electric field is 100 MV/m [6]

which might be the reason for the faster reduction of ECE with reduced temperature below the broad dielectric maximum in the uniaxially stretched films. Increasing polar-correlation length in the relaxor polymer at $E = 0$ state will cause a reduction of $S_p(0, T)$. These results indicate that ECE temperature behavior of relaxor polymer or even normal ferroelectric polymer can be tailored by controlling the polymer film processing conditions.

3.3.2 Giant Electrocaloric Effect in the Irradiated P(VDF-*TrFE*) Relaxor Copolymers

ECE in the high energy electron irradiated *P*(*VDF-TrFE*) 68/32 mol % copolymer was also studied. As has been shown earlier, *P*(*VDF-TrFE*) copolymers can be converted into ferroelectric relaxor under a proper high energy electron irradiation. The ECE measured using direct method for the irradiated *P(VDF-TrFE*) 68/32 mol % relaxor copolymer is presented in Fig. 15. As can be seen, a very large ECE can be obtained at room temperature for a high energy electron irradiated *P*(*VDF-TrFE*) 68/32 mol % copolymers. ECE was measured at several temperatures around room temperature as presented in the inset of Fig. 15 which shows weak temperature dependence and has the ECE peaked around 306 K. Figure 15 also presents the ECE of the irradiated copolymer at 306 K on which the highest measuring field was 160 MV/m and an adiabatic temperature change $\Delta T = 20$ K and isothermal entropy change $\Delta S = 95$ J/(kgK) can be obtained under 160 MV/m, which are higher than the relaxor ferroelectric *P*(*VDF-TrFE-CFE*) terpolymer [10, 12].

Table 1 summarizes the ECE from the normal ferroelectric and relaxor ferroelectric polymers. For the comparison, selected ECE results reported in the literature on inorganic materials, especially inorganic ferroelectric thin films where very high voltage can be applied, are also included. Magnetocaloric (MC) materials have been investigated for many decades and MC materials with giant MC

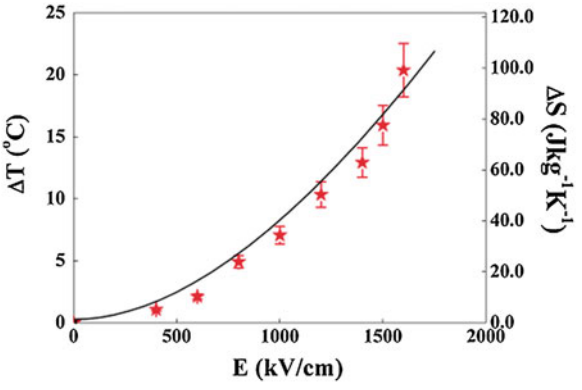

Fig. 15 Directly measured ECE for the high energy electron irradiated *P*(*VDF-TrFE*) 68/32 % relaxor copolymer. Inset presents ΔT versus temperature under 160 MV/m, measured from several samples [10, 12]

effect are also included. As can be seen, the relaxor ferroelectric polymers, because of their large $\Delta T\Delta S$, broad operation temperature range and easy scaling up for various sized cooling devices, offer the most attractive ECE properties for practical cooling device applications.

For practical cooling devices, the efficiency (often measured as the coefficient of performance, COP) is of great importance, where COP is

$$COP = Q_c/W \tag{9}$$

where Qc is the total heat absorbed at the cold end and W is the total work consumed in the cooling cycle in pumping Qc from the cold end at T_C to hot end at T_H. In a cooling device, COP will depend on the refrigerant used, cooling device design, and the temperature span $T_H - T_C$. For the ECE materials, the device efficiency is determined by the heat absorbed or ejected Q under an applied voltage (or input electric energy) which can be related to the isothermal entropy change $Q = T\Delta S$. From the data presented in Fig. 6, the heat absorbed or ejected under 140 MV/m electric field is $Q = 43.2$ J/cm^3 while corresponding total input electric energy density is only $U_e = 3.8$ J/cm^3 (part of which can be recovered as the capacitance energy). In developing ECE materials, besides to achieve large ECE, i.e., large ΔT and ΔS, how to maximize the ratio of Q/U_e is another critical consideration.

4 Conclusions and Outlooks

In this chapter, the electrocaloric effect was introduced and general considerations for polar materials to achieve larger ECE were presented. In general, a polar dielectric with a high polarization level which can be induced by electric field far below the electric breakdown, large number of polar-directions, and short polar correlation length in $E = 0$ state. It was found that the ferroelectric polymers, due to relatively short polar-correlation length and very high breakdown field (>400 MV/m), may generate giant ECE at temperature ranges for practical device applications. For normal ferroelectric *P*(*VDF-TrFE*) 55/45 mol % copolymers, an adiabatic temperature change over 12 °C and an isothermal entropy change over 30 J/(kgK) were obtained under a field of 120 MV/m, consistent with the phenomenological estimation. Moreover, in the relaxor ferroelectric polymers, the further reduction of the polar-correlation length due to the random defects introduced as well as possible increase in the number of local polar-states lead to giant ECE over a very broad operation temperature range. For relaxor *P*(*VDF-TrFE-CFE*) terpolymer, unstretched films, a $\Delta T \sim 16$ °C induced under 160 MV/m which is nearly a constant spanning a temperature range from 0 °C to 50 °C. In contrast, for a relaxor ferroelectric polymer, made from a high energy electron irradiation on *P*(*VDF-TrFE*) 68/32 mol % copolymer, exhibits a peak $\Delta T \sim 20$ °C under 160 MV/m at 33 °C which is reduced to $\Delta T \sim 8$ °C at 26 °C.

These results indicate the intricate correlation between the ECE response and the polymer micro- and nano-structures which can be tailored by the polymer composition and processing conditions. Although giant ECE has been observed in ferroelectric polymers, as presented here, as well as inorganic thin films, our understanding on the fundamentals of ECE in ferroelectric materials is very limited. It can be anticipated that polar-materials with much higher ECE and properties tailored for specific cooling device applications can be realized in the near future as we advance the understanding of ECE in polar-materials and of cooling device designs which make use of the unique properties of ECE materials.

Acknowledgments We acknowledge the support of the US Department of Energy, Division of Materials Sciences, under Grant No. DE-FG02-07ER46410 (X.L., X.Q., and Q.M.Z.), US Army Research Office under grant W911NF-11-1-0534 (S.L. and M.L.). The authors thank B. Rožič, Z. Kutnjak, R. Prac, B. Neese, B. Chu, Y. Wang, E. Furman, L. Gorny, and J. Cheng for their contributions to the ECE works presented in this chapter.

References

1. Correia, T.M., Young, J.S., Whatmore, R.W., Scott, J.F., Mathur, N.D., Zhang, Q.: Investigation of the electrocaloric effect in a $PbMg_{1/3}Nb_{2/3}O_3$-$PbTiO_3$ relaxor thin film. Appl. Phys. Lett. **95**(18), 182904/1-3. ISSN: 0003-6951 (2009)
2. Furukawa, T., Nakajima, T., Takahashi, Y.: Factors governing ferroelectric switching characteristics of thin VDF/TrFE copolymer films. IEEE Trans. Diel. Electr. Ins **13**(5), 1120–1131. ISSN: 1070-9878 (2006)
3. Furukawa, T.: Phenomenological aspect of a ferroelectric vinylidene fluoride/trifluoroethylene copolymer. Ferroelectrics **57**(1-4), 63–72. ISSN: 0015-0193 (1984)
4. Gschneidner Jr, K.A., Pecharsky, V.K., Tsokol, A.O.: Recent developments in magnetocaloric materials. Rep. Prog. Phys. **68**, 1479–1539 (2005)
5. Kar-Narayan, S., Mathur, N.: Predicted cooling powers for multilayer capacitors based on various electrocaloric and electrode materials. Appl. Phys. Lett. **95**, 242903/1-3. ISSN: 0003-6951 (2009)
6. Li, X.Y., Qian, X.S., Lu, S.G., Cheng, J.P., Fang, Z., Zhang, Q.M.: Tunable temperature dependence of electrocaloric effect in ferroelectric relaxorpoly(vinylidene fluoride – trifluoroethylene–chlorofluoroethylene) terpolymer. Appl. Phys. Lett. **99**, 052907/1-3. ISSN: 0003-6951 (2011)
7. Lines, M., Glass, A.: Principles and Applications of Ferroelectrics and Related Materials. Clarendon Press, Oxford (1977)
8. Lovinger, A.J., Furukawa, T.: Ferroelectrics. **50**,227 (1983)
9. Lu, S.G., Rozic B., Kutnjak Z., Zhang Q.M.: Electrocaloric effect in ferroelectric P(VDF-TrFE) copolymers. Integr. Ferroelectr. **125**(1), 176–185. ISSN: 1058-4587 (2011)
10. Lu, S.G., Rozic, B., Zhang, Q., Kutnjak, Z., Li, X.Y., Furman, E., Gorny, J.L., Lin, M.R., Malic, B., Kosec, M., Blinc, R., Pirc, R.: Organic and inorganic relaxor ferroelectrics with giant electrocaloric effect. Appl. Phys. Lett. **97**(16), 162904/1-3.ISSN: 0003-6951 (2010)
11. Lu, S.G., Rozic, B., Zhang, Q.M., Kutnjak Z., Neese, B.: Enhanced electrocaloric effect in ferroelectric poly(vinylidene-fluoride/trifluoroethylene) 55/45 mol % copolymer at ferroelectric-paraelectric transition. Appl. Phys. Lett. **98**(12), 122906/1-3.ISSN: 0003-6951 (2011)

12. Lu, S.G., Rozic, B., Zhang, Q.M., Kutnjak, Z., Pirc, R., Lin, M.R., Li, X.Y., Gorny, J.L.: Comparison of directly and indirectly measured electrocaloric effect in relaxor ferroelectric polymers. Appl. Phys. Lett. **97**(20), 201901/1-3. ISSN: 0003-6951 (2010)
13. Lu, S.G., Zhang, Q.M.: Electrocaloric materials for solid-state refrigeration. Adv. Mater. **21**, 1983–1987. ISSN: 0935-9648 (2009)
14. Mischenko, A.S., Zhang, Q., Scott, J. F., Whatmore, R.W., Mathur, N.D.: Giant electrocaloric effect in thin-film $PbZr_{0.95}Ti_{0.05}O_3$. Science **311**(5765), 1270–1271. ISSN: 0036-8075 (2006)
15. Neese, B., Chu, B.J., Lu, S.G., Wang, Y., Furman, E., Zhang, Q.M.: Large electrocaloric effect in ferroelectric polymers near room temperature. Science **321**(5890), 821–823. ISSN: 0036-8075 (2008)
16. Neese, B., Lu, S.G., Chu, B.J., Zhang, Q.M.: Electrocaloric effect of the relaxor ferroelectric poly(vinylidene fluoride-trifluoroethylene-chlorofluoroethylene) terpolymer. Appl. Phys. Lett. **94**(4), 042910/1-3. ISSN: 0003-6951 (2009)
17. Neese, B.: Ph.D. Dissertation, The Pennsylvania State University (2009)
18. Pirc, R., Kutnjak Z., Blinc, R., Zhang, Q.M.: Upper bounds on the electrocaloric effect in polar solids, Appl. Phys. Lett. **98**(2), 021909/1-3. ISSN: 0003-6951 (2011)
19. Rozic, B., Malic, B., Ursic, H., Holc, J., Kosec, M., Neese, B., Zhang, Q.M., Kutnjak, Z.: Direct measurements of the giant electrocaloric effect in soft and solid ferroelectric materials. Ferroelectrics, **405**, 26–31. ISSN: 0015-0193 (2010)
20. Rozic, B., Neese, B., Lu, S.G., Zhang, Q.M., Kutnjak, Z.: Direct measurements of the electrocaloric effect in P(VDF-TrFE) (68/32) Copolymer Ferroelectric Films. Ferroelectrics **416**, 139–143. ISSN: 0015-0193 (2011)
21. Sinyavsky, Y.V., Pashkov, N.D., Gorovoy, Y.M., Lugansky, G.E., Shebanov, L.: The optical ferroelectric ceramic as working body for electrocaloric refrigeration. Ferroelectrics **90**, 213–217. ISSN: 0015-0193 (1989)
22. Wood, M.E. Potter, W.H.: General analysis of magnetic refrigeration and its optimization using a new concept: maximization of refrigerant capacity. Cryogenics **25**(12), 667–683. ISSN: 0011-2275 (1985)

Lead-Free and "Exotic" Electrocaloric Materials

Anna-Karin Axelsson, Matjaz Valant, Florian le Goupil, Andrey Berenov and Neil Alford

1 Introduction: Moving Towards Lead Free Materials

This chapter describes lead-free electrocaloric materials and will mostly concentrate on bulk form. The electrocaloric (EC) values of these materials will be reported along with other essential factors associated with the electrocaloric effect such as ferroelectric phase transition, polarization, dipole entropy or heat capacity evaluations. Therefore, it is important first to restate some of the findings from the most common electrocaloric materials, the lead-based perovskites, describing some of the most interesting material characteristics from these.

One of the most important factors to consider in the development of effective EC materials is the correlation between the entropy and polarization change under applied electric field and temperature. For a large EC effect, a large entropy change, ΔS, which can be related to a large polarization change, ΔP, must be induced in the material by an external electric field and it is concluded that these conditions are best fulfilled when operating the material close or just above the ferroelectric phase transition.

Most electrocaloric research has so far been focused on perovskite type of relaxor ferroelectrics, such as the lead based compounds like the lead magnesium niobate-lead titanate (PMN-PT) and the lead zinc niobate-lead titanate

(PZN-PT) where a significant EC temperature change up to 2.6 K has been reported for $(Pb,Nb)(Zr,Sn,Ti)O_3$ as reported by Tuttle and Payne [61] and later by Fuith et al. [16]. This value was observed within a rather narrow temperature range around the ferroelectric transition at 160 °C. The high value results from an additional contribution to the EC effect arising from a field induced phase transition. The study also showed that a material's heat treatment and synthesis history

A.-K. Axelsson (✉) · F. le Goupil · A. Berenov · N. Alford
Department of Materials, Imperial College London, Exhibition Road, London SW72AZ, UK
e-mail: a.k.axelsson@imperial.ac.uk

M. Valant
University of Nova Gorica, Materials Research Laboratory, Ajdovscina, Slovenia

T. Correia and Q. Zhang (eds.), *Electrocaloric Materials*,
Engineering Materials 34, DOI: 10.1007/978-3-642-40264-7_6,

plays an important role in the observed EC performance and further how the additional contribution of the field induced polarisation changes close to the ferroelectric phase transition can play a vital role in increasing the EC effect. The significance of the material synthesis and heat treatment history is also found in lead free electrocalorics, in particular where both long-range ordered ferroelectric domains coexist with polar nanodomains, and where the domain wall movement is affected by inclusions, defects, pinning and cation ordering.

Another example of field-induced EC effect was observed in highly ordered $PbSc_{1/2}Ta_{1/2}O_3$ ceramics that can give a change of 2.3 K in a temperature range of Tc ± 5 K [51]. Here the induced phase transition originated from a structural rearrangement from Fm3 m to R3 m phase. The advantage from this induced phase transition is its association with a strong entropy change. The reader is referred to in Chap. 3, Sect. 3 for more details on the electrocaloric effect in PST compounds.

From these studies, important material characterization lessons are learned such as structure ordering, ion substitutions and stoichiometric defects, including oxygen vacancies, that are all crucial for these relatively high EC temperature changes in ceramic electrocalorics and are factors to consider when developing the lead-free counterparts. Furthermore, for practical reasons it is hard to organize an efficient cooling cycle in very narrow working temperature ranges which takes the focus towards disordered relaxor ferroelectrics, such as the probably most investigated electrocaloric compositions $Pb(Mg_{1/3}Nb_{2/3})O_3$-$PbTiO_3$. A wide working temperature range, from 80 to 160 °C, with EC temperature changes of 2.7 K have been achieved using a <011>-oriented PMN-28PT single crystal [41]. The wide working temperature range is a result of the broad and diffuse relaxor ferroelectric transition. When this particular composition is within the morphotropic phase region (30–35 mol % of $PbTiO_3$), a coexistence of both rhombohedral and tetragonal ferroelectric domains are observed just before moving into the paralelectric state with increased temperature. This demonstrates the advantages of utilising relaxor ferroelectrics and, in particular, the advantages of morphotropic phase region for an efficient EC cooling unit.

However, due to the European regulations, these lead containing materials are to be avoided and new research directions need to be focused on lead free counterparts which will be discussed in this chapter. It is therefore important to study the physics behind the above mentioned high performance EC materials and understand the thermodynamics across the ferroelectric phase transition to improve the lead free counterparts which so far have not been so intensively explored.

The quest for higher EC effect in bulk materials will be discussed because a high refrigeration capacity requires greater volumes of cooling unit that cannot be achieved with thin films. This is particularly important for medium and large-scale cooling facilities. Following the first part in this Chapter, which describes lead-free perovskites, a section describing other oxide material groups such as tungsten bronzes and Aurivillius phase structures further shows how material engineering can be beneficial for EC materials for solid-state cooling units. Furthermore, it

should be recognized that there are EC materials that are non-oxide based, which takes us back to some of the early studies of EC materials over 50 years ago; e.g. Rochelle salt. Even further away from oxide ceramics are polymers such as the ferroelectric PVDF-types which have been investigated as an attractive EC alternative and will be described in Chap. 5.

When developing suitable EC materials, a proper understanding of the physics, chemistry and processing of different materials is necessary. In this Chapter we will discuss the different lead-free EC materials, whose performance critically depends on the following characteristics:

Order of phase transition

The entropy of a system increases continuously with temperature up to a phase transition temperature. At this temperature, the entropy changes gradually in the case of a second order transition or in a step-like manner for the first order transition. This means that an entropy change and therefore EC temperature effect [50, 51] is larger for a first order transition [6], however, the first order transition step is abrupt and provides a smaller window of operable EC effect. Furthermore, the application of a strong electric field, which is necessary for high EC temperature changes, can change the initial nature of this phase transition. The entropy change and the specific heat around the different type of ferroelectric phase transition will be discussed below.

Field-induced transition

As described above, the application of electric field can induce a phase transition. Relaxor ferroelectrics in the morphotropic phase region may then follow a field induced first-order transition but only observed at higher applied electric field. In all cases the *total* entropy of the material under adiabatic conditions is constant and different contributions to the entropy changes prevail depending on the field. The latent heat from the field-induced phase transition can significantly contribute to the *effective* EC effect at temperatures already below the so-called depolarization temperature, T_{dp} [43]. Therefore, it is important to distinguish between the true EC effect and the latent heat from the field-induced phase transition. Perantie et al. [42] showed how the latent heat accounts for more than 50 % of the observed effective EC effect starting just before the T_{dp} region, while at T_{dp} the latent heat decreases and the true EC effect is rapidly increasing. The latent heat will be discussed for lead-free electrocaloric KH_2PO_4 in Sect.3

Morphotropic phase boundary:

A morphotropic phase boundary is a region of the temperature-composition (T-x) phase diagram where the crystal structure abruptly changes from one phase to another. It usually involves the formation of intermediate lower symmetry phases (monoclinic) and field-induced polarization rotations. In recent years the term MPB has been mostly used to describe the phase transition from tetragonal

symmetry to rhombohedral symmetry in ferroelectrics. What makes these morphotropic phase boundaries interesting is that they usually show enhanced electromechanical properties. For instance the piezoelectric coefficient around their morphotropic phase boundary of PZT and PMN-PT, which are two of the most studied piezoelectric systems, increase to 750 pm/V [39] and 700 pm/V [8]. It has been reported that these high values could be a result of the field-induced polarization rotations, along with the resulting unit cell deformation [9]. A recent report by Kutnjak et al. [25] on the electric field-temperature-composition (E-T-x) phase diagram of PMN-PT showed the existence of a critical point, where the energy required for the field-induced polarization rotations is significantly decreased. They also showed that, as the composition gets closer to the morphotropic phase boundary, the critical point moves towards lower electric fields values, which would explain the enhanced electromechanical response in this area and how this worked in an advantage for the electrocloric effect. The same group showed by a mean-field calculation that the ECE (normalized to the electric field) was maximized at the critical point [47].

Short range polar domains:

The effective EC temperature change can be extended well over the ferroelectric phase transition when polar nano-domains are present in the material. These chemically disordered clusters create nano-sized polar domains with random orientation of the electric dipoles that are typically embedded in a paraelectric matrix. The correlation length of the dipoles changes with temperature, field and pressure. In particular, at high applied field the effect of the polar nanodomains extends the EC effect well over the Curie temperature and by manipulating shape and volume of these short range domains the EC effect can be effectively tuned. The influence of the shape and volume of the polar nano domain embedded in a paraelectric matrix is described from a functional polar point of view by [48] and further how applied external pressure on these systems can enhance the EC effect has been theoretically described by Dunne et al. [13].

This region where short range polar domains dominate cannot be evaluated by Maxwell relation of entropy and polarization changes and direct EC measurements must be performed for accurate results. Results obtained by direct EC measurements indicate that the presence of the nanodomains extends and increases the reversible EC effect and if a high enough field can be applied prior to dielectric breakdown, several lead-free ferroelectric relaxor ceramics would provide advantages over the lead-based relaxors.

Dielectric strength and conductivity:

It is clear that substantial EC temperature changes, >2 K, are only achievable with very high electric field up to a point when the dipole entropy change saturates (Fig. 1). However, there are physical limitations as to the field strength the materials can withstand [62]. In single crystal piezoelectrics, very soon microcracks develop due to the strain. Other materials simply cannot withstand these

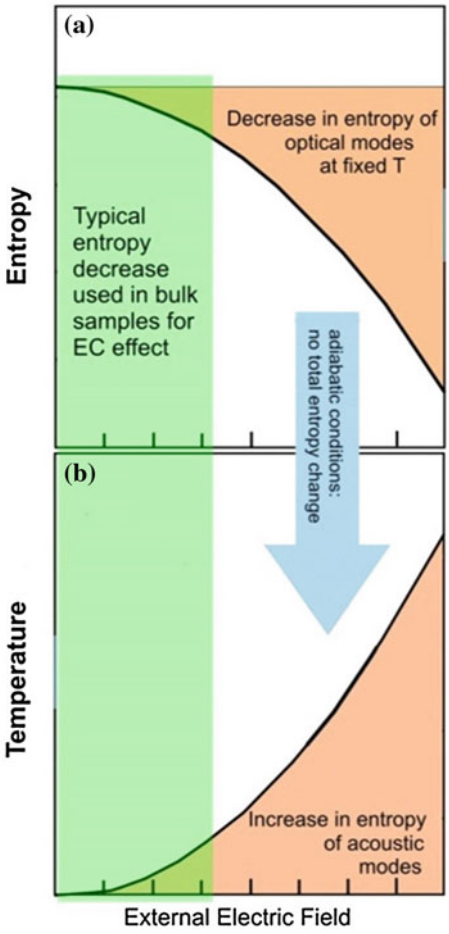

Fig. 1 Schematic presentation of the influence of electric field on entropy changes in the optic **a** and acoustic modes **b** under adiabatic conditions. Only a small section from the entropy changes from the optic modes is achieved before typical bulk materials, like KDP, break down (see *green* shading)

high fields due to poor dielectric strength or electric percolation via the ceramic grain boundaries. Furthermore, a high conductivity, either electronic or ionic, causes leakage current under the applied field, which results in the Joule heating. The Joule heating can be quantitatively determined by application and removal of the electric field as the Joule heating increases the apparent EC heating effect when applying the field and reduces the EC cooling effect upon the removal. Conductivity limits the use of some promising non-oxide materials which are based on extremely high entropy change over field and temperature, S(E,T), as discussed in Sect.3

In Table 1 some references to bulk electrocaloric materials can be seen (extracted from [63]). The values are obtained by either direct or indirect EC evaluation.

Table 1 Reported EC characteristics of the lead-free bulk materials

Material	Form	T (°C)	ΔT (°C)	ΔE (MV/m)	ΔT/ΔE (10^{-6}m•K/V)	Meas. method	Ref.
Co,Sb,doped $Pb(Sc_{0.5}Ta_{0.5})O_3$	Ceramics	18	2.3	N/A	N/A	AC	[51]
$Ba_{0.73}Sr_{0.27}TiO_3$	Ceramics	25	1.00*	2.4	0.42	DSC	[26]
KCL: OH	Single crystal	−273	0.15	2.6	0.06	DTR	[24]
$CdTiO_3$	Ceramics	−213	0.02	1.1	0.02	AC	[65]
$SrTiO_3$	Ceramics	−256	0.06	0.8	0.08	AC	[65]
$SrTiO_3$	Ceramics	−261	0.3	1.99	0.15	DTR	[26]
KTaO3	Single crystal	−260	0.25	1.56	0.16	DTR	[27]
$NaKC_4H_4O_6 \cdot 4H_2O$	Single crystal	22.2	$4{\cdot}10^{-3}$	0.12	0.03	AC	[65]
KH_2PO_4	Single crystal	−150	0.08	0.07	1.14	AC	[65]
KH_2PO_4	Single crystal	−150	0.15	0.45	0.03	AC	[13]
NH_4HSO_4	Single crystal	−2	0.025	0.15	0.17	AC	[4]
$Rb_{0.33}(NH_4)_{0.67}HSO_4$	Single crystal	−3	0.04	0.34	0.12	AC	[33]
$(NH_2CH_2COOH)_3{\cdot}H_2SO_4$	Single crystal	50	0.11	0.16	0.69	AC	[55]
$(NH_2CH_2COOH)_3{\cdot}H_2SO_4$	Single crystal	50	0.11	0.17	0.65	AC	[55]
$(NH_2CH_2COOH)_3 \cdot H_2SeO_4$	Single crystal	22	0.18	0.15	1.20	AC	[33]
$(NH_2CH_2COOH)_2 \cdot HNO_3$	Single crystal	−67	0.054	0.4	0.14	AC	[58]

AC Adiabatic calorimetry, *DTR* Direct temperature reading

* Calculated from Q [17] *DSC* Differential scanning calorimetry

IM Indirect method

2 Lead-Free Perovskites

2.1 Incipient Ferroelectrics: $SrTiO_3$ and $KTaO_3$

$SrTiO_3$ and $KTaO_3$ are two highly polarisable perovskite crystal structures. They belong to a special type of ferroelectrics often referred to as incipient ferroelectrics or quantum paraelectrics. For the electrocaloric effect it is important that their polarization, often described by the electric permittivity, goes to extremely high values at temperatures just before what would have been a ferroelectric phase transition around 10 K. However, quantum fluctuation prevents the occurrence of this transition, which produces a plateau of a constantly high permittivity. Granicher [18] and later Hegenbarth [20] measured the EC-effect in ceramic $SrTiO_3$ at the cryogenic temperatures. However, beyond being interesting for fundamental studies due to their large temperature change of polarisation only a small value of EC effect has been found due to low EC temperature change of merely 0.06 K at 10 K. Higher EC temperature change, 0.3 K at temperatures between 4 and 11 K, was measured on a single crystal $SrTiO_3$ by [22]. Single crystal $KTaO_3$ was considered to be attractive as a material for adiabatic—depolarization cooling.

Lawless [28] investigated how the reversible electrocaloric effect can be utilised as a sensitive tool to measure Gibbs free energy and evaluate a change of specific heat as a function of electric field at cryogenic temperatures. The adiabatic temperature change and isothermal entropy change of bulk $KTaO_3$, and $SrTiO_3$ are considered moderate, which has so far restricted their applications in any of practical cooling devices.

2.2 $BaTiO_3$: Solid Solutions

Another highly polar perovskite, **$BaTiO_3$**, has been investigated as a lead-free electrocaloric candidate, in the form of interdigital capacitor structure (see Chap. 4), single crystals or multilayered capacitor made from tape cast ceramics reaching up to $\Delta T = 4.0$ K at 80 °C under 352 kV/cm [2]. Unlike the more common EC materials based on $PbTiO_3$ which undergo a disordered-order phase transition, the $BaTiO_3$ undergoes a displacive phase transition. The dipole moment in the ferroelectric state arises from the off-centering of the B-site Ti ion inside the oxygen octahedron. For bulk single crystal, a recent publication from Bai et al. in [3], estimated EC temperature effect of $\Delta T = 1.6$ K for $E = 10$ kV/cm around the ferroelectric transition at 130 °C, which was obtained by direct measurements on a modified DSC. The peak of specific heat capacity at this ferroelectric phase transition shifts to higher temperatures with increased electric field and the peak value lowers and broadens. The specific heat values obtained with applied field was then used for an estimation of the entropy change, ΔS as:

$$\Delta S = -\int_0^T \frac{C_E(T,E) - C_E(T,0)}{T} \quad (1)$$

A large EC effect with ΔS of 1.9 J/kg K that corresponds to ΔT = 1.6 K, has been observed for the temperatures just above Tc, where the alignment of individual dipoles contributes the most to the highest ECE, just as described for KDP by Dunne et al. [13].

The electrocaloric value for ΔS was then compared with the ΔS obtained from indirect thermodynamic calculation based on Maxwell relation using P-E measurements and the comparable result provided confidence in the measurements.

Pure $BaTiO_3$ undergoes a ferroelectric-paraelectric phase transition around 130 °C and its non-centrosymmetric ferroelectric state originates from the Ti atoms' displacement along the c-axis from its position inside the octahedral oxygen casing which creates a permanent electric dipole. The ferroelectric transition temperature in **(Ca, Sr, Ba)TiO_3** system depends on both the average value of the A-site cation radii and on the value of standard deviation of ionic radii of individual cations from the average value (A-site cation variance, σ^2) [5]. The decrease of the average ionic radii resulted in the decrease of the values of Tc at constant value of the A-site variance. As a result the substitution of Ba^{2+} in $BaTiO_3$ by a smaller Sr^{2+} cations leads to almost linear increase of T [32] as changes of the cation variance is relatively small. When the average ionic radii in

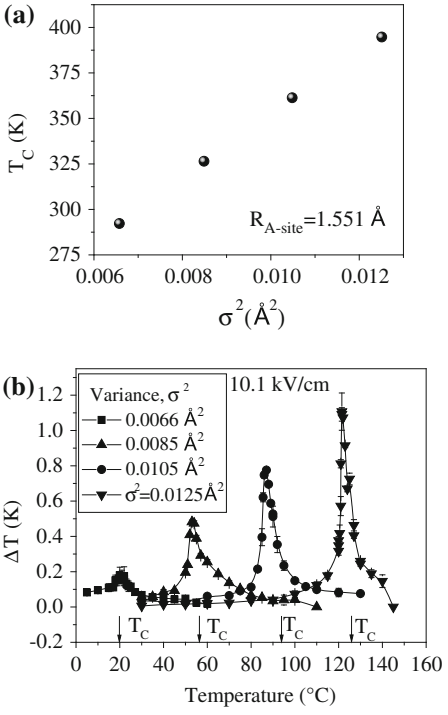

Fig. 2 Effect of a variance of A-site ions in (Ca,Sr,Ba)TiO3 on the Tc **a** and temperature dependences of measured ΔT **b**

(Ca, Sr, Ba)TiO_3 system was kept constant a linear increase of Tc with the cation variance was observed for the compositions with the average ionic radii of 1.594 Å [54] and 1.551 Å (Fig. 2a) The effect of the cation substitution on the Tc is more complex when both the average ionic radii and the cation variance are modified. For example during the substitution of Ba^{2+} in $BaTiO_3$ by even smaller Ca^{2+} ion the values of Tc goes through the maximum [67] due to the competing effects of decreasing the average ionic radii (thus reducing Tc) and increasing cation variance (thus increasing Tc). Berenov et al. [5] have evaluated the EC effect in A-site disordered (Ca, Sr, Ba)TiO_3 perovskites. The extent of cation disorder was quantified by a variance, σ^2, of ionic radii of A-site cations. The increase in the cation variance resulted in the increased tetragonal distortion of the perovskite structure. The measured temperature dependences of ΔT, generated upon the application of 10 kV/cm shown in Fig. 2b, were obtained by direct EC measurements on a modified DSC set up and agree extremely well with the values estimated by indirect method from polarisation loops. The highest measured ΔT (at 10 kV/cm and 121 °C) was 1.1 K for $Ba_{0.78}Ca_{0.22}TiO_3$. Interestingly, the maximum ΔT was found to increase with the Tc and became less field dependent at higher temperatures. Whereas the EC effect observed close to room temperature showed broad temperature maximum and strong field dependence thus suggesting that the (Ca, Sr, Ba)TiO_3 system is potentially interesting for refrigeration applications when the electric fields comparable to the ones applied to lead-based materials are used.

For the EC applications more interesting characteristics are induced when Ti is substituted with Zr in the $BaTiO_3$ system. In $\mathbf{Ba(Zr_xTi_{1-x})O_3}$ (BZT) with $x = 0.25$, a relaxor ferroelectric with a dispersed transition is formed. Unlike the analogue lead containing ferroelectric relaxor, PZT, this material does not show any sign of long range ferroelectric order [49] and it shows some unusual lack of measurable heat capacity change across the phase transition despite the presence of a large and broad frequency depending dielectric peak, as seen in Fig. 3. These characteristics confirm the relaxor phase transition [36]. The difference between PZT and BZT is suggested to be in the nature of the relaxor phase transition. The

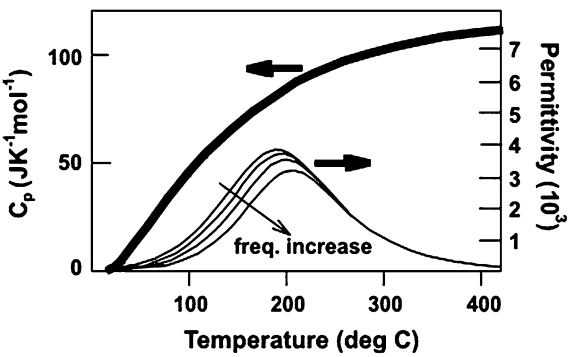

Fig. 3 Comparison of molar heat capacity C_p across the ferroelectric transition and the real part of dielectric constant ε' of BZT35 as described in detail by Nagasawa et al. [36]

lead containing relaxors exhibit the order–disorder phase transition whereas in the BZT it is of displacive type, which would normally give a much smaller entropy change. However, there is as yet no information regarding the contribution these polar nanodomains alignment exert on the electrocaloric effect. In lead containing relaxors this contribution starts to dominate at high electric fields and temperatures above the permittivity maximum. Further details on the difference between the lead containing relaxors versus the $BaTiO_3$ derivatives can be found in the excellent summary and the formation of polar nanodomains from [7] and in the detailed description of lead-free relaxor by Simon and Maglione [53].

Another lead-free relaxor ferroelectric $BaTiO_3$ derivative is barium titanate stannate, $\mathbf{Ba(Ti_{1-x}Sn_x)O_3}$ (BTS). With $x < 0.15$ it is a true ferroelectric whereas towards $x = 0.20$ mixing of Ti and Sn on the B-site starts creating inhomogeneity and a broad diffuse ferroelectric relaxor behaviour is observed [52]. So far no electrocaloric study has been reported on Ba(Ti, Sn)O_3 but the material shows promising high polarisation. A field-induced high pyroelectricity of BTS films was calculated up to 750 nC/cm^2 K, which is yet another indication of promise for a high ECE [37]. Due to intrinsic correlations between pyroelectric, piezoelectric and electrocaloric properties more authors are focusing their EC research on well-known pyro- and piezoelectrics [2, 34, 35]. In a study on lead-free piezoelectric $(Ba_{0.3}Na_{0.7})(Ti_{0.3}Nb_{0.7})O_3$ ceramics with the ferroelectric transition around room temperature the influence of processing parameters on the isothermal entropy change was analysed. It was shown that ΔS can be improved up to 0.026 J/kg K. [1]. This was evaluated by measuring the P-E loops together with the pyroelectric coefficient over temperature, $p(T)$. The distinct maximum of entropy change occurs around 260 K with an applied field of 15 kV/cm.

The entropy change in another piezoelectric $BaTiO_3$–based system, $\mathbf{Na_{0.5}Bi_{0.5}TiO_3–BaTiO_3}$, with mixed occupancy on only A-sites, is much higher. The results were evaluated by measuring P-E loops and the specific heat capacity over T. From these measurements the adiabatic temperature change and isothermal entropy change were calculated by the Maxwell relations. The entropy change was found to be 0.26 J/kg K $\Delta T = 0.18$ K at 40 kV/cm^{-1}.

Lead-free relaxors based on $BaTiO_3$ have also been investigated in several other ternary systems such as $BaTiO_3$-$BaZrO_3$-$CaTiO_3$, $BaTiO_3$-$BaZrO_3$-$BaLiF_3$, $BaTiO_3$-$KNbO_3$-$CaTiO_3$ and $BaTiO_3$-$BaZrO_3$-$CaLiF_3$ mainly by Ravez et al. [46]

3 Non-Perovskite Oxides

3.1 Pyrochlores

$Cd_2Nb_2O_7$ belongs to the pyrochlore family (space group Fd3 m) with corner sharing NbO_6 octahedra and a resulting crisscrossing of the O-Nb–O chains along the (110) direction due to the off-centered position of the niobium inside the octahedral, see Fig. 4.

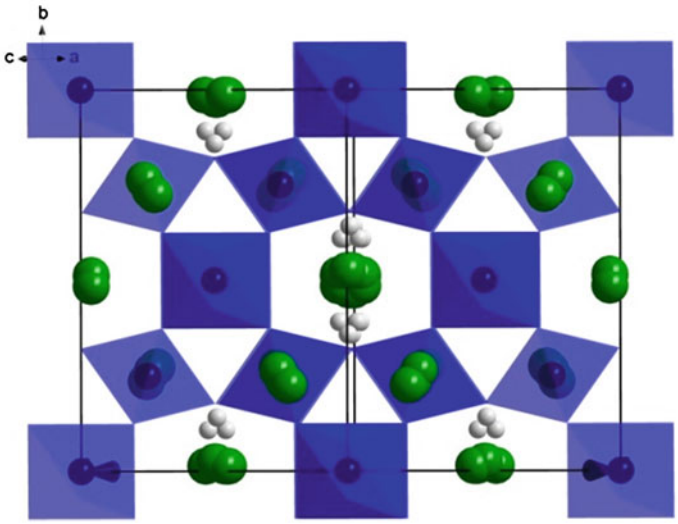

Fig. 4 Disordered pyrochlore crystal structure with the general formula $A_2B_2O_7$ (A—*green*, O—*grey* and B_2O_6 network of *blue* polyhedra)

In 1987 Lawless and Clark evaluated the electrocaloric effect of $(Cd_{0.83}Pb_{0.17})_2Nb_2O_7$ pyrochlores and the influence of Pb substitution on the A-site for the ferroelectric properties. They showed that Pb substitution lowers the Tc below 200 K and changes the mechanism of the phase transition to become a soft-mode driven transition. The purpose of the study was to investigate the dielectric properties, specific heat and electrocaloric effect and further investigate the relation between these properties and the formed soft mode transition. For the specific heat and electrocaloric evaluation a $(Cd_{0.83}Pb_{0.17})_2Nb_2O_7$ multilayer capacitor sample was attached to a temperature-controlled reservoir by a long-time-constant thermal link of indium, which was soldered to a copper mounting pin and placed in high vacuum. This arrangement ensured nearly adiabatic conditions during the application of the electric field. The electric field dependence of the specific heat, was measured over several decades up to 180 kV/cm and compared with specific heat at zero-field. The theoretical evaluation in combination with the experimental data, indicated that a second order transition occurred and provided an unusual high $\Delta S \sim 0.58$ Cal/mol K. From Landau-Ginzberg-Devonshire theory via the relation $\Delta S = 2\pi P^2/C$ ($C =$ Curie constant) they calculated a high value for the spontaneous polarization, 50 $\mu C/cm^2$. The electrocaloric effect reached 0.8 K when applying 120 kV/cm at 94.27 K. The high dielectric strength was possible due to a multilayered capacitor structure.

$Cd_2Nb_2O_7$ is commonly substituted with either Pb on A-site or Ta on B site to tune the ferroelectric transition. Lawless and Clark [29] found out that when comparing Pb-substituted with pure $Cd_2Nb_2O_7$, both the entropy change and polarization around the phase transition, dramatically increased, suggesting that

analogue systems with other lone pair A-site ions could be potentially effective electrocaloric materials worth investigating. It should be noted that only few ferroelectric pyrochlores have been reported so far. One of them is $RbNbWO_6$ [38] with a tetragonal-cubic ferroelectric transition at 390 K that has been studied for thermoelectric applications [23]. The heat capacity showed two small anomalies at 356.5 and 361.6 K. The calculated enthalpy and entropy are 11.7 J mol^{-1} and 0.033 J mol^{-1} K^{-1} for the first phase transition and 10.8 J mol^{-1} and 0.030 J mol-1 K^{-1} for the second, respectively. The origin of the two apparent transitions is not known but indicates the possible existence of a stable state between the ferroelectric tetragonal and paraelectric cubic state. Due to pyrochlores' rather open and flexible structure, stabilized by the B_2O_6 chains, it is possible to develop novel stable phases with tunable EC properties despite large amount of defects.

3.2 Aurivillius Phases

Bismuth layered ferroelectrics (BLSF) or Aurivillius phases are materials with a general composition $Bi_2A_{n-1}B_nC_{3n+3}$. They consist of layers of a perovskite-type $(A_{n-1}B_nC_{3n+1})2-$ sandwiched between layers of bismuth oxide $(Bi_2O_2)^{2+}$, see Fig. 5. The spontaneous polarisation in Aurivillius phases, which is oriented along the a-axis parallel to the stacking layers, originates from a complex combination of several displacive mechanisms. Not only are the B ions off-centered along the a-axis with regard to the oxygen octahedron in the perovskite type layer, but also the A ions. Furthermore, substitutions of the Bi ions in the $(Bi_2O_2)^{2+}$ layer can cause distortion and rotations of the polar perovskite layer. The magnitude of the contribution of each mechanism depends on the n-value in the perovskite type layers. The potential of these materials for EC applications arises from many important factors such as being lead free and having better reliability and less fatigue when

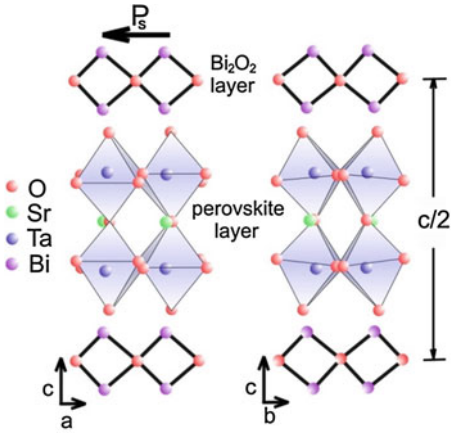

Fig. 5 Example of a two layered $SrBi_2Ta_2O_9$ seen as **a–c** and **b–c** projections of the crystal structure. P_s denotes the spontaneous polarization in the a-axis direction originating from the perovskite layers between Bi_2O_2 insulating sections

compare with more common PZT types [10]. Furthermore, these materials are characterized by high breakdown voltages and reduced leakage currents due to the high electrical resistance provided by the layer of bismuth oxide $(Bi_2O_2)^{2+}$. The high resistance to fatigue has made these materials attractive for non-volatile memories, which is further proof of the long standing stability of these Aurivillius phases for an EC material in a cooling unit exposed to several high voltage pulses per hour.

$SrBi_2Nb_xTa_{2-x}O_9$ is a member of this Aurivillius phase structural family and has been investigated by Le Goupil [30] who analyzed the directly measured EC effect and polarization over field and temperature. By varying the Nb and Ta ratio in the perovskite layer, the position of the Curie temperature (T_c) and spontaneous polarization P_s can be tuned. To shift Tc below 310 °C and further enhance the spontaneous polarization, substitutions of the Bi^{3+} ions in the bismuth oxide layer by rare earth elements such as La^{3+}, Pr^{3+}, Nd^{3+} and Sm^{3+} or substituting Sr^{2+} with Ba^{2+} have shown positive results [21, 40, 59]. These substitutions also lead to a broadening of the relaxor-type phase transition.

The electrocaloric effect of isovalent substitution of Pr^{3+} in the bismuth oxide layer of $SrBi_2(Nb_{0.2}\ Ta_{0.8})_2O_9$ was studied by Le Goupil [30]. As expected the temperature of the relaxor type phase transition was significantly shifted down to values closer to room temperature. The relaxor properties were also found to be enhanced and widened due to increased disorder.

Direct EC effect measurements were performed using a modified-DSC setup described elsewhere [31]. It was found that, as expected, the EC effect followed the trend observed in the real part of the permittivity versus temperature until the ferroelectric phase transition. However, instead of starting decreasing at higher temperatures, it kept on increasing over the higher part of the investigated temperature range of 20–300 °C. The behaviour of the EC effect versus temperature was attributed to the presence of a second EC peak at these higher temperatures. Although the origin of this second EC peak is unclear in the case of complex structure, such as substituted BLSF, it most definitely originates from the high cation disorder that is induced by the substitution, which might result in the formation polar regions. The presence of this high temperature second ECE peak highlights the great potential of Aurivillius phases to obtain the broad range of working temperatures required to establish an efficient ECE cooling cycle closer to room temperature. However, only small values of ECE of <1 K were measured by Le Goupil [30] and more substitutions options ought to be studied in order to obtain a better trade-off between the lowering the phase transition temperature, the resulting decrease in polarization and processability.

The electrocaloric properties of Aurivilius $SrBi_2Ta_2O_9$ phase, in thin film, were recently described by Hamad [19] where phenomenological models and thermodynamic calculation based on measured polarization described several important electrocaloric properties such as electric entropy change, heat capacity change and maximum entropy change. These studies provide explanations as to why more complex structures than the classic perosvskites, can provide novel pyroelectric and electrocaloric properties worth exploring for electrocaloric development.

3.3 Tungsten Bronzes

The EC effect is sensitive to the applied field direction in anisotropic crystals. The influence of the electrothermal interaction on the electro- and thermophysical parameters of pyroactive materials has been studied and has shown that the anisotropic thermophysical tensor component can be used to advantage for EC materials. To make the most of this tensor, materials can be structurally arranged accordingly, either as single crystals, epitaxial thin films or as grain oriented ceramics.

This brings us to tungsten bronzes which are compounds with the general formula A_xMO_{3-y} and are composed of corner sharing MO_6 octahedra. The arrangement of the corner-sharing octahedral creates different types of channels inside the structure and it is the site occupancy of these channels by different cations, which is responsible for the relaxor type properties of tungsten bronzes, see Fig. 6. Strontium barium niobate $Sr_xBa_{1-x}Nb_2O_6$ (SBN) is a tungsten bronze type relaxor ferroelectric material known for its applications in pyroelectricity, piezoelectricity, electroptics, photorefractive optics and non-linear optics. Its crystal structure has the space group P4bm at room temperature, where the unit cell contains ten corner-sharing NbO_6 octahedra of two types ($[Nb(1)O_6]$ and $[Nb(2)O_6]$) that are build up the polar axis in the crystal.

The inhomogeneous distribution of the Sr^{2+} and Ba^{2+} ions and the resulting vacancies cause the structural disorder responsible for the relaxor type properties of SBN, so that SBN with x below 0.5 are normal ferroelectrics and SBN with x above 0.5 show relaxor-type properties. The strength of the relaxation then increases with the strontium content. The fact that it has both long range ferroelectric ordering and a disperse relaxor behaviour due to the coexisting polar nanoregions is interesting, as it allows to draw a parallel with the well-known PMN-PT relaxor system, for which theoretical electrocaloric evaluations [13] has

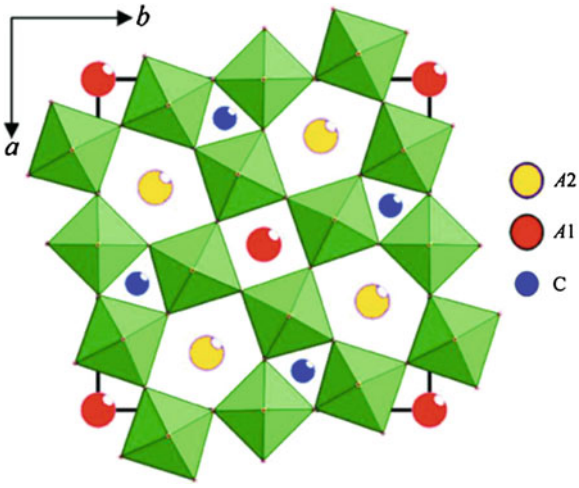

Fig. 6 View along the polar c-axis of the SBN tungsten bronze structure. The corner-sharing NbO_6 *octahedra* form three types of interstitial sites. The *tetragonal* (A1) and *pentagonal* (A2) positions are partially occupied by Sr and Ba atoms (5/6) and partially vacant (1/6)

pointed out the importance of the cross-over region from long range ordering to short range polar nanodoman region.

The electrocaloric theory clearly correlates the polarization tensor and entropy changes and therefore endorses the role of this significant dielectric anisotropy. In an anisotropic material such as SBN, the material response would therefore depend on the relative direction of an applied field and the crystal orientation. Physically, the internal dipoles are constrained to lay in particular directions with respect to the underlying material and not necessarily in the direction of the field. The polarization is linearly related to the field direction. Such linear relationships can be written as follows:

$$\begin{pmatrix} P_x \\ P_y \\ P_z \end{pmatrix} = \kappa_0 \chi \begin{pmatrix} E_x \\ E_y \\ E_z \end{pmatrix}$$

where χ is the dielectric susceptibility tensor. Therefore, it was concluded that the polarisation in the anisotropic SBN depends on the direction of the electric field. The measured EC effect depends on this anisotropy.

The pyroelectric anisotropy in structured $Sr_xBa_{1-x}Nb_2O_6$ ceramics was demonstrated by Venet et al. [64].They investigated properties such as dielectric permittivity, pyroelectric coefficient and dielectric loss and showed the existence of anisotropy between the perpendicular and parallel field directions with respect to the aligned grains in the ceramic. At the room temperature ferroelectric transition of $Sr_{0.53}Ba_{0.47}Nb_2O_6$, a pyroelectric coefficient of 4–5 $\times$ 10^{-2} $\mu C/cm^2$ K coexisted with a dielectric permittivity $\varepsilon = 1000$.

The electrocaloric effect of strontium barium niobate tungsten bronzes was studied by Le Goupil [30] due to both high pyroelectric and polar anisotropic properties and a possible tuneable ferroelectric transition towards room temperature.

For studying the anisotropic effect of $Sr_xBa_{1-x}Nb_2O_6$ (SBN) ceramics, several methods including templated grain growth [14] and hot pressing [64] can be used and can lead to orientations up to 90 % in the <001> direction. Later on, Le Goupil [30] measured the ECE of a hot-pressed textured $Sr_{0.63}Ba_{0.37}Nb_2O_6$ (SBN63) with much smaller degree of orientation and still found an anisotropic electrocaloric effect, which was higher in the direction perpendicular to pressing direction. Although the anisotropy of the electrocaloric effect was not as prominent as seen in the real part of the permittivity, where the T_m maximum value shows a difference of 1,600 between the two directions seen in Fig. 7, these preliminary results show that a large ECE could be achieved in a highly oriented SBN ceramic without the need for costly single crystals.

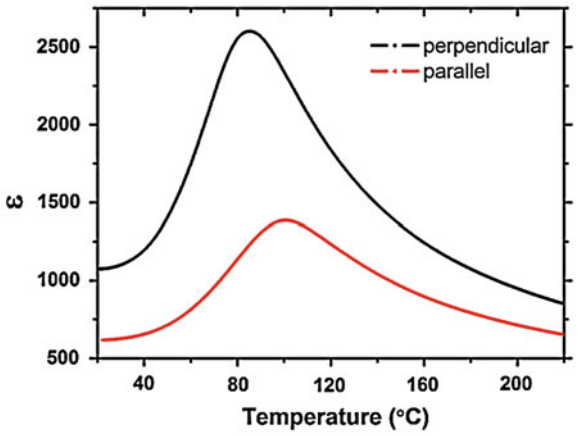

Fig. 7 Real part of the permittivity ε as a function of temperature for the hot-pressed SBN63 for samples cut in the directions parallel and perpendicular to pressing showing high dielectric anisotropy by Le Goupil [30]

4 Glycine-Based and Other Salts

Rochelle Salt is well recognised as the first commercial ferroelectric material. It is built up by potassium sodium tartrate hydrate $KNaC_4H_4O_6 \cdot 4H_2O$ with its ferroelectric axis along the a-axis and its ferroelectric transition is regarded as ordered-disordered. In an applied field there is a cooperative movement of tartrate molecule and water molecules with regard to the potassium cations creating polar states. Wiseman and Kuebler demonstrated already in [65] the simultaneous evaluation of dielectric polarization and the electrocaloric effect on one and the same sample inside a temperature chamber and published the results with a well-illustrated circuit description and evaluation. Rochelle Salt has a ferroelectric phase between the two transition temperatures of $T_{c1} = 297$ K and $T_{c2} = 255$ K and Wiseman's results are reported within this temperature region. They showed that the ECE is the highest near the upper T_c although its absolute value is very small, only 0.03 K. However, Wiseman used the knowledge from the studies of a similar hydrogen bonded ferroelectric salt system with unusual physical properties around the phase transformations. This system was potassium dihydrogen phosphate, KH_2PO_4 (KDB), another well-known ferroelectric salt. Here, each phosphorous atom is tetrahedrally coordinated by four oxygen atoms with the hydrogen atom joining each tetrahedron with its neighbours (Fig. 8). The position of the hydrogen atom in these bondings creates the ferroelectric double well potential.

On this material, Wiseman reported in [66] results of simultaneous measurements of polarization and EC temperature change above and below T_C, as a function of an applied external field. He was able to describe the experimental data for the paraelectric state but for the ferroelectric state the fit was not good despite applying a high-order Gibbs equation of state. From these relatively early electrocaloric measurements, [12] developed a microscopic theory describing the entropy change from both the dipole alignment and the materials phonon modes. This theoretic description was based on Slater's molecular theory of hydrogen

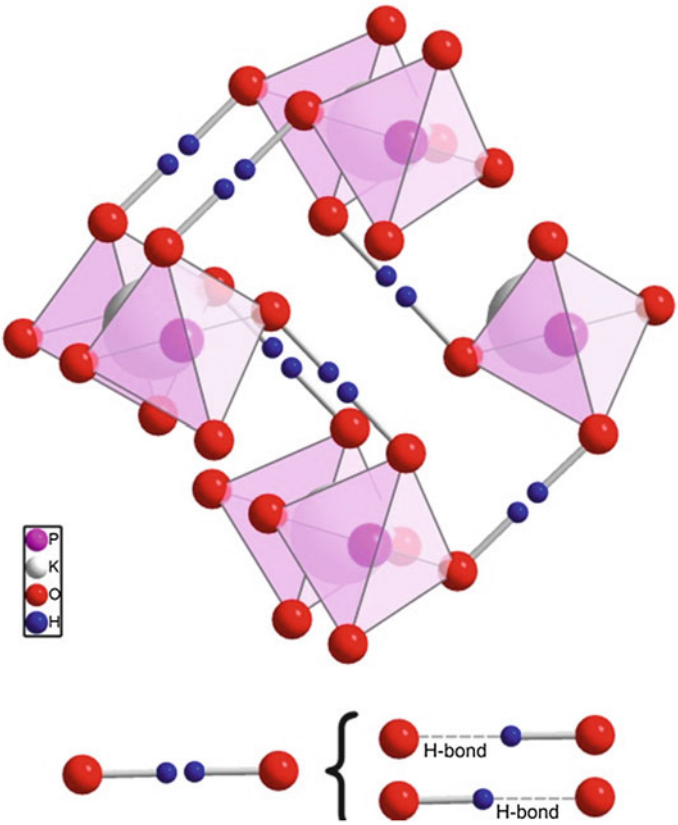

Fig. 8 A fragment of the KDP crystal structure showing the hydrogen bonding between the *octahedral* that is responsible for the double well potential and ferroelectric nature of KDP

bonded ferroelectrics, and showed how in adiabatic conditions and applied external field, the entropy reduction from the dipole alignments is compensated by a rise in temperature in order to keep the total entropy constant. Wiseman's early results and Dunne's later theory clearly show that a high EC temperature change is not possible to obtain within the ferroelectric multidomain state where the major polarization change from the domain wall movements is not associated with high entropy change. However, the observed EC temperature change is not very large for KDP with a ΔT of 0.08 when applying a field of 0.07 MV/m which brings the figure of merit to 1.14×10^{-6} m K/V [4].

These non-ceramics have so far only been investigated at very low electric fields due to their high ionic conductivity but still show remarkably high EC values and are worth further consideration.

The most investigated EC material of the glycine-based sulphates is triglycine sulphate $(NH_2CH_2COOH)_3 \cdot H_2SO_4$ that has been mainly investigated by Stukov from 1966 onwards ([55, 56, 57). The spontaneous polarization in the ferroelectric

state is along the c-axis of a pseudorhombic cell ($P2_1/c$), which undergoes a second order transition at $\sim$271 K. In the same material there is also a first order phase transition from the antiferroelectric to ferroelectric state at $\sim$159 K Flerov [15]. For practical reasons it is only the second order transition that is used for pyroelectric application as the steep $\delta P/\delta T$ is associated with a disadvantageous thermal hysteresis. Another characteristic that may cause disadvantages is its large specific heat jump, which magnitude (or step size) and transition width varies between cooling and heating. Recent electrocaloric and thermophysical evaluation of Triglycine sulphate (TGS) were performed by the group of Ramos [44, 45] who thoroughly evaluated the pyroelectric coefficient and estimated the specific heat changes near critical temperatures.

The triglycine sulphate crystals suffer from polar fatigue when used over longer time. However, the polar fatigue can be reduced when incorporating into its crystal structure so-called *intrinsic bias* by adding L-alanine, which purpose is to stabilize the crystal into a permanent monodomain. The L-alanine provides a unswitchable dipolar moment and the molecules of glycine becomes stabilized by the adjacent doped cells, which results in a reduced jump in the specific heat. From the studies of del Cerro and Ramos [11] it is learned that differential scanning calorimetry provides necessary information across the phase transitions and identification of thermal hysteresis of the physical properties of these interesting electrocaloric materials. And shows how the thermal hysteresis of the specific heat and pyroelectric properties can be reduced by dopants or other structural arrangements. This is particularly important when evaluating the change of entropy ΔS or the change of temperature ΔT across the phase transitions as

$$\Delta T = -T \int_{E1}^{E2} \left(\frac{1}{\rho C_E} \frac{\mathrm{d}P}{\mathrm{d}T} \right) \mathrm{d}E \tag{2}$$

With smart material design there is prospect to reduce the high conductivity in similar salts [60] and develop novel electrocaloric materials.

5 EC in Non-Polar Systems

Because of the fundamental requirement for the presence of the electrocaloric effect, which says that EC effect can appear only in the polar crystal systems, the non-polar systems are normally not considered. However, there are numerous examples when the non-polar system can turn into polar state under application of some external stimulus, such as e.g. electric and magnetic field or interfacial strain, or structural modification that can results from low level doping, presence of impurities or local strain fields. Here we can also consider conductive systems that turn into a polar semiconductive state under similar circumstances. A number of such examples can be listed but only few studies relate these systems to electrocaloric effect.

A non-polar system within working temperature can be converted to a polar system by application of electric field. Strictly speaking, the electric field influences the position of the ferroelectric transition in such a way that it is moved through the working temperature range, which efficiently appears as that the non-polar system has been converted to the polar state. In the case of magnetoelectrics the same effect can be induced by magnetic field. Much more common are cases when the polar state, often the ferroelectricity, is induced in thin films by compressive or tensile interfacial strain caused by the mismatch of the structural pattern of an underlying substrate and the film. A number of such systems have already been identified, among them materials quite. Examples of such materials are GdN, binary rocksalts, $CaTiO_3$ but also incipient ferroelectrics such $SrTiO_3$ and $KTaO_3$. The incipient ferroelctrics can be very efficiently converted to polar state by incorporation of small amount of dopants. They develop a real ferroelectric or even relaxor state that can lead to a significant electrocaloric effect.

These approaches are not yet explored and offer immense possibilities for further research and development in the field of electrocaloric systems. By controlling the magnitude of the applied fields an efficient tuning of the working range of the electrocaloric modules can be achieved together with optimization of the electrocaloric response. Recently another phenomenon, called flexoelectricity, has been described, which might be a source of a significant electrocaloric effect. The flexoelectricity is a property of material that induces a spontaneous polarization under strain gradient. Typically, this happens when the material is bended. However, oxide bulk materials are difficult to bend so the research is oriented more towards the materials in the shape of membranes, cantilevers and thin films. For the same reason polymers and liquid crystals are also investigated. So far no electrocaloric studies have been published yet but such systems should exhibit electrocaloric effect by definition.

A somewhat opposite approach is to convert a conducting system into the semiconductor, which can exhibit electrocaloric effect if it is in a polar state. This can be done by formation of junction barriers, which can be considered as two dimensional structures like p-n junctions, Schottky barriers or heterojunctions. For instance, the p-n junction at low temperatures exhibits very large internal resistance that gives negligible Joule heating. In addition, the internally created electric field can induce the dielectric displacement that is temperature and field dependent, and therefore EC active. For a PbTe barrier structure an EC effect of 1 K was calculated with an electric field of 3 MV/m. Another way to reduce the high bulk conductivity of PbTe is to prepare it in the form of a thin film with a thickness in the order of the Debye screening length ($\sim$50 nm). The carriers trapped in the interface between thin film and substrate would almost completely deplete the film of charge carriers and significant increase its resistance. This enables the film to be EC active with the EC effect similar to the effect in the p-n junction.

These studies give an important suggestion of how to tackle the increased conductivity of the glycine-based salts, which are due to the fact that the high internal crystal entropy exhibits a high electrocaloric effect but cannot withstand high electric fields. If we could decrease the conductivity by the described

techniques and apply the field of 3 MV/m the temperature change would be around 3.5 K. Such fields are considered as moderate and routinely applied to the oxide systems with high dielectric strength. Even higher fields would push this value further up and due to their large internal entropy the saturation would happen much later than for the known systems with so called giant electrocaloric effect.

References

1. Abdelkefi, H., Khemakhem, H., Simon, A.: Maglione M. J. Appl. Phys. **102**, 11 (2007)
2. Bai, Y., Zheng, G., Shi, S.: Direct measurement of giant electrocaloric effect in $BaTiO_3$ multilayer thick film structure beyond theoretical prediction. Appl. Phys. Lett. **96**, 192902 (2010)
3. Bai, Y., Ding, K., Zheng, G.-P., Shi, S.-Q., Qiao, L.: Entropy-change measurement of electrocaloric effect of $BaTiO_3$ single crystal, Physica. Status Solidi. (2012) doi: 10.1002/pssa.201127695
4. Benepe, J.W., Reese, W.: Phys. Rev. B **3**, 3032 (1971)
5. Berenov, A., Imperial college London, Department of Materials, private communication (2013)
6. Birks, E., Dunce, M., Sternberg, A.: A high electrocaloric effect in ferroelectrics. Ferroelectrics **400**, 336–343 (2010)
7. Bokov, A.A., Ye, Z.-G.: Recent progress in relax or ferroelectrics with perovskite structure. J. Mater. Sci. **41**, 31–52 (2006)
8. Choi, S.W., Shrout, T.R., Jang, S.J., Bhalla, A.S.: Ferroelectrics **100**, 29 (1989)
9. Davis. M., Damjanovic, D., Setter, N.: Electric-field-, temperature-, and stress-induced phase transitions in relaxor ferroelectric single crystals. Phys. Rev. B **73**, 014115 (2006)
10. de Araujo, C.A., Cuchiaro, J.D., McMillan, L.D.,. Scott M.C., Scott, J.F.: Fatigue-free ferroelectric capacitors with platinum electrodes. Nature (London) **374**, 627 (1995)
11. De Cerro, J., Martin, J.M., Ramos, S.: Specific heat measurements under non-equilibrium conditions. J. Therm. Anal. **47**(6), 1691–1700 (1996)
12. Dunne, L.J., Valant, M., Manos, G., Axelsson, A.-K., Alford N.: Microscopic theory of the electrocaloric effect in the paraelectric phase of potassium dihydrogen phosphate. Appl. Phys. Lett. **93**(12), 122906 (2008)
13. Dunne, L.J., Valant, M., Axelsson, A.-K., Manos, G., Alford, N.M.: Statistical mechanical lattice model of the dual-peak electrocaloric effect in ferroelectric relaxors and the role of pressure. J. Phys. D. Appl. Phys. **44**(37), 375404 (2011)
14. Duran, C., Trolier-McKinstry, S., Messing, G.L.: Fabrication and electrical properties of textured $Sr_{0.53}Ba_{0.47}Nb_2O_6$ ceramics by templated grain growth. J. Am. Ceram. Soc. **83**, 2203 (2000)
15. Flerov, I.N., Mikhaleva, E.A.: Electrocaloric effect and anomalous conductivity of the ferroelectric NH_4HSO_4. Phys. Solid State **50**(3), 478–484 (2008)
16. Fuith, A., Kabelka, H., Birks, E., Shebanovs, L., Sternberg, A.: Thermodynamic properties at the phase transition of Pb(Zr, Sn, Ti)O3. Ferroelectrics **237**, 153–159 (2000)
17. García, S., Marín, E., Delgado-Vasallo, O., Portelles, J., Siqueiros, J.M., Martínez, E., Heiras, J.: Specific heat of the $Ba_{0.7}Sr_{0.3}Ti_{1-y}Zr_yO$ (y = 0, 0.03, 0.05, 0.1) ferroelectric ceramics obtained by the temperature relaxation method. J. Mater. Sci. **41**(61), 30–33 (2006)
18. Granicher, H.: Helv. Phys. Acta **29**, 210 (1956)
19. Hamad, M.A.: Calculation of electrocaloric properties of ferroelectric $SrBi_2Ta_2O_9$. Phase Transitions **85**(1–2), 159–168 (2012)
20. Hegenbarth, E.: Studies of electrocaloric effect of ferroelectric ceramics at low temperatures. Cryogenics **2**, 242–243 (1961)

21. Huang, S.M., Feng, C.D., Chen, L.D., Wen, X.W.: Solid State Commun. **133**, 375 (2005)
22. Kikuchi, A., Sawaguchi, E.: Electrocaloric effect in $SrTiO_3$. J. Phys. Soc. Jpn. **19**, 1497–1498 (1964)
23. Knyazev, A., Maczka, M., Kuznetsova, N., Hanuza, J., Markin, A.: Thermodynamic properties of rubidium niobium tungsten oxide. J. Therm. Anal. Calorim. **98**, 843–848 (2009)
24. Korrovits, V.K., Liid'ya, G.G., Mikhkel'soo, V.T.: Thermostating crystals at temperatures below 1 K using the electrocaloric effect. Cryogenics **14**(1), 44–45 (1974)
25. Kutnjak, Z., Petzelt, J., Blinc, R.: The giant electromechanical response in ferroelectric relaxors as a critical phenomenon. Nature **441**, 956 (2006)
26. Lawless, W.N., Morrow, A.J.: Specific heat and electrocaloric properties of a $SrTiO_3$ ceramic at low temperatures. Ferroelectrics **15**, 159–165 (1977)
27. Lawless, W.N.: $KTaO_3$ at low temperatures. Phys. Rev. B **16**(1), 433–439 (1977)
28. Lawless, W.N.: Ferroelectrics. **24**, 327 (1980)
29. Lawless, W.N., Clark, C.F.: Dielectric and electrothermal measurements on $(Cd_{0.83}Pb_{0.17})_2Nb_2O_7$ at liquid-nitrogen temperatures. Phys. Rev. B **36**(1) (1987)
30. Le Goupil, F.: Electrocaloric effect in relaxor ferroelectrics : The road to solid state cooling, PhD Thesis, Imperial College London, Department of Materials, London, UK (2013)
31. Le Goupil, F., Berenov, A., Axelsson, A.K., Valant, M., Alford, N.M.: Direct and indirect electrocaloric measurements on $\langle 001 \rangle$-$PbMg_{1/3}Nb_{2/3}O_3$-30$PbTiO_3$ single crystals. J. Appl. Phys. **111**, 24109 (2012)
32. Lemanov, V.V., Smirnova, E.P.: Phase transitions and glasslike behavior in $Sr_{1-x}Ba_xTiO_3$. Phys. Rev. B **54**, 3151 (1996)
33. Mikhaleva, E.A., Flerov, I.N., Bondarev, V.S., Gorev, M.V., Vasiliev, A.D., Davydova, T.N.: Phase transition and caloric effects in ferroelectric solid solutions of ammonium and rubidium hydrosulfates. Phys. Solid State **53**(3), 510–517 (2011)
34. Mischenko, A.S., Zhang, Q., Scott, J.F., Whatmore, R.W., Mathur, N.D.: Giant electrocaloric effect in thin-film $PbZr_{(0.95)}Ti_{(0.05)}O_3$. Science **311**, 1270 (2006)
35. Mischenko, A.S., Zhang, Q., Whatmore, R.W., Scott, J.F., Mathur, N.D.: Giant electrocaloric effect in the thin film relaxor ferroelectric 0.9 $PbMg_{1/3}Nb_{2/3}O_3$-0.1 $PbTiO_3$ near room temperature. Appl. Phys. Lett. **89**, 242912 (2006)
36. Nagasawa, M., Kawaji, H., Tojo, T., Atake, T.: Absence of the heat capacity anomaly in the Pb-free relaxor $BaTi_{0.65}Zr_{0.35}O_3$. Phys. Rev. B **74**, 132101 (2006)
37. Noda, M., Nomura, T., Popovici, D., Murakami, S., Okyama, M.: A highly-sensitive $Ba(Ti_{1-x}Sn_x)O_3$ thin film dielectric bolometer for uncooled IR sensor. Integr. Ferroelectr. Int. J. **63**, 1 (2004)
38. Pannetier, J.: Phase transition in $RbNbWO_6$: The pyrochlore structure revisited. Solid State Commun. **34**(6), 405–408 (1980)
39. Park, S.E., Shrout, T.R.: J. Appl. Phys. **82**, 1804 (1997)
40. Park, S.E., Cho, J.A., Song, T.K., Kim, M.H., Kim, S.S., Lee, H.S.: J. Electroceram. **13**, 51 (2004)
41. Peräntie, J., Hagberg, J., Uusimäki, A., Jantunen, H.: Electric field induced dielectric and temperature changes in a $< 011 >$ oriented $Pb(Mg_{1/3}Nb_{2/3})O_3$-$PbTiO_3$ single crystal. Phys. Rev. B **82**, 134119 (2010)
42. Peräntie, J., Hagberg, J., Uusimäki, A., Jantunen, H.: Field-induced thermal response and irreversible phase transition enthalpy change in $Pb(Mg_{1/3}Nb_{2/3})O_3$-$PbTiO_3$. Appl. Phys. Lett. **94**, 102903 (2009)
43. Pruvost, G., Seveyrat, S., Lebrun, L., Guyomar, L., Guiffard, D.: Electrocaloric properties of high dielectric constant ferroelectric ceramics. J. Europ. Ceram. Soc. **27**, 4021–4024 (2007)
44. Ramos, R., del Cerro, J.: Ferroelectrics **46**, 1–4 (1982)
45. Ramos, J.F., del Cerro, S.: J. Ferroelectr. **81**, 127–130 (1988)
46. Raveza, J.: Simon A. Lead-free ferroelectric relaxor ceramics derived from $BaTiO_3$. Eur. Phys. J. AP **11**, 9–13 (2000)
47. Rozic, B., Kosec, M., Ursic, H., Holc, J., Malic, B., Zhang, Q.M., Blinc, R., Pirc, R., Kutnjak, Z.: J. Appl. Phys. **110**, 064118 (2011)

48. Samara, G.A.: The relaxational properties of compositionally disordered ABO_3 perovskites. J. Phys. Condens. Matter **15**(9), R367–R411 (2003)
49. Ke, S., Fan, H., Huang, H., Helen, L., Chan, W., Yu, S.: Dielectric dispersion behavior of Ba(ZrxTi1 − x)O3 solid solutions with a quasiferroelectric state. J. Appl. Phys. **104**, 034108 (2008)
50. Shebanov, L.A., Birks, E.K., Borman, K.Y.: Electrocaloric effect and the structure of $PbSc_{0.5}Ta_{0.5}O_3$- $PbSc_{0.5}Nb_{0.5}O_3$ solid solutions. Fizika Tverdogo Tela. **30**(8), 2464–2469 (1988)
51. Shebanovs, L., Borman, K., Lawless, W.N., Kalvane, A.: Electrocaloric effect in some perovskite ferroelectric ceramic and multilayer capacitor. Ferroelectrics **273**, 137–142 (2002)
52. Shvartsman, V.V., Kleemann, W., Dec, J., Xu, Z.K., Lu, S.G.: J. Appl. Phys. **99**, 124111 (2006)
53. Simon, A., Maglione, J.R.M.: The crossover from a ferroelectric to a relaxor state in lead-free solid solutions. J. Phys. Condens. Matter **16**, 963–970 (2004)
54. Sinclair, D.C., Attfield, P.J.: The influence of A-cation disorder on the Curie temperature of ferroelectric $ATiO_3$ perovskites. Chem. Commun. **16**, 1497–1498 (1999)
55. Strukov, B.A.: Electrocaloric effects in monocrystalline triglycine sulphate. Kristallografia **11**(6), 892–895 (1966). (in Russian)
56. Strukov, B.A.: Sov. Phys. Crystallogr. **11**, 757 (1967)
57. Strukov, B.A., Taraskin, S.A., Varikash, V.M.: Thermal and electrocaloric properties of ferroelectric triglycine selenate near the Currie point, (in Russian). Fizika Tverdogo Tela **10**(6), 1836–1842 (1968)
58. Strukov, B.A., Savilov, Z.V., Taraskin, S.A., Varikash, V.M.: Spontaneous polarization and electrocaloric effect in diglycine nitrate crystals in a range of phase transition (in Russian). Fizika Tverdoga Tela **28**(3), 733–738 (1986)
59. Sun, L., Feng, C., Chen, L., Huang, S.: J. Am. Ceram. Soc. **90**, 3875 (2007)
60. Szafranski, M.: Simple guanidium salts revisited; Room temperature ferroelectricity in hydrogen bonded supramolecular structures, J Phys. Chem. **115**(27), 8755–8762 (2011)
61. Tuttle, B.A., Payne, D.A.: The effects of microstructure on the electrocaloric properties of Pb(Zr, Sn, Ti)O3 ceramics. Ferroelectrics **87**, 603–606 (1981)
62. Valant, M., Axelsson, A.-K., Le Goupil, F., Alford, N.M.: Electrocaloric temperature change constrained by the dielectric strength. Mater. Chem. Phys. **136**, 277–280 (2012)
63. Valant, M.: Electrocaloric materials for future solid-state refrigeration technologies. Prog. Mater Sci. **57**(6), 980–1009 (2012)
64. Venet, M., Santos, I.A., Eiras, J.A., Garcia, D.: Potentiality of SBN textured ceramics for pyroelectric applications. Solid State Ionics **177**, 589–593 (2006)
65. Weisman, G.G., Kuebler, J.K.: Electrocaloric effect in ferroelectric Rochelle salt. Phys. Rev. **131**(5), 2023–2027 (1963)
66. Wiseman, G.G.: IEEE Trans. Electron. Devices ED-16, **588** (1969)
67. Zhang, L., Thakur, O.P.: Comment on the use of calcium as a dopant in X8R $BaTiO_3$-based ceramics. Appl. Phys. Lett. **90**, 142914 (2007)

Indirect and Direct Measurements of the Electrocaloric Effect

Zdravko Kutnjak and Brigita Rožič

1 Indirect Measurements

Two types of indirect measurements of the EC effect will be described. In the first method the EC change of temperature is calculated from measurements of the field and the temperature dependence of the polarization P(T, E). In the second, by phenomenological approach the entropy change is calculated by expanding the entropy in a power series of polarization. The EC entropy change is then calculated by performing two sets of experiments. In the first set the leading coefficients in the expansion are determined via linear and nonlinear dielectric spectroscopy. In the second set, the P(T, E) is determined. Possible shortcomings and the problems related to the above, indirect methods will be discussed.

1.1 Indirect ECE Determination from Measurements of P(T, E)

The ECE, i.e., the heating or cooling of an electrocaloric material due to the applied electric field under adiabatic conditions, has recently attracted a considerable amount of attention since the first prediction of the giant electrocaloric response in some inorganic and organic materials [1, 3, 19–21, 27, 28]. Specifically, a giant ECE exceeding 12 K was observed in PZT thin films around 222 °C [19]. A similarly large ECE was detected in the ferroelectric (P(VDF-TrFE))

Z. Kutnjak (✉) · B. Rožič
Jožef Stefan Institute, Jamova cesta 39, 1000 Ljubljana, Slovenia
e-mail: zdravko.kutnjak@ijs.si

Z. Kutnjak · B. Rožič
CoE Namaste, Jamova cesta 39, 1000 Ljubljana, Slovenia

Z. Kutnjak
Jozef Stefan International Postgraduate School, 1000 Ljubljana, Slovenia

T. Correia and Q. Zhang (eds.), *Electrocaloric Materials*,
Engineering Materials 34, DOI: 10.1007/978-3-642-40264-7_7,

copolymer around 70 °C, and in the relaxor ferroelectric (P(VDF-TrFE-CFE)) terpolymer near room temperature [21]. These observations were based on indirect measurements of the electrical polarization $P(T, E)$ as a function of the temperature and the electric field E. Using the well-known Maxwell relation $(\partial P/\partial T)_E = (\partial S/\partial E)_T$, the magnitude of the ECE, ΔT_{EC}, of the measured material with a density ρ and a heat capacity C_p under a change of electric field from E_1 to E_2, has been determined from [19–21, 27]

$$\Delta T_{EC} = -\frac{1}{\rho C_p}\int_{E_1}^{E_2} T\left(\frac{dP}{dT}\right)_E dE. \tag{1}$$

This formula is derived by using the Gibbs free energy G for a dielectric material expressed as a function of the internal energy of the system U, the temperature T, the entropy S, the stress X, the strain x, the electric field E and the electric displacement D [13]

$$G = U - TS - X_i x_i - E_i P_i. \tag{2}$$

The Maxwell relation can be derived for (S, T) and (D, E) [11]

$$\left(\frac{\partial S}{\partial E_i}\right)_{T,X} = \left(\frac{\partial P_i}{\partial T}\right)_{E,X} \tag{3}$$

or

$$-\left(\frac{\partial T}{\partial E}\right)_S = \frac{T}{c_E}\left(\frac{\partial P}{\partial T}\right)_E = \frac{T}{c_E} p_E. \tag{4}$$

Here, c_E is the specific heat capacity and p_E is the pyroelectric coefficient at a constant electric field. The entropy S, the strain x_i and the electric displacement are expressed as

$$S = -\left(\frac{\partial G_1}{\partial T}\right)_{X,P},\ x_i = -\left(\frac{\partial G_1}{\partial X_i}\right)_{T,P},\ P_i = -\left(\frac{\partial G_1}{\partial E_i}\right)_{T,X}. \tag{5}$$

The differential of the Gibbs free energy (Eq. 2) is given by

$$dG = -SdT - x_i dX_i - P_i dE_i. \tag{6}$$

Thus, the isothermal entropy change ΔS and the adiabatic temperature change ΔT_{EC} for the ECE material with density ρ can be expressed as [11]

$$\Delta S = \int_{E_1}^{E_2}\left(\frac{\partial P}{\partial T}\right)_E dE \tag{7}$$

$$\Delta T_{EC} = -\frac{T}{\rho c_E}\int_{E_1}^{E_2}\left(\frac{\partial P}{\partial T}\right)_E dE. \tag{8}$$

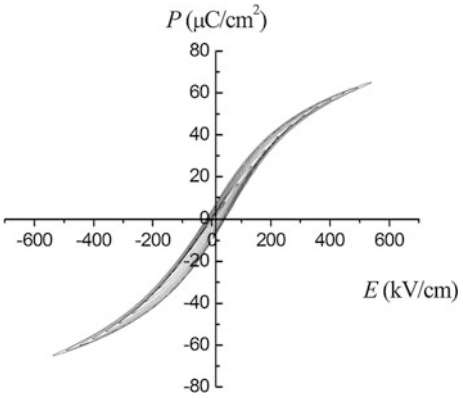

Fig. 1 Typical polarization hysteresis loop, which can be used to determine P(T, E)

From Eqs. (3) and (4) it is evident that the pyroelectric coefficient p_E is proportional to the ECE. The expressions in Eqs. (3) and (8) show that in order to achieve a large EC temperature change ΔT_{EC}, the dielectric material needs to possess a large pyroelectric coefficient over a broad temperature and the electric field range. However, in the case of the ECE in a dielectric material, both the isothermal entropy change ΔS and the adiabatic temperature change ΔT_{EC} are important parameters [18, 32]. By using Eq. (8) and measuring the polarization as a function of the temperature and the electric field it is possible to estimate ΔT_{EC}. By measuring the polarization hysteresis loops at different temperatures (see Fig. 1) the polarization $P(T, E)$ is determined (Fig. 2).

The temperature variations of $(\partial P/\partial T)_E$ are then calculated for different constant fields (Fig. 3). Smooth $(\partial P/\partial T)(E)$ functions at a given temperature are then obtained by fitting the $(\partial P/\partial T)_E$ values at a particular temperature with

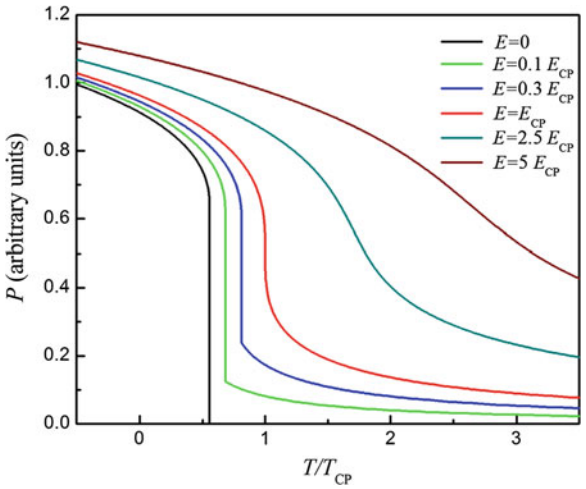

Fig. 2 Polarization as a function of temperature and electric field in the vicinity of the critical point

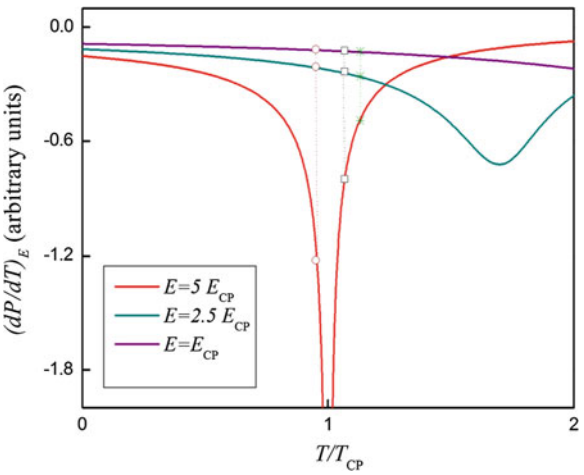

Fig. 3 $(\partial P/\partial T)_E$ as a function of the temperature and the electric field. The *dotted vertical lines* represent the temperatures at which the $(\partial P/\partial T)_E$ values were taken to be shown in Fig. 4

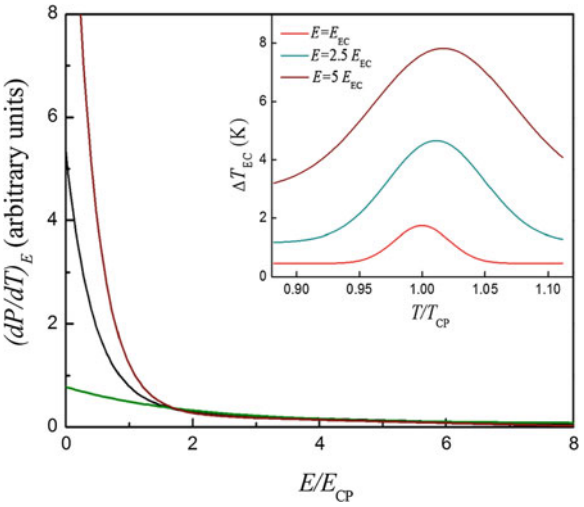

Fig. 4 Smooth $(\partial P/\partial T)(E)$ functions obtained by fitting the $(\partial P/\partial T)_E$ values at a particular temperature (see Fig. 3) with the appropriately chosen ansatz power. The inset shows the final ΔT_{EC} results after integrating the $(\partial P/\partial T)_E$ curves using Eq. (8)

appropriately chosen ansatz power (Fig. 4). These functions are then used in the integration of Eq. (8) for each particular temperature in order to evaluate ΔT_{EC} (T) (inset to Fig. 4).

1.2 Indirect ECE Determination Using a Phenomenological Approach

The adiabatic temperature change ΔT_{EC} can also be derived by using the phenomenological theory [11]. This theory is able to illustrate the macroscopic

phenomena in ferroelectric or ferromagnetic materials close to the phase-transition temperature. In the case of the ECE this phase transition is related to the order–disorder transition, which induces changes in the entropy. The Gibbs free energy is now given in terms of the electric polarization [11]

$$G = \frac{1}{2}\alpha P^2 + \frac{1}{4}\xi P^4 + \frac{1}{6}\zeta P^6. \tag{9}$$

Here, $\alpha = \beta(T - T_C)$ and β, ξ, and ζ denote the temperature-independent phenomenological coefficients. Using the relation $(\partial G/\partial T)_D = -\Delta S$, the entropy change is given by

$$\Delta S = -\frac{1}{2}\beta P^2 \tag{10}$$

and the adiabatic temperature change ΔT_{EC} is calculated from the relation $\Delta T_{EC} = (T\Delta S/c_E)$

$$\Delta T_{EC} = -\frac{1}{2c_E}\beta T P^2 \tag{11}$$

In the case of the second-order ferroelectric-paraelectric phase transition, as for example in the case of the (PVDF-TrFE) 55/45 copolymer [13, 16, 17, 21], the Gibbs free energy as a function of the polarization can be written as

$$G = G_0 + \frac{1}{2}\beta(T - T_C)P^2 + \frac{1}{4}\xi P^4 - EP, \tag{12}$$

where G_0 is the free energy of the paraelectric phase, i.e., independent of the polarization, β and ξ are the temperature-independent phenomenological coefficients, T_C is the Curie temperature, E is the electric field and P is the polarization. The relation between the polarization P and the electric field E is given by the equation of state

$$E = \beta(T - T_C)P + \xi P^3. \tag{13}$$

If $E = 0$ and $T < T_C$ then the polarization deduced from Eq. (13) is

$$P^2 = \beta(T_C - T)/\xi. \tag{14}$$

Further, if $E \neq 0$, then by differentiating Eq. (13) we obtain the reciprocal permittivity ε^{-1}

$$\frac{\partial E}{\partial P} = \frac{1}{\varepsilon} = \beta(T - T_C) + 3\xi P^2 \quad \text{if} \quad T < T_C \tag{15}$$

and

$$\frac{\partial E}{\partial P} = \frac{1}{\varepsilon} = \beta(T - T_C) \quad \text{if} \quad T \geq T_C \tag{16}$$

From Eqs. (14) and (16), i.e., the polarization versus temperature and the permittivity versus temperature relationships, the coefficients β and ξ could be determined from the experimental data. Using Eqs. (10) and (11) the ΔS and ΔT_{EC}, respectively, are then calculated.

It should be noted that the temperature of the ferroelectric-paraelectric phase transition is a function of the DC bias electric field [13]. This means that depending on the magnitude of the electric field the maximum of ΔT_{EC} will also shift to higher temperatures.

In the case of the first-order transition, Eq. (7) needs to take into account the discontinuous change of the polarization at the phase transition

$$\Delta S = \int_0^E \left(\frac{\partial P}{\partial T}\right)_E dE - \Delta P\left(\frac{\partial E}{\partial T}\right). \tag{17}$$

However, as shown above, the coefficient β could be calculated from two equations Eqs. (10) and (16). It was also shown [16] that the secondary pyroelectric effect related to the sample's dimensional changes in the polymer makes a significant contribution to the observed ECE. Thus, the experimentally measured ΔS will be larger than that calculated from Eq. (10). This means that the coefficient β from the slope of curve $\Delta S(P^2)$ will be larger than the β obtained from the dielectric data, i.e., from Eq. (16).

On the other hand, the ECE predictions of the indirect method in ferroelectric materials can only be tested by the direct method, i.e., the so-called electrocaloric thermometry, which is the subject of the next section.

2 Direct Measurements in Bulk and Thick-Film Materials

An overview of direct measurements of the EC change of temperature in bulk and thick-film materials based on standard calorimetric techniques ranging from DSC to modified methods utilizing high-resolution calorimeters will be given in this section. The limitations of each method and the error of the estimation related to the sample geometry and the field range will be discussed.

Compared to the earliest ECE investigations [8, 29, 31], ECE measurements now seem to be a straightforward and rather simple task, which always comes down to precise measurements of the sample temperature during the application of the external electric field, while precisely stabilizing the surrounding bath temperature. Relatively large, custom-made, sample holders in which simple thermocouples were used as thermometers [8, 29, 31] were later replaced by more sophisticated calorimeters ranging from DSC to high-resolution calorimeters using a variety of sensors, including highly sensitive thermistors.

Because in most solid, bulk materials (except ferroelectric polymers) the breakdown voltage is limited, the measured EC change of temperature in bulk materials rarely exceeds 2 K. In such a case the high-resolution calorimetric

techniques have a certain advantage over the low resolution techniques, such as, for instance, infrared imaging or photometry. Therefore, within this section we will limit ourselves to describing calorimetric techniques and will describe other, less accurate, but potentially fast responsive, techniques in the next section dealing with EC measurements in thin films.

2.1 Direct Measurements Using Differential Scanning Calorimetry

By far the most commonly known thermal technique used to study a wide variety of materials is differential scanning calorimetry (DSC). The DSC method has several advantages, such as a relatively good sensitivity for detecting enthalpy changes ($\sim$0.01 J/g), an ability to operate with relatively small samples ($\sim$10 mg or above), and rapid operation procedures with commercially available instruments and software. In normal operation, a constant heat flow dH_r/dt is imposed on the reference sample, resulting in a constant and linear temperature ramp. The feedback-loop system forces the sample temperature to follow that of the reference by changing the sample power input dH_s/dt. The measured quantity is, therefore, the differential power $dH/dt = dH_s/dt - dH_r/dt$. The integral $\int \left(\frac{dH}{dT}\right) dt$ provides the enthalpy related to the thermal process taking place in the sample.

With EC experiments, it is usual for isothermal conditions to be imposed, i.e., the temperature is first stabilized [3, 28]. Then the field is applied, usually in the form of sudden step on a sample immersed in silicon oil, in order to prevent arcs, and the heat flow is measured as a function of time (Fig. 5). From the measured heat flow the EC entropy or EC temperature change can be calculated.

The difficulties with the DSC method are mainly related to the fact that measurements of the ECE usually require modifications to commercial apparatus in order to be able to apply large electric fields, which is sometime difficult to

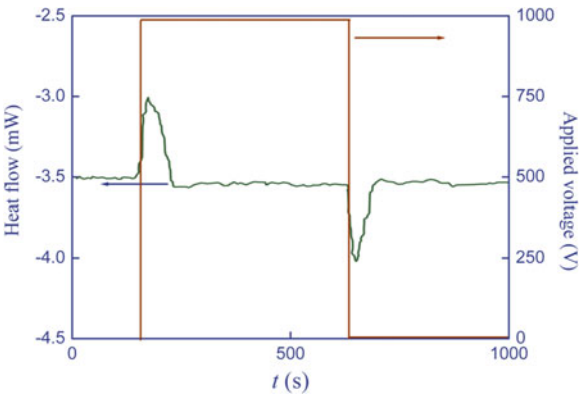

Fig. 5 Typical DSC heat-flow measurement [3]. The applied voltage step signal is also shown

implement with some commercially available machines. Another issue is related to the DSC sensitivity. DSC machines work best for fairly rapid scans, i.e., for sufficiently large heat flows. Typically, the best results would be obtained for scan rates of $dT/dt \geq 1$ K/min. Most machines would require a minimum scan rate of ~ 0.1 K/min, this means that correspondingly low heat flows would be difficult to detect with high accuracy. In most cases of ECE measurements when bulk samples are measured at relatively high electric fields, resulting in a large change of the EC temperature, the DSC represents an ideal EC survey technique. However, DSC runs into trouble when dealing with samples of small dimensions, such as thick and thin films and with small EC temperature changes, resulting in small heat flows.

2.2 Direct Measurements Using Modified High-Resolution Calorimetry

Much greater resolution can be achieved by using the so-called high-resolution calorimetric techniques such as ac and adiabatic calorimetry, which were developed in the 1960s and 1970s, respectively [9, 12]. The essential design features of these techniques are very precise control of the thermal shield and high-resolution measurements of the sample temperature. These two features are especially important in any direct method of determining the magnitude of the EC effect, thus making high-resolution calorimetric techniques very suitable for the above task. Many commercially available or homemade apparatuses can be relatively easily upgraded to perform EC thermometry.

The main important difference between the classic heat-capacity measurements and the EC measurements is that in latter the temperature of the bath is stabilized and the sample temperature is measured as a function of time, while a special form of electrical signal is applied to the sample. In the case of the former the bath temperature is typically scanned, while the sample temperature is measured as a function of time, and a special form of heating power signal is applied to the sample. Therefore, the main issues associated with a high-resolution calorimeter upgrade in order to perform the EC thermometry are (1) mounting additional feeding-through wires reaching the heart of the sample holder, through which the electric field signal is applied to the sample from; (2) an additional high-voltage programmable signal generator; and (3) the adjustment of the measurement triggering system to start the sample temperature measurement in coordination with the external field signal application.

A simple schematic presentation of a homemade, ac, high-resolution, calorimeter upgrade to an EC thermometric system is given in Fig. 6.

Here, instead of the arbitrary signal generator a high-voltage generator driven by an arbitrary signal generator is used to generate the electric field step signal, which is then applied to the sample. Specifically, the calorimeter set-up consists of

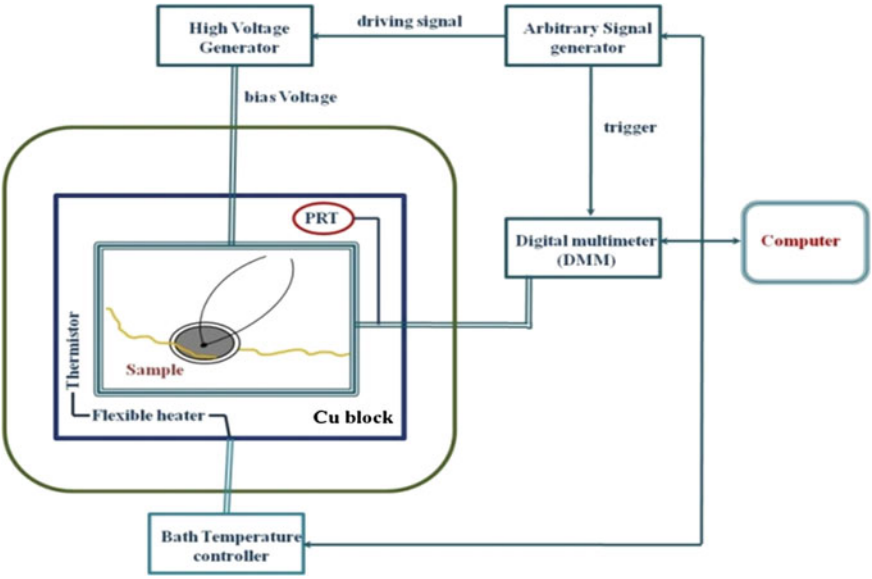

Fig. 6 A simple schematic presentation of the ECE measurement set-up. In contrast to the ac calorimetry, instead of heat power an external field is applied to the sample

the high-voltage generator, the arbitrary signal generator, the digital multimeter (DMM), the temperature controller and a computer. The high-voltage generator and the DMM are trigged by the arbitrary signal generator. The DMM measures the platinum thermometer (PRT) resistance and the resistance of the micro-bead thermistor attached to the sample (denoted by c in the schematic Fig. 7, see also the sample arrangement of the bulk and thick films in Fig. 8). The data are then collected from the DMM by the computer, which via the temperature controller also controls the surrounding bath temperature.

The bath temperature is measured by another platinum thermometer and it is also detected by a thermistor mounted in a copper (Cu) block. The flexible heater attached around the Cu block enables precise temperature stabilization. The temperature of the outer can is controlled by a temperature controller with a

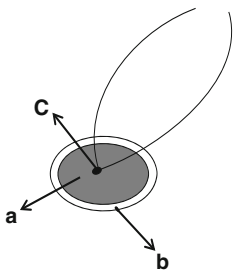

Fig. 7 A sketch of the sample; **a** a part of the sample covered with an electrode; **b** a sample without an electrode, and **c** a small bead thermistor [23]

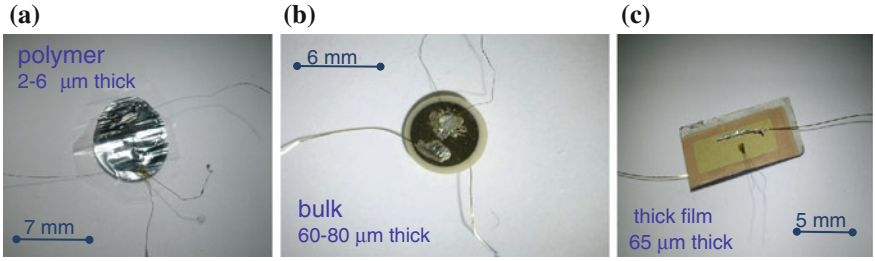

Fig. 8 The typical sample arrangements are shown for **a** polymer, **b** bulk material, and **c** self-standing thick film. A small bead thermistor and the gold wires were directly attached to the samples by heat or electrically conductive paste, respectively

thermistor attached to the can. The shape, length, and the amplitude of the electric pulses are controlled by the computer via the programmable, arbitrary signal generator. More details associated with the electronic aspects of a typical ac calorimeter can be found in Refs. [9, 33].

Various shapes of electric signal can be used; some are shown in Fig. 9. The most typical and widely used is the electric step signal shown in Fig. 10. Here, the signal is symmetric with respect to how the field is applied and switched off. The EC temperature change is measured in the vicinity of both the on and the off slopes (Fig. 10). Such a signal is very useful in order to determine the asymmetry of the EC response if the field is switched on or off, which can give some additional information about the resistive or Joule heating of the sample or the internal dielectric losses related to the broad polarization hysteresis loop or the large switching currents. Significant Joule heating is observed as an additional elevated

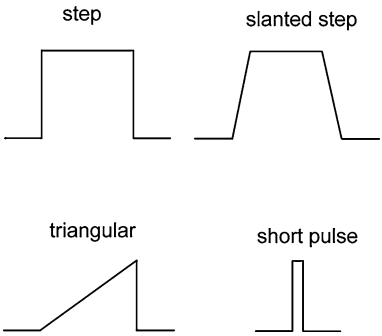

Fig. 9 Different pulses of the electric field used during the ECE measurements. Standard step pulses are usually long enough to allow relaxation of the sample temperature back to the bath temperature, i.e., several times longer than the external thermal relaxation time, while the short pulses are typically longer than the response time of the sensor, but not shorter than the polarization switching time

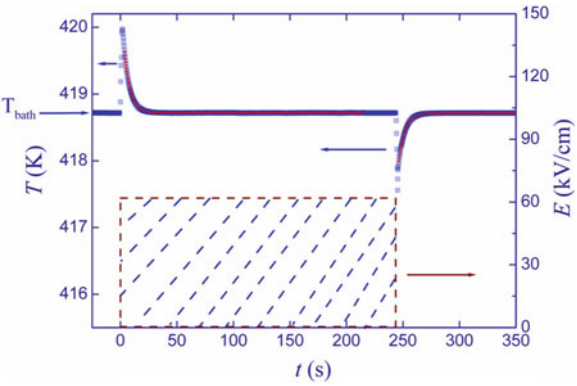

Fig. 10 Measured EC data (*open circles*), the fit (*solid line*), and the schematic representation of the electric field pulse [24]. Here, the symmetry of the EC spikes and no elevated background-temperature level during the pulse duration show negligibly small Joule heating and dielectric losses

temperature long after the initial EC increase of the temperature should relax back to the bath temperature, while the electric field is still on.

Depending on the properties of the sample, sometimes other shapes of the electric pulse are desired. In some materials a relatively large polarization switching current in the case of the electric step pulse can induce or speed up the electrical breakdown of the sample, i.e., can help to reduce the breakdown voltage. In such a case using a slower voltage slew rate in the form of a triangular shaped electric pulse could be helpful. Similarly, electrical pulses can be shaped to have some finitely, instead of infinitely, steep slope.

The time span of the electrical pulses is usually chosen to be long enough to allow relaxation of the sample temperature back to bath temperature, i.e., several times longer than the external thermal relaxation time. However, some times this requires very long pulses, exceeding several hundred seconds, which at higher fields could cause additional damage to the sample. In such a case the application of much shorter pulses is required. If the length of the pulse is getting shorter than the sample's external thermal relaxation time, then the on and off spikes start to interfere, i.e., they start to cancel each other out (see Fig. 11). In such a case a recalibration of the short pulse signal is required by, for instance, comparing the signals obtained while using both the standard and short length pulses at some reasonably low field. The short pulses should typically be longer than the response time of the thermometric sensor, but not shorter than the polarization switching time, which is typically of the order of 10 μs.

Sometimes the application of short pulses with a moderate amplitude could help to anneal frozen-in stresses, which could make the zero electric field state already ordered, thus reducing the EC effect. Such a situation can be easily encountered in thin films on a substrate where the substrate stress field can significantly influence the order of the zero electric field state. In this case a negative EC effect can often

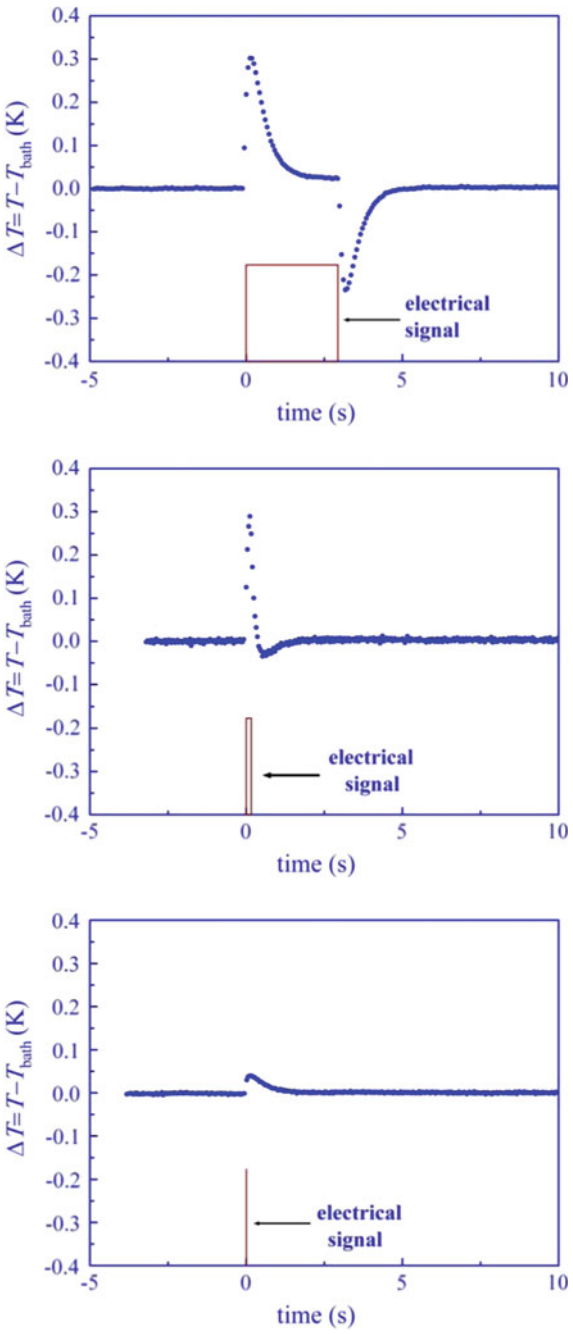

Fig. 11 The effect of the pulse length on the sample's EC temperature response. When the width of the pulse become comparable with the external thermal relaxation time the on and off anomalies start to cancel each other

be observed, in which with increasing field instead of heating, cooling of the sample is observed, as a consequence of the initial creation of the disorder to the stress-field ordered state by the nonparallel electric field.

In data analysis, the long external thermal relaxation time in comparison to the fast electric, as well as the internal thermal response times, allows the application of a zero-dimensional model with sufficient accuracy. For example, the details of the specific rigorous data analysis and the applied zero-dimensional model are given in Ref. [23]. Rigorous data analysis should carefully take into account the different subsystems (such as parts of the sample without electrodes, thermometer, attached wires, inactive substrates, etc.) and the corresponding heat-flow dynamics among them. Figure 12 shows a typical system (see Figs. 7 and 8) consisting of a sample with an attached thermistor coupled to a bath via the thermal resistance, and it is divided into subsystems related to a part of a sample with electrodes, to that without electrodes and to the thermistor. Each subsystem has its own heat capacity C_p, which are known quantities.

Here, T_1, T_2, T_b and T_t denote the temperatures of the part of the sample with the electrode, the part of the sample without electrodes, the bath temperature and the thermistor temperature, respectively. The symbols R_i, i = 1, …, 5, are related to the thermal resistivities between the different parts shown in Fig. 12 and the $C_{p,\,se}$, $C_{p,\,sw}$, $C_{p,\,t}$ are the heat capacities of the part of the sample covered with the electrode, of the part of the sample without the electrode and of the thermistor, respectively.

Due to the small mass of the thermistor and the good coupling between the sample and the thermistor, relatively fast internal thermal response times are achieved in the bulk and thick films in comparison to the external thermal time scale related to the coupling to the bath. Consequently, the system in Fig. 12 can be solved by using a two-step simplification and assuming a step electrical signal [23]

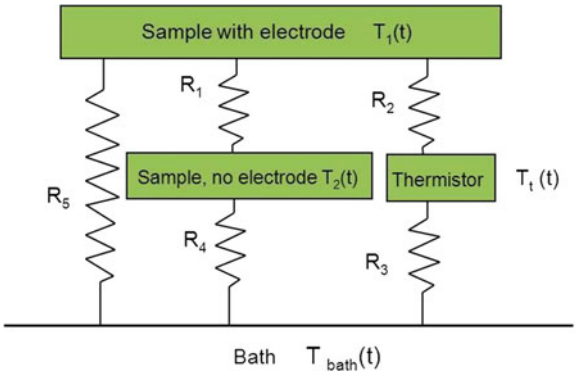

Fig. 12 Schematic representation of the typical sample thermal subsystems and their mutual coupling. Each subsystem has its own heat capacity C_p and the couplings are represented by the thermal resistances R_i, i = 1, …, 5 [23]

$$T_t(t) = T_{bath} + [(1 - A - C)\Delta T_{res} + (B + D)\Delta T_{EC}]e^{-t/\tau_1} + (A\Delta T_{res} - B\Delta T_{EC})e^{-t/\tau_2} + (C\Delta T_{res} - D\Delta T_{EC})e^{-t/\tau_S}, \tag{18}$$

with $T_t(0) = T_{bath} + \Delta T_{res}$ and the constants A, B, C and D defined as

$$\begin{aligned} A &= \frac{\tau_{21}\tau_{32}(\frac{R_1 C_{p,sw}}{\tau_{32}} - 1)}{(R_1 C_{p,sw} + \tau_3)R_2 C_{p,t}} \\ B &= A(1 + \frac{\tau_3}{R_1 C_{p,sw}}) \\ C &= \frac{\tau_{31}\tau_{32}}{(\frac{R_1 C_{p,sw}}{\tau_3} + 1)R_2 C_{p,t}\tau_2} \\ D &= C\frac{\tau_2(1 + \frac{\tau_3}{R_1 C_{p,sw}})}{\tau_3}, \end{aligned} \tag{19}$$

where $\tau_{ij} = \tau_i\tau_j/(\tau_i - \tau_j)$. ΔT_{res} represents the additional Joule heating of the sample due to the finite electric conductivity.

It can be determined very precisely from the difference $\Delta T_{res} = T_t(t_F) - T_t(0)$ between the initial temperature level at t = 0 (field not turned on yet) and the temperature level reached at some long time t_F that exceeds the external thermal time in which the sample reaches equilibrium with the external bath and in which the electric field still remains to be turned on. Analogously, it can also be determined from the data measured when the field is switched off by considering the difference $\Delta T_{res} = T_t(t_F) - T_t(\infty)$. Here, $T_t(\infty)$ represents the temperature level at very long times after the electric field is switched off. It is important to note that ΔT_{res} is found to be negligibly small in most bulk and thick-film samples. For example, as shown in Fig. 12, $T_t(t_F) - T_t(\infty) \approx 0$ indicates no resistive heating of the sample. Only in thin films at higher fields does the resistive Joule heating become important enough to be included in the data analysis. Here, ΔT_{res}, $C_{p,sw}$, $C_{p,t}$, R_1 and T_{bath} are already determined, known quantities, while R_2, τ_i, ΔT_{EC} are fit parameters. R_1 is defined from the heat-transfer equation for a specific geometry of the sample. Such a method of data analysis works fine for describing the $T_t(t)$, as shown by the solid line representing the fit to the measured data in Fig. 13.

Here, the fit parameters can be established very precisely due to the large number of precisely measured data points. In fact, it turned out that such a rigorous analysis is, in most cases, unnecessary due to the rather fast internal thermal relaxation times and a much simplified procedure of data analysis can be employed.

In the case of very fast internal thermal response times, typically of the order of a few milliseconds up to a second, a very fast equilibration of the temperature throughout the whole sample, including electroded and unelectroded parts, any substrate, electrodes, attached thermometer and wires, takes place. Such a thermally equilibrated system now slowly exchanges the heat on a much longer time

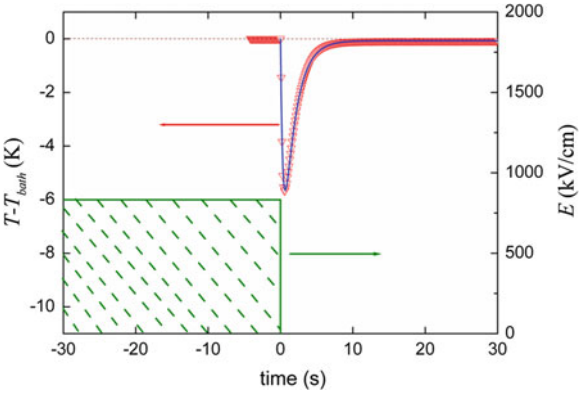

Fig. 13 Directly measured EC data on the P(VDF-TrFE-CFE) terpolymer film blending with 5 wt % of P(VDF-CTFE) copolymer (*solid circles*) [15], the fit to Eq. (18) (*solid line*) and the schematic representation of the electric field pulse duration

scale to the surrounding bath. In this case only the external exponential relaxation of the temperature of the whole internally equilibrated system is first considered [23, 24]

$$T(t) = T_{\text{bath}} + \Delta T e^{-t/\tau}. \tag{20}$$

For simplicity we neglected here the Joule heating, which can be easily taken into account. The determined ΔT from the fits can be typically a few percent to 30 % larger than the observed maximum temperature deviation from the bath temperature. This difference is directly related to the losses to the bath during the internal equilibration between the different components of the system (Fig. 12). The EC temperature change of the participating subsystem ΔT_{EC}, i.e., the part of the sample covered with the electrodes is determined by taking into account the geometry of the system and the heat capacities of its constituents:

$$\Delta T_{\text{EC}} = \Delta T \frac{\sum_{\text{i}} C_{\text{p}}^{\text{i}}}{C_{\text{p}}^{\text{EC}}}. \tag{21}$$

Here, C_{p}^{i} typically stands for the heat capacities of the attached, small, thermistor-supporting wires, electrodes, and part of the sample without electrodes, i.e., all the subsystems participating in the fast internal equilibration. C_{p}^{EC} denotes the heat capacity of the sample covered with electrodes in which the EC effect takes place. C_{p}^{EC} is typically known within 0.3 %. In bulk materials, depending on the sample thickness, the total heat capacity of the other materials attached to the sample was only 3–5 % of the C_{p}^{EC}. Taking into account the few percentage points of error in the determination of these small extra heat capacities and the very reliable determination of ΔT from the simple fit of several hundred data points, the total error of ΔT_{EC} is below 1 % in the case of bulk materials [23, 24].

The above calorimetric method and the simplified data analysis can also be used for EC effect determination in thick films on a substrate or even self-standing thick

films (see Fig. 8c) if the external thermal relaxation time is much longer than the internal thermal relaxation time [10, 24]. In this case again, the external exponential relaxation of the whole system, including the substrate, is monitored and ΔT_{EC} is obtained from Eq. (21). Here, $\sum_i C_p^i$ includes the heat capacities of any substrate layers. While in the case of bulk materials the ratio $\frac{\sum_i C_p^i}{C_p^{EC}}$ is between 1–1.5, in the case of self-standing thick films in which a thick film that is a few tens of μm thick is deposited on a 5–10 μm-thick platinum electrode this ratio is typically less than 1.5, i.e., still close to one. However, in thick films on a substrate $\frac{\sum_i C_p^i}{C_p^{EC}}$ can easily exceed a value of 10, depending on the thick film and the substrate-thickness ratio. The determination of the volume of such systems, which can be measured to within few percent, is thus the main source of the error in the ΔT_{EC} determination. In most cases such an error is typically between 1 and 5 %.

The EC entropy change ΔS is determined from

$$\Delta S = \frac{mc_p \Delta T_{EC}}{T} \tag{22}$$

where T is the temperature at which the ΔT_{EC} was measured, and c_p and m are the sample's specific heat capacity and mass, respectively.

2.3 Examples of Direct Measurements Using a Standard Calorimetric Technique

Here, a few examples of direct ECE measurements performed by using an upgraded, high-resolution calorimeter (see Fig. 6) on various inorganic and organic ferroelectric bulk materials, including self-standing and thick films on a substrate, are presented. The typical stabilization of the bath and the sample-temperature resolution is within 0.1 mK for the below examples.

2.3.1 Ferroelectric Polymers

The directly measured ΔT_{EC} and the specific entropy $\Delta s = \Delta S/V$ change as a function of temperature between 295 and 332 K, and the electric field amplitude for the P(VDF-TrFE-CFE) terpolymers blending with 5 wt % of P(VDF-CTFE) copolymer are presented in Fig. 14. The example of the EC response for this particular material is shown above in Fig. 13. The electrocaloric effect reaches the maximum value at a temperature of around 320 K, i.e., near the relaxor dielectric peak [15]. The maximum temperature change ΔT_{EC} is around 12 K, and the specific entropy Δs is around 50 J/kgK at the magnitude of the electric field of $E = 1.7$ MV/cm.

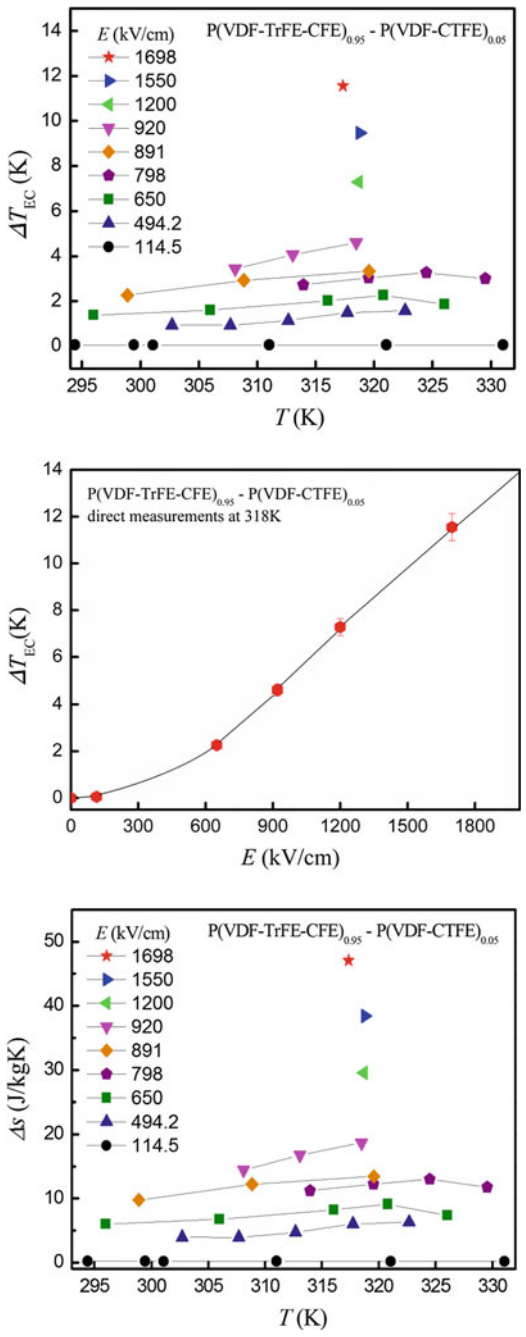

Fig. 14 The ECE temperature ΔT_{EC} and the specific entropy change measured on the P(VDF-TrFE-CFE) terpolymers blending with 5 wt % of P(VDF-CTFE) copolymer as a function of the temperature and electric field [15]

2.3.2 Inorganic Bulk Perovskite Relaxor Ferroelectrics

The directly measured EC temperature ΔT_{EC} and the specific entropy Δs change as a function of temperature between 310 and 440 K and the electric field for the bulk PMN-0.30PT ceramics are presented in Fig. 15.

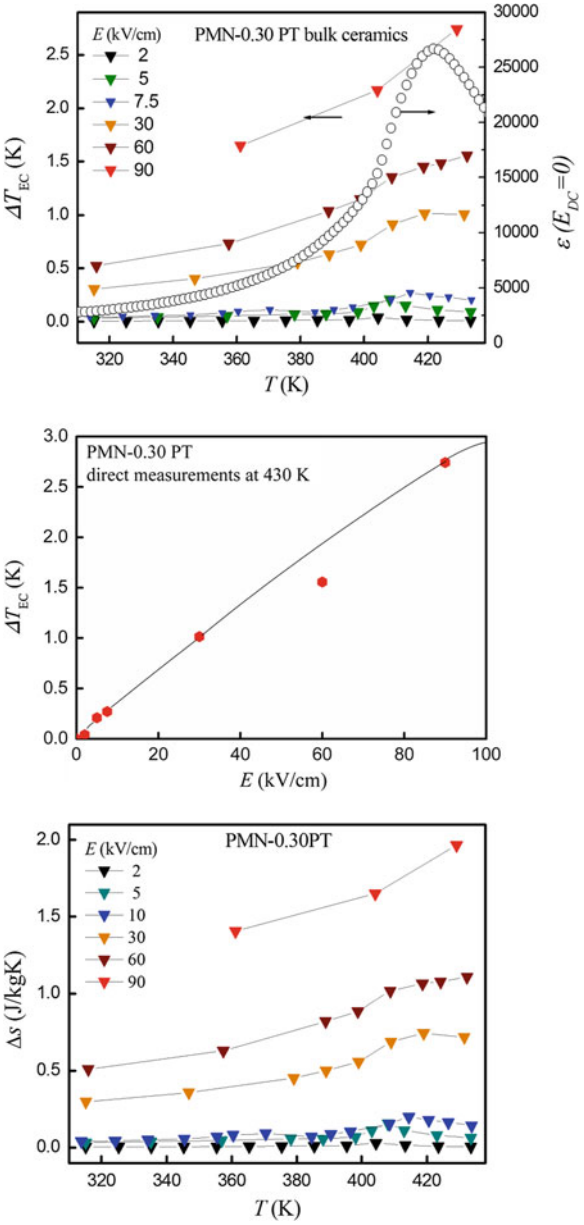

Fig. 15 The ECE temperature ΔT_{EC} and the specific entropy change measured on bulk PMN-0.30PT ceramics as a function of temperature and electric field [24]. The *open circles* denote the dielectric constant measured at a low electric field

The example of the EC response for this particular material was shown before in Fig. 10. The dielectric measurements in bulk PMN-0.30PT and 8/65/35 PLZT show that the ΔT_{EC} exhibits a broad maximum near the phase transition (open circles in Fig. 15), which takes place on the low-temperature slope of the dielectric peak [10, 24]. Moreover, it was observed that at higher electric fields, the maximum of the ΔT_{EC} is shifted towards higher temperatures following the field-induced shift of the ferroelectric transition [10, 24].

The ΔT_{EC} as a function of the electric field amplitude at a constant temperature for the bulk PMN-0.30PT ceramics is presented in Fig. 15. Due to the low breakdown field in the bulk perovskite relaxor ferroelectric materials, the maximum achieved amplitude of the electric pulse was typically below 100 kV/cm. Nevertheless, in comparison to previously published data [1, 3, 19–21, 27, 28], the relatively high ΔT_{EC} obtained at relatively modest fields indicates the existence of a giant ECE in these materials.

For all the measured perovskite relaxor ferroelectric materials the largest effect between 2 and 3 K was observed at the field amplitude between 60 and 90 kV/cm [24] near the electric-field-induced ferroelectric phase transition [1, 3, 19–21, 24, 27, 28, 30]. On the other hand, it was recently shown that even in pure relaxor systems exhibiting a glass state at low temperatures, such as the PMN system, a significant EC effect is observed due to the fact that the ferroelectric transition is induced at the electric field strengths employed in the EC experiment [24]. The amplitude of ΔT_{EC} directly measured for the PMN sample in a broad temperature range shows that the bulk PMN exhibits a weak temperature variation of the ECE near room temperature [24].

In addition, it was also reported recently that in bulk perovskite relaxor ferroelectrics the effective EC responsivity $\Delta T_{EC}/E$ exhibits a significant enhancement in the vicinity of the liquid–vapour type critical point (see Fig. 16) [22, 24].

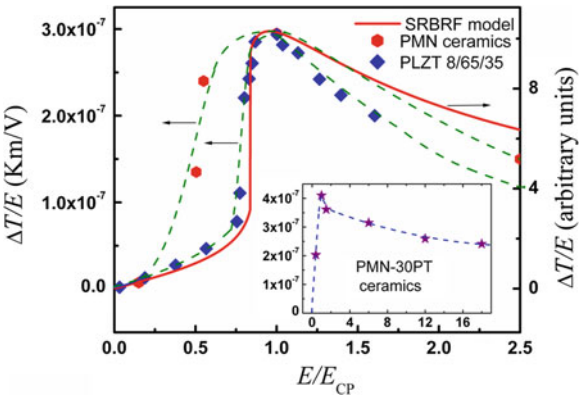

Fig. 16 The EC responsivity $\Delta T_{EC}/E$ as a function of the electric field for PMN, PMN-0.30PT and 8/65/35 PLZT ceramics in the vicinity of the critical point, i.e., measured at the critical temperature T_{CP} under fields below and above the critical field E_{CP} [24]

2.3.3 Thick Perovskite Relaxor Ferroelectric Films on a Substrate

Like with the bulk materials, the thick films on the substrate exhibit rather low break-down fields ~80 kV/cm. Consequently, it is not possible to apply very large electric fields in the EC experiments. Comparing the results obtained at a similar value of the electric field, i.e., about 68 kV/cm, ΔT_{EC} reaches a similar value as in bulk materials, i.e., around 1.8 K in thick films of 8/65/35 PLZT ceramics on the alumina substrate (Fig. 17). Such a result is not surprising, since the thickness of the thick films was about 30 μm, which is much larger than the grain or domain size. The ECE response was investigated here in the temperature range between 350 and 395 K. The maximum is achieved at a temperature of approximately 380 K, i.e., near the induced ferroelectric phase transition.

Figure 18 presents measurements of ΔT_{EC} and EC change of the specific entropy density Δs as a function of the electric field at a constant temperature of 374 K in thick 8/65/35 PLZT films. The specific entropy change Δs for the thick film is 1.5 J/kgK at a field strength of 68 kV/cm, which is also comparable to the bulk value [24].

In the above presented EC results measured on thick films on an alumina substrate using the standard high-resolution calorimetric technique, the ratio $\frac{\sum_i C_p^i}{C_p^{EC}}$ exceeded a value of 100, yet the error of the ΔT_{EC} estimation was less than 5 % and the results were, as expected, in good agreement with the results obtained on bulk 8/65/35 PLZT ceramics, where $\frac{\sum_i C_p^i}{C_p^{EC}} \approx 1.5$ [24].

2.3.4 Self-Standing PMN-0.35PT Thick Films on a Platinum Layer

Like in the case of PMN-0.35PT bulk materials, in PMN-0.35PT thick films on a 10 μm Pt layer it was not possible to use very large electric fields due to the

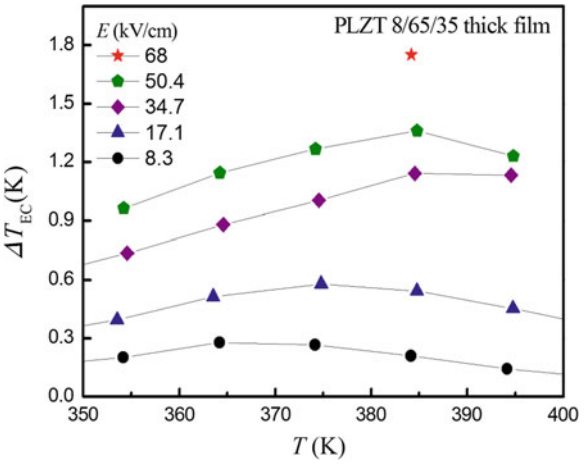

Fig. 17 The ECE temperature change ΔT_{EC} in a thick film of 8/65/35 PLZT ceramics on an alumina substrate as a function of the temperature for different values of the electric field amplitude [25]

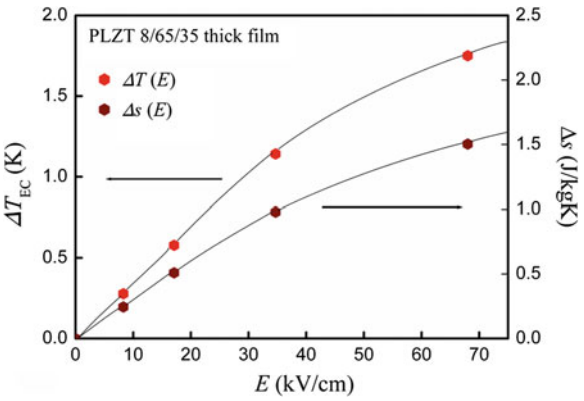

Fig. 18 Electric field variation of the ECE temperature change ΔT_{EC} and the specific entropy change Δs for a thick film of 8/65/35 PLZT ceramics on an alumina substrate measured at a constant temperature of 374 K [25]

relatively low break-down field of about 80–90 kV/cm. However, a large $\Delta T_{EC} \approx 2$ K, comparable to that observed in bulk materials, was still observed for a relatively small amplitude of the electric field $E = 80$ kV/cm, at a temperature of 427 K. The ΔT_{EC} as well as the specific entropy change Δs as a function of the electric field are presented in Fig. 19.

In the case of a self-standing PMN-0.35PT thick film on a Pt layer, the ratio $\frac{\sum_i C_p^i}{C_p^{EC}}$ was similar to that in bulk materials, i.e., close to 1.5, and the error of the estimation of ΔT_{EC} was less than 3 %, and the EC results, which agree with those obtained in bulk samples, show that a slightly different procedure for the thick films' preparation does not have a significant impact on the magnitude of the ECE [24]. We will see in the next section that the story is very different in the case of thin ceramic films.

3 Direct Measurements of Thin Films

Single-layer and multilayer thin ferroelectric films have recently attracted a lot of attention because of their advantages in various applications, ranging from computer memories, large capacitors to MEMS. It was found that the ferroelectric properties are usually smeared over a broad temperature range, that the coercive field could be several times larger than in bulk materials and that the polarization hysteresis loops are slimmer and with lower dielectric loses than in the bulk. Because a thin film can be prepared very uniformly and without many defects, it can survive much larger electric fields, thus pushing the breakdown voltage to very high values, in some materials exceeding several MV/cm.

The fact that in some materials the magnitude of the induced polarization could, in thin films, exceed that in bulk by a factor of 2–3 is especially important, because the entropy change is directly proportional to the square of the field induced change in polarization [14, 22]. All these make thin films very good candidates for

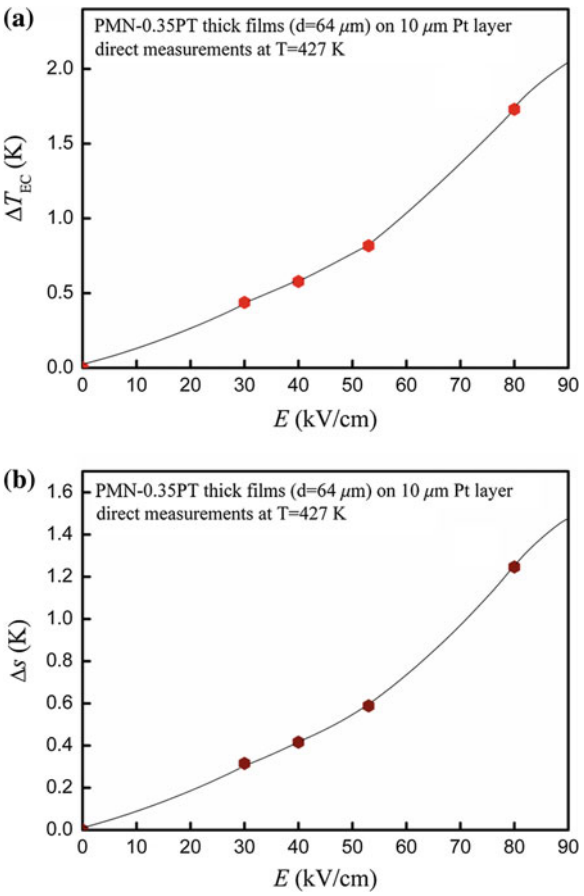

Fig. 19 Electric field variation of **a** the ECE temperature change ΔT_{EC} and **b** the specific entropy change Δs for PMN-0.35PT thick films on a Pt layer measured at a constant temperature of 427 K [26]

materials with a large EC effect and earlier indirect experiments [19] in which ΔT_{EC} exceeded 12 K provided an additional stimulus to carry out direct EC measurements on thin films.

Since then many experiments, mostly indirect, were performed on thin films [1, 19–21, 27]. Only a few results obtained on thin films by direct methods were published so far [14]. The main problem with carrying out direct experiments is related to the very fast relaxation of the EC heat ($\Delta S_{EC}T$) to the relatively thick substrate. For instance, in the case of a 0.5 μm-thick PLZT thin film on a 0.5 mm-thick Si substrate the film would lose 50 % of the EC heat in less than 1 μs. The whole block would come to equilibrium within ≈10 ms, but in this time less than 0.1 % of the original EC heat would remain in the film and correspondingly the original ΔT_{EC} would drop to less than 1/1,000 of the original value. Therefore, if the electric field induces $\Delta T_{EC} \approx 10$ K, after ∼10 ms only a few mK could be detected at the film surface. Such a rapid exchange of the EC heat with the substrate significantly complicates a direct on-line measurement of the ECE in thin films.

Recently, two approaches were adopted in the EC community to tackle this problem. One was based on the same high-resolution calorimetric technique as described above for thick films, which is adopting the measurements of the EC temperature change of the whole block, including the substrate, from which the ΔT_{EC} of the thin-film layer could be estimated within an error estimation of below 10 % [24]. This technique does not require fast thermometry, because it is anyway measuring the thermally relaxed system. The aim of the second approach is to directly determine the ΔT_{EC} of the film layer before it exchanges the heat with the substrate. Here, rapid thermometry techniques are required, which can sample the temperature of the film surface with high accuracy on a frequency scale of MHz or higher. Recently, IR photometry, fast IR cameras, and fast thermometry using the resistivity of thin electrodes as sensors were adopted with some success [7].

In this subsection, an overview of the direct measurements of the EC change of temperature in thin films on a substrate or self-standing polymer films will be provided. The main emphasis will be on direct measurements via the thermal method based on (1) a modified high-resolution calorimetry using a different type of sensors and (2) the EC temperature change observations via high-speed thermometry such as fast measurements of the thin film resistors, infrared (IR) photometry or IR cameras and fast scanning thermal microscopy. The limitations of the different methods and the error estimation will be discussed.

3.1 Direct Measurements in Thin Films Using a Calorimetric Technique

This method can be used for both thin films on a substrate and thin, self-standing polymer films. In the case of thin films on a substrate the samples are, for example, prepared as shown in Fig. 20 for an 8/65/35 PLZT ceramic thin film [14]. In this particular case the 0.45 μm-thick PLZT film was deposited by the sol–gel

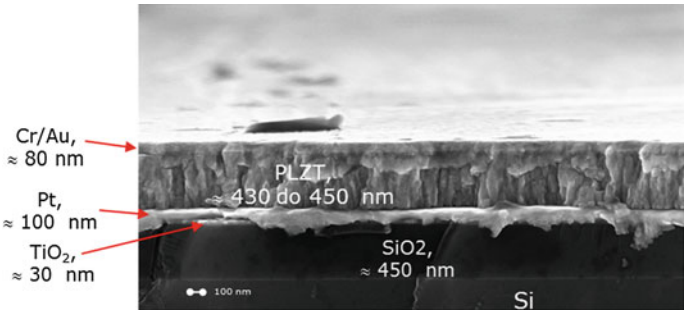

Fig. 20 Example of the 8/65/35 PLZT thin-film configuration obtained by SEM. The PLZT thin film is covered with a Cr/Au (*top*) and a Pt (*below*) electrode and the TiO_2 and SiO_2 layers are below the Pt layer. All these layers are deposited on a thick Si monocrystal [14]

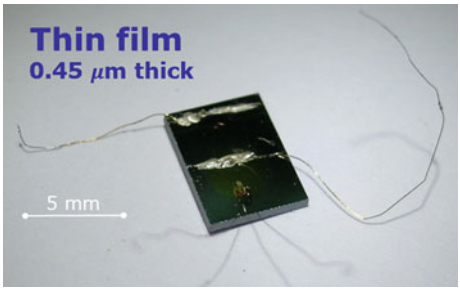

Fig. 21 A typical thin-film sample arrangement for EC measurements using the high-resolution calorimetric technique [14]

technique on a 100 nm-thick Pt layer serving as a bottom electrode. The upper Cr/Au electrode is typically less than 100 nm thick. In order to induce as large an EC heat as possible the diameter of the upper electrode should significantly exceed that typically used for dielectric measurements, i.e., a diameter between 1 and 3 mm is desired. By increasing the surface of the electrodes the break-down voltage usually decreases significantly, but an electric field between 0.5 and 1.5 MV/cm can still be reached. Furthermore, the lower Pt electrode is deposited on 30 nm-thick TiO_2 and 450 nm-thick SiO_2 layers. All these layers are deposited on a 600 μm-thick Si monocrystal substrate. The small bead thermistor is attached to the surface of the film and electrical leads to electrodes, as shown in Fig. 21.

It was found with dielectric experiments that the dielectric constant shows a relatively smooth variation of the temperature in the above ceramic film. As a consequence the ECE in the PLZT thin film is a weak function of temperature in the vicinity of room temperature [14]. Therefore, the EC temperature change ΔT of the whole block, including the substrate, is measured as a function of the applied electric field by applying the same technique as described in Sect. 2.3.3 for thick perovskite relaxor ferroelectric films on a substrate. Here, the ratio $\frac{\sum_i C_p^i}{C_p^{EC}}$ is estimated directly from the measured thicknesses of each deposited layer (Fig. 20) and the carefully weighed masses of the thermistor and the attached thin electrical wires. The specific heat capacities of each material were either determined separately or found in the literature. The determination of the ratio $\frac{\sum_i C_p^i}{C_p^{EC}}$ turns out to be the main source of error, which could reach 10 %. For the above example of the 8/65/35 PLZT thin ceramic film the ratio $\frac{\sum_i C_p^i}{C_p^{EC}} = 3,230 \pm 150$ was estimated within ±5 %.

An example of determining the ECE in thin films is presented in Fig. 22. Here, the relaxing temperature change ΔT for a whole block, including the substrate, due to the heat exchange with the surrounding bath is presented after the electric step pulse was switched on (Fig. 22a) and after the electric field was switched off (Fig. 22b). The initial fast-changing data within the first few seconds is a remnant of the internal sample equilibration taking place on a much faster time scale (within a second). This includes both the vertical heat flow through the substrate

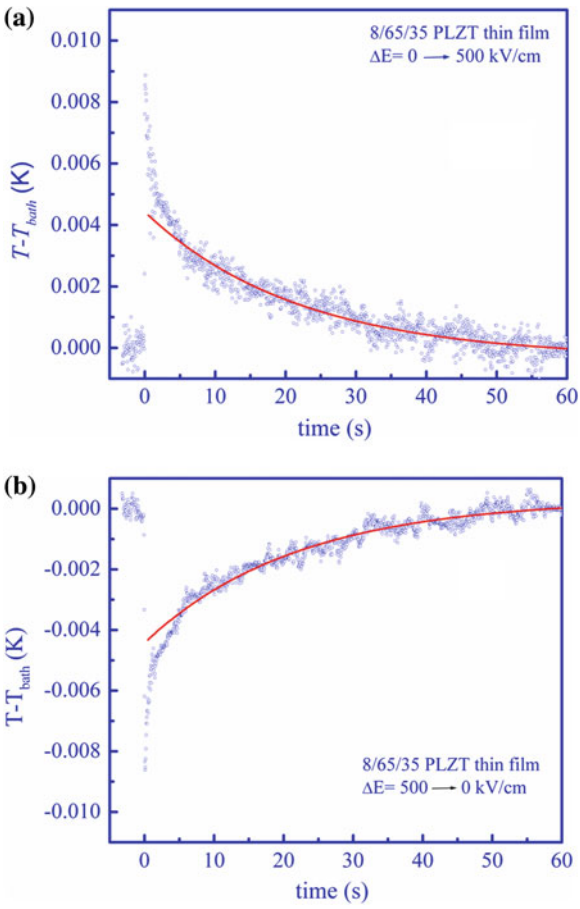

Fig. 22 An example of determining the ECE in thin-film samples. **a** The EC heating response after switching on the electric field. **b** The cooling EC response after the electric field is switched off. The symmetry of the responses indicates negligible Joule heating in this case. The *red lines* present the fitting results to Eq. (20). Note the initial fast-changing data within the first few seconds is the remnant of the internal sample equilibration taking place on a much faster time scale

below the electroded part of the sample (10 ms time scale) as well as the lateral heat flow to the part of the sample without electrodes (0.1–1.0 s time scale). In this case most of the EC heat released within the thin film is already lost to the substrate on a much shorter time scale and only the equilibration of the systems with and without electrodes is still taking place on the time scale of a second.

Due to the very large $\frac{\sum_i C_p^i}{C_p^{EC}}$ ratio, the directly measured ΔT is typically within a few mK. Here, the benefits of an accurate bath stabilization and sample temperature measurement (within 0.1 mK) provided by high-resolution calorimeters become of great importance for keeping the measurement error as low as possible.

ΔT is obtained by fitting the exponentially decaying wings to Eq. (20), describing the heat loss to the surrounding bath, which takes place at a much longer time scale of several 10 s (the fitting curves represented by the solid red line in Fig. 22). The final value of the EC temperature change ΔT_{EC} within the PLZT thin film is then calculated using Eq. (21).

In order to reduce the damage to the sample and to measure the ECE at higher electric fields, short step pulses between $\sim$0.1 and 1 s could be employed. They could also play an important role in annealing the sample's internal mechanical stresses prior to the EC measurements. Such a short-pulse response can be calibrated to data obtained by longer step pulses at a lower magnitude of the electric field (see Fig. 11).

As an example, Figs. 23 and 24 present measurements of the ΔT_{EC} and EC change of the specific entropy density Δs as a function of the electric field at a constant temperature of 318 K in thin 8/65/35 PLZT films. At lower fields up to 100–200 kV/cm, typically a smaller ECE is observed than in the equivalent bulk samples.

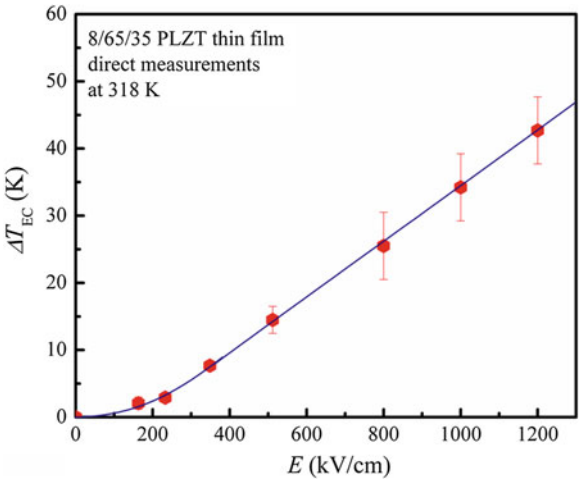

Fig. 23 The ECE temperature change ΔT_{EC} as a function of the applied electric field measured at 318 K in an 8/65/35 PLZT thin ceramic film [14]

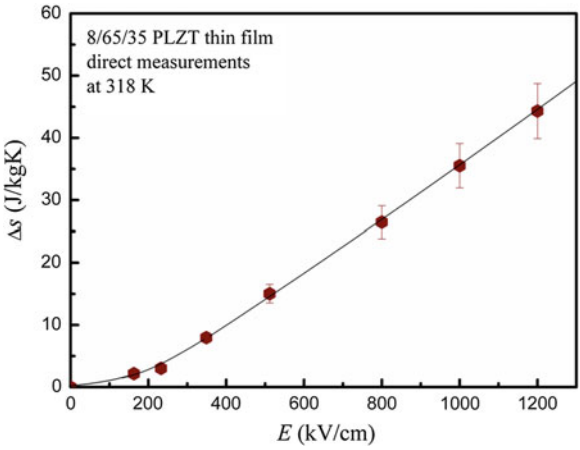

Fig. 24 The ECE specific entropy change Δs as a function of the applied electric field amplitude measured at 318 K in an 8/65/35 PLZT thin ceramic film [14]

This is a consequence of the fact that the coercive field in thin films could exceed, by more than an order of magnitude, the coercive field in bulk samples, i.e., much larger fields are required to induce comparable values of the polarization to those observed in a bulk material.

For the field values above the coercive field (typically $\sim$200 kV/cm) the ECE in thin films exceeds that observed in the bulk samples. One reason is related to the fact that many thin films survive much larger electric fields than bulk samples. At very large fields a significantly larger polarization could be induced than in bulk materials. For instance, in an 8/65/35 PLZT thin film a polarization exceeding 1 C/m^2 could easily be induced at fields exceeding 1 MV/cm. Such a polarization exceeds that in the bulk by more than a factor of two, and since $\Delta S \propto P^2$ a much larger ECE could be expected. It was found that the so-far largest reported ΔT_{EC} exceeding 40 K at 1.25 MV/cm [14] can be induced in an 8/65/35 PLZT thin-film material (Fig. 23). The thin film exhibits a specific entropy change $\Delta s \sim 50$ J/kgK at 1.25 MV/cm (Fig. 24) [14]. From Fig. 23 the EC responsivity $\Delta T_{EC}/E$ can be obtained as a function of the electric field amplitude (Fig. 25). It is evident that the maximum value of the EC responsivity is not achieved even for the highest applied field (Fig. 25). In contrast to bulk materials [24] the $\Delta T_{EC}/E$ maximum value is shifted towards higher electric fields, i.e., the range of fields that are interesting for applications.

Due to their very low thickness the resistivity of thin films could be significantly reduced in comparison to bulk materials, thus potentially resulting in a significant Joule heating, especially at higher electric fields. In the above example, the Joule heating became rapidly significant for the electric fields above 800 kV/cm and at 1.25 MV/cm became comparable to, or even exceeded, the EC temperature change. However, due to the different response times of the EC effect and the sample-to-bath heat exchange, i.e., cooling the sample when the field is switched off, the EC effect can still be discerned, even in samples with considerable Joule heating.

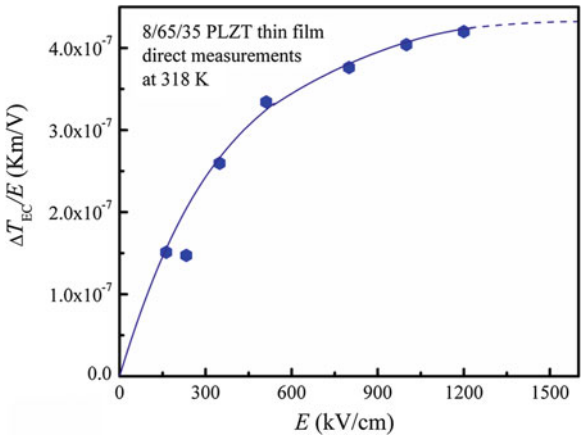

Fig. 25 The EC responsivity $\Delta T_{EC}/E$ as a function of the electric field amplitude measured at 318 K for an 8/65/35 PLZT thin ceramic film [27]

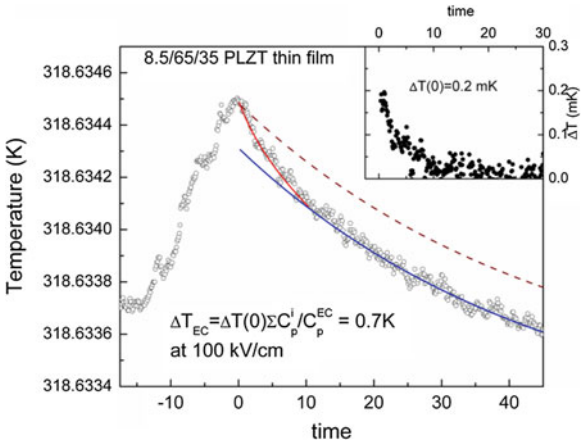

Fig. 26 An example of determining the ECE in a thin-film sample with excessive Joule heating

As an example, let us consider an 8.5/65/35 PLZT thin film, for which the EC measurement is presented in Fig. 26. In contrast to other thin-film samples this particular sample showed an enhanced Joule heating at higher electric fields due to the larger amount of impurities. Here, instead of the step electric pulse, a triangular electric pulse (see Fig. 9) was used. Since the heating power is proportional to the square of voltage, which itself increases linearly before it is switched off, the Joule heating during the linear increase of voltage increases strongly (Fig. 26). During such a slow voltage ramp the electrocaloric heating is practically impossible to discern from the Joule heating, especially if the Joule heating is dominant. After the voltage is switched off the two cooling processes on different time scales start to unfold. First, the electrocaloric cooling (marked by the solid red line in Fig. 26) is a relatively fast process, which takes place on a time scale of a few seconds (defined by the time scale of the internal equilibration of parts of the sample with and without electrodes). The second process related to the release of the excessive Joule heat to the surrounding bath takes, typically, an order of magnitude longer time scale (marked by the solid blue line in Fig. 26). This difference in the time scales could be exploited to discern the magnitude of the EC effect, even in samples in which the Joule heating greatly exceeds the ECE. For instance, if the EC cooling would be negligibly small in the above example, the cooling of the Joule excess heat to the surrounding bath would follow the dashed curve in Fig. 26.

The voltage is linearly increased and then switched off at $t = 0$. The red line represents the fast EC response, reducing rapidly the increased sample temperature due to the Joule heating. The solid blue line marks the release of the remaining excessive Joule heat to the surrounding bath, typically taking an order of magnitude longer time scale. The dashed line denotes the cooling of the Joule excess heat to the surrounding bath, which would take place in the absence of the ECE. The inset shows the EC $\Delta T(t)$, which was obtained by subtracting the blue line from the data. The intrinsic ΔT_{EC} is determined by using Eq. (21).

The vertical difference between the dashed line and actual long-time relaxing tail is directly revealing the magnitude of the ECE (see inset to Fig. 26 in which the extrapolated solid blue line is subtracted from the data). The magnitude ΔT_{EC} of the intrinsic ECE is then determined by using Eq. (21) and the procedure described above.

Such results, which seem to be only of academic value, can still provide valuable information about the magnitude of the ECE in a given material. Namely, in many cases the Joule heating could be resolved later by improving the quality of the material, increasing the thickness of the film or, in some cases, by making the current blockage made of a thin, highly resistive, dielectric layer beneath the electrodes.

As mentioned above, the main source of error in the case of thin films is the large ratio $\frac{\sum_i C_p^i}{C_p^{EC}}$, which could exceed a value of several thousand. Another source of error, especially at higher fields, is due to additional complications in the data analysis related to the Joule heating. However, if the analysis is performed carefully, the error in the ECE estimation can be kept below 10 %.

3.2 Direct Measurements in Thin Films Using a Fast Thermometry Approach

The above-described calorimetric method can provide reliable estimations of the ECE in thin films; however, it cannot provide fast online observations of the heating/cooling effects taking place solely in the thin-film layer on a rapid time scale. In addition, it cannot provide any spatial variations of the ECE on a thin film, which could provide valuable information about the thin-film quality. Very recently, a few additional methods were introduced, ranging from fast infrared photometry (IRP) to fast scanning thermal microscopy (SThM), that tackle these issues. We will briefly describe the most promising fast thermometry methods since these methods were, until recently, still under development and not many confirmed, reliable EC results were published so far.

3.2.1 Direct Measurements in Thin Films Using Fast IR Photometry

Depending on the type of sensors, two different variants of this method were recently introduced [2, 14]. The first method in which an IR temperature sensor was employed can be used for the fast thermometry of thin films (see Fig. 27) [14]. The method was introduced on irradiated thin P(VDF-TrFE) 68/32 mol % copolymer films with great success, although fast thermometry was not actually required for that particular sample [14]. Figure 28 shows a comparison between the EC data obtained by the high-resolution calorimetric technique and IR thermometry. A very good agreement of the data acquired by two completely different

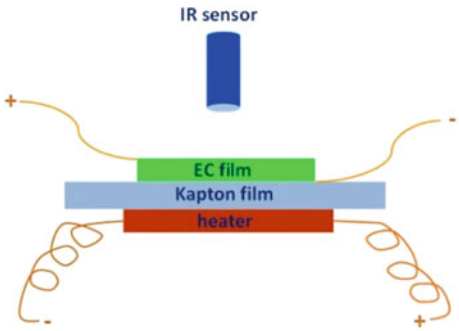

Fig. 27 Schematic ECE measurement set-up exploiting IR sensor for fast thermometry according to [14]

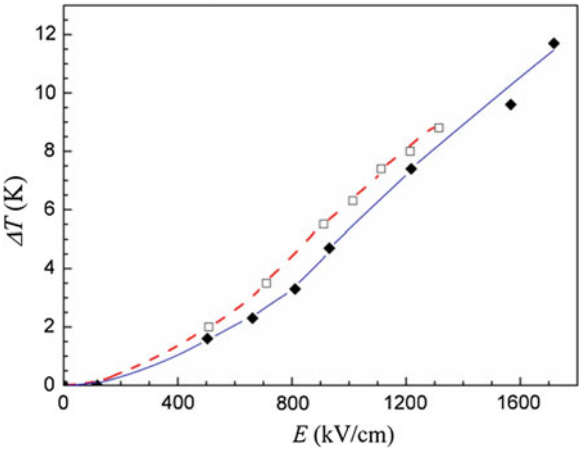

Fig. 28 Comparison between the EC data obtained by the high-resolution calorimetric technique (*solid*) and IR thermometry (*open squares*)

techniques additionally confirms the validity of both techniques and the existence of a large ECE with a ΔT_{EC} approaching 12 K in the blend films of the relaxor terpolymer P(VDF-TrFE-CFE) 59.2/33.6/7.2 mol % with 5 wt % of P(VDF-CTFE) 91/9 mol % copolymer.

With a properly calibrated IR sensor the IR thermometry could easily deliver results within 10 % accuracy. For the observation of the rapid ECE response on a time scale of microseconds, such as the ECE response of solid thin films on a substrate, it is necessary to use IR sensors with a very fast response and sophisticated, fast, high-accuracy, sampling electronics. Because of the short data-sampling window, the so-obtained EC data could suffer from significant noise, exceeding several tens of percent. However, repeating the EC experiment and then averaging multiple stored signals could help to reduce the noise.

The second method that uses a fast IR camera is able to detect not only the time, but also the spatial temperature, variations of the thin films [2, 7]. Since such cameras are usually not fast enough to follow a rapid heat exchange on a microseconds time scale between the film and substrate, it requires a special calibration

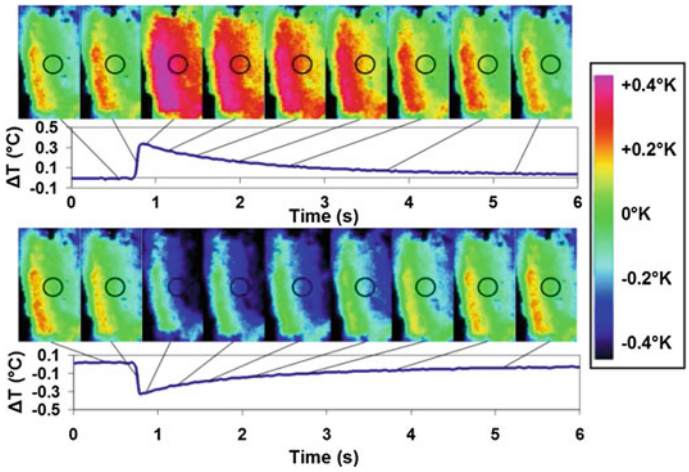

Fig. 29 IR camera images taken at different times after switching the electric field on (*upper* series of photos) and after switching the electric field off (*lower* series of photos). *Circles* denote the place at which the curves of EC temperature change ΔT were determined [7]. Figure courtesy of N.D. Mathur

to discern the proper ECE magnitude, which makes this method less suitable for high-accuracy EC measurements. Nevertheless, on thicker freestanding (polymer) films or thick films on a very thin substrate the method could perform well. Figure 29 shows a series of pictures taken by an IR camera at different times after the application of an electric step pulse to the commercially available bulk multilayer capacitor (MLC) [5].

The main advantage of this method is its spatial resolution, which could be exploited to obtain information about the uniformity and quality of the EC response across the film. As an example, Fig. 30 shows the EC temperature

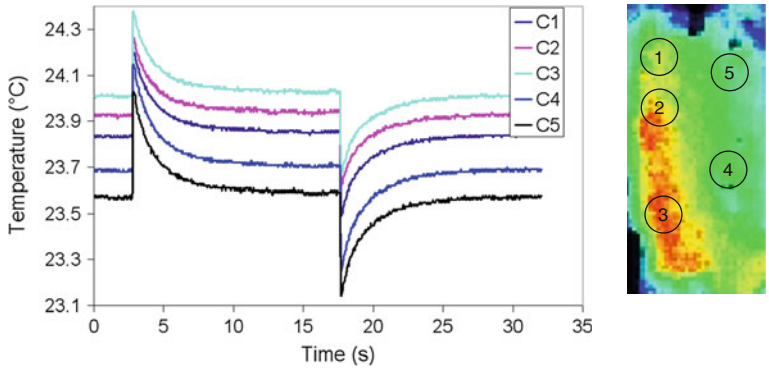

Fig. 30 (*left panel*) EC temperature changes arising at different points on the MLC surface shown on the *right panel* [7]. Figure courtesy of N.D. Mathur

variation across the MLC surface. Here, the EC temperature curves as a function of time (shown in left panel) are deduced for five different points on the MLC surface (right panel). As mentioned before, the drawback of this method is that in thin films on a substrate very fast and high accuracy cameras should be used in order to detect the rapidly vanishing EC temperature change due to the strong thermal coupling with the substrate.

3.3 Direct Measurements in Thin Films Using Fast Scanning Thermal Microscopy

Several attempts were made to shorten the time scale of the thermometer response in order to measure the EC response in thin films. One presented recently by Kar-Narayan et al. [4, 5] exploits the resistivity of a very thin electrode attached to the thin film or even to the above-mentioned, commercially available MLC. Here, the top driving electrode is patterned to form a thin-film metal thermometer whose resistance can be monitored when EC effects in the film are driven by a change in the electric field. Due to the very small mass of such electrodes the response time could be sufficiently low to provide, with appropriate fast data acquisition electronics, a reliable estimation of the EC magnitude in thin films. An experimental set-up and an example of such a measurement, though obtained on a bulk MLC, are shown in Figs. 31 and 32, respectively.

A new, modified method using scanning thermal microscopy (SThM), where a scanning-probe tip containing a resistive thermometer is deployed in contact mode, was recently introduced by the same authors [6]. Here, the scanning-probe tip contains a platinum resistance thermometer which is very sensitive to temperature and can record 0.1 K changes. As in the case of the above approach, using the thin electrode as a thermometer, the small thermal mass of the SThM thermometer-tip in comparison to the EC thin films allows quick and accurate direct measurements of the EC temperature changes (see Fig. 33). The versatility of this method was demonstrated recently in EC studies of organic and ceramic thin-film samples as well as devices [6, 7]. Figure 34 shows an example of the measured EC ΔT in a bulk, commercially available, multi-layer capacitor [5, 7].

Although similar to IR cameras, the SThM has the added advantage that it can produce a map of temperature change, thus providing the spatial resolution. This is particularly attractive for particular problems such as an EC study of epitaxial films in which an in-plane polarization is addressed via a lateral electric field from interdigitated electrodes. One drawback of this method is that a rather long time is required to scan the whole surface as well as the time-consuming calibration on a surface with a known temperature profile.

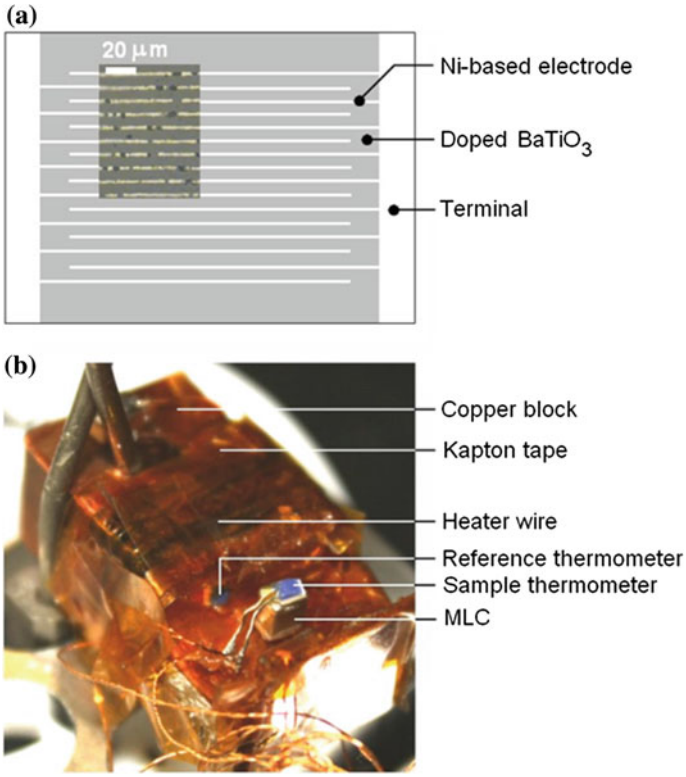

Fig. 31 Schematic ECE measurement set-up exploiting a thin-film thermometer attached to a bulk MLC [5]. Figure courtesy of N.D. Mathur

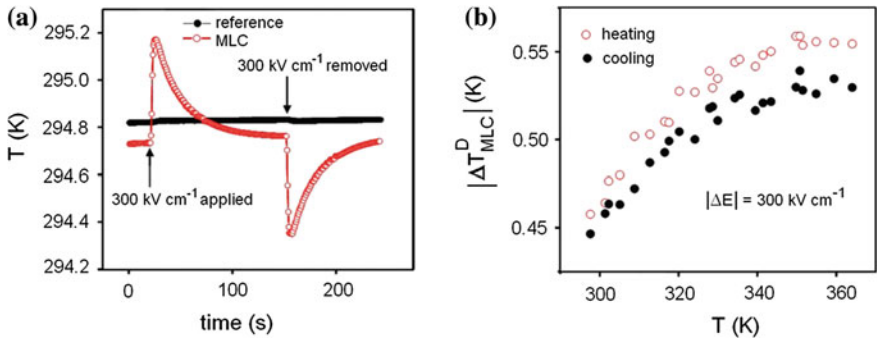

Fig. 32 **a** EC temperature changes arising due to the application and subsequent removal of 300 kV cm^{-1} recorded over time using a thin-film thermometer obtained in MLC [7], and **b** EC temperature change as a function of temperature on heating and cooling [5]. Figure courtesy of N.D. Mathur

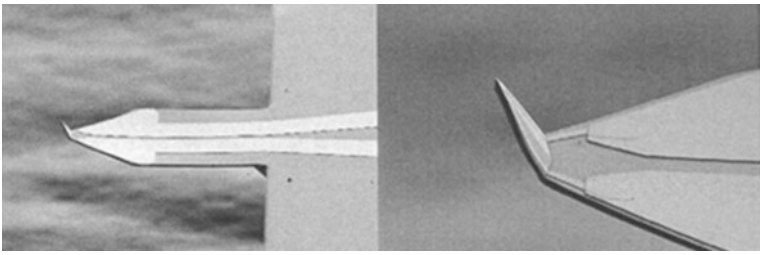

Fig. 33 Schematic ECE measurement set-up exploiting SThM thermometer-tip for fast thermometry [7]. Figure courtesy of N.D. Mathur

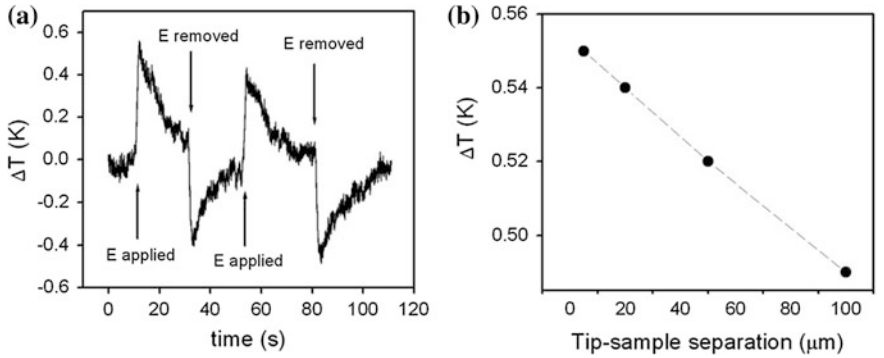

Fig. 34 **a** EC temperature changes arising due to the application and subsequent removal of 300 kV cm^{-1} recorded over time using SThM tip [7], and **b** EC temperature change as a function of tip-sample separation [7]. Figure courtesy of N.D. Mathur

4 Conclusions

Although the ECE has been known for several decades, it has only recently received increased attention from the scientific community due to the discovery of a large ECE in thin films. Early experiments were confined to bulk materials, for which already-developed, standard, calorimetric, or thermometric methods were sufficient. Even today, such methods represent the mainstream for studies of bulk or thick-film materials and they can provide reliable and high-accuracy EC data.

Nevertheless, increased attention to EC materials in the form of thin films has sparked an interest in recent years for new techniques that could overcome the experimental difficulties and provide direct and, possibly, spatial information about the EC in these challenging materials. Here, experimental problems related to the tiny mass of thin films and the corresponding rapid heat attenuation to the substrate render most of the standard techniques obsolete. As we show above, only modified EC thermometry using a high-resolution calorimeter can be adopted to

provide reliable information about the EC in thin-film materials. Due to the lack of high-resolution calorimeters and in order to observe the EC response on a fast time scale that is shorter than the time of the EC heat dissipation to the substrate, other EC measuring techniques are under rapid development.

However, so far, not many publications have appeared with reliable, direct, EC results, besides the standard calorimetric technique on thin films, and it may take a few more years before new techniques will become fully established. Nevertheless, some of those mentioned above have already shown promising initial results and could become standard techniques in the near future.

References

1. Akcay, G., Alpay, S.P., Rosseti, G.A., Scott, J.F.: Influence of mechanical boundary conditions on the electrocaloric properties of ferroelectric thin films. J. Appl. Phys. **103**, 024104 (2008)
2. Defay, E., Crossley, S., Kar-Narayan, S., Mathur, N.: Predicted coefficient of performance for electrocaloric materials in an ideal refrigeration cycle. Presented at International symposium on integrated functionalities, Cambridge, 2011, Abstract book, **61** (2011)
3. Guyomar, D., Sebald, G., Guiffard, B., Seveyrat, L.: Ferroelectric electrocaloric conversion in 0.75(PbMg1/3Nb2/3O3)-0.25(PbTiO3) ceramics. J. Phys. D Appl. Phys. **39**, 4491–4496 (2006)
4. Kar-Narayan, S., Mathur, N.: Direct and indirect electrocaloric measurements using multilayer capacitors. J. Phys. D: Appl. Phys. **43**, 032002 (2010)
5. Kar-Narayan, S., Mathur, N.: New trends in electrocalorics. Presented at International symposium on integrated functionalities, San Juan, 2010, Abstract book, 455–456 (2010)
6. Kar-Narayan, S., Crossley, S., Mathur, N.: Scanning thermal microscopy studies of electrocaloric films and devices. Presented at International symposium on integrated functionalities, Cambridge, 2011, Abstract book, 111 (2011)
7. Kar-Narayan, S., Crossley, S., Abergel, J., Bontempi, A., Baier, N., Defay, E., Mathur, N.D.: Direct electrocaloric measurements using scanning thermal microscopy and infra-red thermometry. Preprint (2012)
8. Kobeko, P., Kurtschatov, J.Z.: Dielectric properties of Rochelle salt crystal. Physik **66**, 192–205 (1930)
9. Kraftmaker, Y.A.: Modulation method for measuring specific heat. Zh. Prikl. Mech. Tekh. Fiz. **5**, 176–180 (1962)
10. Kutnjak, Z., Petzelt, J., Blinc, R.: The giant electromechanical response in ferroelectric relaxors as a critical phenomenon. Nature **441**, 956–959 (2006)
11. Lines, M., Glass, A.: Principles and Applications of Ferroelectrics and Related Materials. Clarendon Press, Oxford (1977)
12. Lipa, J.A., Edwards, C., Buckhingham, M.J.: Precision measurement of the specific heat of CO_2 near the critical point. Phys. Rev. Lett. **25**, 1086–1090 (1970)
13. Lu, S.-G., Rožič, B., Kutnjak, Z., Zhang, Q.M.: Electrocaloric effect (ECE) in ferroelectric polymer films. In: Coondoo, I. (ed.) Ferroelectrics, pp. 99–118. Intech, Rijeka (2010)
14. Lu, S.-G., Rožič, B., Zhang, Q. M., Kutnjak, Z., Li, X., Furman, E., Gorny, L. J., Lin, M., Malič, B., Kosec, M., Blinc, R., Pirc, R.: Organic and inorganic relaxor ferroelectrics with giant electrocaloric effect. Appl. Phys. Lett. **97**, 162904 (2010)
15. Lu, S.G., Rožič, B., Zhang, Q.M., Kutnjak, Z., Li, X., Pirc, R., Gorny, L.J., Lin, M.: Comparison of directly and indirectly measured electrocaloric effect in relaxor ferroelectricpolymers. Appl. Phys. Lett. **97**, 202901 (2010)

16. Lu, S.-G., Rožič, B., Zhang, Q.M., Kutnjak, Z., Neese, B.: Enhanced electrocaloric effect inferroelectric poly(vinylidene-fluoride/trifluoroethylene) 55/45 mol% copolymer at ferroelectric-paraelectric transition. Appl. Phys. Lett. **98**, 122906 (2011)
17. Lu, S.-G., Rožič, B., Kutnjak, Z., Zhang, Q.M.: Electrocaloric effect in ferroelectric P(VDF-TrFE) copolymers. Integr. Ferroelectrics **125**, 176–185 (2011)
18. Mathur, N., Mischenko, A.: Solid state electrocaloric cooling devices and methods. WorldPatent, WO 2006/056809
19. Mischenko, A.S., Zhang, Q., Scott, J.F., Whatmore, R.W., Mathur, N.D.: Giant electrocaloric efect in thin-film Pb0.95Ti0.05O3. Science **311**, 1270 (2006)
20. Mischenko, A.S., Zhang, Q., Scott, J.F., Whatmore, R.W., Mathur, N.D.: Giant electrocaloric efect in thin-film relaxor ferroelectric 0.9PbMg1/3Nb2/3O3-0.1PbTiO3 near room temperature. Appl.Phys. Lett. **89**, 242912 (2006)
21. Neese, B., Chu, B., Lu, S.-L., Wang, Y., Furman, E., Zhang, Q.M.: Large electrocaloric effect in ferroelectric polymers near room temperature. Science **321**, 821 (2008)
22. Pirc, R., Kutnjak, Z., Blinc, R., Zhang, Q.M.: Electrocaloric effect in relaxor ferroelectrics. J. Appl. Phys. **110**, 074113 (2011)
23. Rožič, B., Malič, B., Uršič, H., Holc, J., Kosec, M., Neese, B., Zhang, Q.M., Kutnjak, Z.: Direct measurements of the giant electrocaloric effect in soft and solid ferroelectric materials. Ferroelectrics **405**, 26–31 (2010)
24. Rožič, B., Kosec, M., Uršič, H., Holc, J., Malič, B., Zhang, Q.M., Blinc, R., Pirc, R., Kutnjak, Z.: Influence of the critical point on the electrocaloric response of relaxor ferroelectrics. J. Appl. Phys. **110**, 064118 (2011)
25. Rožič, B., Malič, B., Uršič, H., Holc, J., Kosec, M., Lu, S.-G., Zhang, Q.M., Kutnjak, Z.: The giant electrocaloric effect in inorganic and organic ferroelectric relaxor systems. Ferroelectrics, **430**, 98–102 (2012)
26. Rožič, B., Uršič, H., Holc, J., Kosec, M., Kutnjak, Z.: Direct measurements of the Electrocaloric effect in Substrate-Free PMN-0.35 PT thick films on a Platinum layer. Integr. Ferroelectrics, **140**, 161–165 (2012)
27. Scott, J.F.: Application of modern ferroelectrics. Science **315**, 954 (2007)
28. Sebald, G., Pruvost, S., Seveyrat, L., Lebrun, L., Guyomar, D., Guiffard, B.: Electrocaloric properties of high dielectric constant ferroelectric ceramics. J. Europ. Ceram. Soc. **27**, 4021–4024 (2007)
29. Tuttle, B.A., Payne, D.A.: The effects of microstructure on the electrocaloric properties of Pb(Zr, Sn, Ti)O_3 ceramics. Ferroelectrics **37**, 603–606 (1981)
30. Valant, M., Dunne, L.J., Axelsson, A.-K., Alford, McN.N., Manos, G., Peräntie, J., Hagberg, J., Jantunen, H., Dabkowski, A.: Electrocaloric effect in a ferroelectric $Pb(Zn_{1/3}Nb_{2/3})O_3$-$PbTiO_3$ single crystal. Phys. Rev. B**81**, 214110 (2010)
31. Wiseman, G.G., Kuebler, J.K.: Electrocaloric effect in ferroelectric Rochelle salt. J. Phys. Rev. **131**, 2023–2026 (1963)
32. Wood, M.E., Potter, W.H.: General analysis of magnetic refrigeration and its optimization using a new concept: maximization of refrigerant capacity. Cyrogenic **25**, 667–683 (1985)
33. Yao, H., Ema, K., Garland, C.W.: Nonadiabatic scanning calorimeter. Rev. Sci. Instrum. **69**, 172–178 (1998)

New Approaches to Electrocaloric-Based Multilayer Cooling

Sergey Karmanenko, Alexander Semenov, Antonina Dedyk, Andrey Es'kov, Alexey Ivanov, Pavel Beliavskiy, Yulia Pavlova, Andrey Nikitin, Ivan Starkov, Alexander Starkov and Oleg Pakhomov

1 Introduction

The research and development works directed to a creation of solid state coolers and refrigerators based on the electrocaloric effect have been initiated in various countries, mainly in USA and USSR, in the 70s of the last century [39, 43]. The goal of these works was formed as a creation of microcryogenic cooling systems for infrared radiation receivers for space optoelectronic systems. The following principles of R&D works were formulated at the initial stage:

- The mechanical thermal keys were used for the connection between active electrocaloric elements in order to decrease the temperature of cooling object.
- The temperature decrease in active element was achieved in the process of electric field action on ferroelectric capacitor and the cooling of gas carrier flowing through it.
- Thermodynamic cycle of gas carrier with electrocaloric active elements should be similar to analogical cycles of the gas expansion processes in vapor-compression refrigerators.

At a later date these principles were used in such developments as [42], where various modifications of completely solid state electrocaloric refrigerators featuring with thermal keys were considered. That approach to the creation of the

S. Karmanenko · A. Semenov · A. Dedyk · A. Es'kov · A. Ivanov · P. Beliavskiy · Y. Pavlova · A. Nikitin
St. Petersburg State Electrotechnical University (LETI), St. Petersburg, Russia

I. Starkov
Institute for Microelectronics, Vienna University of Technology, Vienna, Austria

A. Starkov · O. Pakhomov (✉)
National Research University of Information Technologies, Mechanics and Optics (ITMO), St. Petersburg, Russia
e-mail: oleg.cryogenics@gmail.com

T. Correia and Q. Zhang (eds.), *Electrocaloric Materials*, Engineering Materials 34, DOI: 10.1007/978-3-642-40264-7_8,

refrigerating device is based on quasi-static method, where thermodynamic cooling cycle is considered as the serial set of reverse equilibrium processes.

In conventional vapor-compression refrigerators the thermal processes is realized in stationary regime, however at last years the novel refrigerating principles based on dynamic thermal processes have found useful application, such as «Pulse Tube Cryocooler», «Vortex tube», «Gifford–McMahon Cryocooler». Also, quasi-stationary thermal processes take place in Stirling cryocoolers, which use two working body—gas and solid material of the regenerator [2].

In the papers published after 2006 [9, 20, 27] there were presented some variants of new generation of dynamical electrocaloric devices without application of mechanical thermal keys and gas carrier. In the mentioned papers the layered ferroelectric structures were proposed as heat transferring line, where thermoelectric Pelitier elements, liquid crystal films or heat transferring elements are used. Describing the last structure, the authors shown that at the defined conditions ferroelectric layered structure should work as highly efficient solid-state heat pump.

The proposed type of thermal devices based on the solid layered structures possesses a set of principal features. These are the matched dynamical character of switching processes in every ferroelectric layer and a presence of thermal interaction of heat responses across the layered structure. The dynamical matching of electrocaloric and elastocaloric effects give the parametric amplification both electrocaloric response and heat flux in the layered structure [9].

The novel type of EC refrigerator is similar to cryogenic dynamic refrigerator and less resembling than to the quasi-static thermal device. Therefore to create the new generation of EC devices it is necessary to investigate an electrocaloric response at exposure of various structure (harmonic signal, rectangular pulses or the action of other dynamic forms) electric field and study dynamical characteristic of various ferroelectric materials. Theoretical efficiency of multilayer cooling structures could be estimated just by analysis of interfering dynamical processes in adjoining EC elements.

2 Theoretical Basis of Modern Electrocaloric-Based Cooling Structures

2.1 Efficiency of Electrocaloric-Based Cooling in Quasi-Static Approximation

Solid-state converters of thermal energy and energy-saving technologies of cooling form an important trend in research and development at many laboratories and companies during the last few decades. The main advantage of solid-state cooling is determined by a considerably higher density of solids as compared to vapor and gas in vapor-compression systems. The change in the entropy per unit volume in solid materials is 6–8 times higher than in gases [4], which makes it possible to

considerably reduce the size of refrigerators and to produce miniature thermal energy converters.

Among thermal physical phenomena in solids, the conversion of thermal energy in a ferroelectric material [3], occurring as a result of the pyroelectric and electrocaloric effects, has special importance. The ferroelectric converters have high efficiency due to the fact that heating and cooling of the coolant are practically reversible thermodynamic cycles [3, 35, 50].

Until recently it was assumed that the electrocaloric method of cooling has a low efficiency and not suitable for coolers [28, 35]. However, the last theoretical and experimental advances in material science [11, 15, 20, 27, 45] proved that film capacitors based on perovskite, relaxant, and polymer materials [33] can ensure a thermal effect exceeding 10 K in a single switching. At the same time, the key direction in the development of a solid-state cooler is the construction of the effective thermodynamic cycle of a system of thermal converters. Thermodynamic analysis of thermal processes in a ferroelectric energy converter was considered, for example, in [17, 41]. However, the sequence (dynamics) of switching of EC elements and the shape of the applied voltage (which has not been considered before as far as we know) are very important to estimate the effectiveness of converter operation.

An important circumstance for choosing the operation conditions for a thermal line is setting of the temperature interval in which effective conversion of heat occurs. Estimates obtained in [31] show that in the vicinity of the phase transition, the efficiency of conversion of thermal energy into electric energy tends to the efficiency of the Carnot cycle. Which temperature range is most effective for EC cooling in a capacitor? This question will be considered in this chapter devoted to the thermodynamic estimation of the efficiency of conversion of electric energy in a solid-state cooling line including ferroelectric capacitors under the action of electric pulses.

In our publications [10, 36], we analyzed thermal processes in a cooling line including two EC elements and three thermal conductors. Numerical simulation was performed using the finite element method. As a result, it was shown that a steady-state temperature regime is formed in the solid-state cooling line under investigation, and the temperature gradient is directed from the source of the sink of thermal energy. When ferroelectric capacitors based on $Ba_xSr_{1-x}TiO_3$ barium–strontium titanate (BST) ceramic is used, the temperature difference may attain 25 K in the case of perfect heat removal. The necessary condition for the operation of a solid-state line is matching of the operation modes of the capacitors at the maximum of the derivative of electric polarization (dP/dT) or permittivity ($d\varepsilon/dT$) with respect to temperature.

Figure 1 shows the temperature dependence of the permittivity of the BST ceramic and its derivative with respect to temperature. A ferroelectric capacitor operates most effectively as an EC element in the paraelectric phase at the temperature corresponding to the extremum on the $d\varepsilon/dT(T)$ dependence. Therefore, it is expedient to use ferroelectric capacitors for which the temperature corresponding to the extremum on the $d\varepsilon/dT(T)$ dependence increases in the source-sink direction.

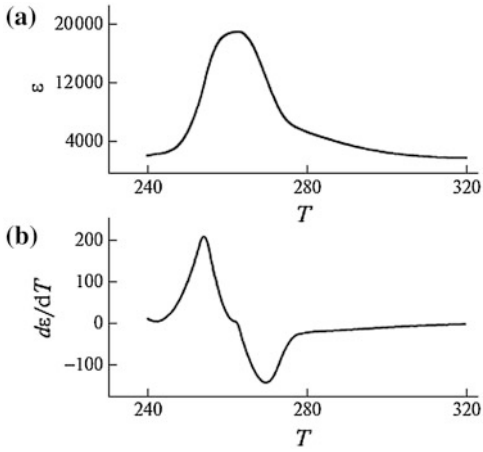

Fig. 1 The temperature dependences of permittivity **a** and its derivative **b** in ferroelectric capacitor based on BST ceramic

We will consider the thermodynamic efficiency of EC cooling in steady state. For a correct analysis we make the following assumptions are valid for quasi-static processes:

- Make-and-break of EC elements is performed by applying periodic voltage pulses. The operation of a cooling structure requires a time shift between sequences of pulses supplied to the first and second EC elements. The time shift in the operation of capacitors is multiple to the thermal constant defined as

$$\tau = \frac{L^2 \rho C}{\lambda},$$

  where L, ρ, C, and λ are the length (thickness), density, heat capacity, and thermal conductivity of the ferroelectric.
- Charging and discharging occur either adiabatically, or isothermally. The thermal and electrical duration of the pulse front in these cases may differ by several orders of magnitude. If the front duration is much smaller than the thermal constant of the transition from one energy state to another, charging (discharging) occurs adiabatically. If the charging time considerably exceeds the time constant, the charging (discharging) process occurs isothermally.
- Heat loss and dissipation of electric energy are negligibly small and are disregarded in analysis.
- The temperature variation during an adiabatic charging of a capacitor is larger than the change in temperature during its adiabatic discharging. The fulfillment of this condition is ensured by the position of the working point, which is chosen on the decreasing segment of function $d\varepsilon/dT(T)$ in the region of the negative extremum of the dependence shown in Fig. 1b. Then, the known relation [5] for the adiabatic EC effect

$$\Delta T_{ad} = \int \frac{T}{C_E}\left(\frac{\partial}{\partial T}\varepsilon(T)\right)EdE = \int \frac{T}{C_E}\gamma(T)EdE,$$

leads to the validity of the assumption under which the heat capacity C_E of an EC element for a given electric field strength has the form [5]

$$C_E = C_0 + E^2 T\frac{\partial^2 \varepsilon}{\partial T^2} \tag{1}$$

In this equation, C_0 is the heat capacity of the capacitor disregarding the action of the electric field.

- The capacitors whose temperature varies periodically in time exchange heat regeneratively via a heat conductor. For this reason, we assume that this element of the cooling line is a regenerator with temperature T_R. A similar assumption is used in thermodynamic analysis of the Stirling and Ericson regenerative cycles.

Let us consider the sequence of processes in a ferroelectric cooling structure taking into account the above assumptions. We will analyze the change in the volume-averaged temperature of the capacitors upon make-and-break of electric field in a steady-state regime. In this case, transient processes can be ignored, and we can assume that the temperature of each capacitor deviates from its steady-state value only as a result of external action. Consequently, the ferroelectric in the steady state performs a thermodynamic cycle consisting of three processes (isothermal, adiabatic, and heat exchange at constant voltage). These processes are shown in Fig. 2, where point *C* lies above point 2 and point 3 lies below point *B*. The former point (2) is located higher due to assumption (i_v), while the latter point (3) lies lower since the difference in the temperature levels of the two elements in the stationary state is smaller than the electrocaloric temperature effect.

The first ("Cold") element performs the *A–B–C* cycle, while the second ("Hot") element performs the 1–2–3 cycle; the processes occur with a time shift determined from the thermal constant of the capacitors. The difference between these elements is that the "Cold" element is discharged isothermally with absorption of heat and is charged adiabatically upon heating, while the "Hot"

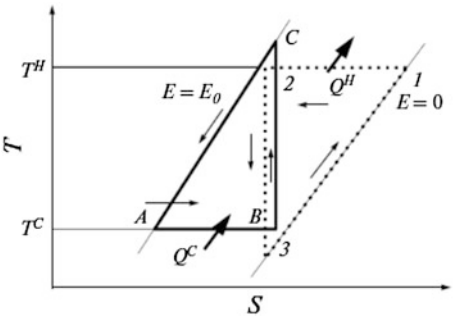

Fig. 2 The thermodynamic switching cycle for EC elements in a solid state line. "Cold" element performs on *A–B–C* cycle, while "Hot" element follows on *1–2–3* cycle

element is charged isothermally with heat release and is discharged adiabatically upon cooling. The above assumptions form the basis of thermodynamic analysis and estimation of the cooling efficiency and refrigeration efficiency Ψ for processes of switching in the solid-state line. Let us consider the cyclic sequence of processes in the cooling system under the above assumptions.

During isothermal discharging in contact with thermal conductors (*A–B*), the "Cold" EC element absorbs heat. The amount of heat *QC* defined, according to [42], as

$$Q_C = T_A\left(\frac{\partial\varepsilon(T_A)}{\partial T}\right)_E E^2 \tag{2}$$

is removed from the object being cooled at temperature TC = TA (the temperature corresponding to point A. The "Hot" element is heated from temperature T_3^H to T_B^C during the period following the discharge (at the initial segment of process 3–1). In the course of process B–C, adiabatic charging of the "Cold" element takes place, and its temperature increases from to $T_C^C > T^H$. In process 3–1, the "Hot" element continues to receive heat at constant electric field strength and is heated from T^H to $T_1^H = T_2^H = T^H$. At the next instant, the ED "Cold" element is charged at temperature $T_C^C = T^H$. The regenerator temperature has a mean value $T_R < T^H$. In process 2–3, the "Hot" element is discharged adiabatically, and its temperature decreases from T_2^H to T_3^H. As a result, a temperature differences appears at the ends of the regenerator, and a heat flow directed from the "Cold" to "Hot" element appears in the regenerator due to thermal conductivity of the material.

In process *C–A*, the "Cold" capacitor is cooled in a constant electric field from temperature T_B^C to $T_A^C = T_C$ due to the temperature gradient. In process 1–2, the "Hot" capacitor is discharged isothermally; therefore, the heat Q_H released to the ambient is given by

$$Q_H = T_H\left(\frac{\partial\varepsilon(T_H)}{\partial T}\right)_E E^2 \tag{3}$$

Amount of heat Q_H is greater than Q_C; the temperature at one end of the regenerator is T^H and at the other end, $T_B^C > T^H$; consequently, a heat flow from the "Cold" to "Hot" element appears in the regenerator. Then, the cycle is repeated.

The possibility of processes *C–A* and 2–3 is determined by the following factors: over a short time interval, the regenerator receives amount of heat Q_{REG} from one side and loses heat Q''_{REG} at the other side; after a certain time, the system must come to thermal equilibrium characterized by zero temperature gradients. However, in the process considered here, a temperature gradient due to the difference in the boundary conditions of the "Hot" and "Cold" elements always exists. Processes *C–A* and 3–1 were considered while solving the thermal conductivity problem, in which the regenerator is treated as a heat-conducting rod with initial temperature *TR* under periodic action of local sources with a phase shift and

asymmetric boundary conditions [36]. It follows from the solution to this problem that temperature at the middle of the regenerator in the steady-state regime is constant, and temperature oscillations occur at its ends with a certain time shift. Consequently, the regenerator whose temperature has decreased due to cooling during the adiabatic discharging of the "Hot" element completely absorbs the heat supplied to the regenerator during heating as a result of adiabatic discharging of the "Cold" element and returns to the initial temperature in accordance with the above assumptions. The removed energy is $Q = C_E(T_3^H - T_A^C)$.This process takes place because the 1–2–3 cycle leads the *A–B–C* cycle. Consequently, the relation between the heat capacity and thermal conductivity of the regenerator determines the lower temperature level (T_C).

Thermodynamic analysis of the physical processes is carried out as a rule by one of the following two methods: method of cycles (circular processes) or thermodynamic potential method. Let us determine the refrigeration efficiency of the cooling structure under investigation using the method of thermodynamic cycles. In accordance with this method of analysis, we must find the amount of thermal energy received by the ferroelectric at a low temperature and the amount of thermal energy given away by the ferroelectric at a high temperature. The difference in these energies is the work of the cycle, and the ratio of the heat received by the ferroelectric to the work is the efficiency of a given thermodynamic cycle (refrigeration efficiency). The absolute thermodynamic efficiency of a thermal cycle is defined as the ratio of the refrigeration efficiency to the refrigeration efficiency of the Carnot cycle.

For each capacitor, heat can be supplied or removed in the course of isothermal discharging or charging or as a result of rapid adiabatic change in temperature. Let us denote the adiabatic change in the temperature of the "Cold" element by ΔT_{ad}^C and the change in the temperature during adiabatic cooling of the "Hot" element by ΔT_{ad}^H. Then, the amounts of heat ΔQ_1^H and ΔQ_2^H supplied to and removed from the "Hot" element are

$$\Delta Q_1^H = C_0^H(T_1^H - T_3^H),$$
$$\Delta Q_2^H = \Delta Q_H = T_H\left(\frac{\partial \varepsilon(T_H)}{\partial T}\right)_E E^2.$$

The work L_H of the cycle performed by the "Hot" element is $L^H = \Delta Q_2^H - \Delta Q_1^H$. The amount of heat ΔQ_1^C and ΔQ_2^C supplied to and removed from the "Cold" element are

$$\Delta Q_1^C = C_E^C(T_C^C - T_A^C),$$
$$\Delta Q_2^C = \Delta Q_C = T_A\left(\frac{\partial \varepsilon(T_A)}{\partial T}\right)_E E^2.$$

Work L^C of the cycle performed by the "Cold" element is $L^C = \Delta Q_2^C - \Delta Q_1^C$. The total work L_Σ of the entire cycle is the sum of these works:

$$L_\Sigma = L^C + L^H = \Delta Q_2^C - \Delta Q_1^H = \Delta Q_C - \Delta Q_H.$$

This result was obtained from the condition of complete heat exchange in the regenerator:

$$\Delta Q_1^H = \Delta Q_1^C,\ C_0^H(T_1^H - T_3^H) = C_E^C(T_C^C - T_A^C)$$

using the above equation, we obtain the following equality:

$$C_0^H \Delta T_{ad}^H = C_E^C \Delta T_{ad}^C.$$

This equality holds in spite of the fact that $\Delta T_{ad}^C < \Delta T_{ad}^H$ since the heat capacity of the ferroelectric depends on the electric field and $C_E^C > C_0^H$. Heating of the "Hot" element occurs is zero electric field, while cooling of the "Cold" element occurs in field E. The heat capacity can be calculated from the expression

$$C_E^C = C_0(T_C) + E^2 T_C \frac{\partial^2 \varepsilon(T_C)}{\partial T^2}.$$

Let us find the refrigeration efficiency Ψ:

$$\Psi = \frac{\Delta Q_C}{L_\Sigma} = \frac{\Delta Q_C}{\Delta Q_H - \Delta Q_C},$$

where energy ΔQ is calculated for the isothermal EC effect:

$$\Delta Q = \int T(\frac{\partial}{\partial T}\varepsilon(T))EdE = \int T\gamma(T)EdE \approx T\gamma(T)E^2$$

Eliminating E_2, we obtain the following expression for the refrigeration efficiency:

$$\Psi = \frac{T_C\gamma(T_C)}{T_H\gamma(T_H) - T_C\gamma(T_C)}.$$

The version of the expansion of the temperature dependence of the derivative of permittivity $\gamma(T) = d\varepsilon/dT(T)$ for barium titanate (see Fig. 1) is a power series including the numerical coefficient up to T^4:

$$\gamma(T) = a + bT + cT^2 + dT^3 - gT^4.$$

The values of these coefficients are chosen by approximating the curve representing the function $\gamma(T)$ using the least square method. This approximation leads to numerical coefficients of the series and the values of the thermodynamic efficiency for EC-line

$$\eta_t = \frac{\Psi}{\Psi_{Carnot}},\ \Psi_{Carnot} = \frac{T_C}{T_H - T_C},$$

where Ψ_{Carnot}—refrigeration efficiency of the Carnot cycle.

At a temperature of 272.5 K of the "Cold" capacitor and the value of $\Delta T = 0.5$ K, the cooling efficiency is 0.57, where ΔT is the range of temperature variation over a switching cycle ($T_H - T_C$). At a temperature 271.5 K and $\Delta T = 0.5$ K, the cooling efficiency is 0.1.

If we assume that $\Delta T = 2$ K and the temperature of the "Cold" capacitor is 271.5 K, the efficiency is 0.6.

Thermodynamic analysis of the cooling process in the solid-state line shows that the maximal value of the efficiency of solid-state coolant is attained for temperatures close to the negative extremum on the temperature dependence of the derivative of permittivity. The thermodynamic efficiency of the EC converter is estimated. Under the assumption that the range of temperature variation in a thermodynamic cycle is $\Delta T = 2$ K and the temperature of the "Cold" BST capacitor is 271.6 K, the efficiency amounts to 0.6 Carnot. This value considerably exceeds the efficiency of vapor-compression refrigerating energy converters.

To attain cooling in a wide temperature range, it is expedient to use cascade systems. In this case, the solid-state cooling line is an element of a refrigerating cascade connecting the object to be cooled and the heat sink (heat exchanger). To elevate the efficiency of a cascade cooling structure, the EC elements are prepared from materials with the Curie temperature (and point of inflection) increasing from element to element. From the standpoint of thermodynamic efficiency, the search for materials with a large thermal EC effect is not the most vital trend in development and designing of solid-state cooling structure. In our opinion, the choice materials with a gently sloping γ(T) dependence in the region of extremum of this function and the possibility to vary the critical temperature of the ferroelectric in a wide range are more important. Solid solutions of ferroelectrics (e.g., BST perovskite and relaxant materials such as PMN–PT), in which the critical temperature can be controlled in a wide temperature range by varying their composition, satisfy these requirements best of all.

2.2 Temperature Drop by Parametric Effect

The principal difference between solid-state cooling and the gas refrigerator is that for the thermo-mechanical systems, the frequency of the gas pressure variation is in the range (0.1–1) Hz. From over hand for the EC cooling rate of the electric field variation frequency is limited only by the relaxation time of polarization. In addition, the polarization depends not only on the electric field, but also from mechanical stress, pressure, etc. Parametric change electrocaloric factor may lead to a substantial increase in the EC effect. In this case the quasi-static approximation is not valid, so you must use a dynamic model.

Consider the EC effect expression, written in terms of polarization P

$$C_E dT = -T\frac{\partial P}{\partial T}dE,\ dT = -\frac{T}{C_E}\frac{\partial P}{\partial T}dE \tag{4}$$

where T is the absolute temperature, P is the polarization, E is the electric field strength, CE is the heat capacity at a constant field strength, and γ is the EC coefficient

$$\gamma_{ec} = -\frac{T}{C_E}\frac{\partial P}{\partial T}.$$

It follows from Eq. (4) that the maximum change in the temperature takes place in a region of maximum pyroelectric coefficient $p = \partial P/\partial T$. For ferroelectrics, this is a region of temperatures close to the Curie point TC, where the Landau–Ginzburg theory of second-order phase transitions is applicable. According to this theory, the polarization as a function of the field strength can be expressed as follows:

$$E = aP + bP^3, \tag{5}$$

where $a = a_0(T - T\text{C})$, a_0 is the Curie–Weiss constant, and b is the coefficient of nonlinearity. A maximum change in the temperature upon a single application or removal of the field, $\Delta T = 40$ K, was observed for a 450-nm-thick $Pb_{0.88}La_{0.08}Zr_{0.65}Ti_{0.35}O_3$ film at a field strength of 1,250 kW/cm. It should be noted that a comparison of the two sides in the formula (4) for the available experimental data shows that the right side is 10–15 % larger than the left side [1, 32]. This fact has been recently explained in [46]. Determination of polarization P is based on the measurement of a hysteresis curve during cyclic variation of the field strength. In this case, it is necessary to take into account the dynamic effects and replace relation (5) by the Landau–Khalatnikov equation:

$$r\frac{\partial P}{\partial \tau} = E - aP - bP^3 \tag{6}$$

where r is the effective "internal" resistance. For small r, the polarization can be expressed as follows [47]:

$$P = P_{st} + P_{dyn}, P_{dyn} = -\frac{r}{a + 3bP_{st}^2}\frac{\partial P_{st}}{\partial t} \tag{7}$$

where P_{st} is the quasi-static polarization determined from Eq. (5) and P_{dyn} is the dynamic correction that accounts for an increase in ΔT in the case of indirect measurements. The adiabatic equation in the Landau–Ginzburg theory is written as follows [55]:

$$T - T_0 = \frac{a_0}{\kappa}(P^2 - P_0^2) \tag{8}$$

where κ is a constant quantity and T_0 and $P_0$are the initial temperature and polarization, respectively. The validity of Eq. (8) has been repeatedly confirmed (see e.g., [1, 23, 25, 32, 55]. Thus, Eq. (5) is applicable to the description of quasi-static processes, while the dynamic processes should be describes using Eq. (6).

In the immediate vicinity of the Curie point, the left-hand side of this equation should be additionally refined by adding terms describing the pyroelectric and piezoelectric currents [47].

The problem encountered in creating cooling structure is the organization of a thermodynamic cycle. Under the adiabatic conditions, the overall change of the temperature upon the application and removal of electric field is zero. Therefore, it is necessary to implement non-adiabatic processes (isothermal, or those with constant E or P). The adiabaticity can be violated, e.g., by using thermal switches or taking into account heat exchange with the environment and the inhomogeneity of the temperature field in a sample [20, 21, 51, 52]. For example, the results of numerical calculations for $BaSrTiO_3$ (BST) [20, 21] showed that, after 1,000 switching cycles, the system attains a steady-state regime, in which the temperature oscillates about the average value that is 20 K below the initial temperature. The measurements of temperature during periodic variation of the electric field were performed by Wiseman [55]. In the first cycle, the application of the electric field led to an increase in the sample temperature by 0.043 K, while switching the field off led to a decrease in the temperature by 0.046 K, so that the total temperature change per cycle was $\delta T = 0.003$ K. This dependence has been qualitatively predicted by Lawless [23]. The EC effect can be amplified by using multilayer structures. In particular, it was shown in [10] that at switching frequency of 1 Hz in BST ceramics the EC effect is increased on 2.5 K by introducing second layer of EC material.

In the present investigation, we have used the dependence of polarization P on an auxiliary parameter, which can be represented by a magnetic field (magnetoelectric effect) or a mechanical stress. Let us consider the free energy functional of the following type:

$$F = F_0(T) + \frac{aP^2}{2} + \frac{bP^4}{4} - EP + \alpha\eta P^2 + \frac{\beta\eta^2}{2} - \eta\sigma \tag{9}$$

where $F_0(T)$ is a certain function of the temperature, η is the second (in addition to P) order parameter, σ is an external field, and α and β are constant coefficients. In what follows, η implies deformation and σ denotes elastic stress, so that β is the elastic modulus and α is the piezoelectric modulus. Note that, for crystals, α, β, η, and σ are tensor quantities [12]. The free energy given by expression (9) describes a piezoelectric effect that is quadratic with respect to polarization P. Writing the condition of minimum for the free energy according to equation (9) yields the following system of equations:

$$(2\alpha\eta + a)P + bP^3 = E,\ \alpha P^2 + \beta\eta = \sigma \tag{10}$$

from which the order parameters P and η are determined as functions of the known variables E and σ. For $\alpha = 0$, the second equation of system (10) describes the usual Hooke's law. Excluding η from this equation, we obtain the following relation:

$$(2\frac{\alpha}{\beta}\sigma + a)P + (b - \frac{2\alpha^2}{\beta})P^3 = E \tag{11}$$

which determines the dependence of polarization P on E, η, and σ. The entropy and heat capacity of the system are determined as follows:

$$S = -\frac{\partial F}{\partial T},\ C_E = -T(\frac{\partial^2 F}{\partial T})_E.$$

Having denoted$F_0''(T) = k$ we obtain the following expression for the EC coefficient:

$$\gamma(T, \sigma) = \frac{pP(T, \sigma)}{k + a_0 pP(T, \sigma)} \tag{12}$$

According to the above formulas the EC coefficient γ depends on stress σ. According to the results of calculations [38], the EC effect in compressed (clamped) BST ceramics is characterized by $\gamma_{cl} \approx 0.6\gamma_{free}$, where γ_{cl} and γ_{free} are the EC coefficients for the clamped and free ceramics. For $BaTiO_3$, the analogous relation is $\gamma_{cl} \approx 0.8\gamma_{free}$ [1]. It is important to note that the process of external field variation can be isothermal (with neglect of the barocaloric effect), which makes it possible to organize the most effective thermodynamic cycle, a four-stage Carnot cycle. First, the electric field is applied to a preliminarily clamped sample, and the sample is adiabatically heated. At the next stage, the external pressure is isothermally reduced to zero. At the third stage, the electric field is switched off. Finally, the sample is isothermally clamped. The resulting change δT in the sample temperature per cycle can be exactly calculated using formulas (4), (8), and (11). It can also be qualitatively estimated through ΔT. Adopting the ratio of $\gamma_{cl}/\gamma_{free} = 0.8$, we obtain $\delta T = 0.2\Delta T$, which significantly exceeds the corresponding value in the absence of a control mechanical stress. Indeed, $\delta T = (0.01 - 0.02)\Delta T$ according to numerical calculations [10, 20, 35] and $\delta T = 0.05\Delta T$ according to experimental data [55].

Since the organization of a Carnot cycle is technically difficult, let us consider a simpler case of periodically varying applied electric field and mechanical stresses:

$$E = E_0 \sin(\omega t),\ \sigma = \sigma \sin(\omega t + \varphi),$$

where E_0 and σ_0 are the amplitudes, ω is the frequency, and φ is the phase shift. In this case, the EC coefficient can be expressed as follows:

$$\gamma \approx \gamma_0(1 + \gamma \sin(\omega t + \varphi)) \tag{13}$$

where γ_0, γ_1, and φ are constant (time-independent) parameters. The results of a numerical solution of (4) and (13) for a lead magnesium niobate–lead titanate (PMN–PT) ceramics are presented in the Fig. 3. As can be seen, a difference between the initial and steady-state temperatures strongly depends on the phase shift, and both heating and cooling of the ceramic sample can take place. Thus, by

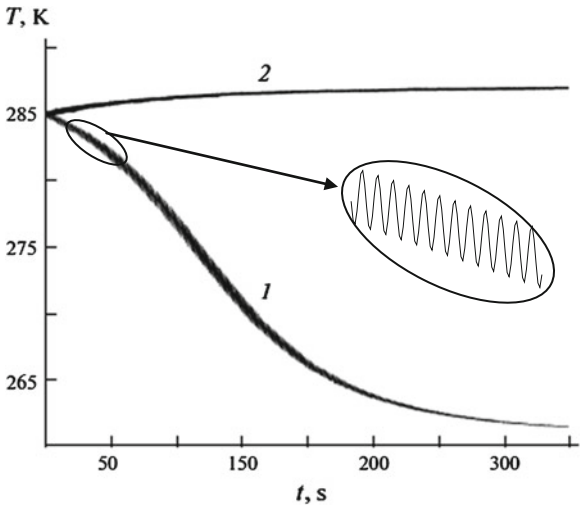

Fig. 3 The time variation of the temperature of PMN–PT ceramics in response to periodic oscillations of the applied electric field and mechanical stress with a relative phase shift of (*1*) $\varphi = \pi$ and (*2*) $\varphi = 0$

consistently varying the electric field and external pressure, it is possible to ensure a five- to ten- fold increase in the EC effect. The same approach can be used to enhance the magnetocaloric effect. It was demonstrated [49] that a 1 GPa pressure applied to $La_{0.69}Ca_{0.31}MnO_3$ single crystals increases the phase transition temperature by 25 K, thus decreasing the magnetocaloric effect to less than half.

Finally, it should be noted that there are different variants in selecting the order parameter η and external force σ. In piezomagnetics, it is possible to develop pressure by applying a magnetic field. The pressure can also be produced using the second layer of a piezoelectric, to which voltage E_2 is applied consistently with E. Another possible variant employs the barocaloric effect controlled by the electric field. In addition, it is possible to use multiferroics, in which the caloric effect not only depends on the main parameters (temperature and field strength), but can also be modulated by some other parameter.

From the presented analysis suggests that the use of nonlinear dynamic effects can produce a significant increase in the cooling effect. A more accurate calculation can be made only if we know the dynamic characteristics of the ferroelectric.

3 Dynamic Characteristics of Electrocaloric Materials

3.1 Dynamic Polarization in Electrocaloric Materials

Differences in the experimental approaches, measurement techniques, and objects used in this study hinder the realistic assessment of possibilities of the EC effect application in solid-state cooling devices. In this context, a topical problem is developing a theoretical approach to description of the EC response in ferroelectric

material excited by periodic variations of the external electric field. This process results in permanent dynamical change of thermodynamic parameters and a temperature inside the EC-cooling structure. More adequate model of EC-based cooling structure could be built just due to physical processes dynamics study.

Traditionally just static model is considered and it does not take into account any dynamic effects. The EC effect in a sample is described by the following classical formula:

$$\Delta T = -T \int_{E_1}^{E_2} \frac{1}{\rho C_E} \frac{dP}{dT} dE = -T \int_{E_1}^{E_2} \frac{\gamma_{ec}}{\rho} dE \tag{14}$$

where ΔT is the sample temperature variation relative to its initial value T, C_E is the heat capacity of the given material at a constant electric field strength, ρ is the material density, $P = P(T, E)$ is the polarization, and E_I and E_2 are the initial and final field strengths, respectively.

Formula (14) is derived in an adiabatic approximation and provides quite accurate description of the EC effect during quasi-static variation of the electric field E [24]. If the sample is involved in heat exchange with the surrounding medium, the temperature distribution becomes inhomogeneous and equation (14) has to be replaced by a more complicated expression [20, 26, 36, 45] that takes into account thermal relaxation processes in the EC element.

This chapter presents the results of an investigation of the influence of a polarization relaxation on the EC effect in a periodically varying electric field. The characteristic relaxation time is assumed to be small compared to the period of oscillations of the electric field.

A dynamic equation relating the electric field E and polarization P in a ferroelectric material was written by Landau and Khalatnikov (Landau et al. [22]) in the following form:

$$\alpha \frac{dP}{dt} = E(t) - aP - bP^3 \tag{15}$$

where $a = a_0(T - T_0)$; α, a_0, and b are constant coefficients; and T_C is the Curie temperature. From the standpoint of physics, a change in the sample polarization is equivalent to the presence of a current $J = \partial P/\partial t$ that, in turn, leads to the appearance of a dynamic field $E_\mathrm{Dyn} = \alpha J$, where α is the effective internal resistance. In what follows, the electric field is assumed to vary with the time according to a harmonic function as $E(t) = E_0 \sin(\omega t)$, where E_0 is the field amplitude and ω is the circular frequency.

Introducing the characteristic relaxation time $t_\mathrm{R} = \alpha/|a|$ and a parameter $s = \omega t\mathrm{R}$, which is assumed to be small ($s \ll 1$), Eq. (15) can be rewritten in the following form:

$$s \frac{dy}{dx} = -\sin(a)y - y^3 + e_0 \sin(x) \tag{16}$$

where $y = \sqrt{\frac{b}{|a|}}P$, $e_0 = \frac{E_0}{|a|}\sqrt{\frac{b}{|a|}}$, $x = \omega t$, are dimensionless quantities. Let us seek a solution to Eq. (16) for a stationary regime, in which case the initial conditions are insignificant [30] and represent this solution in the form of a series in powers of the small parameter s as follows:

$$y = \sum_{n=0}^{\infty} y_n(x)s^n \tag{17}$$

Substituting expression (17) into Eq. (16) and equating coefficients at the same powers of s, we obtain a recurrent set of equations for determining coefficients $y_n(x)$. The first equation that corresponds to the terms not containing s has the following form:

$$\sin(a)y_0 + y_0^3 - e_0\sin(x) = 0 \tag{18}$$

which coincides with the stationary Landau–Ginzburg equation. For y_0 at $T < T_C$, we can select any stable root of the three ones for Eq. (16) or the single root of this equation for $T > T_C$.

From the next equation, which is obtained for the terms involving s, we obtain the following coefficient at the first-order term in series (17):

$$y_1 = -\frac{y_0'}{\mathrm{sgn}(a) + 3y_0^2}.$$

The high order terms with $n > 1$ in series (17) are also readily determined from the subsequent recurrent equations. Restricting the consideration to the first two terms in series (17), we obtain the following approximate formula for the polarization:

$$P(t) \approx P_0(t) + P_1(t) \tag{19}$$

where P_0 is the quasi-static polarization determined from the Landau–Ginzburg equation and P_1 is the dynamic correction to P_0. This correction has the following form:

$$P_1(t) = -\frac{\omega\alpha E_0\cos(\omega t)}{(a + 3bP_0^2)^2} \tag{20}$$

It should be noted that formulas (19) and (20) remain valid in the vicinity of the Curie point, but they are inapplicable at the switching point where $P_0^2 = -a/(3b)$.

These formulas are readily generalized to the case of an arbitrary dependence of polarization P on the field E, which corresponds to the following equation:

$$s\frac{dP}{dt} = F(P, E(t), t) \tag{21}$$

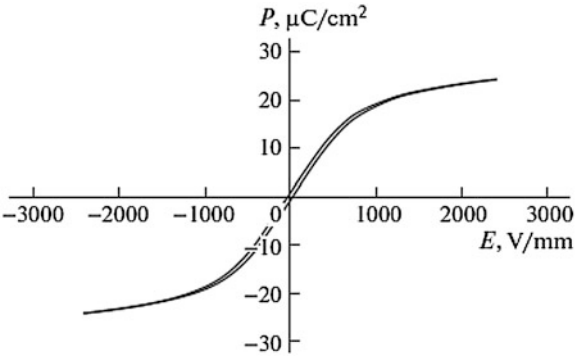

Fig. 4 The polarization hysteresis observed for a paraelectric phase of $Pb(Mg_{1/3}Nb_{2/3})O_3$–$PbTiO_3$ ceramics [12]

Here, $F(P, E(t), t)$ is an arbitrary function, in particular, polynomial of a higher power than that in Eq. (15). The asymptotic behavior of a solution to Eq. (21) in a stationary regime is described by the following expression:

$$P(t) = P_0(t) + s\frac{P_0'}{\frac{\partial F(P,E(t),t)}{\partial P}} + O(s^2) \tag{22}$$

An analysis of the obtained results leads to the following conclusions. First, formulas (19) and (20) can be used to describe the hysteresis in a paraelectric phase (i.e., at $T > T_C$), in which case Eq. (18) has a single solution. According to this, the hysteresis (Fig. 4) observed in experiments [16] is readily explained by correction (20). Indeed, for $E(t) \sim \sin(x)$, this correction can take two values that correspond to the different signs of $\cos(x)$ and lead to the two branches (hysteresis) in the $P(E)$ plot. Using the reported experimental data [16], it is possible to determine the relaxation parameter α for the given ferroelectric material. Denoting the values of polarization at $(E = 0)$ by P_U and $P_D (P_U > P_D)$, we obtain $P_0|E = 0 = 0$ and

$$\alpha = \frac{a(P_U - P_D)}{2\omega E_0}.$$

Second, the presence of correction (20) leads to additional dependence of the dielectric permittivity on the frequency.

Third, we can define the dynamic spontaneous polarization of a ferroelectric material as $P_{SDyn} = P(E = 0)$, that is, as the value of polarization at the intercept of the $P(E)$ curve with the P axis. Then, formula (20) yields the relation

$$P_{SDyn} - P_s = \frac{\alpha\omega E_0}{a^2},$$

where P_S is the static spontaneous polarization. The latter is $P_S = \sqrt{-a/b}$ for $a < 0$, $T < T_C$ and $P_S = 0$ for $T > T_C$. Thus, the dynamic spontaneous polarization is always greater than the static one. In the particular case of a paraelectric

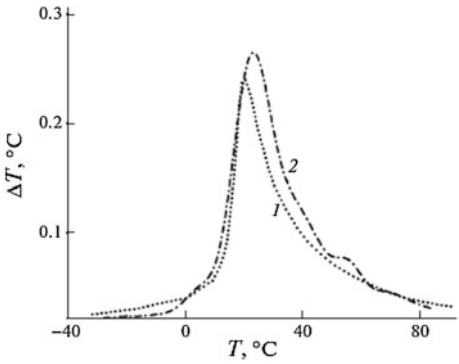

Fig. 5 The temperature dependence of the EC response (*1*)—measured for $Pb(Mg_{1/3}Nb_{2/3})O_3$–$PbTiO_3$ ceramics (Hagberg et al. [16]) and (*2*)—calculated using the temperature dependence of the spontaneous polarization

phase with $P_S = 0$, there exists a dynamic polarization P_{SDyn} that is caused by the periodic variation of the electric field.

Fourth, since formula (14) for the EC effect is obtained in the quasi-static approximation, it involves the static polarization P_0. Therefore, replacing P_0 by the dynamic polarization $P_1 = P_{Dyn}$ in Eq. (14) (as it was done in [29]) leads to an overstated magnitude of the EC effect, whereby the maximum EC response shifts toward higher temperatures. This fact was established in Neese et al. [33], where the difference between the results of calculations (using P) and the data of measurements varied within 15–20 % depending on the temperature.

Figure 5 shows the typical temperature dependence of the E_C response ΔT measured for $Pb(Mg_{1/3}Nb_{2/3})O_3$–$PbTiO_3$ ceramics (curve 1) [16], in comparison to the results of the calculations using the temperature dependence of the spontaneous polarization.

In conclusion, the proposed theoretical approach based on the Landau–Khalatnikov model shows that adequate description of the EC effect for a ferroelectric material in an alternating electric field is provided by E_q. (19) with the temperature-dependent polarization. We believe that the use of a quasi-static model in this case is incorrect and leads to erroneous results.

3.2 Thermal Hysteresis in Ferroelectrics Capacitance

Thermodynamics processes in cooling structure, presented in Sect. 1, along with adiabatic temperature change process, include, as well heating (cooling) process for element under permanent field. This process is accompanied with polarization changing. That is why it is important to know polarization dependence on temperature under heating and cooling modes. It defines specific of operational cooling system prototype based on multilayer structure. Study of thermal hysteresis in layered structures provides necessary data for comparative analysis of various materials applied to cooling structure.

This section presents the results of cooling time regime influence, electric field and electrical conductivity influence on temperature hysteresis of the capacitor structures based on $Ba_xSr_{1-x}TiO_3$ (BST) and $Pb(Mg_{1/3}Nb_{2/3})O_3$–$PbTiO_3$ (PMN-PT) ceramics. The BST ceramics is very common ferroelectric ceramics type for various electronics application [24, 44, 53], however it has rather high level of dielectric losses ($\tan\delta \sim 10^{-2}$) for microwave [53] and temperature control by means of electrocaloric effect applications. Another disadvantage of BST ceramics is not reproducible properties after initial action of electric field (dielectric hysteresis) [13, 53]. An introduction of Mg or Mn dopants [7, 56, 57] allows effectively managing by electric properties of BST ceramics. The better results ($\tan\delta \sim 10^{-3}$) at sufficiently high level of control (dielectric permittivity dependence on electric field) have been achieved using Mg doping [6, 8, 19]. However, the doping of BST ceramics does not give a possibility fixing dielectric hysteresis and satisfying to the requirements for temperature control components using electrocaloric effect [6, 8, 34, 45, 47]. Thus, the study of temperature and electric field influence on dielectric properties of ferroelectric ceramics of two types (BST and relaxor PMN–PT) is perspective and necessary.

Temperature dependences of the capacitance and dielectric losses of ferroelectric ceramics were measured at frequency 1 MHz. It is known that BST solid solutions has no the dispersion of dielectric permittivity (ε) in a range of frequencies $f = (10^2$ to $10^{12})$ Hz. We carried out the frequency measurements of dielectric permittivity and quality factor [34] of BST:Mg investigated ceramic samples in a range (10^3 to $5{\cdot}10^{10}$) Hz that have confirmed an absence of frequency dispersion ε and a little reduction of the quality factor (increase of dielectric losses) with frequency enhancement.

Temperature dependences measurements of the capacitance and dielectric losses were carried out at frequency 1 MHz using automatic impedance digital bridge device E7-12 [34]. The measurement error did not exceed 0.02 pF and the fractional error of dielectric permittivity definition was no more than 0.2 %. The amplitude of a measuring field was stabilized at 2.5 V/cm. The leakage current measurements of sample conductivity were carried out by means of electrometer B7-30 in a range of 10^{-13} to 10^{-5} A. The fractional error of current measurement did not exceed 10 %.

Voltage capacitance characteristics (VCC), current–voltage characteristics (CVC) and temperature dependencies $C(T)$ were measured at various values of bias voltage. The installation was capable of performing measurements for values of bias voltage in the range $U = \pm 1{,}000$ V. During the measurements process the temperature was automatically controlled. The absolute error of temperature measurements did not exceed 0.05 K in the temperature range 78–400 K, temperature variation rate was changed in the range (0.025–0.5) K/s. The temperature cycle of differential capacitance measurements consisted of the cooling process from 290 K down to 140 K and further heating process back to 290 K. The dependencies of differential capacitance on temperature $C(T)$ were measured for ten values of bias voltage—from 0 to 900 V.

Applicability of the ferroelectric material for technical purposes is determined by the values of dielectric permittivity ε, dielectric losses tanδ and tunability coefficient (k). The coefficient is the ratio of the brought dielectric permittivity at zero electrical field to ε value at maximal intensity of electrical field. The Mg additives to BST compound decrease dielectric losses, that it is important for microwave applications. The investigated samples of $Ba_xSr_{1-x}TiO_3$ ($x = 0.55$) have contained 12 wt.% of Mg additive. Latter we will consider this dependence on the dielectric loss tangent of the concentration. The selected BST compound has dielectric losses parameter tan $\delta = (5.5–6.0)\cdot10^{-3}$ that is much lower comparing with original BST compound. Earlier [34] we have shown than the magnesium additive decrease dielectric permittivity, at Mg concentration of (10–25) wt.% dielectric permittivity is standing at the level $\varepsilon = (500–600)$ and the tunability coefficient is sufficiently high that is important as for microwave tunable devices as well as for thermal conversion processes. Thus, the indicated Mg additive concentration corresponds to the required working parameters of the capacitor structures $\varepsilon \geq 500$; tan $\delta \leq 10^{-2}$ and in microwave region $k \geq 1.2$ at the fields $E_{max} = 4–5$ V/μm.

The composition and weight content of Mg additives, the synthesis temperature (1,350–1,540) °C have been chosen to provide a weak interaction between two main phases in ferroelectric ceramic. The porosity of the ceramic samples did not exceed 5 %. The polished ceramic samples having disk shape with the thickness 0.5 mm and diameter 5–6 mm were covered by gold electrodes using magnetron sputtering. The X-ray diffraction analysis has shown that the samples have contained of perovskite cubic phase and the second Mg_2TiO_4 spinel phase. It was found that basic BST perovskite phase has contained magnesium atoms (up to 5 at.%) that change the parameter of a crystal lattice.

The $0.87Pb(Mg_{1/3}Nb_{1/3})O_3$—$0.13PbTiO_3$ (PMN–PT) ceramic samples were sintered using the technology described earlier [16] in the laboratory of microelectronics and material physics of the University of Oulu. The ceramics thickness was 1–1.4 mm and the electrode diameter—7.6 mm. The X-ray diffraction analysis has showed a presence of single perovskite phase.

Temperature measurement cycle for the differential capacitance was based on samples cooling from 290 K down to 140 K and heating back up to 290 K. Differential capacitance dependence of temperature $C(T)$ was measured for ten values (from 0 to 900 V) of the bias voltage at the rate of temperature change of 0,025 K/s. Figure 6 shows the $C(T)$ dependencies for BST sample at absence of electrical field and two values of bias voltage from the indicated region. The dielectric permittivity for the chosen samples had the following maximal values $\varepsilon_m(0) = 6{,}700$, $\varepsilon_m(300\text{ V}) = 4{,}150$, $\varepsilon_m(900\text{ V}) = 1{,}900$. An increase of bias voltage leads to capacitance value decrease; the temperature of C_m is displaced to the right on temperature axis. Such temperature displacement of $C(E, T)$ dependencies is usual for the ferroelectric materials with wide and spread phase transition of the second order [24, 44]. However on dependences of temperature hysteresis both in ferroelectric and in paraelectric phase was observed.

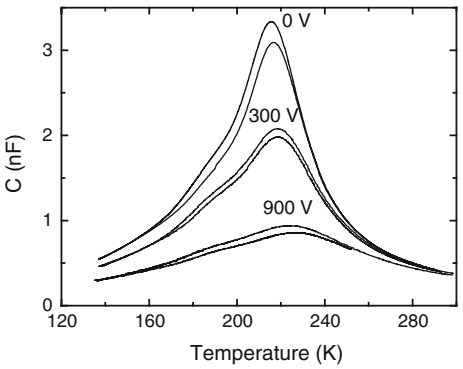

Fig. 6 The temperature dependence of BST ceramics sample capacitance at temperature variation rate 0.025 K/s and several bias voltage values

As a temperature hysteresis we understand not only a displacement of temperature maximum of the sample capacitance at cooling (T_{m1}) and heating (T_{m2}) – ($\Delta T_m = |T_{m1} - T_{m2}|$), but also relative reduction of the maximum values of capacitance at cooling (C_{m1}) and heating

$$(C_{m2}) - (\Delta C_m / C_{m1}) = (C_{m1} - C_{m2}) / C_{m1}.$$

The temperature of capacitance hysteresis of the investigated BST:Mg samples has showed unusual behavior of perovskite material at influence of external electric field. The nonlinearity reduction in most part of perovskite materials show that hysteresis phenomena become less appreciable, i.e. the hysteresis is decreased at influence of electric field $E \sim 10^5$ V/m [44, 53] In our case in the beginning the temperature hysteresis of the ceramic capacitance was decreased at voltage influence, and, from the voltage ~500 V that corresponds E ~ 10^5 V/m, the hysteresis was increased.

The increase of cooling-heating process rate leads to the enhancement of temperature hysteresis. This effect is illustrated in Fig. 7, where temperature dependence of capacitance is presented at zero bias voltage and temperature variation rate 0.5 K/s. It is necessary to notice that the temperature hysteresis was

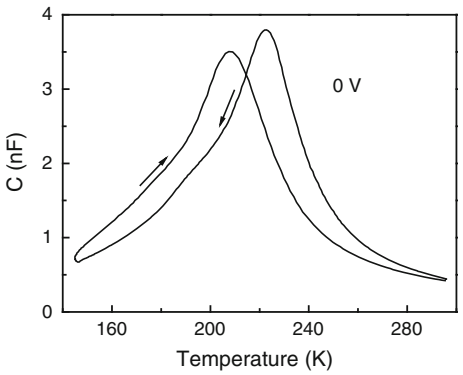

Fig. 7 The temperature hysteresis of BST ceramics sample capacitance at temperature variation rate 0.5 K/s

depended on a speed of cooling and heating of the samples. So the temperature hysteresis in absence of voltage at speed of temperature change ~0.025 K/s has made $\Delta T_m = 2$ K and the maximum of the capacitance temperature dependence at heating of the samples was displaced to higher temperature. The temperature hysteresis for the same sample at temperature variation rate ~0.5 K/s is increased to $\Delta T_m = 27$ K (Fig. 7). Thus a displacement direction to a maximum of temperature dependence T_{m2} is changed on opposite, the temperature hysteresis of the capacitance $\Delta C_m/C_{m1}$ is also increased. The heating mode has appeared more sensitive to a speed of temperature change, than a cooling mode. It has been established that at speed of change of temperature $V \sim 0.05$ K/s the temperature hysteresis ceases to depend on a speed of cooling of the samples [16]. The increase of cooling-heating process rate leads to the enhancement of temperature hysteresis. This effect is shown in Fig. 7. The dependence of temperature hysteresis on temperature variation rate $\Delta T_m(v)$ has a linear character.

The temperature hysteresis in BST:Mg structures was measured in more details and voltage capacitance characteristics were obtained at 300 K (Fig. 8). The capacitance indeterminacy on VCC reached several per cent and it was observed at every value of voltage. Such VCC plot corresponds to the hysteresis loops of large width that is typical behavior for relaxor ferroelectrics. In ferroelectric phase the hysteresis reaches the tens of per cents. At $T = 300$ K and zero bias voltage the permittivity value $\varepsilon(0) = 830$.

Dielectric loss factor at zero bias voltage is $\tan\delta \sim 10^{-4}$ and most part of the samples has demonstrated $\tan\delta$ increase with bias voltage enhancement. Fig. 9 illustrates sharp decrease of $\tan\delta$ at Mg doping additive increase in the region 0–60 wt.% to BST compound. However, from practical point of view the increase of Mg additive higher than 20 wt.% is not appropriate because of considerable decrease of capacitance control factor.

The conductivity of the samples and existence of free charge carriers can render a significant influence on the hysteresis phenomenon [6], therefore the measurements of current–voltage characteristics are helpful. Typical voltage-capacitance and current–voltage characteristics of BST ferroelectric ceramics with Mg additives is presented in Figs. 10 and 11. Figure 11 shows three regions of CVC in

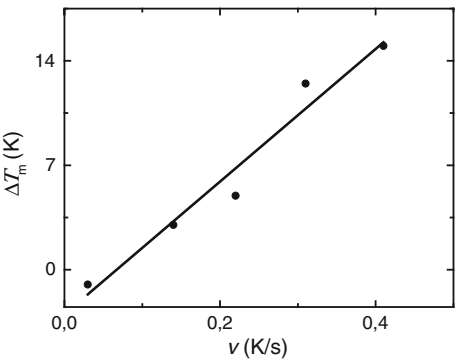

Fig. 8 The shift in temperature hysteresis dependence on temperature variation rate

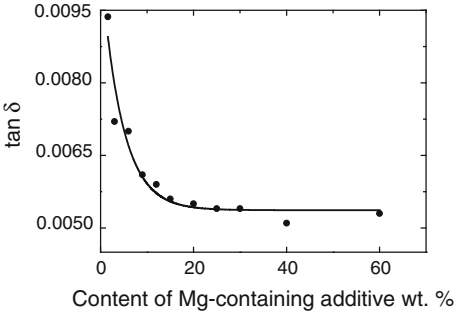

Fig. 9 The dependence of the dielectric losses on the contents of Mg-containing additives ($f = 10$ GHz)

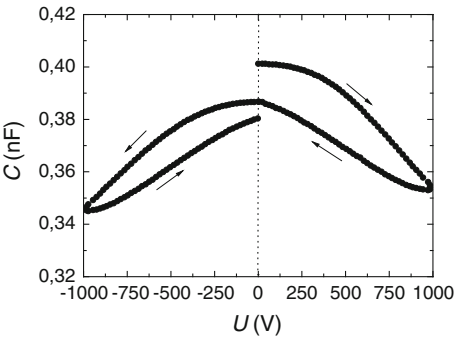

Fig. 10 The capacitance–voltage characteristics of BST based sample

double logarithmic scale. At low voltage the dependence corresponds to Ohm's law. At the following region, where current decrease is observed, a voltage increase is revealed, so some kind of negative differential resistance is identified. At higher voltage (more than 500 V) exponential current growth is exhibited. Estimation of sample resistance for the Ohm-related region results with $R \sim 6 \times 10^{10}\ \Omega$, the specific samples resistivity was found to be $(3.2 \pm 0.4) \times 10^{-10}$. $\Omega^{-1}\text{m}^{-1}$. Earlier we showed in [6] that the presence of negatives differential resistance and exponential growth on CVC is currently leading to high value of hysteresis value.

An observation of same characteristics for PMN–PT ceramics gives the temperature dependencies of the capacitance at zero and two other values of bias voltage, as it is shown in Fig. 12. An increase of bias voltage leads to a lowering of $C(T)$ curves and temperature of the capacitance maximum is shifted insignificantly ($\Delta T_\text{m} = \pm 1$ K). Dielectric hysteresis on $C(U)$ dependences is not observed, as it is shown in Fig. 13. The Ohm's law region and negative differential resistance regions are distinguished clearly, but exponential growth at higher voltages is not found (Fig. 14). The following values of dielectric characteristics for PMN–PT samples was calculated by the experimental results: $\varepsilon_\text{m}(0) = 18{,}000$, $\varepsilon_\text{m}(450) = 16{,}000$, $\varepsilon_\text{m}\ (950) = 12{,}000$. At T = 300 K the dielectric permittivity was 8,200; tan $\delta \sim 10^{-1}$, $R = 2 \times 10^{-10}\ \Omega$.

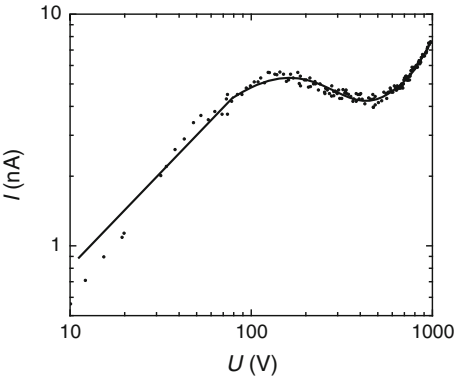

Fig. 11 The current–voltage characteristics of BST based sample

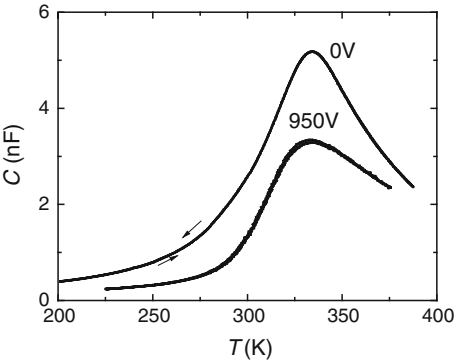

Fig. 12 The temperature dependence of PMN–PT sample capacitance for the several values of bias voltage

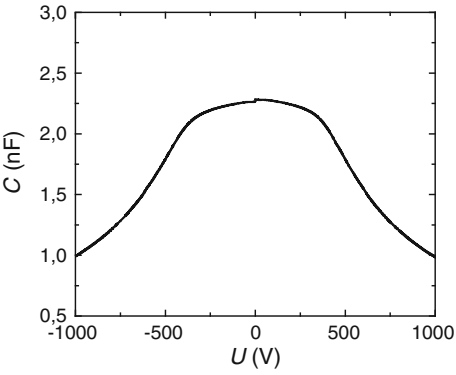

Fig. 13 The capacitance–voltage characteristics of PMN–PT sample

The investigations of voltage capacitance and current voltage characteristics (Figs. 11 and 14) and the dependencies $C(T)$ have shown that the phenomenon of temperature hysteresis exhibited in BST ceramic with Mg-content additives could be explained by means of high level of inhomogeneities, which are contained in

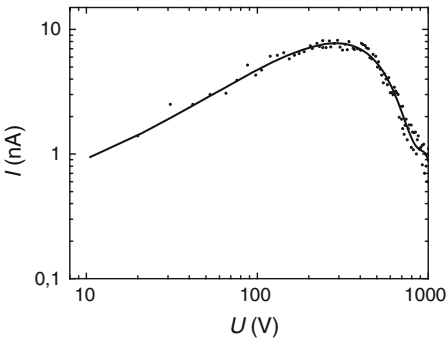

Fig. 14 The current–voltage characteristics of PMN–PT sample

the ceramic samples in comparison to significantly higher homogeneous single-phase PMN–PT ceramics. Scanning electron microscope (SEM) images of BST ferroelectric ceramics containing Mg additives were obtained using the JSM-6460LV JEOL microscope. One of these images is presented in Fig. 15. The BST ceramics contain the crystallites and noncrystalline inclusions of various dimensions (1 … 10 μm). Apparently the ceramics contain at least two phases: main perovskite phase and intergranular contaminations (shown as B and I in Fig. 15). Intergranular medium also contains small crystallites of (0.3 … 5) μm.

The X-ray microstructural analysis have shown that basic BST phase is composed of two perovskite phases with lattice parameters (3.935–3.941) Å and (3.954–3.966) Å. Pure BST ceramics of the chosen composition has lattice parameter of 3.9513 Å. The first phase, which has lower than pure BST ceramics lattice parameter, is related to the phase with lower content of Ba ions. It is known [48, 53] that in some solid solutions of BST the lattice parameter decreases linearly from 4.040 Å (at x = 1) to 3.905 (at x = 0). Slight increase of lattice parameter of the second phase can be associated with partial substitution of Ti^{4+} in BST [18, 19] lattice with Mg^{2+}, or with increase of Ba content up to $x \sim 0.6$ (reference value

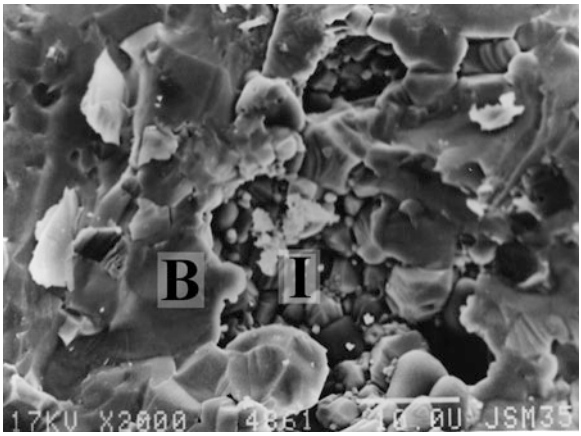

Fig. 15 The scanning electron microscope image of the surface of ferroelectric BST ceramic with magnesium additive

for $x = 0.6$ equals to 3.965 Å). Thus composite BST ceramics with magnesium additives has hetero-phase structure, composed of basic BST phase solid solution and phase with magnesium content. Some ceramics areas composing 1–30 % of the crystalline magnesium containing phase render considerable influence on highly defective phase of ferroelectric ceramics.

The shown micro-inhomogeneities lead to temperature hysteresis, and it could be connected with the following purposes:

- An enhancement of mechanical strains and deformations and following relaxation of the mechanical stress in the process of sequential cooling and heating cycles.
- An appearance of the defects internal electrical fields at the inhomogeneities borders that decrease dielectric permittivity at the region of the fields presence.
- Screening of the free carriers of the polarized regions of the crystals.

The appearance and relaxation of the mechanical strains, i.e. existence of elastic hysteresis mechanism is supported with the fact that temperature hysteresis value depends on sample cooling and heating rate (Figs. 6, 7 and 12).

Existence of internal electric fields of the defects in perovskite ferroelectrics is supported with the dependence of capacitance temperature hysteresis on applied field, and it relates to existence of dielectric hysteresis at all values of bias voltage (Fig. 6). Dielectric hysteresis of capacitance was discussed earlier, [7, 54] and the estimation of internal electric field values was given $E \sim (5 \times 10^5$ to $10^6)$ V/m.

Apparent influence on dielectric [6, 34] and consequently temperature hysteresis is exerted by conductivity of samples. Temperature hysteresis of the ferroelectric capacitance is decreased in the range, where current decreases—the range of negative differential resistance,—and it increases as voltage values, which corresponds to exponential growth of current ($E \sim 2{\cdot}10^5$ V/m). Free charge carriers, screening polarized areas in the single crystals, which do not take part in further processes of repolarization. This is the third cause of temperature hysteresis. This mechanism should have most influence in ferroelectric phase. Second and third causes of temperature hysteresis reveal the mutual influence to each other.

So we have obtained the temperature hysteresis of the capacitance basing on the ceramics $Ba_{0.55}Sr_{0,45}TiO_3$ containing 12 wt.% of Mg complex additive. There is the correlation between temperature hysteresis and the thermocycling regime of the measurement process. The increase of thermocycling process leads to the growth of temperature hysteresis. The high limit rate of temperature variation was 0.05 K/s. Exponential growth of the current at voltage intensity $2{\cdot}10^5$ V/m caused an essential influence on the temperature hysteresis. The phenomenon of temperature hysteresis is connected with high level of the micro inhomogeneities with Mg-containing doping.

3.3 Thermo-Relaxation Time in Electrocaloric Materials

One of the trends in studies is the measurement of temperature variations occurring under the action of an electric field. The temperature effect is measured using direct and indirect methods. The most widely used indirect method is based on the Maxwell relations

$$(dD/dT)_E = (dP/dT)_E = (dS/dT)_T,$$

where S is the entropy, E is the electric field strength, D is the electric induction, P is the polarization, $D = \varepsilon_0 E + P$, ΔT is the adiabatic change in temperature, ΔS the isothermal change in entropy for a material of density ρ, heat capacity C_E, and for electric field variation from E_1 to E_2. The Maxwell relations lead to [7]

$$\Delta S = -\int_{E_1}^{E_2} \left(\frac{dP}{dT}\right)_E dE.$$

Considering the complex nature of ferroelectric relaxor materials, the actual temperature response can not be determined exactly by calculating the temperature effect on the basis of these formulas, and the dynamics of the response cannot be analyzed.

In recent years, the temperature effect has been measured directly with an electric bias voltage applied to ferroelectric capacitors. It was shown that the change in temperature due to the electrocaloric effect (which was obtained by recalculating the temperature dependence of spontaneous polarization) and direct temperature measurements give noticeably different results [46]. On the one hand, this can be explained by not quite correct employment of the quasi-static model for the recalculation. On the other hand, standard measuring facilities introduce distortions comparable with the value of the effect being measured and are characterized by a considerable inertia which is inadmissible for rapidly occurring processes. For example, the heat capacity of a microthermocouple is commensurate with the heat capacity of a ferroelectric film in which the electrocaloric effect is measured.

In this study, we propose a new method for measuring rapid changes in temperature, which is based on the use of a ferromagnetic film resonator as a temperature gauge.

The saturation magnetization M_0 of a ferromagnetic demonstrates a strong temperature dependence [37], which can be used for temperature measurements. Figure 16 shows the $M_0(T)$ curve for an yttrium–iron garnet (YIG) epitaxial film. It is important that in the range of room temperatures (200–400 K), this curve can be approximated by a linear dependence of the type $M_0(T)$ [G] $= 4532 - 9.3\,T$.

Consequently, the resonance frequency of the microwave ferromagnetic film resonator is also a function of temperature, which can form the basis of the precision method for studying rapid variations in temperature.

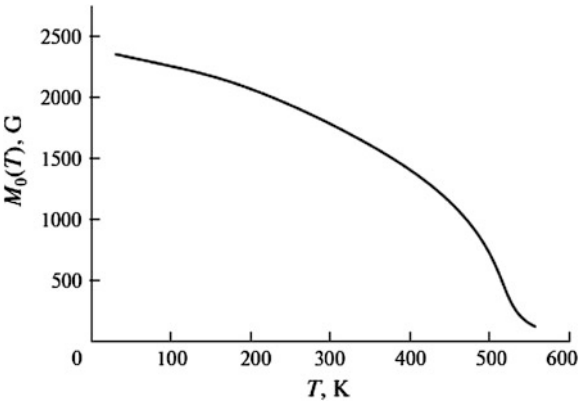

Fig. 16 The temperature dependence of the saturation magnetization for yttrium–iron garnet

Let us drive the expression for the temperature dependence of the resonance frequency of a microwave ferromagnetic film resonator. The dispersion equation for spin waves existing in the ferromagnetic medium can be written in the form [56]

$$\omega^2(kL) = [\omega_H + \omega_M - \omega_M P(kL)] \times [\omega_H + \omega_M P(kL)\sin^2\varphi] \tag{23}$$

where ω and k are the frequency and wavenumber of a spin wave; $P(kL) = 1 - [1 - \exp(-kL)]$, L being the thickness of the ferromagnetic film; ϕ is the angle between the direction of propagation of the wave and magnetic displacement vector H_0, $\omega_H = \mu_0\gamma H_0$, $\omega_M(T) = \mu_0\gamma M_0(T)$, γ being the gyromagnetic ratio, and $M_0(T)$ being the temperature dependence of the saturation magnetization. The eigenfrequencies of the resonator can be obtained from Eq. (23). The wavenumbers for the resonator eigenmodes are quantized as follows:

$$k = k_{gr} = \pi\sqrt{\left(\frac{q}{a}\right)^2 + \left(\frac{r}{b}\right)^2} \tag{24}$$

where a and b are the linear sizes of a thin-film resonator with $L \ll a$ and b, and q and r are the integers determining the multiplicity of the resonance. Proceeding from simple geometrical considerations, we can write angle ϕ in the form

$$\sin^2\varphi = \left(\frac{q/a}{k_{gr}}\right)^2 \tag{25}$$

Figure 17 shows the temperature dependence of the main resonance frequency of a ferromagnetic film resonator magnetized in the plane of the film. Symbols show experimental results and the solid line corresponds to the theoretical calculations based on the linear approximation of the temperature dependence of saturation magnetization.

Differentiating the temperature dependence of the resonance frequency, we can show that the sensitivity of the temperature measurement by the proposed method

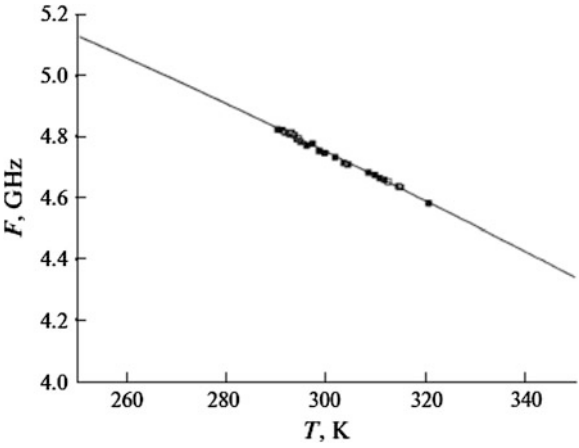

Fig. 17 The temperature dependence of the main resonance frequency of the ferromagnetic film resonator

is 10^{-4} K/kHz. Modern measuring instruments make it possible to measure the frequency in the range of interest up to several kilohertz. To analyze the dynamics of the electrocaloric effect, we used in our experiments a parallel-plate $Pb(Mg_{1/3}Nb_{2/3})O_3$–$PbTiO_3$ (PMN–PT) ferroelectric ceramic capacitor. The Curie temperature of the 0.87PMN–0.13PT material was about 48 °C. The temperature dependences of the permittivity of the ferroelectric ceramic under investigation for different voltages across the capacitor are shown in Fig. 11. Figure 18 shows schematically the measuring circuit diagram. The tangentially magnetized ferromagnetic resonator is excited with the help of a short-circuited microstrip

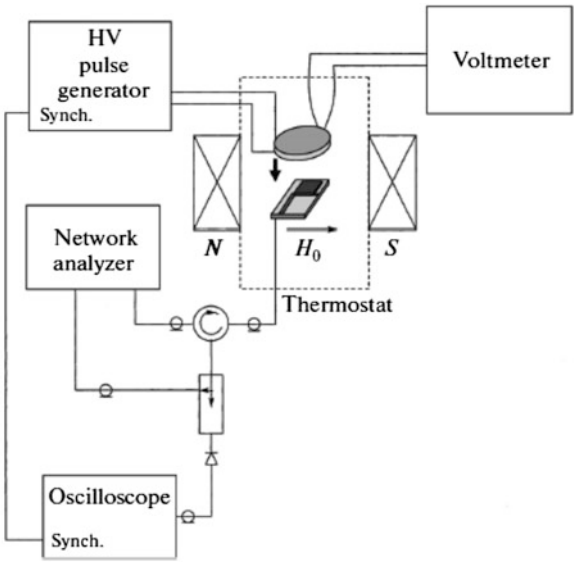

Fig. 18 The schematic diagram of the measuring unit

antenna. The resonator was cut from YIG epitaxial film 5 μm in thickness, which was grown on a 300-μm-thick gadolinium–gallium garnet substrate.

The resonator size in the plane was (2 × 2) mm^2. A ferroelectric capacitor with a high-voltage pulse generator connected to its plates is applied to the resonator on the side of the YIG film. The measuring prototype is placed into a thermostat, and its absolute temperature is measured by a constantan–manganin thermocouple. The external magnetic field in the measuring prototype region is produced by a samarium–cobalt magnet. The signal reflected from the measuring resonator is fed via a circulator to a directional coupler; a part of the signal is fed to the second port of the network analyzer, while the other part is fed to the detector of the oscilloscope synchronized with the high-voltage pulse generator. The resonance characteristic of the ferromagnetic resonator is registered by the network analyzer Rohde & Schwarz ZVA-40. The time variation of the temperature under the periodic action of the electric field (charging–discharging of the capacitor) is registered by the oscilloscope.

Recalculation of the temperature dependence of the resonant frequency shows that the sample is heated by 0.065 K and is cooled by 0.041 K relative to the temperature of the surrounding medium. Figure 19 shows oscillograms of the temperature response, which are plotted from the temperature shift of the ferromagnetic resonance frequency at the instant of the supply and removal of a high-voltage pulse. It can be seen that the time constant describing the temperature variation due to the electrocaloric effect amounts to 4.5 μs. A further change in temperature (cooling or heating) to the ambient level occurs over a period on the order of 10 μs, which is due to the thermal resistance between the sample and the thermostat. In this case, the fact that the Joule loss affects the shape of oscillograms must also be taken into account.

The experiments performed in the indicated temperature range have made it possible to construct the temperature dependence for the temperature response in the electrocaloric effect (Fig. 20).

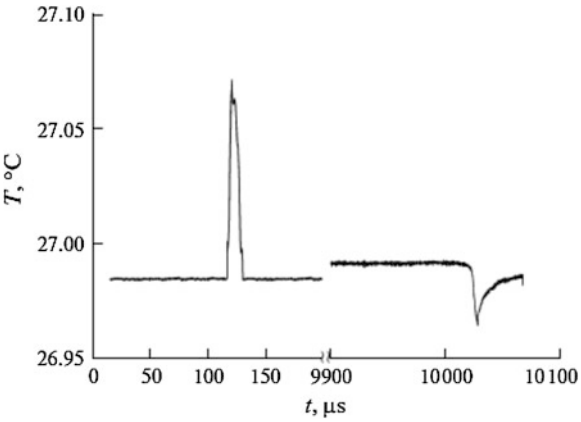

Fig. 19 The oscillograms of the temperature response for ferroelectric capacitor at instants of a high-voltage pulse applying and removing

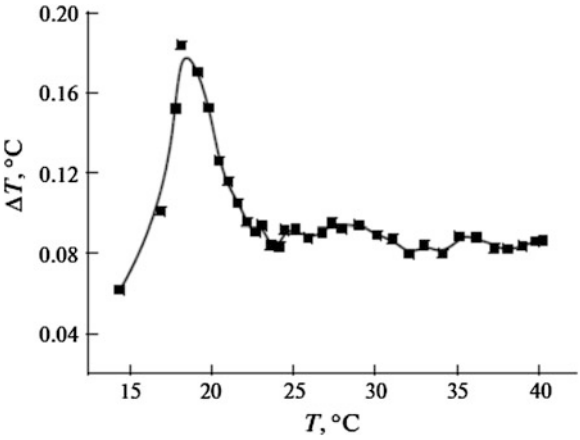

Fig. 20 The temperature dependence of the temperature response for electrocaloric effect in 0.87PMN–0.13PT ferroelectric capacitor

The curve shows that the peak of the electrocaloric effect lies in the range of 18 °C, which coincides with the peak of the derivative $d\mathrm{P}/dT$ this is in good agreement with thermodynamic relation (14).

4 Simulation of Electrocaloric Cooling Structure

4.1 Mathematical Model of Multicaloric Effect

One of the most promising approaches for practical realization of cooling device on the base of the ECE is a multilayered structure of ferroelectric, dielectric and metal alternating layers. The thicknesses of these layers as well as their thermal properties (e.g. thermal conduction and thermal capacity) must be chosen on the criterion of the cooling effect maximization. Moreover, in the case of a layered structure with layers differently distributed over temperature, temperature gradient and as a consequence heat flow take place. Therefore, in order to describe the thermal fields is necessary to use the heat equation not restricted by the simple model as described in Sect. 2. In addition, the presence of elastic stresses (caused by the boundaries of different materials, the thermal expansion of the layers, etc.) must be taken into account. For the purpose of the simultaneous description of electrical, thermal and elastic properties of the system we introduce the following quantities: vector of deformation u_i ($i = 1, 2, 3$), strain tensor

$$\varepsilon_{ij} = \left(u_{i,j} + u_{j,i}\right)/2$$

and stress tensor σ_{ij}. Here and below the symbol $\chi_{i,k}$ means $\partial\chi_i/\partial\chi_k$. Further we will use Einstein's notation for the summation of repeated indices.

The free energy density is given by:

$$F = (\bar{D}, \bar{P}, \varepsilon_{ij}, T) = F_0(T) + F_{Landau} + F_{elast} + F_{grad} + F_{coup} + F_{coup\ grad} \quad (26)$$

where $F_0(T)$ the independent on field part of the free energy. The Landau thermodynamic potential can be written in the form

$$F_{Landau} = \frac{a_i}{2} P_i^2 + \frac{a_{ij}}{4} P_i^2 P_j^2 + \frac{a_{ijk}}{6} P_i^2 P_j^2 P_k^2 - E_i P_i \quad (27)$$

which allows to describe the phase transitions of the first and second kind. Among the Ginzburg–Landau coefficients a_i, a_{ij}, a_{ijk} only the first one depends on the temperature: $a_i = a_{i0}(T - T_C)$, where a_{i0} is the Curie–Weiss constant. The elastic part of the free energy can be written as:

$$F_{elast} = C_{ijkl}\varepsilon_{ij}\varepsilon_{kl} + (T - -T_C)t_{ij}\varepsilon_{ij}. \quad (28)$$

Here C_{ijkl} is the elastic module tensor and t_{ij} is the thermal stress tensor [18]. The necessity of the second term introduction in the right part of (28) can be explained by the following fact. Even small change in temperature of layers with a small thickness results in significant temperature gradient (up to 10^6 K/m [18]). Note that the series expansion (28) is valid only in a small neighborhood of the Curie temperature where ECE is most powerful. The gradient terms can be represented as:

$$F_{grad} = \lambda_{ij} T_i T_j + g_{ijkl} D_{ij} D_{kl} \quad (29)$$

Here λ_{ij} is the thermal conductivity tensor, while g_{ijkl} are electrical gradient tensor coefficients. Let us mention that (29) includes the components of the electric displacement$\bar{D}$instead of polarization $\bar{P}$ (as performed in the standard approach [44]). This is because the presence of $(\nabla \bar{P})^2$ in (29) results in the continuity of the normal component of $\bar{P}$ at the interface, which is in contravention of Maxwell's equations. Piezoelectric part of the free energy can be expressed by the formula [40]:

$$F_{coup} = e_{ijk}\varepsilon_{ij}P_k + e_{ijkl}\varepsilon_{ij}P_k P_l. \quad (30)$$

Here e_{ijk} is the piezoelectric constants tensor and e_{ijkl} are modules of the electrostriction. The first term in (30) describes the piezoelectric effect, which exists under certain restrictions on the symmetry of the ferroelectric material. The second term is responsible for the electrostriction. In the last summand of the free energy we collect the terms which describe the influence on the polarization and temperature (as well as strain gradients of these quantities)

$$\begin{aligned} F_{coup\ grad} =& b_{ij}P_i T_{,j} + b_{ijk}\varepsilon_{ij}T_{,j} + f_{ijk}(T - T_C)\varepsilon_{ij,k} \\ &+ f_{ijkl}P_j\varepsilon_{jk,l} + d_{ijkl}\varepsilon_{ij}P_{k,l} + d_{ij}(T - T_C)P_{i,j}. \end{aligned} \quad (31)$$

There exist six possible variants of the pair-wise interaction for three variables $\bar{P}$, T, ε_{ij} and their gradients (the interaction with the gradient of any quantity of itself is not considered). In other words, the first pair of terms in (31) describes the

impact of ∇T on the polarization (i.e. thermopolarization effect or polarization thermogradient effect) and strain (i.e. elastic thermogradient effect). The second pair takes into account the impact of strain gradient on the temperature (flexo-thermal effect) and polarization (flexoelectric effect). The third pair is used to describe the polarization dependence on the gradient of temperature and deformation (thermal and elastic polarization gradient effects). The quantities b_{ij}, b_{ijk}, P_{ijk}, f_{ijkl}, d_{ij}, d_{ijkl} are the coefficients of the corresponding effects.

Further, the term $F_{coup\ grad}$ is possible to exclude from the consideration assuming the insignificance of described by this summand effects (some of them have not yet been found experimentally). However, in some cases these terms must be included, e.g. for the description of domain wall with high polarization and strain gradients.

Variation of (26) in the variables P, T, u_i gives:

$$E_i = a_i P_i + \frac{a_{ij}}{2} P_i P_j^2 + \frac{a_{ijk}}{3} P_i P_j^2 P_k^2 + e_{kli}\varepsilon_{kl} + e_{kjil}\varepsilon_{ij} P_l - g_{ijkl} D_{ij,kl} \tag{32}$$

It should be noted that there is no summation over i in (32).

$$\left(\lambda_{ij} T_j\right)_i - t_{ij}\varepsilon_{ij} = 0 \tag{33}$$

$$\sigma_{ij} = C_{ijkl}\varepsilon_{kl} + (T - T_C) t_{ij} + e_{ijk} P_k + e_{ijkl} P_k P_l. \tag{34}$$

Equations (32)–(34) should be supplemented by the standard boundary conditions at the interfaces:

$$T_1 = T_2,\ \lambda_{ij}^{(1)} T_{1,j} n_i = \lambda_{ij}^{(2)} T_{2,j} n_i,\ D_i^{(1)} n_i = D_i^{(2)} n_i,\ u_i^{(1)} = u_i^{(2)},\ \sigma_{ij}^{(1)} n_j = \sigma_{ij}^{(2)} n_j \tag{35}$$

which implies the continuity of temperature, heat flux, deformation vector, the normal component of electric displacement, and the stress tensor. The indices 1 and 2 in (35) indicate the value location with respect to number of considered media; n_i are components of the vector normal to the boundary. At the outer boundary it is possible to set temperature $T = T_0$, heat flow $\lambda_{ij} T_{,j} n_j = q_0$ or their linear combination $\lambda_{ij} T_{,j} n_j + H_0(T - T_0) = 0$. Here T_0 is ambient temperature, q_0 is heat flow on the boundary, H_0 is heat transfer coefficient.

The mechanical boundary conditions can consist of setting efforts $\sigma_{ij} n_{ij} = F_j$, displacement $u_i = u_{io}$, or have a mixed form. Here F_i, u_{io} are the components of forces and displacements at the boundary. The interface potential or the electrical intensity $E_i n_i = E_0$ can be used as electrical boundary conditions. Note that it is also possible to consider a combination of aforementioned quantities (impedance type boundary condition).

Let us now proceed to the dynamics of the processes. For the description of the polarization time dependence we use the equation of electrodynamics for non-equilibrium processes (the Landau-Khalatnikov equation)

$$r_i \frac{\partial P_i}{\partial t} = -\frac{\delta F}{\delta P_i},$$

that is

$$r_i \frac{\partial P_i}{\partial t} = E_i - g_{ijkl} D_{k,lj} - a_i P_i - \frac{a_{ij}}{2} P_i P_j^2 + \frac{a_{ijk}}{3} P_i P_j^2 P_k^2 - e_{kli} \varepsilon_{kl} + e_{kjil} \varepsilon_{ij} P_l \quad (36)$$

where r_i is phenomenological constants characterizing the relaxation time. Further, due to the lack of relaxation experimental data deformation component in (36) is considered in the static approximation. To describe the thermal processes we employ the Thompson equation

$$\partial Q = c\rho dT + T\left(\frac{\partial P_i}{\partial T} dE_i + \frac{\partial \varepsilon_{ij}}{\partial T} d\sigma_{ij}\right) \quad (37)$$

From (37) follows the equation of heat conduction

$$c\rho \frac{\partial T}{\partial t} = (\lambda_{ij} T_{,i})_j + Q(T, t, \varepsilon_{ij}, P) \quad (38)$$

where the quantity

$$Q = -T\left(\frac{\partial P_i}{\partial T}\frac{dE_i}{dt} + \frac{\partial \varepsilon_{ij}}{\partial T}\frac{d\sigma_{ij}}{dt}\right) - t_{ij}\varepsilon_{ij} \quad (39)$$

has the sense of the heat source.

The initial conditions for $t < 0$ have the form $T = T_0$, $P_i = P_{i0}$, $u_i = u_{i0}$, and must be self-consistently considered with (32)–(34). For a homogeneous medium the resulting equations are simplified. In this case, $\lambda_{ij} = \lambda\delta_{ij}$, $t_{ij} = t\delta_{ij}$, where $\delta_{ij} = 1$ for $i = j$ and $\delta_{ij} = 1$ for $i \neq j$ (λ is thermal conductivity and the coefficient t is proportional to the coefficient of the thermal expansion). In the next section we consider the equation (3.38) independently from (36) and (34).

4.2 Finite-Elements Simulation of Electrocaloric Cooling Structure

To create an experimental model of EC cooling structure appropriate to define the optimal ratio of the geometric dimensions, the magnitude of heat flux, frequency and pulse shape. This problem can be solved by the computer-based modeling.

At the first stage of modeling, for valuation calculations can be used simplified mathematical model of the electrocaloric cooling, which does not take into account the thermal stresses and thermal hysteresis of polarization.

As the working versions of the EC cooling structure we calculated using the finite element method a few version of cooling.

Let us consider a simple model of the cooling line shown in Fig. 21a. It consists of one electrocaloric element (ECE) separated from the environment by the heat conducting layers $[0 - x_1]$ and $[x_2 - L]$. We will investigate a one-dimensional

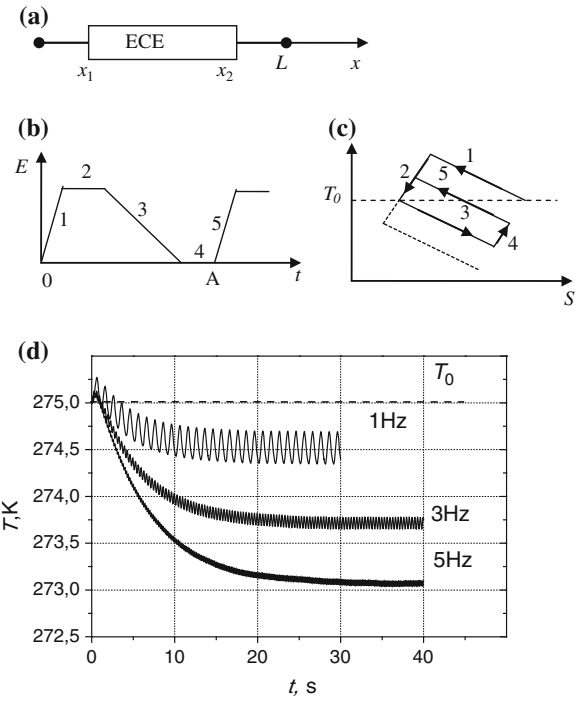

Fig. 21 The schematic diagram of a cooling line containing two ferroelectric capacitors **a**; temperature variation on the free end of the line (x = 0) upon antiphase harmonic switching of the capacitors **b**; thermodynamic cycle **c** in the element ECE; simulated time dependences of the cooling effect at various frequencies **d**

model under the assumption that the temperature changes affect only along the x axis. One boundary ($x = 0$) is thermally insulated, whereas the other boundary is held at a constant temperature T_0 equal to the initial temperature. The heat capacity $C(x)$ and thermal conductivity $\lambda(x)$ of the material are assumed to be constant within each segment of the line. In this case, the temperature distribution $T(x, t)$ along the line can be found by solving the heat conduction equation [18]

$$C(x)\frac{\partial T}{\partial x} = \frac{\partial}{\partial x}\lambda(x)\frac{\partial T}{\partial x} + Q(x,t,T) \tag{40}$$

which satisfies the initial and boundary conditions

$$T(x,0) = T_0; \quad \lambda_0 \left.\frac{\partial T}{\partial x}\right|_{x=0} = 0, \quad T|_{x=L} = T_0 \tag{41}$$

The function $Q(x, t, T)$ determines the quantity of heat released (or absorbed) by a thermal electrocaloric source and is expressed in the form given in [4, 20, 27]:

$$Q(x,t,T) = -T\frac{\partial P}{\partial T}\frac{dE}{dt} \tag{42}$$

where E is the electric field strength of the electrocaloric element and P is the polarization of the dielectric. The function $Q(x, t, T)$ is nonzero only within the

electrocaloric element. The time dependence of the electric field E has the period A and represents a function consisting of pulses shown in Fig. 21b. When a periodic sequence of pulses is supplied to the ferroelectric capacitor, the cycle shown in the T–S diagram (where T and S are the temperature and entropy of the element, respectively) (Fig. 21c) is executed, thus providing cooling of one of the ends of the electrocaloric element.

Interval 1 in Fig. 21 corresponds to charging of the capacitor and polarization of the ferroelectric, which leads to a decrease in the entropy. Within interval 2, the heat released during charging of the capacitor spreads over the structure, the capacitor remains charged, but its temperature is of the order of the initial temperature. Interval 3 corresponds to discharging of the capacitor, which leads to its cooling and an increase in the entropy due to depolarization. Within interval 4, the cooled capacitor is able to absorb the heat from the cooled body located at the point 0. The capacitor starts heating, and the next pulse 5 is supplied to prevent the capacitor from turning back to its initial state. Later on, the cycle is repeated (shown by the dotted line). Owing to the nonlinearity of the derivative of the polarization of the dielectric with respect to the temperature and the appropriate choice of the operating point, the quantity of the heat which the electrocaloric element can absorb during discharging exceeds the quantity of the heat released in the element during charging.

The numerical simulation of the cooling process was performed using the finite-element method.

The initial temperature was taken to be $T_0 = 275$ K, which was maintained at the end of the cooling line ($x = L$). The electric field amplitude was 5 V/μm. The ferroelectric capacitor and heat conducting elements were prepared from the $Ba_{0.6}Sr_{0.4}TiO_3$ (BST) ceramic material with the density $\rho = 6$ g/cm^3, the thermal conductivity $\lambda = 10$ W/(m K), and the heat capacity $c = 900$ J/(kg K).

Periodic pulses of the electric field were supplied to the electrocaloric elements with the frequency $f = 1/A$ ranging from 1 to 5 Hz. The pulses led to a periodic heating (cooling) of the electrocaloric elements and a redistribution of the temperature field along the structure. After a series of cycles in which the electric field was applied to the solid state structure, we determined the temperature distribution between the free end of the cooling line ($x = 0$) and the heat exchanger ($x = L$). Figure 21d presents the results of the computer simulation of the variation in the temperature. These results indicate that the temperature of the free end of the line substantially depends on the frequency of pulses. After a series of switching cycles, the system attains a steady state temperature regime and, then, the temperature oscillates only lightly around the average value.

A similar approach to the simulation of electrocaloric elements was used for a solid state line with two electrocaloric elements (see scheme in Fig. 22a). A heat conductor is located between two electrocaloric elements (ECE1, ECE2). The line contains two more heat conducting elements that connect the electrocaloric elements with the cooled object ($x = 0$) and the heat exchanger ($x = L$), respectively.

The results of the calculation of the thermal processes occurring in this structure are presented in Fig. 22b. When the additional element is used in the solid state

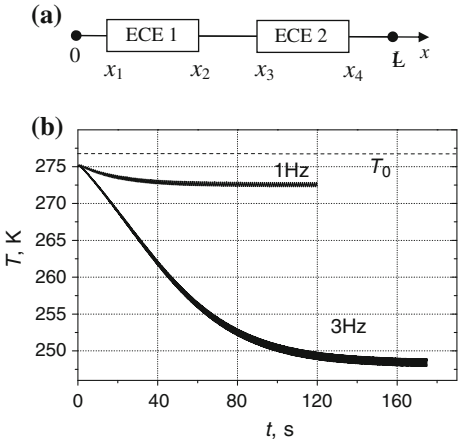

Fig. 22 The electrocaloric two-element line **a** and simulated time dependences of the cooling effect at various frequencies **b**

line, the gain in the temperature is equal to 2.5 K at a frequency of 1 Hz and reaches 25 K at a frequency of 3 Hz. In view of a large number of interrelated parameters of the structure under consideration (such as the lengths of elements and heat links, the phase shift, and the frequency of pulses), the optimum operating parameters of the line with two or more electrocaloric elements can be properly chosen only with the use of automated numerical analysis software and global optimization techniques.

The solid state cooling structure based on electrocaloric elements can have radial film geometry. In this work, we simulated a radial cooling structure based on a circular sapphire substrate with a thickness of 250 μm. A 1 μm thick BST film was deposited on the substrate. A circular double serrated electrodes cooling structure shown in Fig. 23a was formed on the surface of the BST film. A constant temperature was maintained at the outer boundary (periphery) of the radial microstructure. A series of periodic voltage pulses supplied to the electrode ring leads to the release or absorption of the thermal energy in the BST film. The use of ferroelectric films instead of ceramics allows one to substantially increase the repetition rate of switching pulses and, thus, to increase the heat flux power. The periodic temperature inhomogeneity is transferred into the substrate, which serves as a heat conductor. In the microstructure, there arises a heat flux directed along the radius of the structure. For particular physical and geometrical parameters of the microstructure, the heat flux is directed from the center to the periphery, which leads to the heat removal from the heated object placed at the center of the structure or to a decrease in the temperature.

In this work, we simulated a radial cooling structure with one line of electrodes. The diameter of the cooling structure was 0.4 mm, and the electrode gap width was 5 μm. The simulation was performed with the use of the finite element method at frequencies of 2.5 kHz and 10.0 kHz with applied field amplitude of 3 V/μm. Figure 23b presents the time dependences of the change in the temperature at the

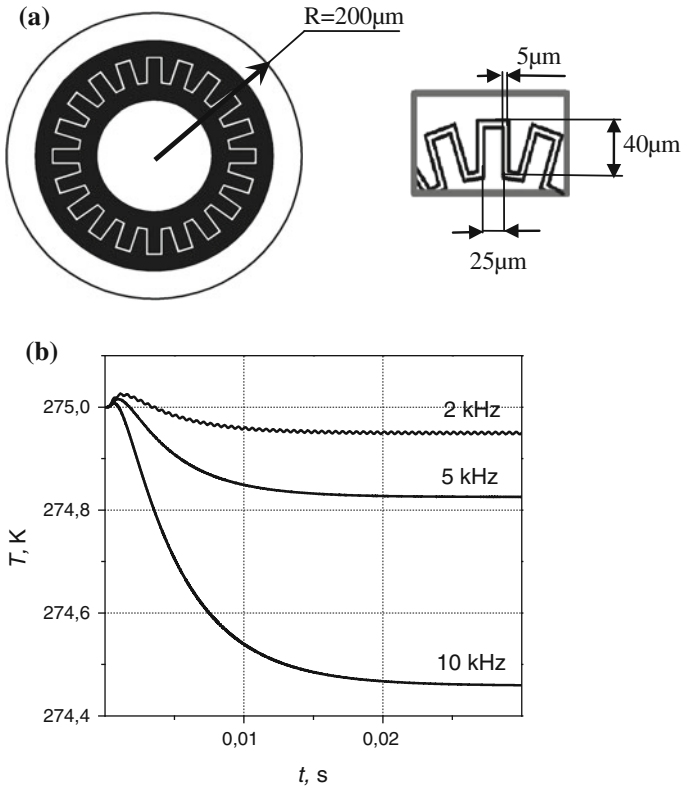

Fig. 23 The planar radial cooling structure prototype **a** and time dependences of the cooling effect in the structure center at various frequencies **b**

central point of the microstructure at different frequencies. The calculation has shown that, in the structure with one ring of electrodes, the decrease in the temperature can reach $\sim$0.5 K at a frequency of 10 kHz.

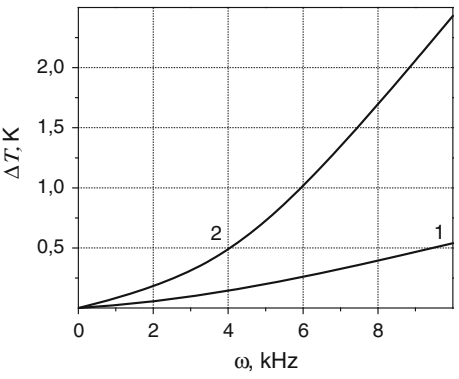

Fig. 24 The frequency dependences of the cooling effect for radial systems with one (curve *1*) and two (curve *2*) electrode lines

Figure 24 shows the frequency dependences of the cooling effect in the radial structure for systems with one (curve *1*) and two (curve *2*) electrode lines. As can be seen from this figure, the temperature difference across the radial cooling structure raises significantly with an increase in the number of serrated circular electrodes.

5 Conclusion

The theoretical and experimental results presented lead us to the conclusion that

- Sequence of several thermodynamic processes united into closed thermodynamic circle is the principle of operation for electrocaloric-based cooling structure. Therefore dynamic processes in ferroelectrics should be considered for adequate analysis of them.
- Criteria for selection and making materials for EC-based cooling structure include value of EC coefficient temperature derivative as well as EC coefficient value. EC-based cooling structure temperature operating point should be selected at maximum value of EC-index temperature derivative.
- Multilayer structure is the most rational solution for EC-based cooling structure. It provides specific heat raising and operational point temperature controlling.
- Cooling efficiency for EC-based cooling structure considerably depends on alternative electrical field frequency. The frequency is limited by EC-effect relaxation time being equal 1 μs. Heating and cooling velocity appreciably affects on thermal hysteresis value at permanent electrical field. Thermal hysteresis generation results in drop of EC-based cooling structure efficiency.
- Parametric effect provides considerable temperature drop in EC-based cooling structure. It could be reached by another caloric-effects (elastocaloric, magnetocaloric, barocaloric, etc.) materials introducing into ferroelectrics multilayer structure. Adjusted various exposure results in multicaloric effect within multilayer structure or EC-effect amplifying in ferroelectrics layers.
- Multilayer structures fabrication, investigation, thermal and physical characterisation should be considered as a perspective trend in electrocaloric-based cooling structure research.

Acknowledgments The Chapter preparing was supported by EU Grant No. 218282, ICPC Nanonet.

References

1. Akcay, G., Alpay, S.P., Matese, J.V., Rossetti, G.A.: Magnitude of the intrinsic electrocaloric effect in ferroelectric perovskite thin films at high electric fields. Appl. Phys. Lett. **90**(25), 252909 (2007)
2. Bazarov, I.P.: Thermodynamics. Pergamon Press, Oxford (1964)
3. Brodyanskii, V.M.: Autonomous Low_Power Criorefrigerators. Energoizdat, Moscow (1984). [in Russian]
4. Bulat, L.P.: Solid-state cooling systems. J. Thermoelectricity **3**, 15–21 (2007)
5. Camia, F.M.: Traite de Thermocinetique Impulsionelle Paris, Dunod (1967)
6. Dedyk, A.I., Kanareikin, A.D., Nenasheva, E.A., Pavlova, Y.V., Karmanenko, S.F.: *I-V* and *C-V* characteristics of ceramic materials based on barium strontium titanate. Tech. Phys. **51**(9), 59–64 (2006)
7. Dedyk, A.I., Karmanenko, S.F., Melkov, A.A., Pavlovskaya, M.V., Sakharov, V.I., Serenkov, I.T.: Influence of Mg and Mn doping on the RF-microwave dielectric properties of $Ba_xSr_{1-x}TiO_3$ films. Ferroelectrics **286**(1), 267–278 (2003)
8. Dedyk, A.I., Nenasheva, E.A., Kanareykin, A.D., Pavlova, JuV, Sinjukova, O.V., Karmanenko, S.F.: Tunability and leakage currents of (Ba, Sr)TiO3 ferroelectric ceramics with various additives. J. Electroceram. **17**(2–4), 433–437 (2006)
9. Epstein, R.I., Malloy, K.J.: Electrocaloric devices based on thin-film heat switches. J. Appl. Phys. **106**(6), 064509 (2009)
10. Es'kov, A.V., Karmanenko, S.F., Pakhomov, O.V., Starkov, A.S.: Simulation of a solid-state cooler with electrocaloric elements. Phys. Solid State **51**(8), 1574–1577 (2009)
11. Flerov, I.N., Mikhaleva, E.A.: Electrocaloric effect and anomalous conductivity of the ferroelectric NH_4HSO_4. Phys. Solid State **50**(3), 478–484 (2008)
12. Ginzburg, V.L.: Usp. Fiz. Nauk **38**(8), 490–525 (1949). (In Russian)
13. Golzman, B.M., Dedyk, A.I., Lemanov, V.V., Ter-Martyrosjan, L.T., Karmanenko, S.F.: Dielectric properties of planar structures based on ferroelectric Ba0.5Sr0.5TiO3.Pis'ma. Zh. Tekh. Fiz. **23**(32), 46–52 (1997)
14. Gurevich, A.G.: Ferrites at Super High Frequencies. Fizmatgiz, Moscow (1960). [in Russian]
15. Guyomar, D., Sebald, G., Guiffard, B., Seveyrat, L.: Ferroelectric electrocaloric conversion in $0.75(PbMg_{1/3}Nb_{2/3}O_3)$–$0.25(PbTiO_3)$ ceramics. J. Phys. D Appl. Phys. **39**(20), 4491 (2006)
16. Hagberg, J., Uusimaki, A., Jantunen, H.: Electrocaloric characteristics in reactive sintered $0.87Pb(Mg_{1/3}Nb_{2/3})O_3$–$0.13PbTiO_3$. Appl. Phys. Lett. **92**(13), 132909 (2008)
17. He, J., Chen, J., Zhou, Y., Wang, J.: Regenerative characteristics of electrocaloric Stirling or Ericsson refrigeration cycles. Energy Convers. Manage. **43**(17), 2319–2327 (2002)
18. Isachenko, V.P., Osipov, V.A., Sukomel, A.S.: Heat Transfer, p. 439. Energiya, Moscow (2001)
19. Karmanenko, S.F., Dedyk, A.I., Isakov, N.N., Gordeichuk, A.S., Semenov, A.A., Ter-Martirosyan, L.T., Hagberg, J.: Study of the effect of manganese impurities on dielectric characteristics of BSTO films. Tech. Phys. **41**(4), 498–502 (2001)
20. Karmanenko, S.F., Pakhomov, O.V., Prudan, A.M., Starkov, A.S., Es'kov, A.V.: Layered ceramic structure based on the electrocaloric elements working as a solid state cooling line. J Eur. Ceram. Soc. **27**(8–9), 3109–3112 (2007)
21. Khodayari, A., Mohammadi, S.: Solid-state cooling line based on the electrocaloric effect. IEEE Trans. Ultrason. Ferroelectr. Freq. Control **58**(3), 503–508 (2011)
22. Landau, L.D., Khalatnikov, I.M.: On the anomalous acoustical absorption near a second-order phase transition. Dokl. Akad. Nauk SSSR. **96**(3), 469–472 (1954)
23. Lawless, W.N.: Specific heat and electrocaloric properties of $KTaO_3$ at low temperatures. Phys. Rev. B. **16**(1), 433–439 (1977)
24. Lines, M., Glass, A.: Principles and Applications of Ferroelectrics and Related Materials. Clarendon Press, Oxford (1979)

25. Lu, S.G., Rožič, B., Zhang, Q.M., Kutnjak, Z., Li, X., Furman, E., Lee, G.J., Lin, M., Malič, B., Kosec, M., Blinc, R., Pirc, R.: Organic and inorganic relaxor ferroelectrics with giant electrocaloric effect. Appl. Phys. Lett. **97**(16), 162904 (2010)
26. Marvan, M., Jonscher, A.K., Fahnrich, J.: Electrocaloric effect as a cause of dielectric loss. J. Eur. Ceram. Soc. **21**(10–11), 1345–1348 (2001)
27. Mischenko, A.S., Mathur, N.D.: GB Patent #2420662 (2006)
28. Mischenko, A.S., Zhang, Q., Scott, J.F., Whatmore, R.W., Mathur, N.D.: Giant electrocaloric effect in the thin film relaxor ferroelectric $0.9PbMg_{1/3}Nb_{2/3}O_3$–$0.1PbTiO_3$ near room temperature. Appl. Phys. Lett. **89**(24), 242912 (2006)
29. Mischenko, A.S., Zhang, Q., Scott, J.F., Whatmore, R.W., Marhur, N.D.: Giant electrocaloric effect in thin-film $PbZr_{0.95}Ti_{0.05}O_3$. Science **311**(5765), 1270–1271 (2006)
30. Mishchenko, E.F., Rozov, NKh: Differential Equations with Small Parameter and Relaxation Oscillations. Nauka, Moscow (1975). [in Russian]
31. Morozovska, A.N., Eliseev, E.A., Svechnikov, G.S., Kalinin, S.V.: Pyroelectric response of ferroelectric nanoparticles: size effect and electric energy harvesting. http://arxiv.org/abs/0908.2311v1 (2009). Accessed 17 Aug 2009
32. Neese, B., Chu, B., Lu, S.G., Wang, Y., Furman, E., Zhang, Q.M.: Large electrocaloric effect in ferroelectric polymers near room temperature. Science **321**(5890), 821–823 (2008)
33. Neese, B., Lu, S.G., Chu, B., Zhang, Q.M.: Electrocaloric effect of the relaxor ferroelectric poly(vinylidene fluoride-trifluoroethylene-chlorofluoroethylene) terpolymer. Appl. Phys. Lett. **94**(4), 042910 (2009)
34. Nenasheva, E.A., Kanareikin, A.D., Dedyk, A.I., Pavlova, Y.V.: Electrically controlled BST-Mg ceramic components for applications in accelerator technology. Phys. Solid State **51**(8), 1557–1560 (2009)
35. Osipov, E.V.: Solid_State Cryogenics. Naukova Dumka, Kiev (1977). [in Russian]
36. Pakhomov, O.V., Starkov, A.S., Karmanenko, S.F., Es'kov, A.V.: Vestn. Mezhdunar. Akad. Kholoda. **2**, 31 (2007) [in Russian]
37. Pavlovskaja, M.V., Balakin, V.A., Dedyk, A.I., Karmanenko, S.F., Sakharov, V.I., Serenkov, I.T.: Influence of electron irradiation on the properties of ferroelectric $Ba_xSr_{1-x}TiO_3$ Films. Integ. Ferroelectr. **61**(1), 149–153 (2004)
38. Prosandeev, S., Ponomareva, I., Bellaiche, L.: Electrocaloric effect in bulk and low-dimensional ferroelectrics from first principles. Phys. Rev. B. **78**(5), 052103 (2008)
39. Radebaugh, R., Lawless, W.N., Siegwarth, J.D., Morrow, A.J.: Feasibility of electrocaloric refrigeration for the 4–15 K temperature range. Cryogenics **19**(4), 187–208 (1979)
40. Semenov, A.A., Karmanenko, S.F., Kalinikos, B.A., Srinivasan, G., Slavin, A.N., Mantese, J.V.: Dual-tunable hybrid wave ferrite-ferroelectric microwave resonator. Electron. Lett. **42**(11), 641–642 (2006)
41. Yu, S.V.: Analysis of the efficiency of an electrocaloric cryorefrigerator. Chem. Petrol. Eng. **31**(9), 501–506 (1995)
42. Sinyavskiy, YuV: Electrocaloric refrigerators: A promising alternative to current low-temperature apparatus. Chem. Pet. Eng. **31**(6), 295–306 (1995)
43. Sinyavsky, Y.V., Pashkov, N.D., Gorovoy, Y.M., Lugansky, G.E., Shebanov, L.: The optical ferroelectric ceramic as working body for electrocaloric refrigeration. Ferroelectrics **90**(1), 213–217 (1989)
44. Smolenskiy, A., Bokov, V.A., Isupov, V.A., Krainik, N.N., Pasinkov, R.E., Shur, N.S.: Ferroelectrics and antiferroelectrics. Nauka, Leningrad (1971)
45. Starkov, A.S., Karmanenko, S.F., Pakhomov, O.V., Es'kov, A.V., Semikin, D., Hagberg, J.: Electrocaloric response of a ferroelectric capacitor to a periodic electric field. Phys. Solid State **51**(7), 1510–1514 (2009)
46. Starkov, A.S., Pakhomov, O.V.: Influence of the dynamic polarization of a ferroelectric material on the magnitude of its electrocaloric response. Tech. Phys. Lett. **36**(1), 1–3 (2010)
47. Starkov, A.S., Pakhomov, O.V., Starkov, I.A.: Effect of thermal phenomena on a second-order phase transition in the Landau-Ginzburg model. JETP Lett. **91**(10), 507–511 (2010)

48. Su, B., Button, T.W.: Microstructure and dielectric properties of Mg-doped barium strontium titanate ceramics. J. Appl. Phys. **95**(3), 1382–1384 (2004)
49. Sun, Y., Kamarad, J., Arnold, Z., Zn, K., Chen, Z.: Tuning of magnetocaloric effect in a $La_{0.69}Ca_{0.31}MnO_3$ single crystal by pressure. Appl. Phys. Lett. **88**(10), 102505 (2006)
50. Sychev, V.V.: Complex THERMODYNAMIC SYSTEMS. Energoatomizdat, Moscow (1986). [in Russian]
51. Synyavsky, Y.V., Brodyansky, V.M.: Experimental testing of electrocaloric cooling with transparent ferroelectric ceramic as a working body. Ferroelectrics **131**, 321–325 (1992)
52. Tishin, A.M., Spichkin, Y.J.: The Magnetocaloric Effect and its Applications. IOP Publishing Ltd., Bristol, UK (2003)
53. Vendik, O.G.: Ferroelectrics at Microwaves. Sov. Radio, Moscow (1979)
54. Vendik, O.G., Dedyk, A.I., Dmitrieva, R.V., Zalonchkovskii, A.Y., Yu, L., Ruban, V.A.S.: Hysteresis of the permittivity of strontium titanate at 4.2 K. Sov. Phys. Solid State **26**(3), 412–415 (1984)
55. Wiseman, C.G.: Electrocaloric effect in potassium dihydrogen phosphate. IEEE Trans. Electron Devices **16**(6), 588–593 (1969)
56. Wu, H.-D., Barnes, F.S.: Doped $Ba_{0.6}Sr_{0.4}TiO_3$ thin films for microwave device applications at room temperature. Integ. Ferroelectr. **22**(1–4), 291–305 (1998)
57. Yoon, K.H., Lee, J.C., Park, J., Kang, D.H., Song, C.M., Seo, Y.G.: Electrical properties of Mg doped $(Ba_{0.5}Sr_{0.5})TiO_3$ thin films. Jap. J. Appl. Phys. **40**(12), 5497–5500 (2001)

Energy Harvesting from Temperature: Use of Pyroelectric and Electrocaloric Properties

Gaël Sebald, Sébastien Pruvost and Daniel Guyomar

1 Introduction

Advance in electronics favors the emergence of autonomous and self-powered devices embedding their own energy source, thus leading for example to the concept of "smart dust" [52]. Such a device should be able to perform advanced computing, sensing and communicating functions. For powering the device, research in higher energy and small-size batteries is important, but for long lasting or harsh environment applications, such solution lacks in reliability and maintenance costs. A much promising solution is to harvest necessary energy in the surrounding of the device such as vibrations, light, flows or heat. In case of vibration-based energy harvester, several devices from millimeter scale down to microscale have been presented, with average powers in the 10 μW to 10 mW range [42]. In addition, some advanced energy conversion techniques may enhance the output power [9].

In case of limited vibrations levels, it is of primary importance to find alternative energy sources. In this chapter, we will describe principles and performances of energy harvesting from temperature fluctuations using pyroelectric effect. Such energy conversion concept appeared far before the current needs of embedded energy sources and energy harvesting developments. Earlier theoretical considerations predicted a very low efficiency of pyroelectric energy conversion (less that 1 % in most cases) [8], but significant experimental developments were published by Olsen and co-workers in the 80s [35–39]. However pyroelectric power generators have not attracted much interest until recent years, with the fast increasing development of energy harvesting techniques. Ikura et al. investigated

G. Sebald (✉) · D. Guyomar
Université de Lyon, INSA-Lyon, Laboratoire de Génie Electrique et de Ferroélectricité (LGEF), Villeurbanne Cedex 69621, France
e-mail: gael.sebald@insa-lyon.fr

S. Pruvost
Université de Lyon, INSA-Lyon, Ingénierie des Matériaux Polymères (IMP) UMR CNRS 5223, Villeurbanne Cedex 69621, France

T. Correia and Q. Zhang (eds.), *Electrocaloric Materials*, Engineering Materials 34, DOI: 10.1007/978-3-642-40264-7_9,

ferroelectric polymers exhibiting very large output power [14]. From our previous work, we showed that working in the vicinity of phase transitions enhances energy conversion, such lead-based relaxor single crystals [10, 17], or relaxor ceramic [44, 45]. The main drawback of the previously-mentioned work is that power electronics still require to be developed, since large voltages (thousands of volts) should be applied with fully reversible amplifiers.

Therefore, another possibility is to work with linear pyroelectric materials. Main advantage is that it is very similar to piezoelectric case, and techniques for piezoelectric energy harvesting can be transferred to the pyroelectric case [10–12, 44, 45]. In this framework, several materials optimizations were published using laminate composites [3, 2]. Pyroelectric energy harvesting may be considered as an energy source for larger scale devices, where thermoelectric modules could be replaced by adequate pyroelectric elements and cyclic pumping unit [31, 32, 51] or thermal heat switches [6], offering the advantage of higher efficiency compared to their thermoelectric counterpart [46].

This chapter is organized in three sections. The first one is devoted to the use of linear pyroelectric effect. In this case, piezoelectric and pyroelectric energy harvesting is much similar except frequencies and electric field order of magnitudes. All the developments devoted for piezoelectric energy harvesting could theoretically be transferred to the pyroelectric case, where one simply replaces a mechanical stress by the temperature [44, 45].

The second part deals with what we call “electrocaloric” energy harvesting. In this case, we take advantage to an energy conversion in the nonlinear regime. Especially, it is shown that the maximum energy conversion is obtained when working in the vicinity of structural phase transitions, where pyroelectric activity is highly nonlinear. Output energy is much larger than that using linear pyroelectric effect. In addition, with some precautions and strong hypothesis, it is possible to estimate the energy harvesting ability of a given material knowing its electrocaloric effect. Some examples are given and constitute the highest achievable output power density. Throughout the chapter, we show the efficiency of energy conversion and relative efficiency, calculated as the efficiency divided by Carnot cycle efficiency. The unit of output energy density was chosen to be mJ cm^{-3} throughout the chapter.

Final section is devoted to several practical issues: how to create a time varying temperature signal, and the problem of power electronics?

2 Linear Pyroelectric Energy Harvesting

2.1 Thermodynamic Cycles

When dealing with energy harvesting from heat, consideration of energy cycles is necessary to quantify exchanged electrical energy (area of polarization—electric field cycle) and heat (area of entropy—temperature cycle) with outer medium.

Constitutive equations of pyroelectric materials are

$$dD = \varepsilon_{33}^{\theta} dE + p d\theta \tag{1}$$

$$d\Gamma = p dE + c_E \frac{d\theta}{\theta} \tag{2}$$

where D, E, θ and Γ are electric displacement, electric field, temperature and entropy respectively.

The coefficients are defined as:

$$\varepsilon_{33}^{\theta} = \left.\frac{dD}{dE}\right|_{\theta}, \; p = \frac{dD}{d\theta} = \frac{d\Gamma}{dE}, \; c_E = \left.\frac{dU}{d\theta}\right|_{E} \tag{3}$$

where $\varepsilon_{33}^{\theta}$, p, c_E and U are the dielectric permittivity, pyroelectric coefficient, caloric capacity at constant electric field and internal energy respectively. Coefficients defined in 1–3—in the general case—are functions of temperature and electric field. In this section devoted to pyroelectric energy harvesting, we consider only constant coefficients. This may be held true for weak electric fields, limited temperature variations and far from any phase transition.

Based on these equations, we then give as example two energetic cycles for energy harvesting. Details may be found in [44, 45]. The first cycle is Carnot cycle. The Carnot Cycle is defined as two adiabatic and two isothermal curves on the (DE) and ($\Gamma\theta$) cycles as shown in Fig. 1. Efficiency of such cycle is

$$\eta_{Carnot} = 1 - \frac{\theta_c}{\theta_h} \tag{4}$$

where θ_c and θ_h are cold and hot reservoirs temperatures respectively.

Electric field should be controlled according to the temperature variation, and the necessary electric field amplitude E_M is given by

$$\ln\left(\frac{\theta_h}{\theta_c}\right) = -\frac{p}{c_E} E_M \tag{5}$$

For a given temperature variation, it is then possible to calculate the whole electric field profile that should be applied for Carnot cycle. Overall efficiency of the cycle does not depend on materials properties, and constitutes the very upper limit of efficiency. Nevertheless, for most available materials, electric field E_M would be far above the dielectric breakdown. For example, considering a $Pb(Mg_{1/3}Nb_{2/3})_{0.75}Ti_{0.25}O_3$ material [43], and a temperature variation of 10 K, we would obtain a value $E_M = 140$ MV m^{-1} for a ceramic, and 70 MV m^{-1} for a single crystal. Such values are excessive for practical applications.

The second thermodynamic cycle that we present here is the Synchronized Electric Charge Extraction (or SECE). It was developed for the case of piezoelectric energy harvesting [23] and can be transferred to the pyroelectric case.

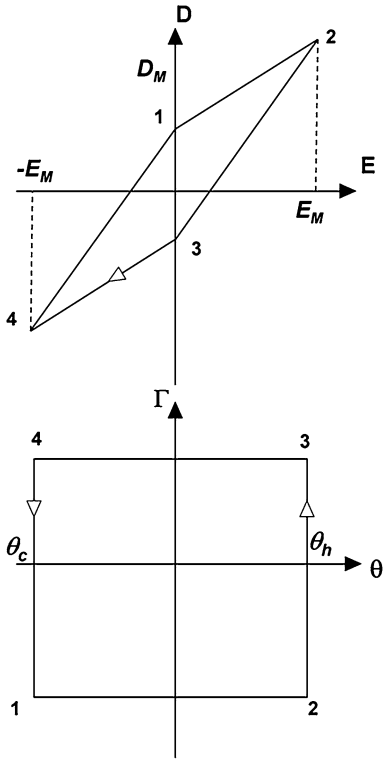

Fig. 1 Carnot cycle for a linear pyroelectric material

From the thermodynamics point of view, it consists of a Stirling cycle. This technique may be seen as one of the most natural cycles, and corresponding (DE) and ($\Gamma\theta$) cycles are given in Fig. 2. Electrical energy is transferred to a storage cell every time the electrostatic energy of the pyroelectric element reaches a maximum (paths 2–3 and 4–1). Otherwise, the pyroelectric element is left in electrical open-circuit condition (path 1–2 and 3–4).

For a limited temperature variation, total heat transferred to the cold reservoir Q_c and hot reservoir Q_h are

$$Q_c = c_E(\theta_c - \theta_h) + \frac{p^2}{2\varepsilon_{33}^{\theta}}(\theta_h - \theta_c)^2 \tag{6}$$

$$Q_h = c_E(\theta_h - \theta_c) + \frac{p^2}{2\varepsilon_{33}^{\theta}}(\theta_h - \theta_c)^2 \tag{7}$$

The total electric work W is found using that the internal energy does not change at the end of one cycle

$$W = -\frac{p^2}{\varepsilon_{33}^{\theta}}(\theta_h - \theta_c)^2 \tag{8}$$

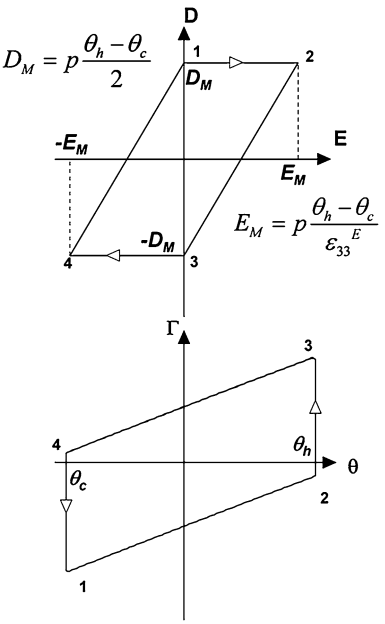

Fig. 2 Synchronous electric charge extraction (SECE) cycle for a linear pyroelectric material

Introducing the electrothermal coupling factor k^2

$$k^2 = \frac{p^2\theta_h}{\varepsilon_{33}^{\theta} c_E} \tag{9}$$

Conversion ratio gives

$$\eta_{SECE} = \frac{|W_E|}{Q_h} = \frac{k^2}{1 + 0.5k^2\eta_{Carnot}}\eta_{Carnot} \tag{10}$$

k^2 is a dimensionless number giving the electrothermal coupling factor (at temperature θ_h), similarly to the electromechanical coupling factor (coupled coefficient divided by the product of non-coupled ones). We recall here the assumption of constant coefficients versus electric field and temperature. SECE cycle may be seen as an equivalent Stirling cycle transposed in the pyroelectric case. In the case of fluid-compression based heat engine, polarization corresponds to the volume and the electric field corresponds to the pressure. SECE energy conversion is practically feasible, especially in terms of voltage control and levels, but its performance is much less than that of Carnot cycles, due to the very small values of k^2 usually observed in pyroelectric materials. This latter parameter is of primary importance when dealing with pyroelectric energy harvesting.

2.2 Pyroelectric Materials Suitable for Linear Energy Harvesting

Pyroelectric materials are usually optimized for pyroelectric sensors, and the figures of merit are defined for improving voltage and current sensitivities for sensing functions. For energy harvesting, the involved parameters are slightly different. Comparison of the performances of pyroelectric materials for energy harvesting is two-fold. First, for a given temperature variation, the output electrical energy is proportional to the figure of merit FOM_E. From 8, the power FOM_E is

$$FOM_E = \frac{p^2}{\varepsilon_{33}^{\theta}} \tag{11}$$

Then, the efficiency of energy conversion is related to the ratio of harvested energy on the absorbed heat. It is given by a single parameter that is the electrothermal coupling factor. From 10, the FOM_η [44, 45] is

$$FOM_\eta = k^2 = \frac{p^2 \theta_h}{\varepsilon_{33}^{\theta} c_E} \tag{12}$$

In Table 1 are displayed several materials for comparison. The electrothermal coupling factor is small for lead based ferroelectrics (<3 %) [5, 21, 22, 33, 40, 48, 54, 55]. More recently, some materials and systems were studied and optimized for energy harvesting specifically, and a huge gain in coupling was obtained. For example, Chang and Huang fabricated 2-2 laminate composites in which the thermal expansion of a non-pyroelectric layer stresses a pyroelectric and piezoelectric element [2, 3]. In this way, the secondary pyroelectric effect in greatly enhanced compared to pyroelectric effect at zero-stress condition. The gain is very impressive with an electrothermal coupling of the laminated structure $k_{lam}^{2} = 14.69$ %.

Navid et al. investigated purified and porous polymers for pyroelectric applications including energy harvesting [31, 32]. They obtained an improvement of electrothermal coupling factor of 80.7 % on purified films compared to commercial films.

Polymer films exhibit the lowest coupling factor, and PMN-PT single crystals the highest. The two only exceptions are for laminate composites with an outstanding improvement of FOM_η by a factor of 5.5 and an improvement of the energy figure of merit FOM_E by a factor of 4 compared to <111>Pb($Mg_{1/3}Nb_{2/3}$)$_{0.72}Ti_{0.28}O_3$ single crystals. For energy harvesting, this means an improvement on the energy and efficiency by the same factors.

Table 1 Pyroelectric properties for different class of materials

Material	p ($\mu C\ m^{-2}\ K^{-1}$)	ε_{33}^{E} (ε_0)	c_E	FOM_E	FOM_η	References
<111>$Pb(Mg_{1/3}Nb_{2/3})_{0.72}Ti_{0.28}O_3$	1,071	660	2.5	196	2.36	Davis et al. [5]
<111>$Pb(Mg_{1/3}Nb_{2/3})_{0.67}Ti_{0.33}O_3$	979	650	2.5	166	2.00	Davis et al. [5]
PZT ceramic	533	1,116	2.5	29	0.35	Ng et al. [33]
PLZT 0.5/53/47 ceramic	360	854	2.5	17	0.21	Peláiz Barranco et al. [40]
PbCaTiO3 ceramic	220	253	2.5	22	0.26	Yamaka [54]
PZT 700 nm ceramic	211	372	2.5	14	0.16	Zhang and Whatmore [55]
PVDF polymer	33	9	1.8	14	0.23	Lang and Muensit [22]
PZT0.3/PU0.7 vol% composite	90	23	2	40	0.60	Lam et al. [21]
PZT5H-CPVC (R = 0.005) laminated composite	4,468	2,874	N/A	784	13.06	Chang and Huang [3]
PZT5H-PTFE (R = 0.005) laminated composite	3,416	2,874	N/A	459	14.69	Chang and Huang [3]
Pure 60/40 P(VDF-TrFe) polymer	4.5	28.8	3.2	0.1	0.0007	Navid et al. [31, 32]
Purified 60/40P(VDF-TrFe) polymer	5.09	28.8	2.3	0.1	0.0013	Navid et al. [31, 32]
Porous 60/40 P(VDF-TrFe) polymer	4.3	39.9	1.8	0.1	0.0009	Navid et al. [31, 32]

All properties are given at room temperature

2.3 Experimental Evidence of Pyroelectric Energy Harvesting

Guyomar et al. demonstrated the pyroelectric energy harvesting on PVDF films subjected to a temperature varying air flow [10–12]. This study showed that a micro-generator composed of 8 g of PVDF produces 0.32 mW electrical power with 14 K peak-to-peak temperature amplitude and 0.2 Hz frequency (i.e. 0.35 mJ cm^{-3} per cycle and 0.07 mW cm^{-3}). A special emphasis was put on the use of nonlinear treatment of pyroelectric voltage in order to increase the effective electrothermal coupling factor as well as storing the harvested energy. This nonlinear processing technique leads to 200 % power improvement compared to the 'Standard' interface. However, this micro-generator had very low relative efficiency (0.02 and 0.05 % for the standard interface and nonlinear one respectively). Theoretical predictions show that $Pb(Mg_{1/3}Nb_{2/3})_{1-x}Ti_xO_3$ single-crystals could strongly improve those results. Later, the equivalence between pyroelectric and piezoelectric energy harvesting was established [10–12]. The nonlinear techniques of energy conversion work in the same manner whatever the origin of variation of the polarization (stress or temperature), and theoretical and experimental results for different energy harvesting techniques are shown in Fig. 3.

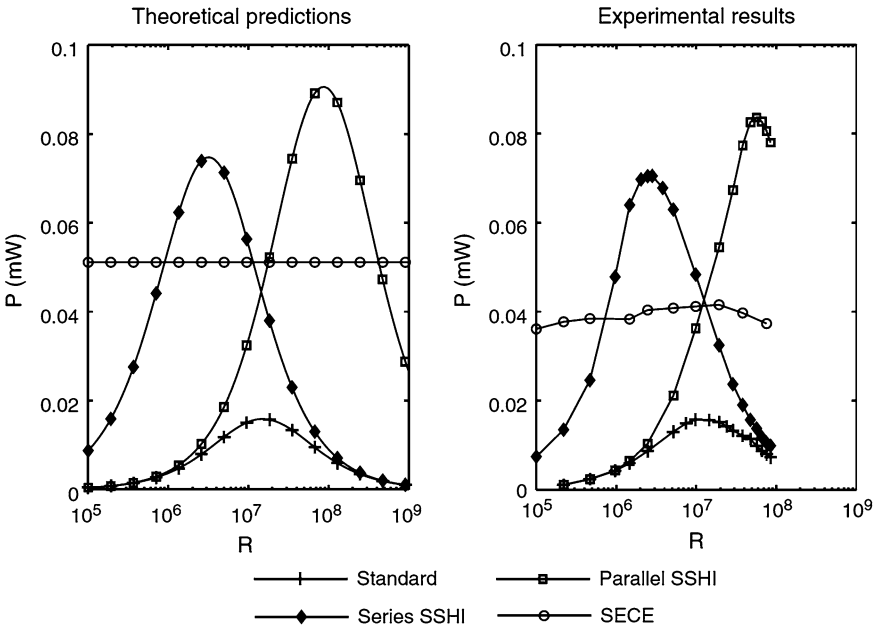

Fig. 3 Pyroelectric energy harvesting on 32 g PVDF films, subjected to a temperature variation of 1.33 K at 0.5 Hz. The different techniques correspond to different nonlinear treatment en pyroelectric voltage. After Ref. [10]

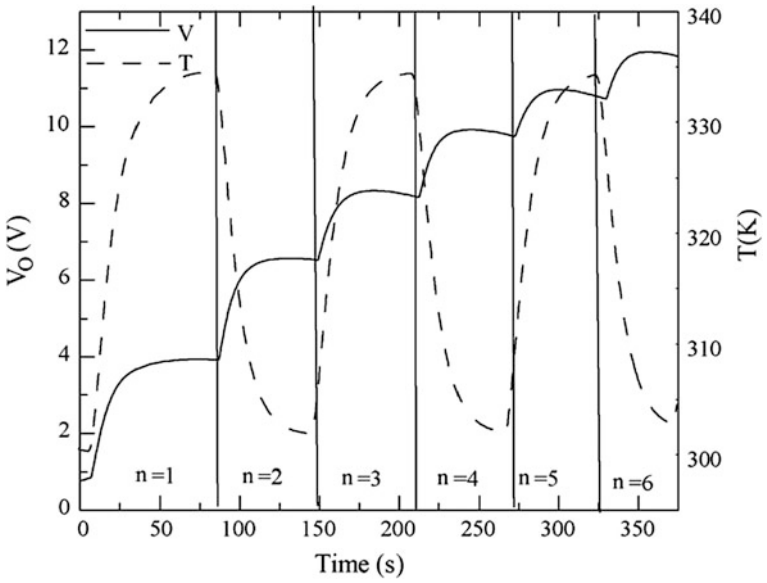

Fig. 4 Temperature energy harvesting experiment from Cuardas et al. [4]. Voltage is measured across a 1μF storage capacitor. After 3 cycles, the voltage reaches 12 V and a stored energy of 72 μJ, and a mean power of 0.18 μW

Cuardas et al. studied screen-printed PZT and PVDF for energy harvesting and reported interesting output energy of 0.5 mJ after a large number of cycles [4]. Their experiment consisted of pyroelectric cells based on fabricated screen-printed PZT films and commercial PVDF films. Dimensions of PZT pyroelectric cells were typically 4×4 cm^2 and an active thickness of 100 μm. Thermal fluctuations were applied between 300 and 360 K and currents were measured in the order of 10^{-7} A and charges in the order of 10^{-5} C. A typical result is displayed in Fig. 4.

Mane et al. [27] investigated commonly available soft lead zirconate titanate (PZT), a pre-stressed PZT composite, and a single-crystal of $Pb(Mg_{1/3}Nb_{2/3})_{0.7}Ti_{0.3}O_3$. The maximum power density of 8.64 μW cm^{-3} is generated with a $Pb(Mg_{1/3}Nb_{2/3})_{0.7}Ti_{0.3}O_3$ single crystal at an angular velocity of 0.64 rad/s with a rate of 8.5°/s. In this work, the energy is not calculated and only the maximum power is considered. A rough estimation of the energy is 0.06 mJ cm^{-3}.

For thick films, Xie et al. published some experimental results of pyroelectric energy harvesting for different ferroelectric materials [53]. Peak power densities were measured in the range 0.1–0.3 μW cm^{-3} for a temperature variation between room temperature and 125 °C at a maximum of 15–20°/s^{-1}. In their work, they underlined the importance of pyroelectric coefficient for maximizing output power, as denoted in this chapter through 11.

These results obtained by different research teams suggest that pyroelectric energy harvesting is feasible and constitutes an alternative energy source apart from vibrations. However, it is still necessary to identify time varying temperature

sources as discussed in Sect. 4.1. The problem of energy management was solved by using standard rectifying bridge operation or interfaces previously developed for piezoelectric energy harvesting, but practical implementation still requires further development (see Sect. 4.2).

Finally, we show in Table 2 the simulated output energy for a 10°C temperature variation on some linear pyroelectric materials taken from Table 1. The output energy and efficiency are calculated from 8 and 10 respectively. Most of the materials exhibit output energy in the range 1–4 mJ cm^{-3}. Two significant exceptions are worth noting. $Pb(Mg_{1/3}Nb_{2/3})_{1-x}Ti_xO_3$ single crystals exhibit especially large pyroelectric coefficient and the resulting output energy reaches almost 20 mJ cm^{-3}. Then, the relative efficiency reaches 2.4 %. Laminate composites also exhibit very large output energy (78 mJ cm^{-3}) and relative efficiency (almost 12 %), thanks to the huge increase of the secondary pyroelectric effect. The electric field appearing in open-circuit condition on the pyroelectric material is calculated for a 10 °C temperature increase. Values of 1.8 MV m^{-1} and 4.4 MV m^{-1} are found for $Pb(Mg_{1/3}Nb_{2/3})_{1-x}Ti_xO_3$ single crystal and laminate composite respectively. This constitutes very high electric field where linearity of materials is at stake. Then, the feasibility of energy harvesting at a 10 °C temperature variation and linear properties is much questionable.

3 Electrocaloric Energy Harvesting

When materials exhibit large pyroelectric activities, their open-circuit electric field will probably exceed linear regime limit. For example, a 2 MV m^{-1} electric field on the <111>$Pb(Mg_{1/3}Nb_{2/3})_{1-x}Ti_xO_3$ single crystal will completely depolarize it when the electric field will be opposed to the remnant polarization axis.

Working with nonlinear materials is a change in paradigm. Getting away from practical systems and thinking in terms of energy conversion cycles are the key points for investigating new materials class. This section is devoted to what we call electrocaloric energy harvesting, where the outstanding electrocaloric effect will be associated to very high energy harvesting capability.

3.1 Thermodynamic Cycles

In order to perform an energy conversion cycle, the electrical quantities of electrocaloric material have to be controlled synchronously with temperature signal. If one consider the electric field as an electrical pressure and the electric displacement as an electrical volume, all typical energy cycles may be transposed from compressible gas cycles to electrocaloric energy harvesting. Then, two typical energy cycles are presented below. An exhaustive survey of all available energy cycles was early proposed by Olsen et al. through several publications

Table 2 Energy harvesting from linear pyroelectric materials and Olsen (Ericsson) cycles on nonlinear materials

Material		c_E (MJ m^{-3})	E_{low} (MV m^{-1})	E_{high} (MV m^{-1})	θ_c (°C)	θ_h (°C)	W(mJ cm^{-3})	η/η_{carnot}	References
Linear material	<111>$Pb(Mg_{1/3}Nb_{2/3})_{0.72}Ti_{0.28}O_3$	2.5	0	1.8	25	35	19.6	2.4	Davis et al. [5]
	PZT	2.5	0	0.5	25	35	2.9	0.35	Ng et al. [33]
	PVDF	1.8	0	4.1	25	35	1.4	0.23	Lang and Muensit [22]
	PZT0.3/PU0.7 vol%	2	0	4.4	25	35	4.0	0.60	Lam et al. [21]
	PZT5H-CPVC (R = 0.005)	2	0	1.8	25	35	78	11.8	Chang and Huang [3]
	Purified 60/40P(VDF-TrFE)	2.3	0	0.2	25	35	0.01	0.001	Navid et al. [31, 32]
Nonlinear material	$Pb_{0.99}Nb_{0.02}(Zr_{0.68}Sn_{0.25}Ti_{0.07})_{0.98}O_3$	2.5	0.8	2.8	149.8	161.4	70	9.0	Olsen and Brown [35]
	$Pb_{0.99}Nb_{0.02}(Zr_{0.68}Sn_{0.25}Ti_{0.07})_{0.98}O_3$	2.5	0.8	2.8	149.8	177.6	150	3.5	Olsen and Brown [35]
	$Pb_{0.99}Nb_{0.02}(Zr_{0.68}Sn_{0.25}Ti_{0.07})_{0.98}O_3$	2.5	0.8	3.2	146.8	191.8	350	3.2	Olsen and Brown [36]
	P(VDF)	1.8	22	53	23	67	30	0.29	Olsen and Brown [37]
	60/40P(VF2-TrFE)	2.3	6.23	27.6	50	100	165	1.23	Kouchachvili and Ikura [18]
	Purified 60/40P(VDF-TrFe)	2.3	7	34	40	97	279	1.59	Kouchachvili and Ikura [19]
	$Pb(Zn_{1/3}Nb_{2/3})_{0.955}Ti_{0.045}O_3$ single crystal	2.5	0	2	100	110	35	5.36	Khodayari et al. [17]
	$Pb(Zn_{1/3}Nb_{2/3})_{0.955}Ti_{0.045}O_3$ single crystal	2.5	0	2	100	200	243	0.46	Khodayari et al. [17]
	$Pb(Mg_{1/3}Nb_{2/3})_{0.68}Ti_{0.32}O_3$ single crystal	2.5	2	9	80	170	100	0.22	Kandilian et al. [15]
	$Pb(Mg_{1/3}Nb_{2/3})_{0.9}Ti_{0.1}O_3$ ceramic	2.6	0	3.5	27	77	186	0.99	Sebald et al. [44, 45]
	$Pb(Mg_{1/3}Nb_{2/3})_{0.9}Ti_{0.1}O_3$ ceramic	2.6	0	3.5	27	37	50	5.89	Sebald et al. [44, 45]
	P(VDF-TrFe) commercial	2	20	50	25	110	521	1.38	Navid et al. [30]
	P(VDF-TrFE-CFE)	2	0	80	0	25	240	5.7	Zhu et al. [57]

Linear materials: estimated values based on the properties of the materials. Nonlinear materials: experimental values of harvested energy

[35–39] and later by He et al. [13]. As for linear energy harvesting, Carnot cycles are totally impractical due to the limit in electrocaloric effect and the limited electric fields that the material can withstand. Even using the best electrocaloric materials, it is impractical to impose heat exchange conditions, such as successive adiabatic and isothermal conditions. Therefore, Ericsson cycle is most studied energy cycle for electrocaloric energy harvesting, although experiments using Stirling cycles were also published [10–12, 17, 44, 45]. A Stirling cycle consists of two isotherms and two isodisplacement (isocharge) portions. Open-circuit condition is used to obtain the constant electrical displacement portions. The cycle may be described as follows. Starting at point 1 in Fig. 5 the material is firstly at low temperature θ_c and voltage V_1. The material is open circuited and heated to a temperature θ_h. The material reaches the voltage V_2 for the temperature θ_h (point 2). The material is then discharged down to voltage V_3 at constant temperature θ_h (point 3). The material is then cooled down to temperature θ_c in open circuit, and its voltage reaches V_4 (point 4). Finally, the material is recharged from voltage V_4 to voltage V_1 at constant temperature θ_c. The enclosed area of the polarization—electric field diagram corresponds to the converted energy.

Figure 6 shows the polarization—electric field diagram of an Ericsson cycle. The cycle begins by charging the material at low temperature θ_c by increasing the voltage from V_1 to V_2. Next, the element is discharged by heating the element from θ_c to θ_h at constant voltage V_2.Then, the material is discharged by reducing the voltage from V_2 to V_1at constant temperature θ_h. Finally, the material is recharged by cooling it from θ_h to θ_c at constant voltage V_1. As for the Stirling cycle, the enclosed area is equal to the converted energy.

There is no clear advantage for Stirling cycles compared to Ericsson cycles. It gives output energy of the same order of magnitude. The point is the design and implementation of the electrical system performing the energy cycle. From a practical point of view, for experimental testing of materials, the Ericsson cycle is easier to achieve since the voltage in continuously controlled by a high voltage amplifier.

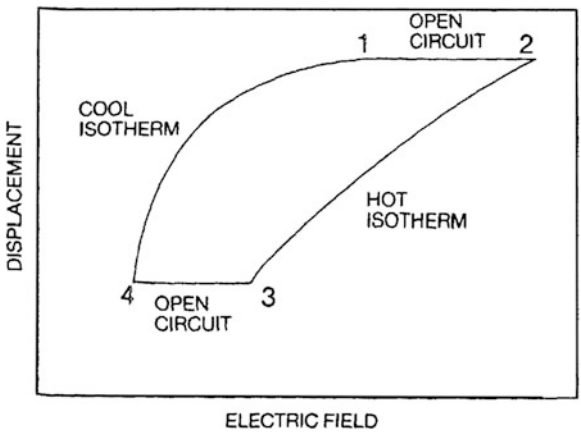

Fig. 5 Thermodynamic cycle for electrocaloric energy harvesting—Stirling cycle. After Ref. [37]

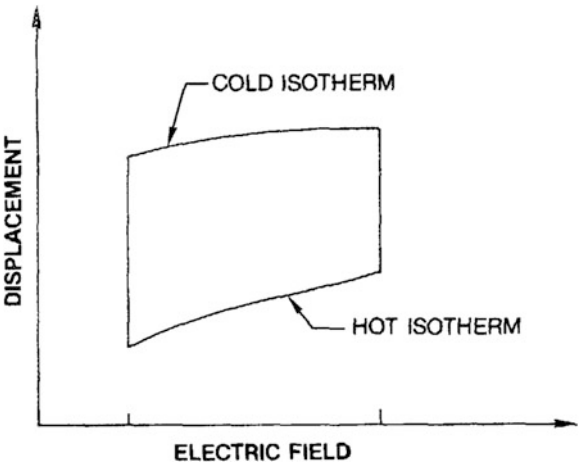

Fig. 6 Thermodynamic cycle for electrocaloric energy harvesting—Ericsson cycle (named later Olsen cycle in more recent publications). After Ref. [37]

3.2 Examples of Materials and Performances

Several groups published experimental energy harvesting results exploiting thermodynamic cycles and nonlinear materials. Many materials give output energy in the range 100 mJ cm^{-3} (or 100 J/L) for a temperature variation of several tens of degrees. In Table 2 are shown the output energy for different materials. It is non-exhaustive survey of presented results, and we chose some pertinent examples. The different columns display important parameters for energy harvesting. When not given in the reference, the volumetric heat capacity is taken to an average value of 2.5×10^6 J m^{-3}m K^{-1} for bulk ceramics and single crystals and 2×10^6 J m^{-3} K^{-1} for polymers. The induced error would be limited to a $\pm$ 50 % since dispersion of heat capacity is rather small. The working electric fields are calculated, whereas it is applied values for Ericsson cycles. The working temperatures are also displayed. The value of output energy is taken from the references. The relative efficiency is calculated using

$$\frac{\eta}{\eta_{Carnot}} = \frac{W}{c_E(\theta_h - \theta_c)} \frac{1}{\eta_{Carnot}} = \frac{W\theta_h}{c_E(\theta_h - \theta_c)^2} \tag{13}$$

For several materials, it is necessary to apply an electric field with the lowest value different from zero. Due to phase transitions induced by the electric field, or polarization losses, some parts of the enclosed area of the polarization—electric field diagram may correspond partially to supply energy and not harvested energy. The lower values of electric field are displayed in Table 2.

Olsen and Brown [35] tested $Pb_{0.99}Nb_{0.02}(Zr_{0.68}Sn_{0.25}Ti_{0.07})_{0.98}O_3$ ferroelectric ceramic working in the vicinity of Curie transition temperature. The net electrical energy density which may be produced when cycling between 0.8 and 2.8 MV m^{-1} and 149.8 and 161.4 °C (11.6° temperature span) is 70 mJ cm^{-3}.

Operation between 149.8 and 177.6 °C gives 150 mC cm^{-3}. Later Olsen and Evans [36] proposed a more exhaustive investigation on the same material and obtained 350 mJ cm^{-3} for a temperature variation of 45° starting at 146.8 °C and an electric field cycling between 0.8 and 3.2 MV m^{-1}. The same group moved then to PVDF polymers [37]. Thicknesses of the films were comprised between 30 and 70 μm. Conduction effect was the limiting factor in the utilization for energy harvesting. Output energy of 30 mJ cm^{-3} was however experimentally obtained for a temperature varying from 23 to 67 °C and electric field from 22 to 53 MV m^{-1}.

After those pioneering work, 17 years later, Ikura presented results on 25 μm thick 60–40 % P(VDF-TrFE) copolymer film. The conduction losses were better controlled than for previous tested polymers. The voltage was controlled between 100 and 1,200 V and temperature between 30 and 82 °C. The output energy density was found to be in the range 15–52 mJ cm^{-3} depending on sample [14].

Later, Kouchachvili and Ikura [18] studied the impact of the preconditioning of the pyroelectric films on the net power output. Pre-polarization (poling) of pyroelectric films has a significant beneficial effect by decreasing internal conduction during power conversion. The output energy was then increased up to 95–165 mJ cm^{-3} for a temperature varying from 50 to 100 °C. The same group proposed further improvements, such as the purification of the films, and obtained output energy 295 mJ cm^{-3} [19] between 40 and 97 °C.

In most cases, the best results are obtained when working in the vicinity of phase transitions which enlarges energy conversion capability [44, 45]. An example was then detailed in the case of $Pb(Mg_{1/3}Nb_{2/3})_{1-x}Ti_xO_3$ ceramic working in the vicinity of Curie transition: starting temperature is the room temperature and a temperature cycle with amplitude of 50° is then applied to the ceramic. Performing Ericsson cycles, a maximum of 186 mJ cm^{-3} was obtained for an applied electric field cycle of 3.5 MV m^{-1}. Similar results were found using $Pb(Zn_{1/3}Nb_{2/3})_{0.955}Ti_{0.045}O_3$ single crystal. The ferroelectric phase symmetry can be rhombohedral, tetragonal, orthorhombic or cubic. The different phase transitions are induced both by the electric field and the temperature. Crossing a phase transition induces huge variations of polarization that may enhance the energy conversion capability [41]. When performing Ericsson cycle on this material, a large amount of energy may then be harvested, up to 242.7 mJ cm^{-3} for a 60 °C temperature variation starting from 100 °C [17]. Later, the same group showed the importance of frequency effects (frequency should be held below 1 Hz), and the effectiveness of asymmetric Ericsson cycles [57].

For $Pb(Mg_{1/3}Nb_{2/3})_{0.7}Ti_{0.3}O_3$ single crystals, the Curie transition occurs around 135 °C. Then, an energy density of 100 mJ cm^{-3} per cycle may be harvested, with working temperature of $\theta_c = 80$ °C and $\theta_h = 170$ °C and cycling the electric field between 0.2 and 0.9 MV m^{-1} [15].

The highest output energy ever published was presented by Navid and Pilon with pure and purified P(VDF-TrFE) polymer and Olsen cycles [34], A maximum of 521 mJ cm^{-3} was obtained using $\theta_c = 25$ °C and $\theta_h = 110$ °C under low and high applied electric fields of about 20 and 50 MV m^{-1} [30].

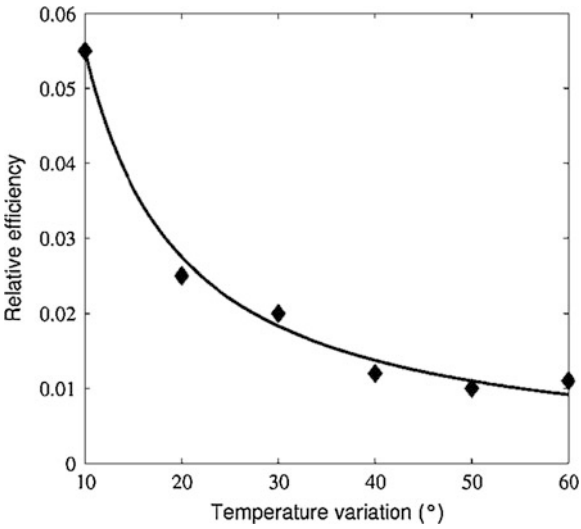

Fig. 7 Efficiency related to Carnot cycle with Ericsson cycle on $Pb(Zn_{1/3}Nb_{2/3})0.955Ti_{0.045}O_3$ single crystal and the temperature θ_c = 100 °C. *Line* is drawn to guide eyes. After data from Ref. [17]

A very interesting case was investigated by Zhu et al. [56]. P(VDF-TrFE-CFE) terpolymer is utilized between 25 and 0 °C. It takes advantages of the variation of dielectric permittivity when lowering the temperature. They observed that the permittivity increases when increasing the temperature. Using an adapted energy cycle, they predicted a harvested energy of 240 mJ cm^{-3} for a 25 °C temperature variation and an electric field of 80 MV m^{-1}. Experimentally, the electric field was limited to 25 MV m^{-1} due to electrical conduction, and the associated energy was 50 mJ cm^{-3}.

Apart from the maximum output energy, the question of efficiency is interesting. The relative efficiency for each presented experiment is displayed in Table 2. For most materials it is limited to a few percent. When increasing the temperature variation, the output energy increases whereas the efficiency is roughly constant [17]. It is usually observed that the output energy is proportional to the temperature difference. In addition, the absorbed heat from the hot reservoir is also proportional to the temperature difference. However, the efficiency of Carnot cycle is also proportional to the temperature difference. As shown in 13, when the output energy increases as the temperature difference, then the relative efficiency will vary like the inverse of the temperature difference. This kind of dependence was experimentally shown by Khodayari et al. [17] and displayed in Fig. 7.

3.3 From Electrocaloric Properties to Energy Harvesting

In this section, we aim at demonstrating the equivalence between electrocaloric effect (for refrigeration) and electrocaloric energy harvesting. After performing an

Ericsson cycle, sum of heat and sum of electric energy are the same since the initial state and final state are the same (considering that the internal energy is a state function). In addition, we use two important assumptions: pyroelectric coefficient does not depend on temperature, but only on electric field, and calorific capacity does not depend on electric field or temperature. We also assume that Maxwell relationships (that gives equivalence between pyroelectricity and electrocaloric activity) fully applies. It is true for an ergodic system and was experimentally verified for ferroelectric single crystals [43] but was found inapplicable for polar-glass type polymers (stretched P(VDF-TrFE-CFE) terpolymer) [25]. The harvested energy writes

$$W = -(\theta_h - \theta_c) \int_0^{E_M} p dE \tag{14}$$

This equation may be rewritten as

$$W = -\frac{(\theta_h - \theta_c)}{\theta_h} \int_0^{E_M} p\theta_h dE. \tag{15}$$

Recalling that the electrocaloric heat generated when charging the dielectric material is

$$Q_{ECE} = \int_0^{E_M} p\theta_h dE. \tag{16}$$

We can then write the harvested energy as a function of electrocaloric heat Q_{ECE} and efficiency of Carnot cycle as

$$W = -\eta_{Carnot} Q_{ECE.} \tag{17}$$

Let's now calculate the efficiency of the Ericsson cycle. Energy taken from the hot temperature medium is

$$Q_{hot} = c_E(\theta_h - \theta_c) + Q_{ECE.} \tag{18}$$

The efficiency is then

$$\eta = \frac{|W|}{Q_{hot}} = \eta_{Carnot} \frac{1}{1 + \frac{c_E(\theta_h - \theta_c)}{Q_{ECE}}}. \tag{19}$$

The conversion ratio compared to Carnot conversion ratio decreases with the temperature difference. A material having a very large electrocaloric activity will result in a large pyroelectric energy harvesting.

There are a limited number of investigations on Ericsson cycles, whereas a lot of bibliographic data may be found on electrocaloric activity. From these data,

although devoted to electrocaloric cooling, it is possible to predict energy harvesting ability. Such estimations were calculated and some chosen results are displayed in Table 3 for a temperature variation of only 10°. For bulk materials, where the dielectric breakdown electric field is small, the electrocaloric activity is limited. Relative efficiencies lies in the range of 5–10 % [1, 43–45, 47]—with an exception for PZST75/20/5 that exhibit an unusually high electrocaloric activity for a bulk material [50]. For thin films and polymers, the maximum electric field is huge (up to 180 MV m^{-1}) [24, 28, 29] and electrocaloric activity is very large as well. Consequently, the expected output energy and efficiency are outstanding. The best result was obtained with stretched P(VDF-TrFE-CFE) terpolymer [26], with an output energy per cycle of almost 1 J cm^{-3} and a relative efficiency of 60 %.

Finally, the promising results presented above should be counter-balanced with the presence of a substrate in most cases. The heat that is supplied to the material should also be utilized for heating up the substrate and the overall efficiency would decreases drastically when the substrate heat capacity is much larger than that of the active layer. Ways for avoiding this drawback would be to use multilayer systems [16] or self-supported layers (such as for P(VDF-TrFE-CFE) terpolymer).

4 Practical Considerations

To the best of our knowledge, pyroelectric or electrocaloric energy harvesting demonstrators were not yet fabricated as fully functional systems. Either the temperature is applied by manual cyclic operation, either the electrical quantities are controlled by voltage amplifiers whose power consumption is larger by decades to the harvested power, or both. The most plausible published systems are those working with linear pyroelectric materials, thank to power electronics that already exist (set of transistors and diodes). But even in this case, the transistor commands are externally controlled by a calculator. In this section are presented the two main requirements for further advanced engineering.

4.1 Temperature Varying "Source"

Temperature is more likely stable over long time periods and varies over space rather than time. Temperature differences of several degrees naturally appear in an indoor room, whereas time variations will be related to the night and day cycle or natural convective air flow for example. However, for embedded electronics working both indoors and outdoors, a pyroelectric energy harvester may be subjected to large temperature variations several times a day, and may reach significant output power. A very simple example of this kind was shown in [46], where a temperature sensor was fixed on a wear. A predictive output power of 1 μW cm^{-3} was estimated with power peaks above 200 μW cm^{-3}. However, applications—where temperature

Table 3 Estimated energy harvesting capability from electrocaloric materials

Material		θ_{ECE} (°C)	c_E (MJ m^{-3})	Q_{ECE} (J cm^{-3})	E (MV m^{-1})	θ (°C)	W (mJ cm^{-3})	η/η_{carnot}	References
Bulk materials	$0.95PbSc_{0.5}Ta_{0.5}O_3$–$0.05PbSc_{0.5}Sb_{0.5}O_3$	1.6	2.6	4.2	2.5	−5	151	13.8	Shebanov and Borman [48]
	$Pb(Mg_{1/3}Nb_{2/3})_{0.85}Ti_{0.15}O_3$ ceramic	1.7	2.6	4.5	1.6	18	149	14.6	Shaobo and Yanqiu [47]
	$Pb(Mg_{1/3}Nb_{2/3})_{0.90}Ti_{0.10}O_3$ ceramic	–	2.6	1.4	3.5	30	45	5.1	Sebald et al. [44, 45]
	<111>$Pb(Mg_{1/3}Nb_{2/3})_{0.75}Ti_{0.25}O_3$ single crystal	–	2.6	2.5	2.5	110	64	8,7	Sebald et al. [43]
	PLZT	0.6	2.6	1.6	2	37	50	5.7	Birks et al. [1]
	PZST75/20/5	2.6	3.8	9.8	3	161	221	20.7	Tuttle and Payne [50]
Thin films	$Pb(Mg_{1/3}Nb_{2/3})_{0.75}Ti_{0.25}O_3$thin film	5	3.0	15	90	75	419	33.3	Mischenko et al. [28, 29]
	PbZr0.95Ti0.05O3 thin film	12	2.5	30	78	220	596	54.5	Mischenko et al. [28, 29]
Polymers	P(VDF-TrFe) 55/45 mol	12	2.0	24	180	67	685	54.5	Lu et al. [26]
	P('VDF-TrFe-CFE)59.2/33.6/7.2 stretched	15	2.0	30	150	30	958	60.0	Li et al. [24]

The energy density is calculated for a temperature variation of 10°

varies over time—would be most probably for niche markets. Moreover, for stochastic temperature variations, it is necessary to trig the electrical quantities on the temperature signal thus requiring advanced sensing systems.

On the other hand, it is possible to create time variation starting from static hot and cold reservoirs. The idea is roughly to bring the sample in contact (directly or though a heat conductive fluid) cyclically to the hot and the cold reservoirs. In the previous sections of this chapter, the only output energy densities were considered. In order to get an output power, the period of temperature variation is required. An effective heat transfer system should be able to impose a large temperature variation to a pyroelectric or electrocaloric material, at the highest possible frequency in order to obtain the highest output power.

Theoretical work from Sklar [49] established the feasibility of low-power pumping. Simulation results showed that the necessary pumping power of the fluid may be less than 2 % of the total harvested power.

Navid et al. [31, 32] also used simulations to quantify the necessary pumping power to heat up and cool down an electrocaloric element from 145 to 185 °C. Using a two-dimensional mass, momentum and energy equations, heat input, pumping power and electrical output power were calculated for several geometries. They pointed out the importance of device length and the viscosity of the working fluid. A maximum of 5.2 % in efficiency was then demonstrated, thus corresponding to a relative efficiency of 55.4 % with commercial 1.5 cst silicone oil as the working fluid and PZST as the pyroelectric material. The associated power density was 38.4 mW/cm^{-3} of material. The predicted efficiency is the highest ever published for pyroelectric energy harvesting. Further experimental systems must be designed, fabricated and tested for validation, because this constitutes a scientific breakdown compared to thermoelectric energy harvesting whose efficiency is limited to 10 % of Carnot efficiency.

The same group also published at the same time a partial experimental validation of those principles [34]. They performed Olsen cycles on copolymer 60/40 [P(VDF-TrFE)] thin films sandwiched between metallic electrodes. They especially focused on maximizing the output electrical power. Although much interesting, this chapter did not give details about power consumption of the fluid pumping, and the electrical part did not harvest energy, but only applied the required cyclic high voltages. Nevertheless, the output power is very high: a maximum energy density of 130 mJ cm^{-3} was achieved at 0.061 Hz frequency with temperature oscillating between 69.3 and 87.6 °C. Furthermore, a maximum power density of 10.7 mW/cm^{-3} was obtained at 0.12 Hz between 70.5 and 85.3 °C. The low and high electric fields amplitudes were 20.2 and 73.9 MV m^{-1}. This technique offers the advantage of ultra-high efficiency. Indeed, for a given volume of material, the corresponding heat reservoirs are the adjacent volumes, and the released heat to the cold reservoir corresponds to the input heat for the next element.

Another technique would be to design and fabricate heat switches. After Epstein and Malloy [6], heat switches may be based on thin layers of liquid crystals. When a voltage is applied to a liquid with crystal mixtures or carbon

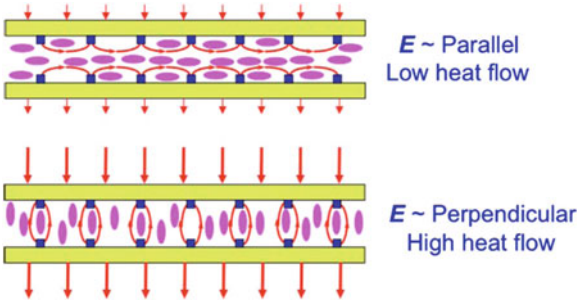

Fig. 8 After Ref [6], edge view of a liquid crystal heat switch showing the interdigitated electrodes (*rectangles*) and the liquid crystal directors (indicated by the orientation of the *ellipses*). The electric field direction (*curved arrows*) and the liquid crystal directors can be switched between being predominately parallel to the film of liquid crystal (*top panel*) and mainly perpendicular to the film (*bottom panel*)

nanotubes in suspension, the molecules can be switched from a predominant parallel alignment with the electrodes, towards a predominant perpendicular alignment with the electrodes as shown in Fig. 8. Thermal conductivity is therefore greatly modified. In their work, they present in a comprehensive manner the key points in the design of heat switches, although no quantification of expected effectiveness is provided.

An illuminating concept was proposed by Fang et al. [7]. It is based on the nanoscale radiative heat transfer between parallel plates. Considering hot and cold plates at 283 and 383 K, a pyroelectric element is moved toward the heat reservoirs using an external actuator. The heat exchange increases with the inverse of the distance, but when reaching very small distances, it grows up exponentially (near-field contribution, distance below 1 nm). Heat transfer coefficient increases by two decades when reducing the distance by one decade. In their work, a model of radiative heart transfer is detailed and they predict an overall 0.2 % efficiency on energy harvesting using 60/40P(VDF-TrFE) and 0.84 mW cm^{-2}. They finally predict that using $Pb(Mg_{1/3}Nb_{2/3})_{0.9}Ti_{0.1}O_3$ composite thin films, the efficiency could reach 1.3 %, that is to say 5 % of Carnot efficiency.

As a conclusion, much innovative solutions were proposed to obtain a time varying temperature signal at reasonable energy cost. For every solution discussed above, further quantification of involved energies is still required. What the power consumption of thermal switch based on liquid crystals? For a pumping system, the hydraulic losses are quantified, but the efficiency of the pump itself is not yet considered.

4.2 Power Management

Among all scientific and technological features of electrocaloric energy harvesting, the power management is a problem that was rarely tackled. Most of the effort focused on materials and heat transfer problems, and the feasibility of Ericsson cycles was never discussed. However, in most cases, voltages should be in the kV range, and currents in the μA range. An electrical system applying the high voltage while being fully reversible simply does not exist. Of course, there exist some power electronics schemes of reversible amplifiers, like a H-bridge operation [44]. This solution is theoretically most suitable for all kind of cycles, including Ericsson or Stirling cycles. However, the existence of necessary electronic components is much questionable (high voltages, low frequency, low currents, ultra-low leakage). The fast development of power electronics were attracted by low voltage and high current systems, such as solar panels and electromagnetic applications. Then, the design of voltage converters with high voltages and low current is an important challenge. A simple way for understanding this limitation is to consider the impedance of a MOSFET transistor when it is switched off. Impedance values are in the 10–100 MΩ range. Then, the capacitance of a PZT ceramic of a 1 cm^2 and a thickness of 300 μm is in the 3nF order of magnitude. Time constant of this RC circuit is then roughly 0.03–0.3 s. Realistic operating frequencies are below 1 Hz (period above 1 s), and most of the generated energy will be lost in the electrical system impedance. This means that resistive losses appear due to the off-state of the transistor—and we don't consider here many other sources of losses and efficiency decrease. Moreover, an H-bridge operation requires a continuous control of the transistors commands, and the subsequent power consumption might be large compared to the harvested power.

In case of linear energy harvesting, although being of much lower power outputs, the management of the energy is much easier as it can be transferred from the piezoelectric case. For standard technique, the electrical system consists of diodes whose impedances are much higher than that of transistors [4]. On the contrary, advanced energy conversion techniques, such as Synchronized Switch Harvesting on Inductor (SSHI) or Synchronous Electric Charge Extraction [10, 12] suffer the same limitations as for electrocaloric energy harvesting, although the simplicity of transistors commands makes it more convincing. Self-powered advanced energy conversion systems are already available for piezoelectric energy harvesting [20], and its transfer towards pyroelectric case should be possible.

5 Conclusions

Energy harvesting from temperature variations was demonstrated with different pyroelectric and electrocaloric materials. For limited temperature variation, linear pyroelectric materials may bring up much valuable results with efficiencies related

to a Carnot cycle as high as 14 % (case of laminated materials). <111> $Pb(Mg_{1/3}Nb_{2/3})_{0.72}Ti_{0.28}O_3$ single crystals could also exhibit a high relative efficiency of 2.8 % thanks to their excellent pyroelectric properties. Electrical system is already developed for piezoelectric energy harvesting and same system can be used for pyroelectric energy harvesting.

For larger temperature variations, the electric field that appears on linear pyroelectric material induces nonlinear behavior and depolarization for ferroelectrics. In this case, it is better to use electrocaloric materials working in the vicinity of phase transitions and thermodynamic cycles, such as Ericsson (or Olsen) cycles or Stirling cycles. Output energy density was experimentally demonstrated to be as high as 500 mJ cm^{-3} on polymer films for a 60° temperature variation.

Finally we showed in this chapter that the best materials for electrocaloric cooling should be also the best ones for energy harvesting. Based on Maxwell relationships, it was shown that output energy and relative efficiency could be as high as 1 J cm^{-3} and 60 % respectively for a limited 10° temperature variation. However, for some electrocaloric polymers the equivalence based on Maxwell relationship cannot be held true due to the nonergodicity of the material [25].

A pyroelectric or electrocaloric energy harvesting system includes a temperature source, an active material and an electrical system to harvest the converted energy. The only material part was deeply investigated, with excellent results. For the temperature source part, promising solutions were proposed such as thermal heat switches or low power pumping. For electric system able to perform a thermodynamic cycle on the material—and triggered on the temperature variation, it is still required to develop new solutions.

References

1. Birks, E., Shebanov, L., Sternberg, A.: Electrocaloric effect in PLZT ceramics. Ferroelectrics **69**(1), 125–129 (1986). doi:10.1080/00150198608008134
2. Chang, H.H.S., Huang, Z.: Substantial pyroelectric effect enhancement in laminated composites. Appl. Phys. Lett. **92**(15), 152903 (2008). doi:10.1063/1.2907701
3. Chang, H.H.S., Huang, Z.: Laminate composites with enhanced pyroelectric effects for energy harvesting. Smart Mater. Struct. **19**(6), 065018 (2010). doi:10.1088/0964-1726/19/6/065018
4. Cuadras, A., Gasulla, M., Ferrari, V.: Thermal energy harvesting through pyroelectricity. Sens. Actuators, A **158**(1), 132–139 (2010). doi:10.1016/j.sna.2009.12.018
5. Davis, M., Damjanovic, D., Setter, N.: Pyroelectric properties of (1−x)Pb(Mg[sub 1/3]Nb[sub 2/3])O[sub 3]-xPbTiO[sub 3] and (1−x)Pb(Zn[sub 1/3]Nb[sub 2/3])O[sub 3]-xPbTiO[sub 3] single crystals measured using a dynamic method. J. Appl. Phys. **96**(5), 2811 (2004). doi:10.1063/1.1775308
6. Epstein, R.I., Malloy, K.J.: Electrocaloric devices based on thin-film heat switches. J. Appl. Phys. **106**(6), 064509 (2009). doi:10.1063/1.3190559
7. Fang, J., Frederich, H., Pilon, L.: Harvesting nanoscale thermal radiation using pyroelectric materials. J. Heat Transf. **132**(9), 092701 (2010). doi:10.1115/1.4001634
8. Fatuzzo, E.: Theoretical efficiency of pyroelectric power converters. J. Appl. Phys. **37**(2), 510 (1966). doi:10.1063/1.1708205

9. Guyomar, D., Badel, A., Lefeuvre, E., Richard, C.: Toward energy harvesting using active materials and conversion improvement by nonlinear processing. IEEE Trans. Ultrason. Ferroelectr. Freq. Control **52**(4), 584–595 (2005). doi:10.1109/TUFFC.2005.1428041
10. Guyomar, D., Sebald, G., Pruvost, S., Lallart, M., Khodayari, A., Richard, C.: Energy harvesting from ambient vibrations and heat. J. Intell. Mater. Syst. Struct. **20**(5), 609–624 (2008). doi:10.1177/1045389X08096888
11. Guyomar, D., Pruvost, S., Sebald, G.: Energy harvesting based on FE-FE transition in ferroelectric single crystals. IEEE Trans. Ultrason. Ferroelectr. Freq. Control **55**(2), 279–285 (2008). doi:10.1109/TUFFC.2008.646
12. Guyomar, D., Sebald, G., Lefeuvre, E., Khodayari, A.: Toward heat energy harvesting using pyroelectric material. J. Intell. Mater. Syst. Struct. **20**(3), 265–271 (2008). doi:10.1177/1045389X08093564
13. He, J., Chen, J., Zhou, Y., Wang, J.T.: Regenerative characteristics of electrocaloric Stirling or Ericsson refrigeration cycles. Energy Convers. Manage. **43**(17), 2319–2327 (2002). doi:10.1016/S0196-8904(01)00183-2
14. Ikura, M.: Conversion of low-grade heat to electricity using pyroelectric copolymer. Ferroelectrics **267**(1), 403–408 (2002). doi:10.1080/713715909
15. Kandilian, R., Navid, A., Pilon, L.: The pyroelectric energy harvesting capabilities of PMN–PT near the morphotropic phase boundary. Smart Mater. Struct. **20**(5), 055020 (2011). doi:10.1088/0964-1726/20/5/055020
16. Kar-Narayan, S., Mathur, N.D.: Direct and indirect electrocaloric measurements using multilayer capacitors. J. Phys. D Appl. Phys. **43**(3), 032002 (2010). doi:10.1088/0022-3727/43/3/032002
17. Khodayari, A., Pruvost, S., Sebald, G., Guyomar, D., Mohammadi, S.: Nonlinear pyroelectric energy harvesting from relaxor single crystals. IEEE Trans. Ultrason. Ferroelectr. Freq. Control **56**(4), 693–699 (2009). doi:10.1109/TUFFC.2009.1092
18. Kouchachvili, L., Ikura, M.: Pyroelectric conversion–effects of P(VDF-TrFE) preconditioning on power conversion. J. Electrostat. **65**(3), 182–188 (2007). doi:10.1016/j.elstat.2006.07.014
19. Kouchachvili, L., Ikura, M.: Improving the efficiency of pyroelectric conversion. Int. J. Energy Res. **32**(4), 328–335 (2008). doi:10.1002/er.1361
20. Lallart, M., Guyomar, D.: An optimized self-powered switching circuit for non-linear energy harvesting with low voltage output. Smart Mater. Struct. **17**(3), 035030 (2008). doi:10.1088/0964-1726/17/3/035030
21. Lam, K.S., Wong, Y.W., Tai, L.S., Poon, Y.M., Shin, F.G.: Dielectric and pyroelectric properties of lead zirconate titanate/polyurethane composites. J. Appl. Phys. **96**(7), 3896 (2004). doi:10.1063/1.1787586
22. Lang, S.B., Muensit, S.: Review of some lesser-known applications of piezoelectric and pyroelectric polymers. Appl. Phys. A **85**(2), 125–134 (2006). doi:10.1007/s00339-006-3688-8
23. Lefeuvre, E., Badel, A., Richard, C., Petit, L., Guyomar, D.: A comparison between several vibration-powered piezoelectric generators for standalone systems. Sens. Actuators, A: Physical **126**(2), 405–416 (2006). doi:10.1016/j.sna.2005.10.043
24. Li, X., Qian, X., Lu, S.G., Cheng, J., Fang, Z., Zhang, Q.M.: Tunable temperature dependence of electrocaloric effect in ferroelectric relaxor poly(vinylidene fluoride-trifluoroethylene-chlorofluoroethylene terpolymer. Appl. Phys. Lett. **99**(5), 052907 (2011). doi:10.1063/1.3624533
25. Lu, S.G., Rožič, B., Zhang, Q.M., Kutnjak, Z., Pirc, R., Lin, M., Li, X., et al.: Comparison of directly and indirectly measured electrocaloric effect in relaxor ferroelectric polymers. Appl. Phys. Lett. **97**(20), 202901 (2010). doi:10.1063/1.3514255
26. Lu, S.G., Rožič, B., Zhang, Q.M., Kutnjak, Z., Neese, B.: Enhanced electrocaloric effect in ferroelectric poly(vinylidene-fluoride/trifluoroethylene) 55/45 mol% copolymer at ferroelectric-paraelectric transition. Appl. Phys. Lett. **98**(12), 122906 (2011). doi:10.1063/1.3569953

27. Mane, P., Xie, J., Leang, K.K., Mossi, K.: Cyclic energy harvesting from pyroelectric materials. IEEE Trans. Ultrason. Ferroelectr. Freq. Control **58**(1), 10–17 (2011). doi:10.1109/TUFFC.2011.1769
28. Mischenko, A.S., Zhang, Q., Scott, J.F., Whatmore, R.W., Mathur, N.D.: Giant electrocaloric effect. Science **311**(5765), 1209d–1209d (2006). doi:10.1126/science.311.5765.1209d
29. Mischenko, A.S., Zhang, Q., Whatmore, R.W., Scott, J.F., Mathur, N.D.: Giant electrocaloric effect in the thin film relaxor ferroelectric 0.9 PbMg[sub 1/3]Nb[sub 2/3]O[sub 3]–0.1 PbTiO[sub 3] near room temperature. Appl. Phys. Lett. **89**(24), 242912 (2006). doi:10.1063/1.2405889
30. Navid, A., Pilon, L.: Pyroelectric energy harvesting using Olsen cycles in purified and porous poly(vinylidene fluoride-trifluoroethylene) [P(VDF-TrFE)] thin films. Smart Mater. Struct. **20**(2), 025012 (2011). doi:10.1088/0964-1726/20/2/025012
31. Navid, A., Lynch, C.S., Pilon, L.: Purified and porous poly(vinylidene fluoride-trifluoroethylene) thin films for pyroelectric infrared sensing and energy harvesting. Smart Mater. Struct. **19**(5), 055006 (2010). doi:10.1088/0964-1726/19/5/055006
32. Navid, A., Vanderpool, D., Bah, A., Pilon, L.: Towards optimization of a pyroelectric energy converter for harvesting waste heat. Int. J. Heat Mass Transf. **53**(19–20), 4060–4070 (2010). doi:10.1016/j.ijheatmasstransfer.2010.05.025
33. Ng, W. Y., Ploss, B., Chan, H. L. W., Shin, F. G., & Choy, C. L. (n.d.). Pyroelectric properties of PZT/P(VDF-TrFE) 0-3 composites. ISAF 2000. Proceedings of the 2000 12th IEEE International Symposium on Applications of Ferroelectrics (IEEE Cat. No.00CH37076) (Vol. 2, pp. 767–770). IEEE. doi:10.1109/ISAF.2000.942432
34. Nguyen, H., Navid, A., Pilon, L.: Pyroelectric energy converter using co-polymer P(VDF-TrFE) and Olsen cycle for waste heat energy harvesting. Appl. Therm. Eng. **30**(14–15), 2127–2137 (2010). doi:10.1016/j.applthermaleng.2010.05.022
35. Olsen, R.B., Brown, D.D.: High efficiency direct conversion of heat to electrical energy-related pyroelectric measurements. Ferroelectrics **40**(1), 17–27 (1982). doi:10.1080/00150198208210592
36. Olsen, R.B., Evans, D.: Pyroelectric energy conversion: hysteresis loss and temperature sensitivity of a ferroelectric material. J. Appl. Phys. **54**(10), 5941 (1983). doi:10.1063/1.331769
37. Olsen, R.B., Bruno, D.A., Briscoe, J.M.: Pyroelectric conversion cycles. J. Appl. Phys. **58**(12), 4709 (1985). doi:10.1063/1.336244
38. Olsen, R.B., Bruno, D.A., Briscoe, J.M., Jacobs, E.W.: Pyroelectric conversion cycle of vinylidene fluoride-trifluoroethylene copolymer. J. Appl. Phys. **57**(11), 5036 (1985). doi:10.1063/1.335280
39. Olsen, R.B., Bruno, D.A., Briscoe, J.M., Jacobs, E.W.: High electric field resistivity and pyroelectric properties of vinylidene fluoride-trifluoroethylene copolymer. J. Appl. Phys. **58**(8), 2854 (1985). doi:10.1063/1.335857
40. Peláiz Barranco, A., Calderón Piñar, F., & Pérez Martínez, O. (2001). PLZT Ferroelectric Ceramics on the Morphotropic Boundary Phase. Study as Possible Pyroelectric Sensors. Physica status solidi (a), **186**(3), 479–485. doi:10.1002/1521-396X(200108)186:3<479::AID-PSSA479>3.3.CO;2-D
41. Pruvost, S., Hajjaji, A., Lebrun, L., Guyomar, D., Boughaleb, Y.: Domain switching and energy harvesting capabilities in ferroelectric materials†. J. Phys. Chem. C **114**(48), 20629–20635 (2010). doi:10.1021/jp105262h
42. Roundy, S., Leland, E.S., Baker, J., Carleton, E., Reilly, E., Lai, E., Otis, B., et al.: Improving power output for vibration-based energy scavengers. IEEE Pervasive Comput. **4**(1), 28–36 (2005). doi:10.1109/MPRV.2005.14
43. Sebald, G., Seveyrat, L., Guyomar, D., Lebrun, L., Guiffard, B., Pruvost, S.: Electrocaloric and pyroelectric properties of 0.75Pb(Mg[sub 1/3]Nb[sub 2/3])O[sub 3]–0.25PbTiO[sub 3] single crystals. J. Appl. Phys. **100**(12), 124112 (2006). doi:10.1063/1.2407271

44. Sebald, G., Lefeuvre, E., Guyomar, D.: Pyroelectric energy conversion: optimization principles. IEEE Trans. Ultrason. Ferroelectr. Freq. Control **55**(3), 538–551 (2008). doi:10.1109/TUFFC.2008.680
45. Sebald, G., Pruvost, S., Guyomar, D.: Energy harvesting based on Ericsson pyroelectric cycles in a relaxor ferroelectric ceramic. Smart Mater. Struct. **17**(1), 015012 (2008). doi:10.1088/0964-1726/17/01/015012
46. Sebald, G., Guyomar, D., Agbossou, A.: On thermoelectric and pyroelectric energy harvesting. Smart Mater. Struct. **18**(12), 125006 (2009). doi:10.1088/0964-1726/18/12/125006
47. Shaobo, L., Yanqiu, L.: Research on the electrocaloric effect of PMN/PT solid solution for ferroelectrics MEMS microcooler. Mater. Sci. Eng., B **113**(1), 46–49 (2004). doi:10.1016/j.mseb.2004.06.010
48. Shebanov, L., Borman, K.: On lead-scandium tantalate solid solutions with high electrocaloric effect. Ferroelectrics **127**(1), 143–148 (1992). doi:10.1080/00150199208223361
49. Sklar, A. A. (2005). A Numerical Investigation of a Thermodielectric Power Generation System. Georgia Institute of Technology. Retrieved from http://hdl.handle.net/1853/14020
50. Tuttle, B.A., Payne, D.A.: The effects of microstructure on the electrocaloric properties of Pb(Zr, Sn, Ti)O_3 ceramics. Ferroelectrics **37**(1), 603–606 (1981). doi:10.1080/00150198108223496
51. Vanderpool, D., Yoon, J., Pilon, L.: Simulations of a prototypical device using pyroelectric materials for harvesting waste heat. Int. J. Heat Mass Transf. **51**(21–22), 5052–5062 (2008). doi:10.1016/j.ijheatmasstransfer.2008.04.008
52. Warneke, B., Last, M., Liebowitz, B., Pister, K.S.J.: Smart dust: communicating with a cubic-millimeter computer. Computer **34**(1), 44–51 (2001). doi:10.1109/2.895117
53. Xie, J., Mane, X.P., Green, C.W., Mossi, K.M., Leang, K.K.: Performance of thin piezoelectric materials for pyroelectric energy harvesting. J. Intell. Mater. Syst. Struct. **21**(3), 243–249 (2009). doi:10.1177/1045389X09352818
54. Yamaka, E.: Structural, ferroelectric, and pyroelectric properties of highly c-axis oriented Pb1−xCaxTiO3 thin film grown by radio-frequency magnetron sputtering. J. Vac. Sci. Technol. A: Vac. Surf. Films **6**(5), 2921 (1988). doi:10.1116/1.575452
55. Zhang, Q., Whatmore, R.W.: Improved ferroelectric and pyroelectric properties in Mn-doped lead zirconate titanate thin films. J. Appl. Phys. **94**(8), 5228 (2003). doi:10.1063/1.1613370
56. Zhu, H., Pruvost, S., Guyomar, D., Khodayari, A.: Thermal energy harvesting from Pb(Zn[sub 1/3]Nb[sub 2/3])[sub 0.955]Ti[sub 0.045]O[sub 3] single crystals phase transitions. J Appl. Phys. **106**(12), 124102 (2009). doi:10.1063/1.3271144
57. Zhu, H., Pruvost, S., Cottinet, P.J., Guyomar, D.: Energy harvesting by nonlinear capacitance variation for a relaxor ferroelectric poly(vinylidene fluoride-trifluoroethylene-chlorofluoro ethylene) terpolymer. Appl. Phys. Lett. **98**(22), 222901 (2011). doi:10.1063/1.3595325

Future Trends in Electrocaloric Materials

N. D. Mathur

Let us compare the field of electrocaloric with the more mature field of magnetocaloric, i.e. the magnetic analogue where thermal changes are driven in magnetic materials by changes of applied magnetic field. Both fields of research became popular in recent times following the observation of giant effects. The giant electrocaloric effects reported in [5] were achieved by driving a well-known ferroelectric material with an order-of-magnitude larger electric field, and this was made possible by switching from bulk to thin-film samples. By contrast, the giant magnetocaloric effects reported by Pecharsky and Gschneidner in [6] were achieved in a little-known bulk material, namely $Gd_5Si_2Ge_2$. Both fields subsequently witnessed the demonstration of giant effects in other materials, with giant magnetocaloric effects developed in various bulk materials, and giant electrocaloric effects developed in thin-films of well-known ferroelectric materials.

The field of magnetocalorics is now so mature that there exist over forty prototype heat pump devices [8], typically referred to as refrigerators. The first to operate near room temperature was developed by Brown [2] using gadolinium, a material that showed a magnetocaloric effect of 14 K on changing the applied flux density by 7 T. This work introduced the regenerator concept by showing that 47 K could be developed along a column of fluid by moving the gadolinium up and down while varying the applied magnetic field. The regenerator concept was also used in the electrocaloric refrigerator that was fabricated in the USSR over two decades ago [7], but given the need to make an electrical connection to the plates of lead scandium tantalate, the fluid was cycled around the device and the electrocaloric working body was held fixed.

One is immediately led to ask whether electrocaloric cooling or magnetocaloric cooling is more promising. The magnetocaloric prototypes are technologically very impressive, but it seems that they have not been commercialised, perhaps

N. D. Mathur (✉)
Materials Science, University of Cambridge, 27 Charles Babbage Road, Cambridge CB3 0FS, UK
e-mail: ndm12@cam.ac.uk

T. Correia and Q. Zhang (eds.), *Electrocaloric Materials*, Engineering Materials 34, DOI: 10.1007/978-3-642-40264-7_10,

because it is not possible to achieve a high enough cooling power, for a high enough temperature span, in an energy efficient manner. Moreover, magnetocaloric materials of interest tend to require expensive rare earth elements, and cheap permanent magnets cannot generate the large fields required. By contrast, electrocaloric ceramic and polymers are typically cheap, and it is easy to generate a driving voltage. This is a good starting point from which to develop a demonstrator refrigerator and investigate its performance.

The first challenge is to select the electrocaloric material. Should it be a polymer or a ceramic? A detailed comparison of some existing electrocaloric materials is presented in ref. [4], where it is shown that the results depend on whether one normalises electrocaloric heat by mass or volume, and where the electrical energy associated with electrocaloric effects is taken into account by introducing a materials efficiency that does not depend on the details of any refrigeration cycle. This materials efficiency could represent a helpful guide for selecting energy efficient electrocaloric materials.

The second challenge is to investigate the performance of electrocaloric materials. The indirect method based on the thermodynamic analysis of electrical data is relatively easy to implement, and it may remain useful for rapid characterization of new materials. However, direct measurements of heat and temperature change are ultimately required in order to inspire confidence. There are now several methods for doing this, as discussed in Chap. 7, and we can hope to look forward to direct electrocaloric measurements of thin films with substrates present. If this can be achieved routinely, then the indirect method could even become redundant.

The third challenge is to fabricate electrocaloric working bodies for heat pumps. As discussed in Chap. 4, neither thin films nor bulk materials are immediately suitable, whereas multilayer capacitors (MLCs) represent a potentially ideal embodiment. In practice, two issues must be addressed for the fabrication of useful electrocaloric MLCs. First, it is necessary to optimise the geometry while taking into account the operating frequency, e.g. using finite element analysis [3]. Second, it is potentially challenging to fabricate electrocaloric MLCs that can reliably withstand high electric fields. Given that breakdown field scales inversely with sample thickness, these two issues are related and must be solved simultaneously.

The fourth challenge is to identify suitable applications. It might prove overly difficult to compete with the well-established vapour-compression technology used in domestic refrigerators, but niche applications could be possible. Electrocaloric refrigeration could out-compete the vapour-compression method in applications that require small heat pumps with fast turn on times. If electrocaloric cooling proves to be energy efficient, which is currently a known unknown, then it could also out-compete other cooling technologies such as Peltier coolers, which are currently available but highly inefficient. It may turn out that electrocaloric cooling can be very efficient if the temperature change is small and the operating frequency is high, e.g. for applications in HVAC (heating, ventilation, and air conditioning).

The fifth challenge is to design heat pumps based on electrocaloric working bodies such as MLCs. There may be lessons to learn from the magnetocaloric prototypes [8], but a fresh approach could be attractive given that the driving field

is applied in a different way, and given that high-frequency operation is more plausible in the absence of eddy currents. Heat-pump design is a job for suitably knowledgeable engineers, and the challenge for the scientific community is to provide them with the best possible electrocaloric working bodies. Given the need for cyclical operation, the performance of heat switches should prove very important, but it may be possible instead to use thermal diodes in the form of heat pipes [1].

The five challenges identified above are substantial, and contingent on one another. Improved materials performance remains important, particularly in terms of electrocaloric temperature change, which drives heat flow. For any given electrocaloric materials, one needs the confidence to demonstrate electrocaloric working bodies around which engineers may design a heat pump. Without being able to know how well such a heat pump would perform, it is hard to have this confidence. But without demonstrating electrocaloric working bodies, it is hard to know how well an electrocaloric heat pump could perform. This vicious circle could be broken by either modelling, or blind faith.

Magnetocaloric refrigeration was once the future, but today it is the field of electrocalorics that feels young. Electrocalorics will need to look over its shoulder at the field of elastocalorics, which is starting to gain momentum, but perhaps the simplicity of voltage-controlled thermal effects gives electrocalorics an edge. Even if no useful heat pumps eventually result from our endeavours, electrocaloric research could lead to energy harvesting applications as discussed in Chap. 9. So will the scientific process beat on, against the current uncertainties in funding, to build on what we know from the past.

References

1. Basiulis, A., Berry, R. L.: *U. S. Patent* 4,757,688 (1988)
2. Brown, G.V.: J. Appl. Phys. **47**, 3673–3680 (1976)
3. Crossley, S. *PhD thesis*, University of Cambridge (2013)
4. Defay, E., Crossley, S., Kar-Narayan, S., Moya, X., Mathur, N. D.: *Advanced Materials*, **25**, 3337–3342 (2013)
5. Mischenko, A.S., Zhang, Q., Scott, J.F., Whatmore, R.W., Mathur, N.D.: Science **311**, 1270–1271 (2006)
6. Pecharsky, V.K., Gschneidner Jr, K.A.: Phys. Rev. Lett. **78**, 4494–4497 (1997)
7. Sinyavsky, Y., Brodyansky, V.M.: Ferroelectrics **131**, 321–325 (1992)
8. Yu, B., Liu, M., Egolf, P.W., Kitanovski, A.: Int. J. Refrig **33**, 1029–1060 (2010)